Performance of Multi-Antenna Enhanced HSDPA

Berger, Lars Torsten

Publication date:
2005

Document Version
Publisher's PDF, also known as Version of record

Performance of Multi-Antenna Enhanced HSDPA

Generalised MIMO DS-CDMA SINR Formulation and Interference Modelling for Run-Time Efficient HSDPA Network Performance Studies

by

Lars Torsten Berger

A Dissertation submitted to
the Faculty of Engineering and Science of Aalborg University
in partial fulfilment of the requirements for the degree of
Doctor of Philosophy,
April 2005, Aalborg, Denmark.

Supervisors
Professor Preben Mogensen, Ph.D.,
Aalborg University, Denmark.
Wireless Network Specialist Troels E. Kolding, Ph.D.,
Nokia Networks Aalborg R&D, Denmark.
Assistant Professor Laurent Schumacher, Ph.D.,
University of Namur, Belgium.

Defense Chairman
Associate Professor Troels Sørensen, Ph.D.,
Aalborg University, Denmark.

Opponents
Professor Jørgen Bach Andersen, Dr. techn., Dr. tekn. h.c.,
Aalborg University, Denmark.
Professor Witold A. Krzymień, Ph.D., P.Eng.,
University of Alberta, Canada.
Principle Scientist Olav Tirkkonen, Dr. techn.,
Nokia Research Center, Helsinki, Finland.

R05-1007
ISSN 0908-1224
ISBN 87-90834-76-3

Meinen Eltern
Marlies und Walter Berger

Abstract

The performance of multiple antenna enhanced *high speed downlink packet access* (HSDPA) is investigated using link and network simulations. The simulation model is based on a generalised MIMO DS-CDMA SINR formulation as well as a novel other-sector interference model for run-time efficient network performance simulations. With these tools the benefit of different multi-antenna processing schemes is assessed and benchmarked against known as well as novel analytical bounds.

The derived MIMO DS-CDMA SINR formulation extends a standard SISO formulation to handle general MIMO configurations. The formulation is based on a virtual channel concept, where a virtual channel represents the radio propagation channel after transmit weight application. Thereby it allows the description of complex scenarios, where different signals are simultaneously delivered using different multiple antenna transmission strategies. Spatial multiplexing with channelisation code reuse as well as multiple scrambling code deployments are supported.

Cellular MIMO system performance heavily depends on mean powers and spatial correlations of desired as well as dominant interfering signals. For MIMO performance assessment an other-sector interference model is developed based on a standard hexagonal grid macrocellular scenario set-up. The model allows the combination of detailed link and run-time efficient network simulations. Only two parameters - a user's average own-to-other-sector received power ratio and a user's azimuth angle of connection to the serving sector's antenna array - are required to describe the user's average performance. For each parameter-pair a time evolving SINR trace, affected by spatially coloured and time variant interference, is stored in a user-performance database. Different network simulations then reuse the processing intensive SINR link level simulation results by indexing into this database. The model delivers comparable accuracy to brute-force cellular scenario simulations, while reproducible network performance results can be obtained within 20 minutes on a conventional 3 GHz PC.

With the derived MIMO DS-CDMA SINR formulation and the developed other-sector interference model, performance of *closed loop transmit diversity mode 1* (CLM1) and dual stream *spatial multiplexing* (SMP) is assessed. Single and dual rx antenna RAKE and MMSE receivers are considered. Measured in terms of sector throughput, 2×2 CLM1 configurations with highly correlated tx antennas perform best, delivering between 70% to 200% gain over 1×1 SISO references.

Further, at high instantaneous SINR, SMP enhances throughput performance due to dynamic range extension.

Dansk Resumé [1]

Denne afhandling undersøger link- og netværks-performance af *high speed downlink packet access* (HSDPA) i kombination med multiple antenner. Der anvendes en simuleringsmodel baseret på en generaliseret MIMO DS-CDMA SINR formulering, og en ny unik nabo-celle interferensmodel der muliggør effektiv afvikling af netværks-performance simuleringer. Med disse værktøjer er værdien af forskellige multiple antennekoncepter vurderet og sammenholdt med kendte såvel som nye unikke analytiske grænseværdier.

Den udledte MIMO DS-CDMA formulering udvider en standard SISO formulering til at håndtere generelle MIMO konfigurationer. Formuleringen er baseret på definition af en virtuel kanal, hvori er inkluderet effekten af radiokanalen og den anvendte antennevægt ved transmission. Dette virtuelle kanalkoncept tillader en beskrivelse af komplekse scenarier hvor forskellige signaler samtidigt overføres ved brug af forskellige strategier for multiple antenne transmission. Det er således muligt at inkludere genbrug af channelisation-koder og at anvende multiple scrambling-koder i forbindelse med spatial multiplexing.

Performance af cellulære MIMO systemer afhænger i høj grad af middeleffekt og antennekorrelation forbundet med ønsket såvel som dominerende interfererende signaler. For vurdering af MIMO performance er der således udviklet en nabo-celle interferensmodel baseret på et standard heksagonelt macro-cellulært netværk. Modellen tillader kombinationen af detaljerede link- og kørselseffektive netværks-simuleringer hvor kun to parametre - en brugers middeleffektforhold mellem egen- og nabo-celle modtaget effekt og samme brugers azimut til egen sektors antennekonfiguration - er nødvendige for at beskrive brugerens middelperformance. Hvert par af parametre indekserer en bruger-performance database med et modsvarende tidsforløb af SINR influeret af korreleret og tidsvarierende interferens. Forskellige netværkssimuleringer genbruger således de ellers beregningskrævende SINR link-performance resultater. Modellen giver tilsvarende nøjagtighed som mere direkte implementerede simuleringer, alt imens reproducerbare performance resultater kan genereres indenfor 20 minutter på en konventionel 3 GHz PC.

Den udledte MIMO DS-CDMA formulering og den udviklede nabo-celle interferensmodel er anvendt til at vurdere performance af *closed loop transmit di-*

[1] Translation by Troels Sørensen, CSys Devision, Aalborg University, Denmark.

versity mode 1 (CLM1) og *spatial multiplexing* (SMP), inkluderende enkelt- og dobbelt-antenne baserede RAKE og MMSE modtagere. Målt ved den supporterede trafikbelastning per sektor opnås den bedste performance for 2×2 CLM1 konfigurationer med høj korrelation mellem tx-antenner, svarende til en forbedring i forhold til 1×1 SISO på mellem 70% og 200%. Endvidere forbedrer SMP den supporterede trafikbelastning ved høj øjeblikkeligt SINR som følge af et forbedret dynamikområde.

Preface and Acknowledgments

This dissertation is the result of a three and a half years' project carried out at the *Division for Cellular Systems* (CSys), Department of Communication Technology, Aalborg University under supervision and guidance from Professor Preben E. Mogensen (Aalborg University, Denmark), Dr. Troels E. Kolding (Nokia Networks Aalborg R&D, Denmark), and Assistant Professor Laurent Schumacher (University of Namur, Belgium). The dissertation has been completed in parallel with the mandatory coursework, teaching, and project work obligations in order to obtain the Ph.D. degree. On the 27^{th} May 2005 the work has been successfully defended against questions from the assessment committee and from the public audience. The committee consisted of Professor Witold A. Krzymień (University of Alberta, Canada), Principle Scientist Dr. Olav Tirkkonen (Nokia Research Centre, Helsinki, Finland), and Professor Jørgen Bach Andersen (Aalborg University, Denmark, Chairman of the committee). The defence was chaired by Associate Professor Troels Sørensen (Aalborg University, Denmark). The research has been financed by Nokia Networks Aalborg R&D and was partly also supported by the European Union's IST METRA and I-METRA projects [METR01], [I ME03].

First of all I would like to thank my M.Sc. supervisors Mark Beach and Dean Kitchener, who introduced me to the mystery of MIMO communications. Secondly, I would like to thank my Ph.D. supervisors for their guidance, advice and co-operation. Every one of them has contributed significantly to this work, each in a very individual way, and I am very thankful and happy to have had such a diverse group of highly qualified supervisors.

Further, I would like to thank the members of the assessment committee who through their detailed reading and constructive feedback have helped to correct and clarify individual points throughout this dissertation.

Besides, the constant friendly support, and the proofreading from the multitasking enabled secretaries Lisbeth Schiønning Larsen and Jytte Larsen is highly appreciated.

Clearly the presented work would not have been possible without being part of an inspiring network of colleagues, enabling interesting discussions and collaboration. In this respect I would like to particularly point out the good collaboration with Juan Ramiro Moreno, Pablo Ameigeiras Gutiérrez, Troels Sørensen, Persefoni Kyritsi, Pedro Fernandes, Jorge Mártires, Laurent Bonnot, Frank Frederiksen, and Klaus. I. Pedersen, which have led to common publications. Further, I would

like to specifically thank Wei Na, Claudio Rosa, Per-Henrik Michaelsen, Konstantinos Dimou, Jean-Philippe Kermoal, Joachim Dahl, Søren Skovgaard Christensen, Christoffer Roedbro and Yasushi Takatori for their valuable input.

I am also very grateful to have had a very nice bunch of friends around me that made my stay here in Aalborg very enjoyable. To list all of them would clearly stretch these acknowledgements a bit. Thus I constrain myself to mention José Outes Carnero, Carl Wijting, and Emmanuel Fleury with whom I shared a lot of fun, and who also had always an open ear when things were not going as planned.

Finally, I would like to thank those who, despite quite some physical distance, have been closest to my heart throughout this challenging time. The love and affection of my familiy – Heinrich Schäfers, Marlies, Walter and Ina Berger – , as well as of my girlfriend Magüi Morell González have enabled this work.

Lars Torsten Berger

June 2005

Notation

Acronyms and mathematical conventions are listed below for quick reference. They are additionally defined at their first occurrence.

Acronyms

2G	*second generation*
3G	*third generation*
3GPP	*Third Generation Partnership Project*
ACK	*acknowledgement*
AoA	*angle of arrival*
AoC	*line of sight angle of connection*
AoD	*angle of departure*
AS	*rms angle spread*
AWGN	*additive white Gaussian noise*
CDMA	*code division multiple access*
CLM1	*closed loop transmit diversity mode 1*
CLM2	*closed loop transmit diversity mode 2*
cdf	*cumulative probability density function*
CQI	*channel quality indication*
CRC	*cyclic redundancy check*
CSys	*Division for Cellular Systems*
DCH	*dedicated channel*
DIR	*dominant interference ratio*
DSCH	*downlink shared channel*
DS-CDMA	*direct sequence* CDMA
ECR	*effective code rate*
EGC	*equal gain combining*

FDD	*frequency division duplex*
G-factor	*cell geometry factor*
G	*cell geometry factor*
GSM	*Global System for Mobile Communication*
GHz	*gigahertz*
HARQ	*hybrid automatic retransmission request*
hc	*highly correlated*
HSDPA	*high speed downlink packet access*
HS-DSCH	*high-speed downlink shared channel*
HS-SCCH	*high speed shared control channel*
I-METRA	*intelligent multi-element transmit and receive antennas*
i.i.d	*independent identical distributed*
IER	*interference error ratio*
IR	*incremental redundancy*
IPI	*inter path interference*
IST	*Information Society Technologies*
ITU	*International Telecommunication Union*
km/h	*kilometer per hour*
m	*meter*
M.Sc.	*Master of Science*
MAC	*medium access control*
Mc/s	*megachip per second*
MCS	*modulation and coding scheme*
METRA	*multi-element transmit and receive antennas*
MHz	*megahertz*
MIMO	*multiple input multiple output*
MISO	*multiple input single output*
MMSE	*minimum mean square error*
MRC	*maximum ratio combining*
NACK	*negative acknowledgement*
Node-B	*UTRAN terminology for base station*
OPC	*optimum combining*
OWNP2	*own site plus 2 other sector interference model*
PARC	*per antenna rate control*

PAS *power azimuth spectrum*
PCPICH *primary common pilot channel*
PDP *power delay profile*
pdf *probability density function*
PEP *packet error probability*
PF *proportional fair*
PIC *parallel interference cancellation*
PSC *primary scrambling code*
QAM *quadrature amplitude modulation*
QPSK *quadrature phase shift keying*
Rel'99/4 *release 99/4*
Rel'5 *release 5*
Rel'6 *release 6*
rms *root mean square*
rx *receive*
RR *round robin*
S-PARC *selective* PARC
SAW *stop-and-wait*
SDMA *space division multiple access*
SIMO *single input multiple output*
SINR *signal to interference plus noise ratio*
SISO *single input single output*
SCH *synchronisation channel*
SIC *successive interference cancellation*
SNR *signal to noise ratio*
SMP *spatial multiplexing*
SMP$_x$ SMP *with full weight selection freedom*
SMP$_{dual}$ SMP *limited to dual stream transmission*
SMP$_{sel}$ SMP *limited to selection transmit diversity*
SMS *short message service*
SSC *secondary scrambling code*
STTD *space-time transmit diversity*
SVD *singular value decomposition*
TTI *transmit time interval*

TPC	*transmission power control*
tx	*transmit*
UE	*user equipment*
UMTS	*Universal Mobile Telecommunication System*
UTRAN	*UMTS terrestrial radio access network*
wc	*weakly correlated*
WCDMA	*wideband code division multiple access*

Mathematical Conventions

Although some parameters and values will be presented in dB, calculations are always displayed using linear values. Further, following conventions are used throughout.

$\mathbf{A}$	Bold upper case indicates a matrix.
$\mathbf{a}$	Bold lower case indicates a vector. Exceptions to above rule have been made for the virtual channel power vectors $\mathbf{P}^i$ and $\mathbf{P}^{k,i}$, as well as for the virtual channel power allocation matrix ω^j.
A, a	Non-bold indicates scalar.
$a \times b$	Matrix dimension indication, *i.e.* a rows times b columns.
$\mathbf{I}_a$	An $a \times a$ identity matrix.
$(\mathbf{A})_{[:,1:4]}$	Indexing notation, *e.g.* the first to fourth columns of $\mathbf{A}$.
$(\mathbf{a})_{[2]}$	Indexing notation, *e.g.* the second element of $\mathbf{a}$.
$(\cdot)^*$	Complex conjugate.
$(\cdot)^T$	Transpose.
$(\cdot)^H$	Hermitian, *i.e.* complex conjugate transpose.
$(a)^x$	a to the power of x.
a^x	a with superscript index x.
$\{\mathrm{A}\}$	Sequence of realisations of A.
$\mathrm{Re}\{\cdot\}$	Real component of complex number.
$\lceil \cdot \rceil$	Rounding up to the nearest integer.
$\lvert \cdot \rvert$	Absolute.
$\lim_{z \uparrow a}$	Taking the limit, approaching a from below.
$\lim_{z \downarrow a}$	Taking the limit, approaching a from above.
$\wedge$	AND
$\vee$	OR
$\forall$	FOR ALL

$\in$	IS ELEMENT OF
$\left\|\mathbf{a}\right\|_p$	Vector norm defined as $\left\|\mathbf{a}\right\|_p = \left(\sum_i \left\|\mathbf{a}_{[i]}\right\|^p\right)^{\frac{1}{p}}$. The 2-vector norm is abbreviated as $\left\|\mathbf{a}\right\|$.
$\mathrm{E}_x\left\{f(x)\right\}$	Expectation with respect to x.
$\mathrm{E}_{x,y}\left\{g(x,y)\right\}$	Expectation with respect to x and y.
$\mathrm{Var}\left\{x\right\}$	Variance of random variable x, $\mathrm{Var}\left\{x\right\} = \mathrm{E}\left\{\left(x - \mathrm{E}\left\{x\right\}\right)^2\right\}$.
$\mathrm{Std}\left\{x\right\}$	Standard deviation of random variable x, $\mathrm{Std}\left\{x\right\} = \sqrt{\mathrm{Var}\left\{x\right\}}$.
$\mathrm{E}_x\left\langle f(x)\right\rangle_a$	Ensemble average over a realisations of x, $\mathrm{E}_x\left\langle f\left(x\right)\right\rangle_a = \frac{1}{a} \cdot \sum_{i=1}^{a} f\left(x_i\right)$
$\mathrm{Var}_x\left\langle f(x)\right\rangle_a$	Variance estimate taken from a realisations of x, $\mathrm{Var}_x\left\langle f(x)\right\rangle_a = \frac{1}{a-1} \cdot \sum_{i=1}^{a}\left(f\left(x_i\right) - \mathrm{E}_x\left\langle f\left(x\right)\right\rangle_a\right)^2$ Standard deviation estimate taken from a realisations of x, $\mathrm{Std}_x\left\langle f(x)\right\rangle_a = \sqrt{\mathrm{Var}_x\left\langle f(x)\right\rangle_a}$
$\widetilde{\sigma}_x$	Short notation for the estimate of the relative standard deviation of x, $\widetilde{\sigma}_x = \frac{\mathrm{Std}_x\left\langle f(x)\right\rangle_a}{\mathrm{E}_x\left\langle f(x)\right\rangle_a}$. The number of realisations a will be clear from the context.
$\left[F\left(x\right)\right]_b^a$	Evaluate the function $F\left(x\right)$ at the borders a and b, $\left[F\left(x\right)\right]_b^a = F\left(a\right) - F\left(b\right)$.
$\delta\left(a-b\right)$	Dirac-Delta-Function, *i.e.* 1 for $a = b$ and 0 otherwise.
$\mathrm{pr}\left(x\right)$	Probability density function of x.
$\mathrm{Pr}\left(x\right)$	Cumulative probability density function of x.
$N_{something}$	Indicates number of *something*. This number is constant at least for a simulation set up.
$\widetilde{N}_{something}$	Indicates number of *something*, but different from above this number can change with time.
$\overline{x}$	Short notation for the mean of x.
$\widehat{x}$	Short notation for the estimate of x.

Contents

Chapter 1

Introduction

1.1 Motivation and Scope

After the success stories of voice and *short message service* (SMS) data communication over the *second generation* (2G) mobile communication standard *Global System for Mobile Communication* (GSM), the *third generation* (3G) *Universal Mobile Telecommunication System* (UMTS) standard [Rich00] starts to provide the end user with a whole new range of wireless data communication services, like multimedia messaging, web browsing, online gaming, streaming, *etc.* [Holm04, Chp. 2]. While this opens up new sources of revenue for equipment manufacturers, as well as service and contents providers [UMTS03], it puts on the other hand increased network capacity demands on the UMTS. Increasing the number of base station sites, using more frequency bands as well as physical layer and *medium access control* (MAC) layer enhancements of the existing network infrastructure are candidate solutions. With increasing costs for base station site acquisition and maintenance, as well as with scarcely available and pricey frequency spectrum, enhancements to the physical and MAC layer are attractive. Therefore the *Third Generation Partnership Project* (3GPP) [3GPP04j], in charge of UMTS standardization, introduced *high speed downlink packet access* (HSDPA) as part of its *UMTS terrestrial radio access network* (UTRAN) *release 5 standard* (Rel'5), with significant updates to physical and MAC layer procedures [Hedb00], [Kold03b]. Due to these updates *single input single output* (SISO) HSDPA has the potential to more than double previous UTRAN Rel'99/4 packet data capacity [3GPP01a], [Chiu04]. Higher layer protocol enhancements [3GPP04c], as well as *multiple input single output* (MISO), *single input multiple output* (SIMO), and *multiple input multiple output* (MIMO) antenna processing schemes in Rel'6 and beyond are expected to increase this capacity further [Holm04, pp. 338-339]. Moreover, upgrading the receiver from standard RAKE receivers, to more advanced *minimum mean*

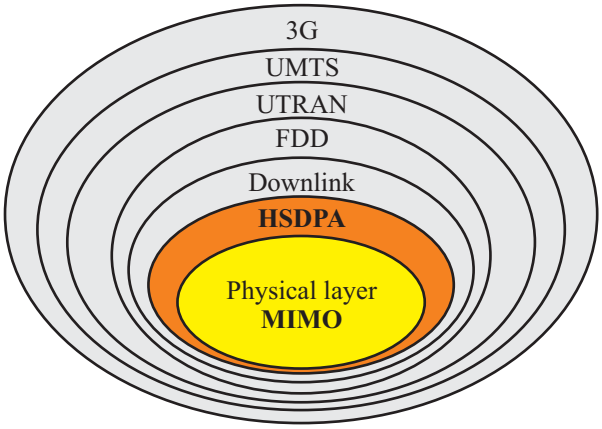

Figure 1.1: HSDPA physical layer enhancements based on MIMO antenna processing as the main focus of this dissertation in the broader context of 3G.

square error (MMSE) receivers can enhance physical layer performance [Proa01], [Klei97].

As visualised in Figure 1.1 MIMO antenna processing techniques are the key physical layer enhancements to be investigated in the following. The scope is limited to UTRAN *frequency division duplex* (FDD), where uplink and downlink channels occupy different parts of the frequency spectrum. The biggest share of Europe's UTRAN frequency allocation is devoted to FDD, and it is the duplexing strategy used in Europe's first commercial UTRAN deployments [Holm04, Chp. 1].

1.2 WCDMA

Multiple access interference poses the key limitation to network throughput. The following introduces the sources of multiple access interference and looks at advanced receivers to combat interference.

1.2.1 Code Division Multiple Access

Besides separating uplink and downlink channels in different frequency bands the wireless resources time, frequency, and transmit power need to be shared between multiple users, or more generally between multiple data sequences. *Code division multiple access* (CDMA) is the standard multiple access scheme in 3G to share these resources. Different flavours of CDMA, rooting back over half a century to Shannon and Pierce [Elle84], [Scho94], exist and are reviewed in [Pras98], [Rap-

p99]. UTRAN uses *direct sequence* CDMA (DS-CDMA), where every symbol of the data signal sequence is multiplied with multiple code chips from a CDMA code sequence. Direct sequence spreading causes the resulting spread signal to occupy a wider bandwidth than the original signal, and multiple spread data sequences can be transmitted simultaneously in the same frequency band. The basic principle of DS-CDMA is visualised in Figure 1.2.

The DS-CDMA receiver despreads the received chip sequence with the right code, *i.e.* with the complex conjugate of the original code sequence, which coherently combines the individual chips into the original data symbol. In a frequency selective channel multiple versions of the originally transmitted chip sequence reach the receiver. Despreading each delayed component with a correspondingly delayed code leads to multiple soft estimates of the original data symbol that can, for example, be combined using the *maximum ratio combining* (MRC) principle [Kahn54], [Bren55], [Jake94, p. 316]. This kind of DS-CDMA receiver, patented in 1956 [Scho94] [Pric58], became known as the RAKE receiver. Using several despreaders, also referred to as correlators or RAKE fingers, the receiver *rakes up* the different delayed signal components [Rapp99, Chp. 6],[Holm04, Chp. 3]. The different delays are inferred by a multipath rich scattering environment, where the signals travel over radio propagation paths with different physical length [Rapp99, Chp. 4]. Hence, the RAKE receiver is able to exploit frequency diversity. The diversity order is determined by the number of delayed components exploited by the RAKE receiver's despreaders.

In UTRAN the chip rate is set to 3.84 Mc/s. The carrier spacing is 5 MHz. It is a transmit filter requirement that one carrier's transmit power has an attenuation of at least 45 dB in adjacent bands [3GPP04a]. The occupied bandwidth is around three times the bandwidth used in the first commercially deployed IS-95 CDMA networks [Pras98]. Based on the fact that this bandwidth is often wider than the coherence bandwidth of the radio propagation channel [Rapp99, p. 163], the UTRAN air interface is called *wideband code division multiple access* (WCDMA) [Pras98], [Tann04].

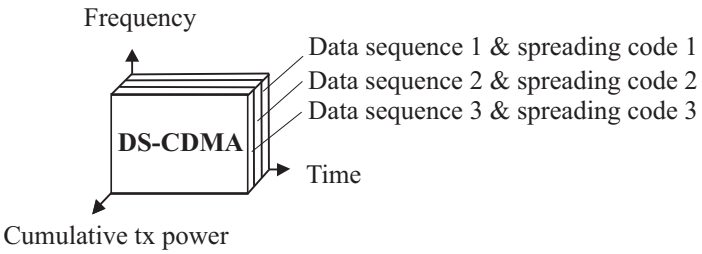

Figure 1.2: Basic DS-CDMA multiple access principle.

1.2.2 Own and Other-Sector Interference

In the downlink of a multi cellular UTRAN FDD deployment multiple access interference can come from signals transmitted in the same sector or signals transmitted in other sectors. Such a cellular multiple access interference situation is depicted in Figure 1.3 (a), while UTRAN spreading code construction is shown in Figure 1.3 (b).

Spreading codes are constructed through chip-by-chip multiplication of orthogonal Walsh-Hadamard codes, *i.e.* with zero cross correlation at zero lag, and segments of 'quasi-orthogonal' Gold codes sequences, *i.e.* with very low cross correlation independent of the lag [Stub97, pp. 422-425], [3GPP03c]. A data symbol is spread with N_{sf} chips, where N_{sf} denotes the spreading factor. Different sectors use different scrambling codes. Hence, signals received from other sectors are experienced as other-sector interference. Due to coherent combining of the desired signal's chip-sequence the desired signal power incurs a despreading gain of N_{sf} over other-sector interference. This gain is also known as processing gain.

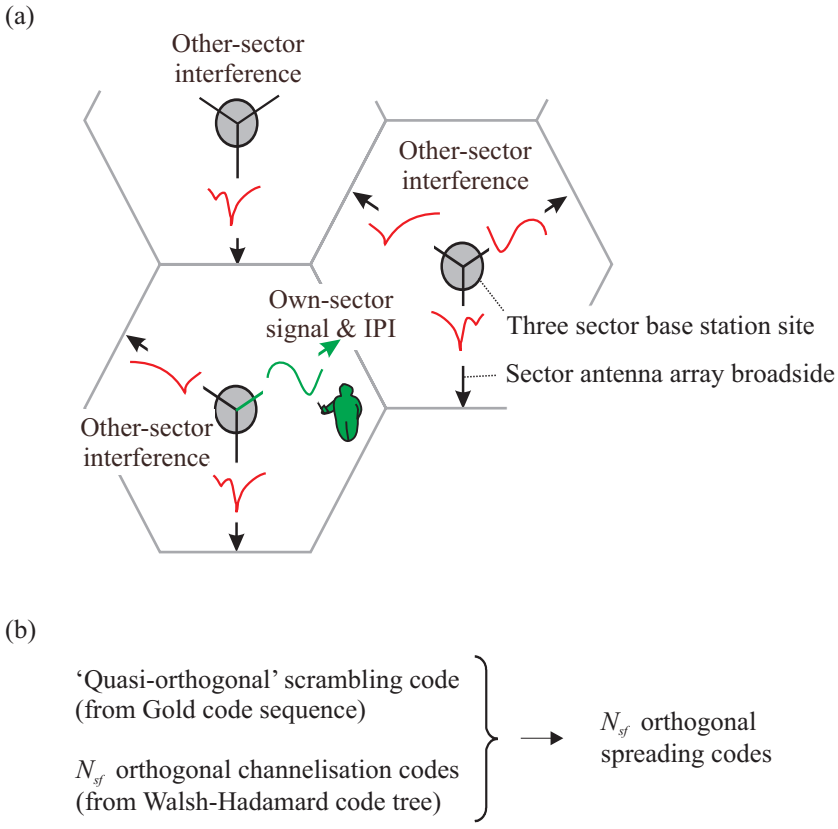

Figure 1.3: (a) Multiple access interference situation. (b) Spreading code construction.

In standard network configurations signals transmitted in the same sector use the same scrambling code, but different orthogonal channelisation codes. Signals received with the same delay are therefore orthogonal. However, the number of orthogonal codes is limited to the number of chips used for spreading every data symbol, *i.e.* to N_{sf}. Increasing the spreading factor implies decreasing the symbol rate to comply with the fixed chip rate. Signal sequences that are not received with the same delay as the desired signal have non zero cross-correlation and therewith cause so-called *inter path interference* (IPI). In a heavily loaded system IPI, from the own signal and other users' signals, can drastically degrade RAKE receiver performance [Klei97].

1.2.3 Receiver Enhancement Candidates

Advanced DS-CDMA receiver techniques based on multi-user detection and/or channel equalisation have been developed to overcome IPI. Optimal multi-user maximum-likelihood sequence detection [Verd86], as well as sub-optimal multi-user detection as surveyed and treated in [Duel95], [Klei96], [Bueh00] are deemed as too complex for downlink reception due to processing power constraints at the mobile terminal [Mosh96]. However, based on the fact that in a single sector SISO downlink all spread signal sequences reach a user through the same time dispersive multipath channel, Klein proposed pre-equalisation [Klei97]. This time aligns delayed signal components before the despreading operation. It therewith re-establishes orthogonality between the own-sector signals and avoids IPI. Over the years many different linear equalisation based receiver architectures emerged, *e.g.* [Ghau98], [Fran98], [Hool99], [Wern99], [Zolt99], [Krau00], [Hool01], [Lena-01b], [Lena01a], [Mail01], [Hadi02], [Krau02], [Fran02]. Further performance improvement is among others in [Woln98], [Wang02b], [Wang02a] attributed to non-linear *successive* or *parallel interference cancellation* receivers (SIC), (PIC). Nevertheless, for simplicity the following considers only linear RAKE and linear MMSE receivers. This selection is led by the fact that these two receivers constitute the fundamental building blocks of most non-linear receivers as well. The RAKE receiver is seen as baseline reference that performs MRC of the delayed signal sequences. The MMSE receiver, also referred to as optimum filter or Wiener Filter [Hayk96, Chp. 5], whitens coloured interference, and performs *optimum combining* (OPC) over delayed signal sequences.

1.3 UTRAN and HSDPA Evolution

Data and signalling channels are used to assure error free data packet delivery to the users. The following first introduces essential channels for basic operation and

then looks at HSDPA channels, among others, also with respect to their specific interference contribution.

1.3.1 Basic Operation

To establish and maintain data communication between a base station and a mobile station, which in UTRAN terminology are also referred to as Node-B and *user equipment* (UE), different data and signalling channels are needed. When entering a network, the UE first performs a cell search procedure to obtain synchronisation with the basic time entities, *i.e.* the chip, the slot, and the frame boundaries, where a slot contains 2560 chips, and a frame contains 10 slots. To obtain synchronisation two scrambling codes are cyclically broadcast in each sector. They are referred to as *synchronisation channel* (SCH). Details on the cell search procedure are available in [3GPP04g]. After a successful cell search procedure the UE not only knows the timing within a sector, but also the primary scrambling code that in a standard set-up is used to scramble all further signalling and data channels in the sector. So is a *primary common pilot channel* (PCPICH) constantly broadcast in the sector using the primary scrambling code and a 256 chip long Walsh-Hadamard code sequence. Based on this pilot channel the UE performs channel estimation and extracts also average received power information from the neighbouring sectors. Up to eight additional signalling channels are active in the downlink direction. Their detailed functionality can be found in [3GPP04f].

Specifically for communication a *dedicated channel* (DCH) is established between Node-B and UE. This DCH is power controlled, meaning that the Node-B adjusts the DCH power according to *transmission power control* (TPC) requests it receives from the UE via uplink signalling [3GPP04g]. Further, the DCH supports soft handover, which is the ability to receive multiple copies of the same data from two different sectors [Holm04, pp. 58-60]. Once established, the spreading factor on the DCH is fixed, and the DCH might for example be used to deliver delay stringent speech services to the user. For packet data, like for example the download of a web page, high peak data rates with low duty cycle are required. To accommodate these needs a *downlink shared channel* (DSCH) has been defined in addition to the DCH. Using this DSCH, users that for a short time require a high data rate can share the orthogonal code resources in a time division multiple access manner.

Convolutional or turbo forward error correction coding [Hayk94], [Guiz04] is used to protect the data transmission on DSCH and DCH. Should a data packet not be correctly decodable, the UE discards it and asks for a retransmission. This procedure is also known as *hybrid automatic retransmission request* (HARQ) Type-I [Lin84], [Malk01], [Rosa04, p. 48]. Further, like the DCH the DSCH uses power control and can additionally dynamically update its spreading factor on a frame-to-

frame basis. However, it does not support soft handover. Before receiving a packet over the DSCH the UE receives a message on an associated DCH informing it when to expect the DSCH packet and with which format the packet is encoded. A simplified sketch of the basic UTRAN channel structure is given in Figure 1.4.

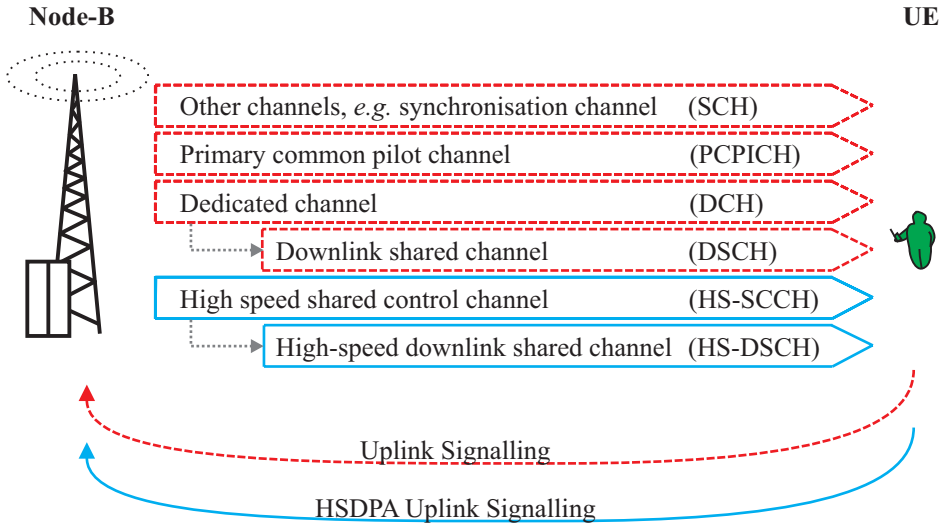

Figure 1.4: Simplified UTRAN downlink channel structure. No explicit distinction is made between transport and physical channels. Basic channels are dashed. Channels introduced in connection with HSDPA operation are marked solid.

1.3.2 The HSDPA Evolution

The downlink DCH and DSCH, displayed in Figure 1.4, are already part of the UTRAN Rel'99/4 specifications [Holm04, Chp. 1]. With the introduction of HSDPA in Rel'5 additional uplink and downlink signalling as well as a *high-speed downlink shared channel* (HS-DSCH) were introduced [3GPP03b], [3GPP02a]. Packet data previously transmitted over the DSCH can be transmitted using the HS-DSCH instead. The *high speed shared control channel* (HS-SCCH) informs the UE prior to a HS-DSCH packet data transmission about its timing and encoding format.

The main difference of the HS-DSCH with respect to the DSCH is that power control and dynamic spreading factors are replaced by dynamic multicode operation, adaptive modulation scheme selection and adaptive forward error correction coding [Chua96], [Kold01], [Kold03b]. *E.g.* when the *signal to interference plus noise ratio* (SINR) of a link is low, the HS-DSCH uses a more robust modulation scheme than when it is high, which proves to be more spectrally efficient [Gold97].

Besides, a UE can request a fast retransmission in case the initially received data packet could not be decoded error free. The HARQ-retransmission procedure in HSDPA is part of layer one signalling and can therefore be executed much faster then the layer two HARQ-retransmission procedure used on the DCH and DSCH channels [Kold03b], [3GPP02a]. Further, should a retransmission be needed, the UE does not discard the original packet, but keeps the symbol information in memory, which is also known as HARQ Type-II/III [Malk01], [Rosa04, p. 48]. After reception of the retransmission the UE combines the packets, which increases the overall SINR. Different combining methods exist [Mand74], [Lin84], [Chas85], and performance evaluation of HSDPA HARQ schemes can be found in [Malk01], [Das01], [Fred02].

Moreover, HSDPA introduces the option of link quality dependent scheduling, meaning that HS-DSCH resources can be assigned to users when they are in good multipath conditions. Related information-theoretical treatment of link quality dependent scheduling can be found in [Knop95], [Tse98], [Hanl98]. More application oriented work, leading to a variety of packet scheduling algorithms, is presented in [Bhag96], [Holt00], [Bend00], [Elli02]. Throughout the following the so-called *proportional fair* (PF) packet scheduling algorithm [Holt01] will be used as it delivers an appealing trade-off between fair user resource sharing and network capacity enhancement [Kold02], [Amei03], [Kold03a]. By scheduling the user that is in the best downlink situation with respect to its mean the PF scheduler introduces selection diversity to the system [Jake94, pp. 313-316]. As it selects from a pool of users, this form of selection diversity is also referred to as *multi-user diversity* [Heat01]. Additionally, a downlink quality blind *round robin* (RR) scheduling algorithm is selected as base line reference, which allocates downlink time to the users in a sequential manner [Elli02].

Simulated performance results for single antenna HSDPA systems, using standard RAKE receivers, can, among others, be found in [Love01], [Peis02], [Kold02], [Park03], [Chiu04], [Pede04]. Although absolute performance numbers are difficult to compare due to varying simulation set-ups, the general conclusion is that HSDPA in UTRAN Rel'5 is able to roughly double the network capacity compared to basic Rel'99/4 DCH/DSCH operation.

1.3.3 HSDPA Specific Interference Variation

As introduced in the previous subsection link adaptation and the PF scheduling mechanism base their decisions on the users' instantaneous downlink quality. Especially to obtain multi-user diversity, it is essential that the users' achievable data rates are time variant [Holt01], [Visw02], [Bonn03]. This relates to SINR variations within the system's dynamic range. However, performance of link adaptation and PF scheduling mechanisms degrade when a user's SINR changes significantly

from the time of SINR estimation to the time of actual downlink transmission. Previous studies included SINR variations caused by terminal movement [Berg03], [Rami03a], [Rami03b]. Network level simulations showed that at terminal velocities exceeding 20 to 30 km/h the performance benefit of HSDPA is limited, as the inherent closed loop mechanisms lose track of the actual downlink channel conditions [Rami03a], [Rami03b].

Throughout the following results are obtained for 3GPP *mobility distribution 3* [3GPP04d], where all users move with the same speed of 3 km/h. This mobility distribution is considered to reflect the situation of HSDPA data service users. Related work on user mobility distribution measurement and modelling is available in [Brat99], [Brat03]. At 3 km/h terminal speed SINR variations due to Doppler are trackable and do neither harm link adaptation nor packet scheduling [Rami03a], [Rami03b]. Harmful interference variations might, however, come from fast and untrackable on/off pulsing of other sector's HS-DSCH transmissions. Such a situation is depicted in Figure 1.5 (a).

On/off switching of the HS-DSCH transmit power can occur in conservative configured systems that do not run under full load, but reserve a certain fraction of their tx power, denoted η^{HSDSCH}, to serve HSDPA users with very little delay if requested. Similarly, multiple tx antenna schemes that either switch between antennas or change tx antenna weights, for example, switching from the optimal weight configuration of one user to the optimal configuration of another, might cause abrupt and thus untrackable interference variations. These variations are specific to an HSDPA system, as a large part of the total sector tx power might be allocated to a single user, therefore not allowing for interference averaging effects. Using an example where all interfering sectors switch their HS-DSCH transmission from on to off, the resulting SINR difference, denoted ΔSINR , is upper bounded by

$$\Delta SINR \leqslant \frac{1}{1-\eta^{HSDSCH}} \quad . \tag{1.1}$$

This bound is plotted in Figure 1.5 (b). It can be seen that in an HSDPA dominated network, where 70 % of a sector's tx power is reserved for HS-DSCH transmission, the ΔSINR is upper bounded by approximately 5 dB. SINR variations of that scale might impact the closed loop HSDPA link adaptation and packet scheduling mechanisms. Further, turbo decoder performance degrades with increasing SINR variance experienced on the input data sequence [Brun04], [Berg04a].

1.4 Multiple Tx and Rx Antenna Deployments

The three multiple antenna gain mechanisms, (i) array gain, (ii) diversity order increase, and (iii) interference suppression are introduced. Further, selected antenna

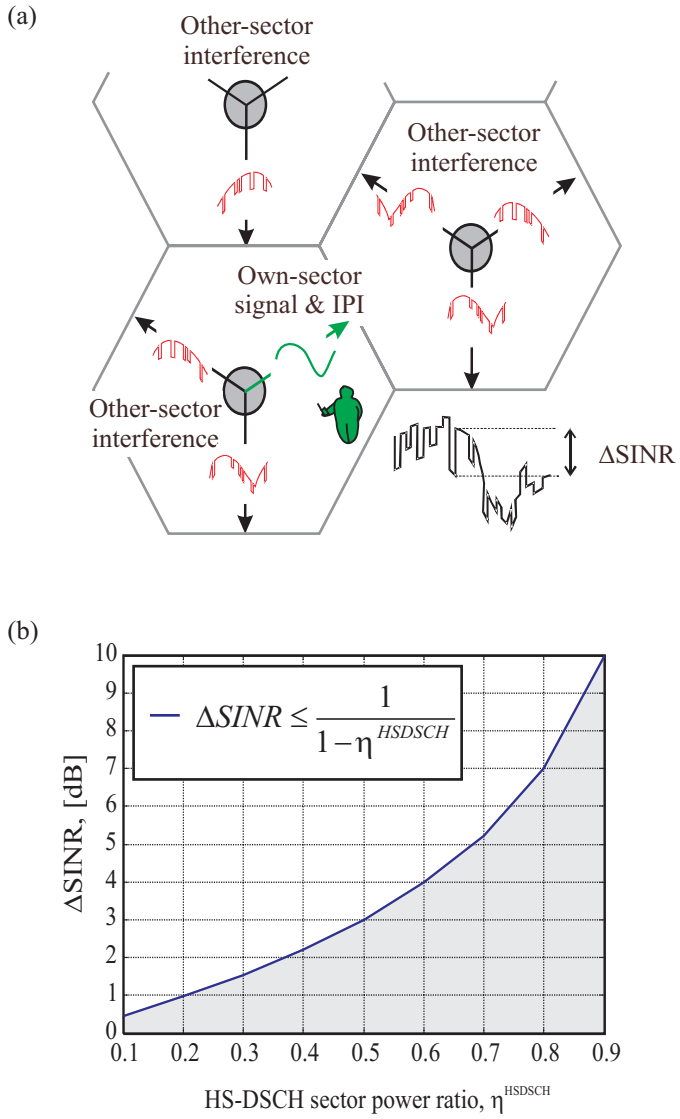

Figure 1.5: (a) Other-sector interference variability influencing a user's SINR trace. (b) Bound on the SINR variation, caused by all interferers switching the HS-DSCH tx power from on to off.

processing schemes, aiming at exploiting these gains, are considered with potentially several processing schemes simultaneously active within a sector.

1.4.1 Multiple Antenna Gain Mechanisms

Multiple antenna techniques have the potential to increase user data rate, system throughput, coverage, and quality of service with respect to delay and outage [Ande99]. Thus they pose an attractive enhancement technique to many SISO communication systems, and numerous studies on multiple antenna communication have been published in recent years. Comprehensive overviews can, among others, be found in [Hott03], [Gesb03], [Paul03] . In general, three different multiple antenna gain mechanisms exist:

(i) *Array gain* is the ratio of the mean SINR when a multiple antenna scheme is used to the mean SINR of a reference [Hamm00]. Under the prerequisite that the antenna signal processing algorithm does not attempt to suppress interference, the array gain, denoted β, is upper bounded by the product of the number of *transmit* (tx) antennas, N_{tx}, and the number of *receive* (rx) antennas, N_{rx}, *i.e.* $\beta \leq N_{tx} \cdot N_{rx}$ [Ande00].

(ii) *Diversity order increase* is reflected through an SINR variance reduction experienced over the multiple antenna link [Hamm00]. Antenna diversity allows the receiver to obtain the signal information in several ways. If one way fails, there might be others that do not. Again assuming that the antenna processing algorithm does not aim at interference suppression, the diversity order increase is upper bounded by $N_{tx} \cdot N_{rx}$ [Ande00].

(iii) *Interference reduction* increases the mean SINR and can in case of variable interference also reduce the SINR variance. The number of uncorrelated spatial interferers that can at the receiver be entirely suppressed is upper bounded by $N_{rx} - 1$. Looking at tx interference suppression, the transmitter at best might be able to avoid being received in up to $N_{tx} - 1$ locations and in correlated environments it can steer a null in up to $N_{tx} - 1$ directions [Vaug03, pp. 41-43].

The idea of *spatial multiplexing* (SMP), sparked by [Wint84], [Wint87], [Tela95], [Fosc96], [Paul97], and [Fosc98], is built on tx and/or rx interference suppression. A spatial multiplexing system transmits multiple data streams within the same geographical area, reusing all other resources, *e.g.* frequency, time and codes. Different data streams are, however, transmitted from different antennas or through different transmit antenna weights. In a multipath rich environment this leads to a situation where at the receiver the different streams exhibit different spatial signatures that have been imposed by the scattering medium. The receiver can then use spatial interference suppression to discriminate the different streams on the basis of their

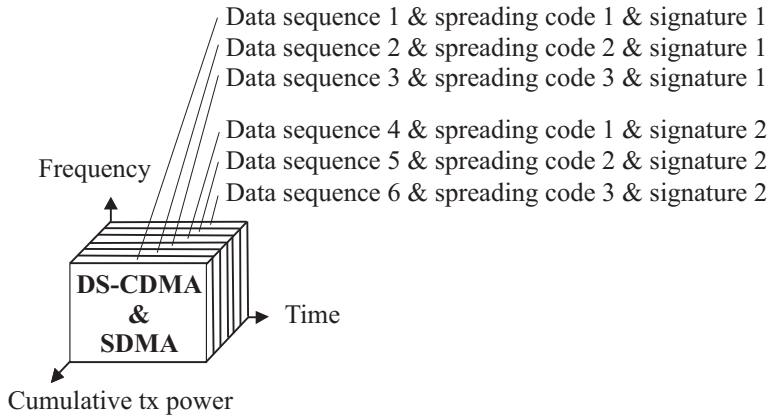

Figure 1.6: Basic DS-CDMA-SDMA multiple access principle.

signatures. Combined with DS-CDMA, spatial multiplexing, also known as *space division multiple access* (SDMA) [Rapp99, pp. 409-410], allows to increase the number of data streams that can be sent simultaneously. This is indicated in Figure 1.6 using an example of two spatial multiplexed streams. A *stream* is throughout defined as the collection of data sequences and spreading codes transmitted using a common spatial signature.

Seen in terms of Shannon capacity [Shan48] it is more spectrally efficient to send two streams with half the SINR than sending a single stream with full SINR, *i.e.*

$$\log_2\left(SINR+1\right) \leq 2 \cdot \log_2\left(\frac{SINR}{2}+1\right) \quad , \tag{1.2}$$

where equality holds for an SINR approaching zero and spatial multiplexing becomes specifically interesting for very high SINR. However, the price to pay for dual stream transmission is not only the division of the transmitted power between the two streams, but also a higher own-sector co-stream interference level. Additionally, the receiver will have to trade off own-sector co-stream interference suppression and other-sector interference suppression, typically leading to a decrease in the achievable SINR per stream [Paul03, Chp. 11].

How much array gain, diversity order increase and interference suppression gain can be obtained, depends besides on the number of tx and rx antennas, on the amount of available channel knowledge, multipath fading statistics, antenna correlation, antenna power imbalances, the presence of dominant interferers, and antenna processing [Vaug03]. Specifically with respect to UTRAN FDD a wide range of antenna processing schemes has been developed as introduced in the following subsection.

1.4.2 Multiple Antenna Enhancement Candidates

Using the argument that rx antenna deployments are not attractive from a battery-power consumption and terminal-cost point of view [Hott03, Chp. 1], a lot of emphasis has in previous years been put on the development of open as well as closed loop tx antenna processing techniques. *Closed loop* means that the base station tries to exploit downlink channel knowledge for antenna processing, and *open loop* means that it does not. A review of tx diversity schemes for the 3G standards in general can be found in [Derr02]. For data transmission UTRAN FDD Rel'99/4 specifications only include one open, and one closed loop transmit diversity technique with two sub cases (*mode 1* and *mode 2*) [3GPP02b] [Rami04a].

The open loop technique, called *space-time transmit diversity* (STTD), is based on a space time block coding algorithm presented in [Alam98]. It aims at diversity order increase, but does not use channel knowledge. Without using channel knowledge it is not possible to exploit tx array gain. STTD is therefore limited to reducing the SINR variance experienced on a link.

In *closed loop transmit diversity*, *i.e.* CLM1 and CLM2, the UE signals downlink channel information to the base station, where it is used to perform restricted tx MRC [Lo99], [Paul03, pp. 230-231]. This delivers, similarly to rx MRC, array gain and in case of uncorrelated tx antennas also a diversity order increase.

In UTRAN FDD Rel'5/6, CLM1 and STTD are the only two transmit diversity schemes standardised for use with the HSDPA channels [3GPP04f, p. 18]. For future releases it seems, from a practical point of view, possible to deploy up to four tx and rx antennas [3GPP04d], paving the way for SIMO and MIMO antenna configurations to be reconsidered for HSDPA physical layer enhancements. This has sparked a firework of 17 multiple antenna scheme proposals that can differ considerably in their tx and rx architectures as well as in the employed uplink signalling [3GPP04h], [3GPP04d].

To limit the scope throughout this dissertation CLM1 and a dual stream spatial multiplexing techniques, similar to *per antenna rate control* (PARC) [3GPP04d] and *selective* PARC (S-PARC) [3GPP04d], and in the following simply referred to as SMP$_x$ are selected for investigation. SMP$_x$ either transmits dual stream or selects only the better antenna for data transmission. Antenna selection provides the simplest form of tx array gain, and switching off the co-stream to avoid excessive co-stream interference can be seen as a simple form of tx interference suppression [Mart03], [Fern04]. This choice is motivated by the fact that CLM1 is already standardised for HS-DSCH transmission. Further, the idea of PARC like adaptive spatial multiplexing, as realised through SMP$_x$, is one key element of many proposals in [3GPP04d]. With this selection it is possible to study all three multiple antenna gain mechanisms. In this respect it should be noted that CLM1, especially

when deployed with high tx antenna correlation, can be seen as a simple beamforming configuration. Beamforming using larger tx array sizes, *e.g.* up to 8 tx antenna elements, is investigated in [Baum03], [Rami03a], [Pede03], [Rami04a], [Rami04b], and the corresponding specifications can be found in [3GPP04b].

STTD has not been selected as it shows little potential already in a single link situation [Hedb00], [Berg02], [Inga04]. Moreover, its channel averaging property was found to conflict with the concept of multi-user diversity with the risk of inflicting system performance losses [Kogi01], [Hoch02], [Berg03], [Rami03b]. However, it is noted that STTD might be useful to establish reliable communication with a high velocity user, whose downlink quality cannot be tracked [Rami03b], or for broadcast channels that are to be simultaneously received by a group of users. As a consequence STTD is the only tx diversity strategy standardised for the transmission of the HS-SCCH [3GPP04f, p. 18].

To limit the possible receiver options only single and dual antenna receivers are considered. Dual antenna RAKE receivers are selected to perform antenna branch MRC. Dual antenna MMSE receivers are selected to perform antenna branch OPC [Vaug88]. The antenna combining choice is therefore a natural extension of the receivers' multipath combining operation into the spatial domain. Focussing on antenna configurations up to 2×2 is influenced by the fact that the 2×2 case is an obligatory test case in the 3GPP MIMO scheme standardisation process [3GPP04d]. An overview of the selected multiple antenna processing configurations is provided in Table 1.1.

Related multiple antenna HSDPA performance studies have already become available in [Rami03a], [Rami03b], [Love03], [Poll04], [Sama04]. They give a

Tx-rx scheme			(i) Array gain	(ii) Diversity order increase	(iii) Spatial interference supp.
1×1	SISO	RAKE	–, –	–, –	–, –
1×1	SISO	MMSE	–, –	–, –	–, –
1×2	SIMO	RAKE	–, y	–, y	–, –
1×2	SIMO	MMSE	–, y	–, y	–, y
2×1	CLM1	RAKE	y, –	y, –	–, –
2×1	CLM1	MMSE	y, –	y, –	–, –
2×2	CLM1	RAKE	y, y	y, y	–, –
2×2	CLM1	MMSE	y, y	y, y	–, y
2×2	SMP$_x$	RAKE	y, y	y, y	y, –
2×2	SMP$_x$	MMSE	y, y	y, y	y, y

Table 1.1: Selected multiple antenna processing options to be considered throughout. The first entry in the columns (i) to (iii) relates to tx processing, while the second entry relates to rx processing. 'y' means *yes*, the antenna processing tries to exploit this gain mechanism.

clear indication that the selected multiple antenna enhancements, to be investigated throughout, each have the potential to improve HSDPA network performance.

1.4.3 Other Channel Transmissions

The downlink channels at focus in this dissertation have been displayed in Figure 1.4. In case CLM1 is used for HS-DSCH transmission, specific rules with respect to the transmission of the other downlink channels exist [3GPP04f], [Rami-04a]. An overview of these rules is given in Table 1.2 (a).

The PCPICH is required for downlink channel estimation. Two orthogonal pilot symbol sequences are broadcast from each antenna. They are scrambled with the primary scrambling code and spread with the same 256 chip long Walsh-Hadamard code. Moreover, the HS-SCCH is broadcast using STTD. The associated DCH uses the same transmission scheme as the HS-DSCH.

For comparison purposes, rules, similar to the once applied to CLM1, are adopted for the non standardised SMP. These rules are summarised in Table 1.2 (b). As in the CLM1 case two orthogonal pilot sequences are broadcast from the tx antennas. The HS-SCCH is broadcast using STTD. The DCHs are transmitted either from antenna 1 or antenna 2. This selection allows even simple single antenna terminals to receive the DCH without being disturbed by DCH co-stream interference.

In a frequency flat fading environment own-sector channels transmitted under orthogonal spreading codes do not cause interference. However, as introduced in

(a) CLM1

Channel	**Tx scheme**
PCPICH	2 orthogonal sequences
HS-DSCH	CLM1
HS-SCCH	STTD
DCH	CLM1

(b) SMP

Channel	**Tx scheme**
PCPICH	2 orthogonal sequences
HS-DSCH	SMP
HS-SCCH	STTD
DCH	Tx from either antenna 1 or 2

Table 1.2: Other channel transmission in case the HS-DSCH uses CLM1 (a) or SMP (b).

Subsection 1.2.2, IPI occurs in time dispersive multipath environments. Different tx strategies on the own-sector channels can complicate the equalisation problem and need to be considered in link performance assessments.

1.5 System Performance Evaluation

An evaluation strategy is required to assess the benefit of the selected physical layer enhancements. Analytical assessment, system simulations, and field trials are reviewed as possible means. Special emphasis is put on a quasi-static system simulation methodology selected for performance evaluation throughout.

1.5.1 Analytical Assessment

Closed form analytical assessment is desirable as it delivers the most in-depth insight into mechanisms and their interconnection. For simple flat fading situations extensive work on the performance of RAKE and MMSE receivers, that can be regarded as MRC and OPC respectively, is available in [Boga80], [Vill99], [Pham99], [Rao01], [Akyi01], [Akyi02], [Cui04], [Tokg04]. While these analytical results deliver valuable bounds, they are not able to describe common effects that can be encountered in a complex communication system such as UTRAN.

1.5.2 Performance Simulation

As extensive full system field trials are time consuming and impose an immense financial burden, Monte Carlo system simulations are the means of choice for initial system performance assessment and algorithm development [Jeru00], [Tran04]. Model abstraction and simplification become essential to find a practical trade-off between simulation inaccuracy and processing load as sketched in Figure 1.7.

Which parts of the system can be simplified depends on the questions to be answered. To assess the performance of radio resource management strategies and for network optimisation, dynamic network simulation tools would be required [Hama99], [Hopp01], [Nous02], [Rami03a], [Oute04], [Pede04]. Those dynamic network simulation tools are able to adapt to time varying data traffic situations in neighbouring sectors, but usually apply a higher abstraction level with respect to physical layer effects. However, within this dissertation the main focus is on physical layer enhancements. Their main differences surface when observing the obtainable SINR statistics including their temporal variation. Detailed propagation and link level descriptions are essential, whereas a higher abstraction level can be tolerated when modelling network issues. In this respect so called *quasi-static*

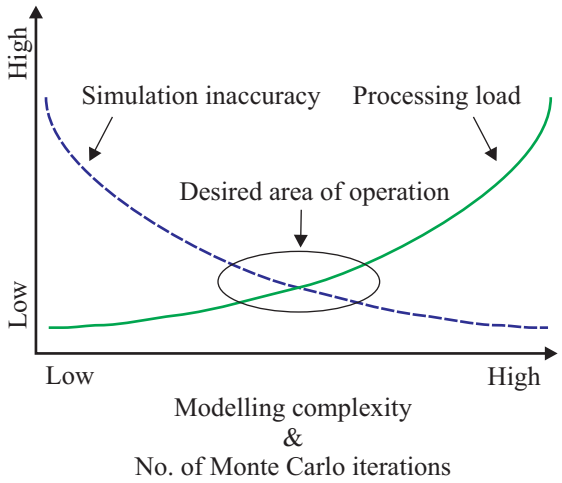

Figure 1.7: Simulation accuracy - processing load trade-off, inspired by [Tran04, p. 13].

network simulations [Rata02] are predestined, where only processes like multipath fading, tx powers, and tx weights are updated dynamically, while a user's average propagation situation remains constant. As a consequence, they do not allow to model live-death processes of multipaths [Papa90], nor do they update the multipath's angular characteristics.

1.5.3 Quasi-Static Simulation Methodology

Due to its accurate link level simulation capabilities and a modest degree of network level simulation complexity compared to fully dynamic network simulators a quasi-static simulation methodology was selected for MIMO scheme performance evaluation within 3GPP standardisation [SCM 03]. The modelling framework is set by a standard macrocellular network scenario as indicated in Figure 1.8 [SCM 03], [3GPP03a]. It consists of a hexagonal regular grid cellular set-up, where the centre target cell is surrounded by three tiers of interfering cells. Three sectors per site lead to a total of 57 sectors, where the main lobes of the directional sector antenna elements are oriented as indicated by the solid arrows. The SINR situation of a user, 'dropped' at an arbitrary position within the centre target cell, can be determined using models for all sectors' tx power variations, tx weight updates, path losses, shadow fades, and multipath fades. Such drop based simulation approach is, for example, taken in [SCM 03]. Over a certain number of drops users are uniformly distributed in the centre cell area. Their SINRs are calculated, and network level processes like data rate adaptation, packet scheduling, and HARQ are executed to determine the sector throughput. The disadvantage of such drop based simulation strategy is that a decoupling of network processes and link processes is hardly realisable. Moreover, such drop based simulation approach tends to blend

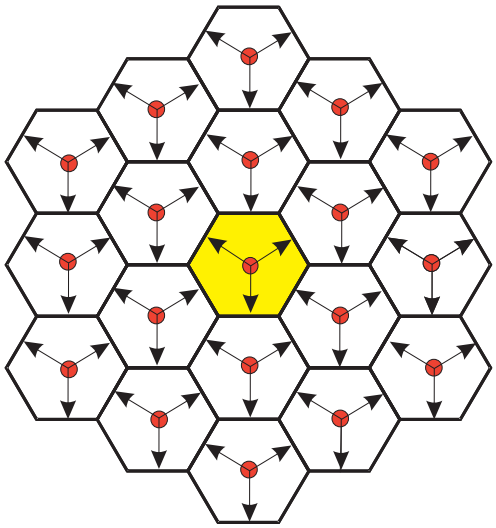

Figure 1.8: Standard regular grid cellular scenario set-up, based on [SCM 03], [3GPP03a], [3GPP04d].

out interesting link level effects, such as the effect of a single dominant interferer, if their occurrence probability on network level is low. The intention in the following is therefore to use a quasi-static, but *decoupled* link and network level simulation methodology as indicated in Figure 1.9.

Decoupling requires a link-to-network interface concept, where the network simulator reads link level performance results from a database. This has the advantage that time consuming link level simulation results can be pre-computed and reused, for example, to test the performance of different network level packet scheduling strategies. Moreover, decoupling between link and network level allows easy access to specific link level SINR situations, *e.g.* such with a single dominant other-sector interferer.

To be practical, a decoupled lookup approach requires that a small number of user-parameters are identified that describe a user's average interference situation, since for every possible user-parameter set link level results will have to be generated and stored in the database. A network level simulator then utilizes user-parameter distribution functions to assign user-parameters to every new user. In the sequel these user-parameters allow to retrieve time evolving user performance from the database. Size, and eventually the build-up time of the link level performance database are determined by the number of user-parameters and the sampling resolution of each user-parameter. Hence, the advantages of link level result reusability and detailed insight into the link level performance in individual user-parameter situations come at the price of operating within a discrete user-parameter space. Further, the other-sector interference has to be pre-computed and is thus independent of the traffic situation in the target cell.

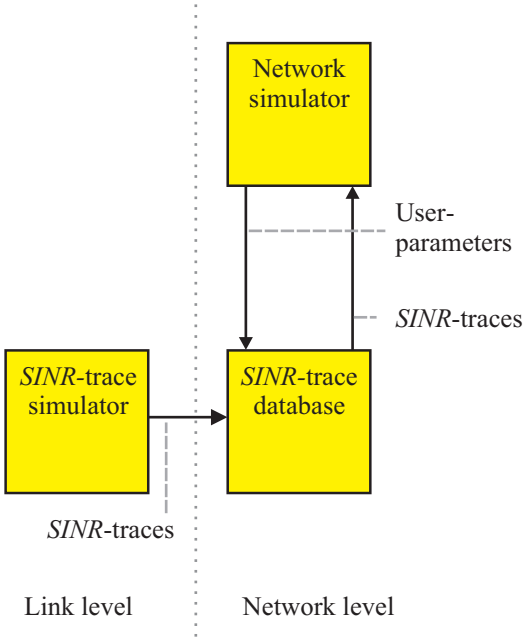

Figure 1.9: Decoupled link and network simulation methodology for run-time efficient network performance evaluation.

1.6 Objectives

The overall objective of the presented work is to use an existing quasi-static SISO HSDPA network simulator to *investigate the performance of multi-antenna enhanced HSDPA, with specific emphasis on own and other-sector interference effects*. This requires a MIMO DS-CDMA SINR formulation that incorporates own and other-sector interference. Further, it requires an other-sector interference model on which basis interference can be pre-computed. The objective can thus be split into three subtasks as outlined in the following:

1.6.1 MIMO DS-CDMA SINR Formulation

MIMO DS-CDMA SINR performance depends on the propagation environment, the transmission and reception schemes, as well as on the cross correlation properties of the deployed spreading codes.

One objective is to develop a general mathematical framework that can be used to describe and simulate the SINR performance of different MIMO DS-CDMA system configurations. MISO and SIMO configurations are to be included as sub cases. The mathematical frameworks should be sufficiently general to describe situations where different data and signalling channels are transmitted under different

tx antenna processing strategies.

1.6.2 Other-Sector Interference Model

An existing quasi-static HSDPA network level simulator is to be used for network level performance simulation. The existing simulator reads SISO SINR performance traces from a link level database. The only user-parameter required for trace look-up is a user's average own-to-other-sector received power ratio. Further the existing simulator uses *additive white Gaussian noise* (AWGN) other-sector interference.

Advanced multi antenna MMSE receivers have the capability of spatial other-sector interference suppression. The spatial interference suppression benefit depends on the power ratios of dominant other-sector interferers. Further, the severity of other-sector interference variation, that can either be due to on/off switching of interfering HSDPA channels or due to tx weight updates, depends on the dominant interfering sectors' power ratios as well as their tx correlations.

Hence, the second objective is to develop an other-sector interference model that accounts for dominant other-sector power ratios and tx correlations. To confine the amount of SINR traces that have to be generated and stored in the link level performance database it is essential that the model uses as few parameters as possible to describe a user's average interference situation.

1.6.3 MIMO HSDPA Performance Assessment

Applicability of the general MIMO DS-CDMA SINR description and the other-sector interference model are to be demonstrated in a MIMO HSDPA case study. Specifically the basis techniques closed loop transmit diversity and spatial multiplexing are to be assessed. Single and dual antenna receivers are to be used. The basic RAKE receiver should serve as a reference to the more advanced MMSE receiver. To assure their validity the obtained simulation results are to be benchmarked against analytical bounds. Questions to be answered in this context are:

- To which extent do multiple antenna link level effects influence network level performance?
- Which impact does other-sector interference variation have on link and network performance?
- How does tx correlation influence CLM1 performance?
- How significant is the performance estimation error when approximating other-sector interference with a simple AWGN interference model?

- Are simple analytical bounds able to quantify and explain effects encountered in link simulations?

1.7 Outline and Contributions

The dissertation is divided into six chapters as illustrated in the top row of Figure 1.10. With exception of *Introduction* and *Conclusion*, each chapter relates to one appendix listed in the second row. The bottom two rows display corresponding publications. Connections and influences between the different parts are indicated via arrows.

1.7.1 Context to Chapter 2 - MIMO HSDPA

Chapter 2 presents the basic HSDPA mechanisms, *i.e.* data rate adaptation, fast layer one HARQ with packet combining, and link quality dependent scheduling. Thereafter the operation of the selected physical layer enhancements, *i.e.* CLM1, SMP$_x$, MMSE, and their interaction with PF scheduling is presented. In specific flat fading cases, closed form expressions for the SINR statistics before and after PF scheduling are obtained. These analytical bounds are based on sources from the open literature, which were adjusted as required. More extensive derivations are provided in Appendix A. The obtained bounds deliver insight into the interaction of multiple antenna schemes and PF scheduling. Further, they enable simulation result validation. Especially the approach used to obtain the mean SINR gain of OPC over MRC, and the approach used to obtain a closed form SINR distribution of 2×2 SMP$_x$-OPC, are novel.

Chapter 2 relates to [Rami04a], [Berg03] and [Fern04]. [Rami04a] delivers background information on antenna techniques in UTRAN FDD Rel'99/4. It is partly based on the earlier publication [Schu02b]. The contribution to [Rami04a] and [Schu02b] consisted of discussion, literature search, and co-authoring editorial work. [Berg03] presents analytical as well as simulation results for the interaction of open and closed loop tx diversity with PF scheduling. The contribution to [Berg03] manifests itself, besides in main editorial work, also in deriving the analytical results, as well as the implementation of a preliminary simulator. Especially the first co-author, Troels E. Kolding[1], provided HSDPA system level expertise and editorial work, while the remaining authors contributed through valuable discussion. [Fern04] looks at scheduling aspects in spatial multiplexing systems. The contribution to [Fern04] manifests itself in the provision of link level performance results as well as in co-authoring editorial work, discussion and guidance.

[1] Nokia Networks Aalborg R&D, Denmark (Supervisor).

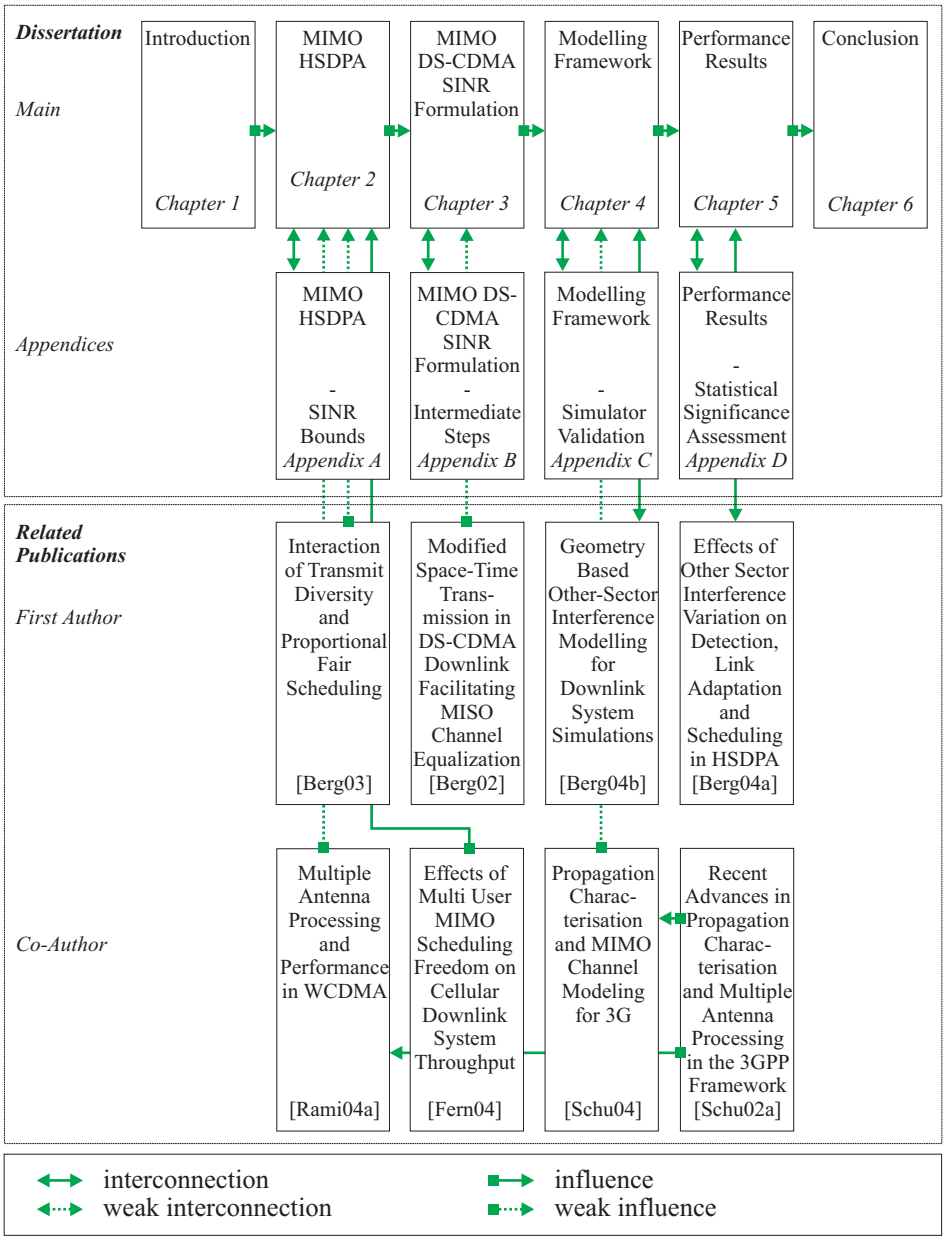

Figure 1.10: Outline and related publications.

1.7.2 Context to Chapter 3 - DS-CDMA MIMO SINR Formulation

Chapter 3 delivers a general mathematical framework to express the instantaneous symbol level SINR in time dispersive MIMO DS-CDMA systems. The formulation is generally applicable to DS-CDMA and not limited to HSDPA. It uses a *virtual channel* concept, where a virtual channel represents the radio propagation channel after transmit weight application. Accurate own-sector interference description is achieved through mapping the signalling and data channel powers to these virtual channels. Free allocation of orthogonal and pseudo random DS-CDMA codes is possible, enabling the modelling of spatial data stream multiplexing under the same orthogonal code resources as well as the deployment of multiple pseudo random scrambling codes within the same sector. Both options are currently considered in 3GPP standardisation. More involved derivations are presented in Appendix B. The MIMO DS-CDMA SINR formulation is based on the SISO DS-CDMA SINR formulation in [Fran02], and similarities can also be observed with the formulation in [Moto02]. However, to the best of the author's knowledge there has not been a similarly flexible public reference at the time of derivation.

[Berg02] is a pre-study to get familiar with different linear receiver types, *i.e.* the operation of the RAKE, zero forcing and MMSE receiver. The contribution to [Berg02] manifests itself in building a preliminary link simulator, including space-time coding and equalisation functionality, invention of a novel, but non standard compliant, space-time block encoding structure that allows to overcome own-sector interference problems by space-time equalisation, and main editorial work. The co-author, Laurent Schumacher[2] , provided a MIMO channel simulator, as well as link simulator sub modules, co-authoring editorial work and overall guidance.

1.7.3 Context to Chapter 4 - Interference Modelling

Chapter 4 presents the decoupled quasi-static simulation methodology. A user's average own-to-other-sector received power ratio and its azimuth angle of connection to the serving sector's antenna array are used to describe the user's average interference situation. Further, a metric for a user's SINR variability is introduced. It allows to assess the impact of SINR variation on turbo decoder performance. Chapter 4 relates to Appendix C, where the different sub-simulators are validated. The developed other-sector interference model is novel. Further, the turbo decoder performance description, inspired by Troels E. Kolding, is novel. Frank Frederiksen[3] generated the required turbo decoder performance curves. Simulator validation in Appendix C is partly based on performance comparison against results

[2]University of Namur, Belgium (Supervisor).
[3]Nokia Networks Aalborg R&D, Denmark (Colleague).

from Nokia internal simulators. Per-Henrik Michaelsen[4] provided results from a dynamic network level simulator to validate distributions used in the other-sector interference modelling process. Wei Na[5] provided SINR statistics for link level simulator validation.

Chapter 4 relates to [Schu04] and [Berg04b]. [Schu04], partly based on [Schu02b], provides background information on MIMO channel measurement campaigns and MIMO channel modelling strategies. The contribution to [Schu02b] and [Schu04] is based on discussion, literature review, and co-authoring editorial work. The novel other-sector interference simulation methodology was first published in [Berg-04b]. The contribution to [Berg04b] manifests itself in interference model development and main editorial work. The co-authors provided valuable discussion and guidance, with the first co-author, Troels E. Kolding, also supplying basic cellular scenario simulator functionality.

1.7.4 Context to Chapter 5 - Performance Results

Chapter 5 presents simulated MIMO HSDPA performance results. Effects of dominant other-sector interference and CLM1 tx antenna correlation are analysed at link and network level. The obtained simulation results are benchmarked against analytical bounds and are also compared against simulation results where other-sector interference is modelled as AWGN. Statistical significance of the simulation results is assessed in Appendix D. Although MIMO HSDPA performance results start to become available, *e.g.* [Rami03a], [Rami03b], [Love03], [Poll04], [Sama04], the results in Chapter 5 are still novel due to their level of detail with respect to own and other-sector interference modelling.

Chapter 5 relates to [Berg04a], where the effects of other-sector interference variation on detection, link adaptation and packet scheduling are assessed. Besides main editorial work, the contribution to [Berg04a] is reflected in generating novel link level performance results. The co-authors, Troels E. Kolding and Frank Frederiksen, provided network simulation results, while the remaining co-authors provided discussion and guidance.

1.7.5 Related Work

As part of the dissemination of scientific knowledge a total of 11 students have been supervised during their 9^{th} and 10^{th} semester M.Sc. projects. Due to close relation to the presented work it is worth mentioning the M.Sc. thesis '*Closed-Loop Transmit Diversity and Opportunistic Beamforming for HSDPA*' [Bonn03],

[4] Nokia Networks Aalborg R&D, Denmark (Colleague).
[5] Aalborg University, Denmark (Colleague).

showing that CLM1 generally outperforms opportunistic beamforming. Further, the M.Sc.-thesis '*MIMO Scheduling and Cooperative Detection for Systems Beyond 3G*' [Mart03] investigated the benefit of MIMO scheduling freedom, *e.g.* the option of spatial multiplexing with independent simultaneous data stream transmission to different users, and the potential benefits of user cooperation over, for example, a Bluetooth or similar short range connection. It was found that spatial multiplexing MIMO scheduling freedom including the option of disabling a data stream transmission to avoid excessive co-stream interference has the potential to increase system throughput. However, the potential of user cooperation in situations with sufficient exploitable multi-user diversity was found to be negligible.

Chapter 2

MIMO HSDPA

Key HSDPA and multiple antenna mechanisms are introduced. Simplifying assumptions are used to obtain

- the SINR-to-throughput relationship under HSDPA link adaptation,
- the single user SINR distributions of CLM1 and SMP,
- and the multi-user SINR distributions after PF scheduling.

These results show the interaction of multiple antenna schemes and PF scheduling. They further visualise the impact of the SINR distribution on the achievable link throughput. Results on the interaction of open and closed loop tx diversity with PF scheduling were published in [Berg03]. The derived expression for the cost of SMP dual stream transmission is novel. Presented analytical bounds will serve as one means for link simulator validation.

2.1 Introduction

The chapter is split into two main sections as outlined in Figure 2.1.

Figure 2.1: MIMO HSDPA chapter outline.

Section 2.2 presents the key mechanisms of the HSDPA concept and is confined to the level of detail needed to follow the work presented throughout. Further details can be found in the corresponding specifications [3GPP04f], [3GPP04e], [3GPP04g], and reviews of the HSDPA concept are available in [Kold03b], [Park03].

Section 2.3 introduces CLM1 and SMP$_x$ operation. More details on CLM1 can be found in [3GPP04g]. SMP$_x$ is not standardised. 3GPP descriptions of the related PARC and S-PARC multiple antenna proposals can be found in [3GPP04d].

Further, analytical SINR performance results are presented for the antenna processing configurations listed in Table 1.1. Derivations assume a flat Rayleigh fading channel and at most one dominant flat Rayleigh fading interferer. More elaborate derivations are provided in the corresponding Appendix A. The simplifying assumptions taken throughout the chapter and Appendix A make it possible to derive closed form analytical performance bounds and to visualise key effects. In Chapter 4 they are replaced with more complex simulation models.

2.2 HSDPA

This section describes the key HSDPA mechanisms link adaptation, and packet scheduling, and introduces models to visualise their performance.

2.2.1 Key Mechanisms

As introduced in Chapter 1, link adaptation, instead of link stabilisation through power control, is one of the key mechanisms to enhance the spectral efficiency of packet data transmissions over the HS-DSCH. It requires that the Node-B has access to quasi instantaneous downlink quality information. This is achieved through uplink signalling. The key HSDPA mechanisms are presented in Figure 2.2 and are on the basis of the labels outlined in alphabetical order.

(a) All UE measure their link quality and (b) feed this information in form of *transmission power control* (TPC) and *channel quality indication* (CQI) commands back to the Node-B. (c) Based on this feedback the Node-B takes data rate adaptation and packet scheduling decisions. (d) Thereafter the Node-B sends a message to the scheduled UE over the HS-SCCH. The message informs the UE that it will receive a data packet on the HS-DSCH. Further, the specific modulation and coding format as well as information about the orthogonal code resources used on the HS-DSCH are contained in this message. With this information the UE is able to receive the data packet on the HS-DSCH. (e) The received data symbols

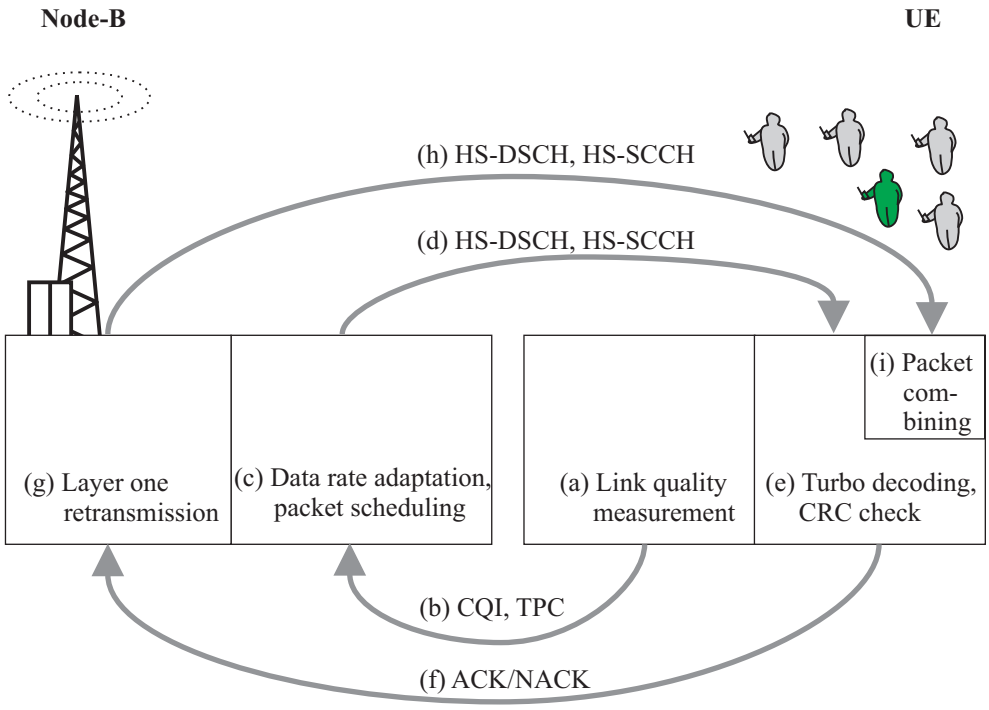

Figure 2.2: Key HSDPA mechanisms.

are fed into the UE turbo decoder. Using a *cyclic redundancy check* (CRC) on the decoded data the UE determines whether the data packet is error free. If so, the packet is passed on to higher layers for further processing, and (f) an *acknowledgement* (ACK) is signalled back to the Node-B. If the packet is not correctly decodable, its bits remain in the UE buffer, and a *negative acknowledgement* (NACK) is signalled back to the Node-B. (g) Upon reception of a NACK the Node-B performs fast layer one retransmission of the data packet, (h) using the HS-SCCH and HS-DSCH as previously. To assure smooth data packet flow a *stop-and-wait* (SAW) retransmissions protocol is used, where several SAW processes can be simultaneously active. (i) At the UE the packets are combined and fed into the turbo decoder. Should a packet after a certain number of retransmissions still not be correctly decodable, it is discarded. The consequent packet loss is to be resolved by higher layer protocols.

2.2.2 Link Adaptation

Link adaptation is based on the four mechanisms, *i.e.* (i) modulation scheme adaptation, (ii) effective coding rate adaptation, (iii) adaptation of the number of multicodes, and (iv) HARQ with packet combining.

The modulation schemes *quadrature phase shift keying* (QPSK) and 16 *quadrature amplitude modulation* (QAM) are supported (i). The code rate is adapted via bit puncturing or bit repetition (ii). Therewith it is possible to cover a range of *effective code rate*s (ECRs) between 0.15 to 0.98, where the ECR is defined as

$$ECR = \frac{\tilde{N}_{input\_bits\_to\_turbo\_encoder}}{\tilde{N}_{output\_bits\_from\_rate\_matcher}} \quad . \tag{2.1}$$

The combination of a modulation scheme and an ECR is throughout referred to as a *modulation and coding scheme* (MCS).

Instead of changing the spreading factor and the tx power, as done for the DSCH, the Node-B has the option of dynamically allocating one or more orthogonal spreading code resources to the HS-DSCH transmission (iii). These spreading codes are referred to as multicodes. With a spreading factor of 16 the number of orthogonal code resources is upper limited to 16. However, the maximum number of multicode resources that can be allocated to the HS-DSCH is upper limited to 15. At least one code with $N_{sf} = 16$ must be available for the transmission of other channels such as the PCPICH, the DCH and the HS-SCCH. These other channels share the last code using spreading factors from 32 up to 256.

HARQ with packet combining allows the usage of aggressive data rate adaptation mechanisms and is thus a key part of the link adaptation process. If an identical data packet is retransmitted, the received symbols can be combined using MRC, which in this specific context is also known as Chase combining [Chas85]. If the retransmitted packet contains originally punctured bits, the packet combining mechanism is referred to as *incremental redundancy* (IR) [Mand74].

The main related HSDPA baseband processing blocks are in conceptual form depicted in Figure 2.3.

A packet is defined as the amount of data transmitted on the HS-DSCH within one *transmit time interval* (TTI). A TTI comprises three slots, with 2560 chips per slot. Its time span, denoted T_{TTI}, is 2 ms, and link adaptation is performed on a TTI-to-TTI basis. Following the base band processing blocks in the upper half of Figure 2.3 from left to right, CRC bits are attached to every packet before it is fed into a turbo encoder. A fixed code rate of 1/3 is used. Only specific packet bit lengths can be transmitted. A rate matcher is used to adjust the packet to a predefined packet bit length. To do this it can either puncture or repeat bits. The rate matched bit sequence is interleaved and mapped to data symbols. QPSK and 16 QAM are supported. Thereafter the symbol sequence is multiplexed into subsequences. Every subsequence is spread with a spreading code, in this context referred to as multicode. Thereafter the spread subsequences are added and transmitted.

The reverse procedure takes place at the UE as presented in the lower half of

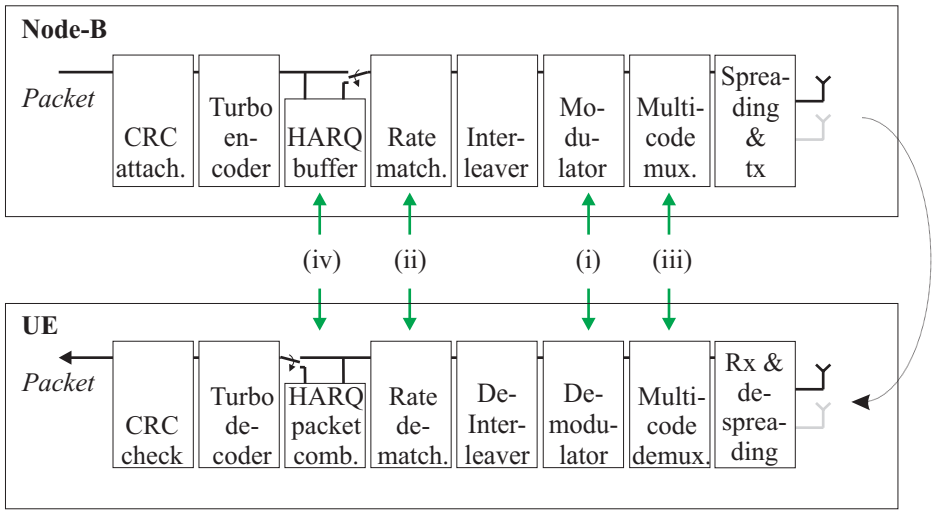

Figure 2.3: Sketch of the main HSDPA baseband processing operations.

Figure 2.3. The chip sequences are received and despread. The subsymbol streams corresponding to the different multicodes are de-multiplexed, mapped into bits and reliability information, de-interleaved, rate matched and fed to the turbo decoder. A CRC determines whether the decoded packet is error free. If not, a retransmission is requested, which is taken out of the Node-B HARQ buffer. Upon arrival at the UE the retransmitted packet is combined with the original packet, which was preliminarily stored in the UE HARQ buffer.

There is no standardised link adaptation algorithm. However, a commonly used algorithm selects the packet bit length, the modulation scheme, and the number of multicodes so that the first transmission of a packet is received with an average *packet error probability* (PEP) of 10% [Kold03b], [Lao03], [Chiu04]. Link adaptation performance is in the following subsection visualised in form of an example.

2.2.3 Link Adaptation Performance

To have a reference SINR measure throughout, which is independent of link adaptation decisions, the average SINR per TTI is defined. It is the ensemble average over all symbol SINRs in a TTI, assuming that all the HS-DSCH tx power is allocated to a single multicode, *i.e.*

$$SINR_{TTI} = \mathrm{E}\left\langle SINR \right\rangle_{480} \quad , \tag{2.2}$$

where $SINR$ represents the SINR per symbol. Further, at a spreading factor of 16 one TTI with one multicode contains 480 symbols. In multicode operation it is assumed that the tx power is evenly split between the multicodes. Multicode

operation therefore allows the actual experience power level of a transmission to be adapted on a TTI-to-TTI basis. Using $\tilde{N}_{code}$ multicodes the SINR per multicode is

$$\frac{1}{\tilde{N}_{code}} \cdot SINR_{TTI} \quad .$$

Further, the effective SINR is defined as the SINR after packet combining. For the first transmission of a packet there is no packet combining. The effective SINR of the first transmission thus writes

$$SINR_{eff}\,[1] = \frac{1}{\tilde{N}_{code}} \cdot SINR_{TTI}\,[1] \quad , \tag{2.3}$$

where $[\cdot]$ is the packet transmission index.

Changing $\tilde{N}_{code}$ not only adapts the effective SINR but also leads to varying packet bit lengths. In general, turbo decoder performance is affected by the SINR and by the packet bit length [Bene96], [Toml02]. Taking for example the effective SINR needed to obtain a 10% PEP in connection with $\tilde{N}_{code} = 1$ and comparing it with the case of $\tilde{N}_{code} = 10$, the turbo decoder requires approximately 0.2 dB less $SINR_{eff}$ for the longer packet [Kold01, Fig. 7]. Turbo decoder PEP performance as a function of $SINR_{eff}$ is plotted in Figure 2.4. It is based on Nokia internal turbo decoder performance measurements, where the SINR per symbol is kept constant for the duration of a TTI. The results are obtained for a single multicode. Using the same results to determine the performance with several multicodes, *i.e.* with longer packet bit length, is slightly conservative, but suffices to present the underlying effects.

HSDPA rate matching and modulation scheme selection allow the generation of a very fine, but irregular spaced set of MCSs. The turbo decoder performance curves in Figure 2.4 merely deliver 12 MCS examples. The corresponding user data rates, *i.e.* excluding overhead, are presented in Table 2.1. The user data rate for a single multicode is denoted $MCSR$. Approximations of the user data rates with multicode operation can be obtained via scaling. An approximation for the maximum user data rate as displayed in the last column of Table 2.1 is for example obtained as $15 \cdot MCSR$.

The 12 MCS examples from Figure 2.4 and Table 2.1, paired with 15 multicode options lead to 180 possible MCS-multicode link adaptation combinations. They are denoted with index z. The average packet throughput, PTP, of the first transmission corresponding to MCS-multicode combination z is calculated as

$$PTP_z\,[1] = \underbrace{(1 - PEP_z\,[1])}_{\substack{\text{Fraction of data}\\ \text{that goes through}\\ \text{error free.}}} \cdot \underbrace{MCSR_z \cdot \tilde{N}_{code,z}}_{\substack{\text{Data rate in case}\\ \text{of error free}\\ \text{transmission.}}} \quad , \tag{2.4}$$

where PEP_z, as a function of $SINR_{eff}$, can be read from Figure 2.4.

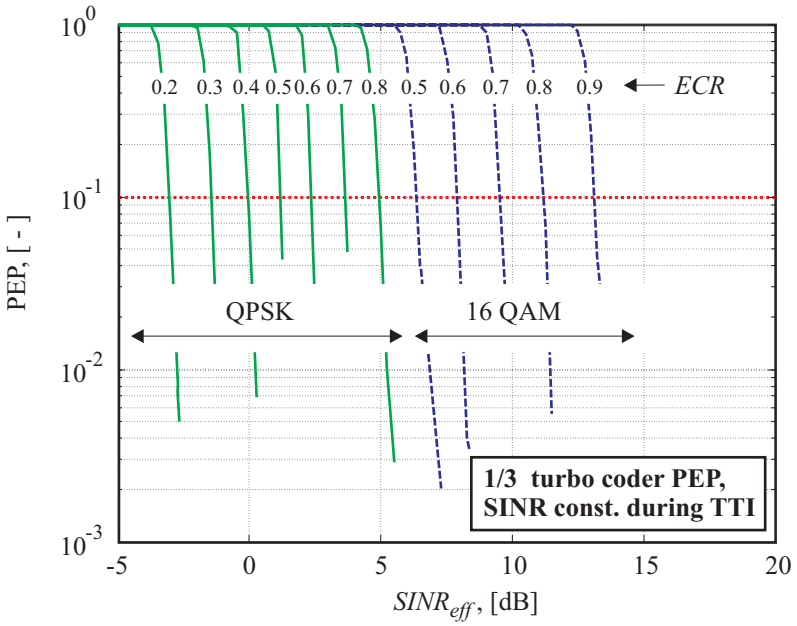

Figure 2.4: Turbo decoder PEP performance as a function of $SINR_{eff}$. Results are obtained from Nokia internal measurements.

MCS	Modulation scheme	Bits per symbol	ECR [1], [–]	$MCSR$ [2], [kb/s]	$15 \cdot MCSR$ [1], [Mb/s]
1	QPSK	2	0.2	94	1.4
2	QPSK	2	0.3	142	2.1
3	QPSK	2	0.4	190	2.9
4	QPSK	2	0.5	238	3.6
5	QPSK	2	0.6	286	4.3
6	QPSK	2	0.7	334	5.0
7	QPSK	2	0.8	382	5.7
8	16 QAM	4	0.5	478	7.2
9	16 QAM	4	0.6	574	8.6
10	16 QAM	4	0.7	670	10.1
11	16 QAM	4	0.8	766	11.5
12	16 QAM	4	0.9	862	12.9

Table 2.1: Modulation and coding scheme options. [1] Rounded to the nearest decimal. [2] Rounded to the nearest integer.

Using the 10% PEP link adaptation algorithm the link adaptation decision for a specific MCS-multicode combination, Z, is taken as

$$Z = \underset{1 \cup z \big|_{PEP_z[1] \leqslant 0.1}}{\arg\max} \{PTP_z[1]\} \quad . \tag{2.5}$$

In other words, from the group of all z that achieve a first transmission PEP equal to or smaller than 10%, joint with $z = 1$, corresponding to the lowest first transmission throughput, the option Z will be selected, which corresponds to the maximum first transmission throughput.

Compared to conventional Rel'99/4 operation the relatively high 10% PEP target on the HS-DSCH becomes possible due to the option of fast layer one HARQ. Should a packet be erroneously received, a fast retransmission takes place. Chase combining the per transmission SINRs of original and all retransmissions delivers an effective SINR of

$$SINR_{eff}\left[\tilde{N}_{trans}\right] = \frac{1}{\tilde{N}_{code}} \cdot \sum_{r=1}^{\tilde{N}_{trans}} SINR_{TTI}[r] \quad , \tag{2.6}$$

where $\tilde{N}_{trans}$ is the number of transmissions. Assuming uncorrelated interference and noise the first retransmission hence increases the effective SINR by around 3 dB. As can be seen from Figure 2.4, an effective SINR increase of 3 dB decreases the PEP by orders of magnitude. In an ideal system with no link adaptation errors this would mean that the probability that a second retransmission is needed approaches 0. Looking at the performance of HSDPA IR combining it is found that especially at high ECRs, where a lot of bits are punctured in the first transmission, IR bits in the retransmission can deliver up to 1 dB additional effective SINR gain over Chase combining [Fred02].

To determine the link throughput including the effect of HARQ with packet combining, the average throughput per packet is a generalisation of (2.4). All retransmissions use the same MCS-multicode combination Z. To enable simple notation $PEP_Z[0]$ is defined as $PEP_Z[0] = 1$. Thereupon the average packet throughput per (re)transmission writes

$$PTP_Z[r] = \underbrace{(1 - PEP_Z[r])}_{\substack{\text{Fraction of data} \\ \text{that goes through} \\ \text{error free.}}} \cdot \underbrace{\prod_{n=0}^{r-1} PEP_Z[n]}_{\substack{\text{Fraction of data that} \\ \text{needs to be (re)transmitted.}}} \cdot \underbrace{MCSR_Z \cdot \tilde{N}_{code,Z}}_{\substack{\text{Data rate in case of} \\ \text{error free transmission.}}} \quad . \tag{2.7}$$

The link throughput, TP, can then be written as

$$TP = \frac{\sum_{r=1}^{\tilde{N}_{trans}} PTP_Z[r]}{\sum_{r=1}^{\tilde{N}_{trans}} \prod_{n=0}^{r-1} PEP_Z[r]} \tag{2.8}$$

where the denominator accounts for the overhead used by the retransmissions.

On the assumption that the SINR in the first transmission and in the first retransmission are approximately identical, *i.e.* $SINR_{TTI}\,[1] = SINR_{TTI}\,[2]$, and that the packet is received error free after the second transmission, *i.e.* $\tilde{N}_{trans} = 2 \wedge PEP_Z\,[2] = 0$, the link throughput from (2.8) simplifies to

$$TP = \frac{MCSR_Z \cdot \tilde{N}_{code,Z}}{1 + PEP_Z\,[1]} \quad . \tag{2.9}$$

This SINR-to-throughput relationship is plotted in Figure 2.5. Additionally an adapted version of the Shannon capacity [Shan48], [Holm04, p. 327] and a linear approximation are plotted. It can be seen that the HS-DSCH has a spectral efficiency that is ideally around 4.5 dB to 5 dB below Shannon capacity. Further, up to an $SINR_{TTI}$ of around 13 dB the SINR-to-throughput relationship is approximately linear. Exceeding 13 dB the slope starts to decrease drastically until it reaches at approximately 27 dB a point where an SINR increase no longer results in additional throughput benefit. This shows that the dynamic range for a single stream, single scrambling code, HSDPA system is limited to a total of around 32 dB.

The original vertical grid in Figure 2.5 has been replaced by vertical lines that represent the 10% SINR requirement from which onwards an MCS paired with a

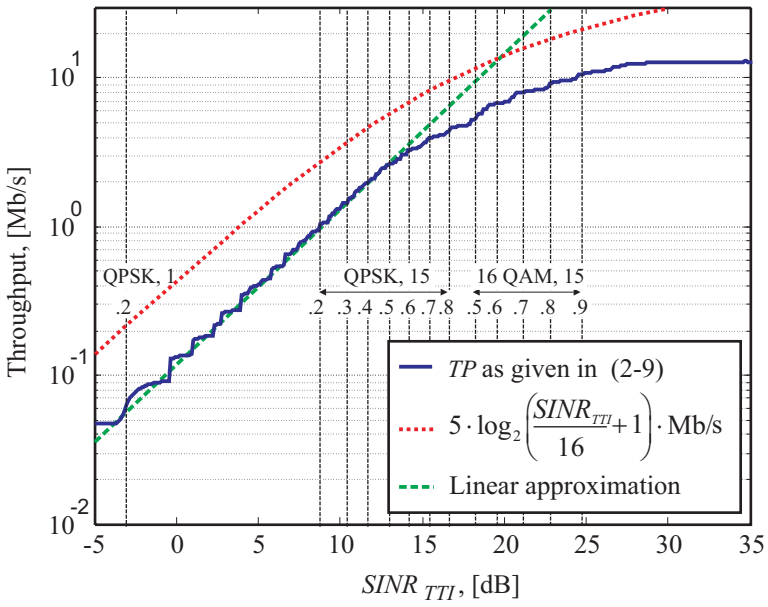

Figure 2.5: SINR-to-throughput relationship.

certain number of multicodes can be used. The SINR requirements correspond to the 10% PEP points in Figure 2.4. Starting from left to right the 1^{st} vertical line indicates the minimum SINR requirement to support QPSK with one multicode and an ECR of 0.2. Below this SINR the PEP will exceed 10%. The 2^{nd} to 7^{th} vertical lines indicate the entire range of QPSK options, *i.e.* MCS 1 to MCS 7, each in connection with 15 multicodes. The remaining vertical lines relate to the entire range of 16 QAM options, *i.e.* MCS 8 to MCS 12, also each in connection with 15 multicodes. This modified grid will be used throughout to establish a simple connection between SINR and throughput.

2.2.4 Packet Scheduling

The packet scheduling strategy is, like the link adaptation strategy, vendor specific. However, the RR and PF packet scheduling algorithms are among those commonly used in MIMO scheme performance comparisons [3GPP04d]. The RR scheduler allocates downlink resources to the users in a round robin fashion independent of the users' downlink conditions [Kold02]. It is blind with respect to the instantaneous downlink quality and can therefore not benefit from the fact that some users might be in more favourable conditions than others.

The PF scheduler, whose detailed implementation can be found in [Kold03a], is with minor modifications based on the proportional fair principle [Holt00], [Bend00], [Holt01], [Elli02]. The basic idea is to schedule a user when it is in instantaneously favourable conditions with respect to its mean. In a simplified form, a user U is selected from a pool of N_{queued} users according to

$$U = \underset{u \in [1,...N_{queued}]}{\arg\max} \left\{ \frac{TP_u}{\overline{TP}_u} \right\} \quad , \tag{2.10}$$

where TP_u and $\overline{TP}_u$ indicate instantaneous supportable throughput of user u and actually received throughput of user u averaged over a certain time window.

2.2.5 Packet Scheduling Performance

An analytical description of the PF scheduling algorithm can be obtained on simplifying assumptions similar to those in [Holt00]:

- All users' fading statistics are *independent identical distributed* (i.i.d). Users move with the same speed, have equal access probability, and utilize the same antenna processing scheme.
- A sufficiently long averaging window is used, so that the users' average received data rates are stationary.

- All users' SINRs stay within the dynamic range of the system, where an increase of SINR corresponds to throughput increase.
- The symbol level SINR does not change significantly over a TTI, *i.e.* $SINR \approx SINR_{TTI}$.

These assumptions allow to rewrite the original PF scheduling metric from (2.10) as

$$\begin{aligned} U &= \underset{u\in\left[1,\ldots N_{queued}\right]}{\arg\max} \left\{ \frac{TP_u}{\overline{TP}_u} \right\} \\ &= \underset{u\in\left[1,\ldots N_{queued}\right]}{\arg\max} \left\{ \frac{SINR_u}{\overline{SINR}_u} \right\} \end{aligned} \quad . \tag{2.11}$$

PF scheduling can therefore be seen as a selection diversity process with the selection diversity order N_{queued}. The probability that the SINR of a scheduled user lies below a reference, $SINR_{ref}$, can on the basis of [Jake94, p. 315] be written as

$$\begin{aligned} &\Pr\left(SINR_{scheme,PF,N_{queued}} < SINR_{ref}\right) \\ &= \Pr\left(\bigcup_{u=1}^{N_{queued}} \frac{SINR_{scheme,u}}{\overline{SINR}_{scheme,u}} < \frac{SINR_{ref}}{\overline{SINR}_{scheme,u}} \right) \\ &= \Pr\left(SINR_{scheme,u} < SINR_{ref}\right)^{N_{queued}} \end{aligned} \quad . \tag{2.12}$$

To visualise this effect simple 1×1 SISO antenna schemes and flat Rayleigh fading links between the Node-B and all UE are assumed. Additionally, it is assumed that the received interference is experienced as AWGN. In this case the single link SINR *cumulative probability density function* (cdf) is given by [Jake94, p. 314]

$$\Pr\left(SINR_{1\times1SISO} < SINR_{ref}\right) = 1 - e^{-\left(\frac{SINR_{ref}}{\overline{SINR}_{branch}}\right)} \quad , \tag{2.13}$$

where $\overline{SINR}_{branch}$ represents the mean SINR of a flat Rayleigh fading link. Applying (2.12) delivers the SINR cdf after PF scheduling, *i.e.*

$$\begin{aligned} &\Pr\left(SINR_{1\times1SISO,PF,N_{queued}} < SINR_{ref}\right) \\ &\qquad = \left(1 - e^{-\left(\frac{SINR_{ref}}{\overline{SINR}_{branch}}\right)}\right)^{N_{queued}} \end{aligned} \quad . \tag{2.14}$$

The post PF scheduling SINR cdfs of a user with an $\overline{SINR}_{branch}$ of 10.5 dB is plotted in Figure 2.6 for N_{queued} taking the values $\{1, 2, 4, 10\}$. The unusual branch SINR is selected with the aim of producing reference cdfs that will turn out useful within the validation process of the link simulator. It can be seen that

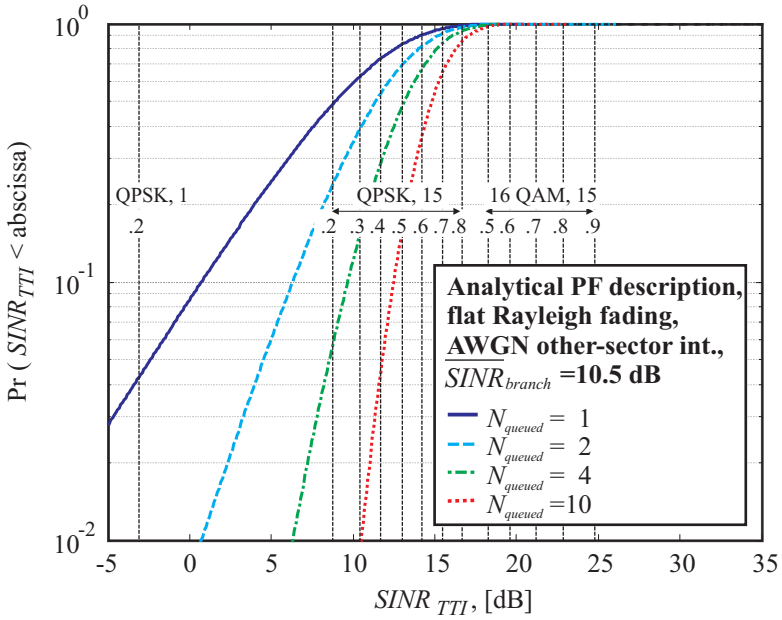

Figure 2.6: Basic selection diversity effect caused by the PF scheduling algorithm. The example uses flat Rayleigh fading 1×1 SISO links with AWGN interference and up to 10 queued users.

PF scheduling not only increases the diversity order by N_{queued}, but also the mean SINR, which for the 1×1 SISO scheme is given by [Jake94, (5.2-8)]

$$\mathrm{E}\left\{SINR_{1\times 1 SISO,PF,N_{queued}}\right\} = \overline{SINR}_{branch} \cdot \sum_{u=1}^{N_{queued}} \frac{1}{u} \quad . \tag{2.15}$$

In the specific 2, 4, and 10 user test cases the mean gain over the $N_{queued} = 1$ case amounts to around 1.76 dB, 3.19 dB, and 4.67 dB respectively.

2.3 MIMO

This section introduces the basic operation of the multiple tx antenna schemes CLM1 and SMP$_x$. Using a single receive antenna or dual antenna MRC/OPC, their SINR cdfs are presented in a flat Rayleigh fading situation.

2.3.1 Array Gain, Mean SINR Gain

The array gain of any $scheme2$ over any $scheme1$ is defined as [Hamm00]

$$\beta_{\substack{scheme2,\\ scheme1}} = \frac{\overline{SINR}_{scheme2}}{\overline{SINR}_{scheme1}} \quad . \tag{2.16}$$

In frequency selective fading situations the array gain can more generally be seen as a mean SINR gain, and it might not solely be caused by antenna array processing possibly including spatial interference suppression, but also by channel equalisation. Specifically with respect to the 1×1 SISO reference case a shorter notation is used, *i.e.*

$$\beta_{scheme2} = \frac{\overline{SINR}_{scheme2}}{\overline{SINR}_{1\times 1 SISO}} \quad . \tag{2.17}$$

2.3.2 CLM1 Operation

The intention of CLM1 is to maximise the received signal power at the UE. This is achieved by transmit weight application at the Node-B, so that the signal transmitted from both tx antennas is as much as possible co-phased when it reaches the UE rx antenna(s). Basic CLM1 operation is sketched in Figure 2.7.

Co-phasing both transmitted signal components leads to a mean SINR gain as well as to a diversity order increase similar to the one for tx *equal gain combining* (EGC) [Jake94, pp. 319-320]. This might increase the data rate that can be transmitted at a certain PEP target. RR or PF scheduling can be performed on the improved link. To confine the amount of required uplink weight signalling, only four tx weight sets, displayed in Table 2.2, are applicable.

Only phase weighting is allowed, while the tx power is evenly split between the two tx antennas. One uplink feedback bit can be signalled per uplink slot, which means that the complete weight information is available at the Node-B after 2 slots, *i.e.* after around 1.34 ms. More implementation specific information can be found

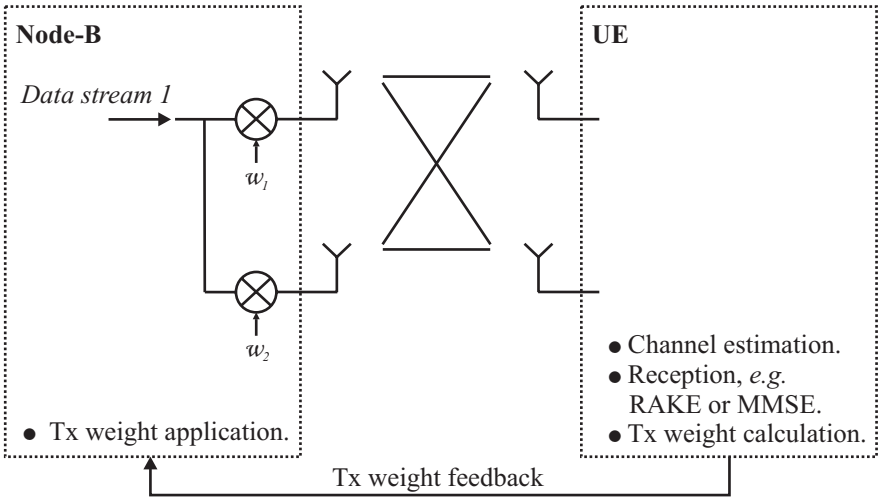

Figure 2.7: Basic CLM1 operation.

CLM1 tx weight sets	
w_1	w_2
$\frac{1}{\sqrt{2}}$	$\frac{1}{\sqrt{2}} \cdot e^{j\frac{1}{4}\pi}$
$\frac{1}{\sqrt{2}}$	$\frac{1}{\sqrt{2}} \cdot e^{j\frac{3}{4}\pi}$
$\frac{1}{\sqrt{2}}$	$\frac{1}{\sqrt{2}} \cdot e^{j\frac{5}{4}\pi}$
$\frac{1}{\sqrt{2}}$	$\frac{1}{\sqrt{2}} \cdot e^{j\frac{7}{4}\pi}$

Table 2.2: Applicable CLM1 tx weight sets.

in [Rami04a], [3GPP04g], [Hott03, Chp. 10].

2.3.3 SMP$_x$ Operation

The intention of SMP$_x$ is to maximise the throughput. 3 transmission options exist, *i.e.* either to transmit a single data stream with full power from transmit antenna 1 or 2 or to transmit two data streams from each antenna splitting the available power evenly between the tx antennas. This situation is depicted in Figure 2.8, and the corresponding tx weights are given in Table 2.3. The weight notation is chosen in order to include the antenna switching option.

In the PARC proposal [3GPP04d], where both data streams are transmitted to the same user, the UE predicts which transmission option would deliver the highest

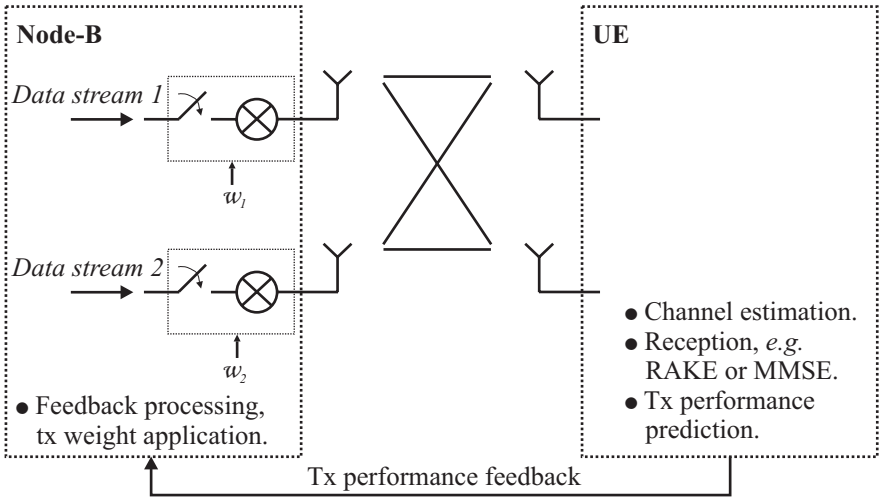

Figure 2.8: Basic SMP$_x$ operation.

SMP$_x$ tx weight sets	
w_1	w_2
1	0
0	1
$\frac{1}{\sqrt{2}}$	$\frac{1}{\sqrt{2}}$

Table 2.3: Applicable SMP$_x$ weight sets.

throughput and feeds only information about the best option back to the Node-B. In the S-PARC proposal [3GPP04d] N_{tx} CQI words are signalled back to the Node-B. With this link quality knowledge the Node-B is put into the position to perform tx weight selection, link adaptation and scheduling.

SMP *with full weight selection freedom* (SMP$_x$) as considered here is more general than PARC and S-PARC. In a rich scattering environment the SINRs that the same UE can obtain on stream 1 and stream 2 are likely to be uncorrelated. This means there is a high probability that one stream has a high SINR while the other has a low SINR. Hence, having the option to transmit to different UE can improve system performance [Fern04], [Mart03]. Such an approach can be realised with a smart multi stream capable packet scheduler, which has the option to decide on a TTI-to-TTI basis whether to schedule

(i) only one UE using a single stream,

(ii) one UE using dual stream,

(iii) or different UE using one stream each.

This requires a generalisation of the scheduling strategy given in (2.10) to accommodate the additional scheduling freedom, *i.e.*

$$\underset{\substack{u_1 \in [1,\dots N_{queued}] \\ u_2 \in [1,\dots N_{queued}] \\ m_1 \in [1,2] \\ m_2 \in [1,2] \wedge m_2 \neq m_1}}{\arg\max} \left\{ \frac{TP_{u_1,m_1}}{\overline{TP}_{u_1}}, \frac{TP_{u_1,m_1}\,|_{coint}}{\overline{TP}_{u_1}} + \frac{TP_{u_2,m_2}\,|_{coint}}{\overline{TP}_{u_2}} \right\} \quad , \tag{2.18}$$

where the additional index m relates to either tx antenna 1 or 2. The first element in the decision rule of (2.18) corresponds to case (i). It represents an antenna selection option combined with a multi-user selection option, *i.e.* take the tx antenna user combination with the highest predicted-to-average throughput ratio. The second element in (2.18) corresponds to case (ii) and (iii), *i.e.* for each tx antenna

select the user with the highest predicted-to-average throughput ratio, where the predicted throughput $TP_{u,m}\,|_{coint}$ is calculated on the assumption of co-stream interference. This scheduling concept has been developed in [Mart03], and the results were published in [Fern04]. The main findings were that having the full scheduling freedom, as expressed by (2.18) delivers a benefit over any of the more restrictive sub cases (i), (ii) or (iii). Further, the selection probability was shown to depend on the degree of transmit correlation and the amount of frequency selectivity in the propagation environment.

However, scheduling dual streams does not only require a more advanced packet scheduler working under the decision rule of (2.18), but also the ability to predict $TP_{u_1,m_1}\,|_{coint}$ and $TP_{u_2,m_2}\,|_{coint}$. As shown in Figure 2.5 throughput per stream depends on the SINR per stream. Further, as will be shown in Chapter 3, the SINR per stream depends on the multicode link adaptation decision on the interfering co-stream. Therefore (2.18) imposes a joint optimisation problem, for which a solution is not implemented in the existing network level simulator to be used for HSDPA network performance assessment. To obtain an idea of the SMP$_x$ network level performance the full scheduling freedom SMP$_x$ decision rule from (2.18) is broken up into two subcases, *i.e.*

$$\underset{\substack{u_1\in[1,\ldots N_{queued}]\\ m_1\in[1,2]}}{\arg\max}\left\{\frac{TP_{u_1,m_1}}{\overline{TP}_{u_1}}\right\}\quad, \tag{2.19}$$

and

$$\underset{\substack{u_1\in[1,\ldots N_{queued}]\\ u_2\in[1,\ldots N_{queued}]\\ m_1\in[1,2]\\ m_2\in[1,2]\wedge m_2\neq m_1}}{\arg\max}\left\{\frac{TP_{u_1,m_1}\,|_{coint}}{\overline{TP}_{u_1}}+\frac{TP_{u_2,m_2}\,|_{coint}}{\overline{TP}_{u_2}}\right\}\quad. \tag{2.20}$$

The decision rule in (2.19) combines scheduling with antenna selection transmit diversity which throughout is referred to as SMP$_{sel}$. The decision rule in (2.20) corresponds to a forced dual stream transmission and is throughout referred to as SMP$_{dual}$. No restriction is made on scheduling to the same or to different users.

2.3.4 Multiple Antenna SINR Performance

Both tx schemes can be received with RAKE or MMSE receivers. The RAKE receiver performs MRC, while the MMSE receiver performs OPC. Combining is performed over delayed signal components and, if present, over the multiple rx antennas. In cases where the interference appears as AWGN, *e.g.* in a frequency flat fading situation with no dominant other-sector or co-stream interferers, MRC

and OPC are identical, *i.e.* there is no benefit of MMSE over RAKE reception. As closed form expressions of the SINR cdfs after MRC and OPC with coloured interference become very quickly very mathematically involved and are still part of ongoing research [Cui04], [Tokg04], the following analytical assessments are limited to a flat Rayleigh fading environment with decorrelated antenna elements and either AWGN interference or AWGN interference plus a single dominant flat Rayleigh fading interferer.

N_{branch} rx or tx antenna combining delivers in a pure AWGN interference situation an SINR cdf of [Jake94, p. 319]

$$\begin{aligned}&\Pr\left(SINR_{N_{branch}} < SINR_{ref}\right)\\&= 1 - e^{-\left(\frac{SINR_{ref}}{\overline{SINR}_{branch}}\right)} \cdot \sum_{n=1}^{N_{branch}} \frac{\left(\frac{SINR_{ref}}{\overline{SINR}_{branch}}\right)^{n-1}}{(n-1)!}\end{aligned}, \tag{2.21}$$

where $\overline{SINR}_{branch}$ represents the reference mean SINR per branch as introduced in (2.13).

In the special case of one dominant interferer the SINR cdf after dual branch OPC can on the basis of [Vill99, (18)] be written as

$$\begin{aligned}&\Pr\left(SINR_{2branch-OPC} < SINR_{ref}\right)\\&= \frac{1}{2 \cdot \overline{INR}} \cdot e^{\frac{-SINR_{ref} \cdot (1+2 \cdot \overline{INR})}{\overline{SNR}}} - \left(\frac{1}{2 \cdot \overline{INR}} + 1\right) \cdot e^{\frac{-SINR_{ref}}{\overline{SNR}}} + 1\end{aligned}, \tag{2.22}$$

where $\overline{SNR}$ represents the mean signal to AWGN power ratio, and $\overline{INR}$ represents the mean dominant interference to AWGN power ratio.

The mean array gain in pure AWGN interference can for the standard multiple antenna schemes 1×2 SIMO, 2×1 CLM1, and 2×2 CLM1 for example be found in [Ande00], [Gerl02], and [Hama01a] respectively. Details as well as the derivation of the mean gain of 2×2 SMP$_{sel}$ can be found in Appendix A.1. As a source of quick reference the array gain ratios of the different schemes are presented in Table 2.4. These ratios will be revisited for simulation result validation. Moreover, SINR cdfs with exception of 2×2 SMP$_{dual}$ can be obtained on the basis of (2.21), with the help of the SINR cdf adjustment parameters presented in Table 2.4, *i.e.*

$$\begin{aligned}&\Pr\left(SINR_{scheme} < SINR_{ref}\right)\\&= 1 - e^{-\left(\frac{SINR_{ref}}{\overline{SINR}_{branch} \cdot \beta_{scheme,\,N_{branch}}}\right)} \cdot \sum_{n=1}^{N_{branch}} \frac{\left(\frac{SINR_{ref}}{\overline{SINR}_{branch} \cdot \beta_{scheme,\,N_{branch}}}\right)^{n-1}}{(n-1)!}\end{aligned}. \tag{2.23}$$

	1×1 SISO	1×2 SIMO	2×1 CLM1	2×2 CLM1	2×2 SMP$_{sel}$	2×2 SMP$_{dual}$
	$\beta_{\substack{scheme\_c,\\ scheme\_r}}$, [dB]					
1×1 SISO	0	3.01	2.32	4.66	4.39	-3.01
1×2 SIMO	–	0	-0.69	1.65	1.38	-6.02
2×1 CLM1	–	–	0	2.34	2.07	-5.33
2×2 CLM1	–	–	–	0	-0.27	-7.67
2×2 SMP$_{sel}$	–	–	–	–	0	-7.40
2×2 SMP$_{dual}$	–	–	–	–	–	0
	SINR cdf adjustment parameters, [–]					
N_{branch}	1	2	2	4	4	–
$\beta_{\substack{scheme\_c,\\ N_{branch}}}$	1	1	$\frac{1}{2}+\frac{1}{2\sqrt{2}}$	$\frac{1}{2}+\frac{3}{128}\cdot\pi^2$	$\frac{1}{2}+\frac{3}{16}$	–

Table 2.4: Array gain ratios and SINR cdf adjustment parameters. Numbers are for a flat Rayleigh fading environment with other-sector interference experienced as AWGN. $scheme\_c$ refers to a scheme along the column and $scheme\_r$ to a scheme along the row. 2×2 SMP$_{dual}$ performance is only valid for OPC, while all others are valid for OPC and MRC.

The SMP$_{dual}$-OPC situation can be seen as $2branch-OPC$, where dominant interference is coming from the spatial multiplexed co-stream. The equal tx power split leads to

$$\overline{SNR}=\frac{\overline{SINR}_{branch}}{2} \quad . \tag{2.24}$$

In a flat fading channel only the co-stream signal transmitted under an identical code resource as used for the desired signal causes interference. The number of co-stream code resources used within a TTI is denoted $\tilde{N}_{codeco}$. As the co-stream power is equally split between the co-stream code resources, the mean dominant to

AWGN interference ratio is

$$\begin{aligned}\overline{INR} &= \frac{1}{\tilde{N}_{codeco}} \cdot \overline{SNR} \\ &= \frac{1}{\tilde{N}_{codeco}} \cdot \frac{\overline{SINR}_{branch}}{2} \quad . \end{aligned} \tag{2.25}$$

Inserting (2.24) and (2.25) into (2.22) delivers the SINR cdf for each stream of 2×2 SMP$_{dual}$-OPC.

Using an $\overline{SINR}_{branch}$ of 10.5 dB the SINR cdfs of all schemes are presented in Figure 2.9. Additionally the SINR cdf of 2×1 STTD is plotted. It is obtained from the SINR cdf in (2.23), with 2 branches and a mean adjustment of 0.5. Figure 2.9 (a) shows the SINR cdfs for a multi-user selection diversity order of 1, which relates to RR scheduling. Figure 2.9 (b) shows the SINR cdfs for a multi-user selection diversity order of 10, which relates to PF scheduling from a pool of $N_{queued} = 10$ users.

Comparing the SINR statistics of the single stream schemes it can be seen that 2×2 CLM1 performs best, closely followed by 2×2 SMP$_{sel}$. In fact the antenna diversity order of both schemes is identical and, as can be seen from Table 2.4, the SINR mean ratio of both schemes amounts to 0.27 dB. Comparing 1×2 SIMO with 2×1 CLM1 it can be seen that 1×2 SIMO performs superior with a mean SINR advantage of 0.69 dB.

Looking specifically at the interaction of antenna diversity and multi-user selection diversity it can be seen that the SINR cdf slopes become more and more similar, indicating that increases in diversity order deliver diminishing returns at high overall diversity orders. This can, for example, be seen in Figure 2.9 (b) comparing 2×1 CLM1 with 2×2 CLM1. Although the product of antenna and multi-user selection diversity is 20 and 40 respectively their SINR cdf slopes appear rather similar. Hence, at very high overall diversity orders mean SINR performance becomes the important criterion to distinguish scheme performance on link level.

Looking specifically at the interaction of multi user selection diversity and 1×1 SISO and comparing it against 2×1 STTD, it can be seen that for $N_{queued} = 1$, 80% of the STTD users have a better SINR performance than the SISO users, while 20% perform worse. For $N_{queued} = 10$ the cross over point between SISO and STTD has shifted. Now around 90% of the STTD users perform worse than the SISO users. Using the vertical grid these SINR statistics can be related to the obtainable throughput. In Figure 2.9 (b) it can for example be seen that 20% of the SISO users can support QPSK, with 15 multicodes and an ECR of 0.8, while with STTD the best 20% only support QPSK, with 15 multicodes and an ECR of 0.7. For the upper 20% of the users the throughput loss due to STTD is 12.5% in

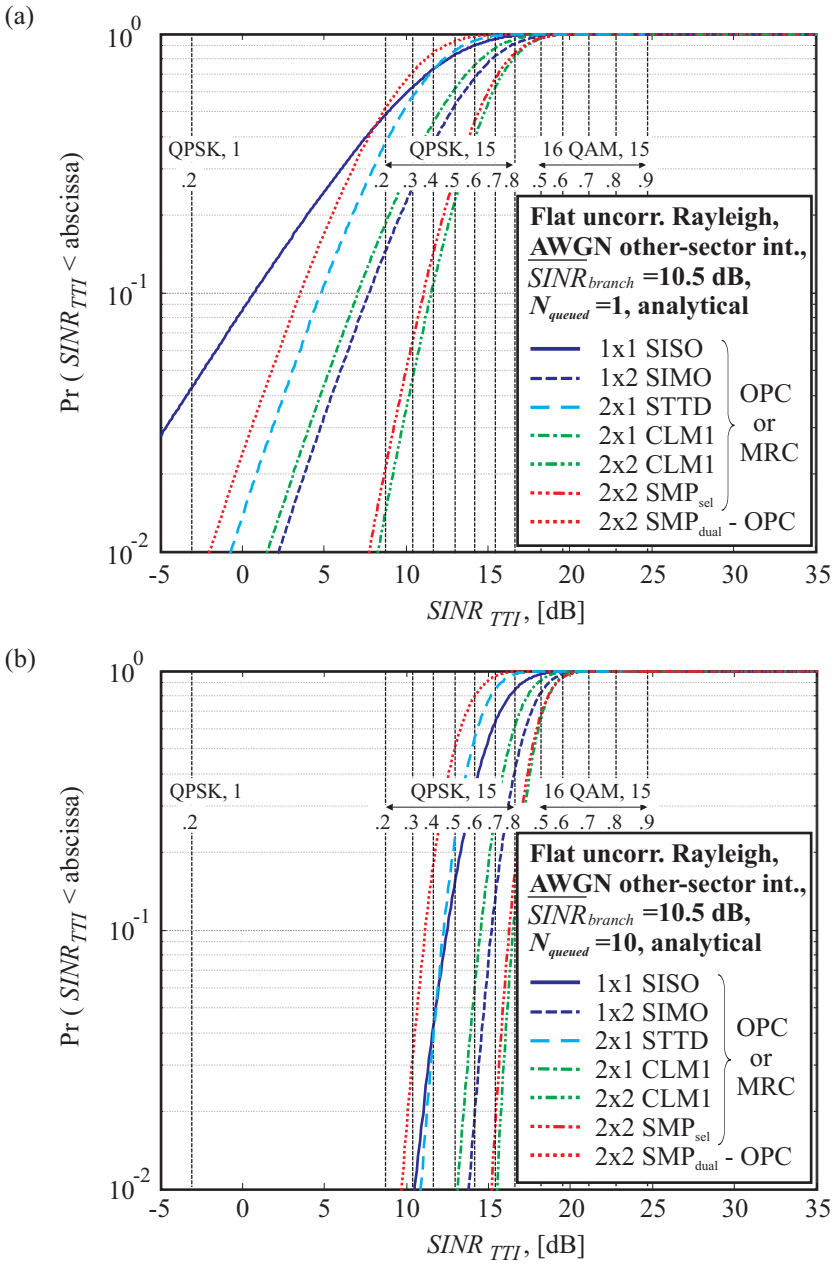

Figure 2.9: Analytical results for the SINR distributions in a flat Rayleigh fading environment with decorrelation between the antenna elements. Other-sector interference is experienced as AWGN. (a) cdfs for $N_{queued} = 1$ and (b) cdfs for $N_{queued} = 10$.

this simplified example. As a comparison, the total system throughput loss due to STTD is in [Rami03a, p. 140] obtained as 15%, which is the reason why STTD has not been considered for further study throughout.

Looking at the SINR cdfs of 2×2 SMP$_{dual}$-OPC, their performances appear worse than those of all other schemes. However, 2×2 SMP$_{dual}$-OPC is among the presented the only dual stream scheme. The worse SINR statistics reflect the price of co-stream interference. Overall 2×2 SMP$_{dual}$ throughput is thus given by twice the throughput that can be obtained from the presented 2×2 SMP$_{dual}$-OPC SINR statistics.

The mean SINR of 2×2 SMP$_{dual}$-OPC is obtained on the basis of (2.22), (2.24) and (2.25). It amounts to

$$\begin{aligned} &\overline{SINR}_{2\times 2SMP_{dual}-OPC} \\ &= \frac{\overline{SINR}_{branch}}{2} \cdot \left(\frac{2 + \frac{1}{\tilde{N}_{codeco}} \cdot \overline{SINR}_{branch}}{1 + \frac{1}{\tilde{N}_{codeco}} \cdot \overline{SINR}_{branch}} \right) \quad . \end{aligned} \tag{2.26}$$

Detailed calculations can be found in Appendix A.2.

The cost of dual stream transmission priced in terms of mean SINR per stream with respect to any other $scheme$ can on the basis of (2.26) and (2.16) be written as

$$\underset{scheme}{\beta_{2\times 2SMP_{dual}-OPC,}} = \frac{\overline{SINR}_{2\times 2SMP_{dual}-OPC}}{\overline{SINR}_{scheme}} \quad . \tag{2.27}$$

This is plotted in Figure 2.10. It can be seen that the higher the $\overline{SINR}_{branch}$ the more expensive it is to switch on the second stream. This can intuitively be explained by the fact that the co-stream interference power contributes to the denominator of the instantaneously achievable SINR. At low $\overline{SINR}_{branch}$ this co-stream interference contribution increases the denominator only marginally. However, at higher instantaneous SINR, where the denominator without co-stream interference is relatively small, the co-stream interference contribution increases the denominator significantly. This makes co-stream transmission from a $\underset{scheme}{\beta_{2\times 2SMP_{dual}-OPC,}}$ point of view more expensive at higher $\overline{SINR}_{branch}$. However, as seen from the asymptotic behaviour, the expenses are tightly upper and lower bounded. The bounds for $\overline{SINR}_{branch} \uparrow \infty$ are given in the last column of Table 2.4.

2.4 Summary

The key HSDPA mechanisms, *i.e.* link adaptation and packet scheduling, have been introduced. In the ideal situation that 15 multicodes are set aside for HS-DSCH transmission, it was shown that the HSDPA system's dynamic range stretches over

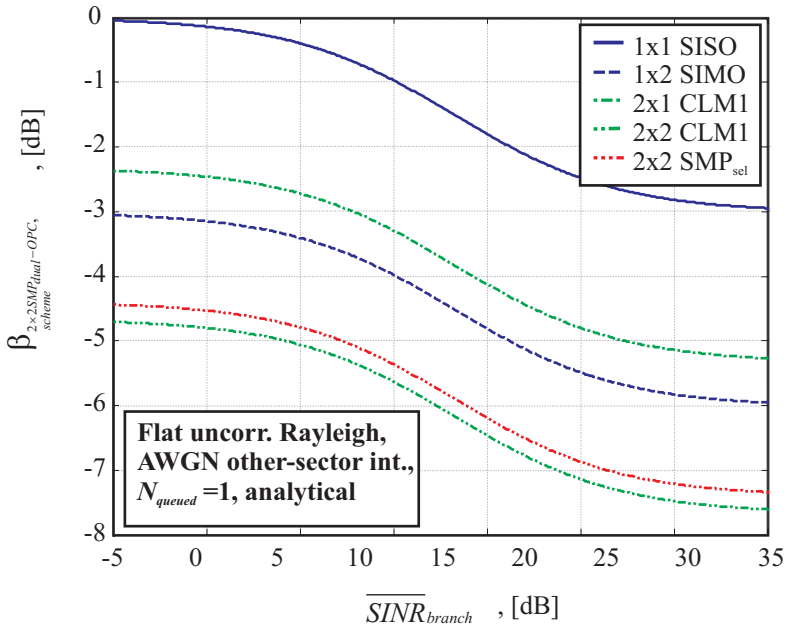

Figure 2.10: Mean SINR gain of 2×2 SMP$_{dual}$ over single stream schemes in flat Rayleigh fading with decorrelated antenna elements and AWGN other-sector interference.

approximately 32 dB. This dynamic range can be extended at the lower end by packet retransmission and packet combining. Going towards the upper end the SINR-to-throughput relationship is approximately linear up to an SINR of around 13 dB. Exceeding 13 dB less and less benefit can be obtained from SINR increases until finally at 27 dB reaching a point where further SINR increase does not result in further throughput benefit.

Besides, the PF scheduling algorithm introduces selection diversity to the system by scheduling preferably those users that are in instantaneously good downlink conditions with respect to their mean. This leads to a situation where especially the mean SINR benefits that can be obtained from multiple antenna schemes become attractive while antenna diversity order increase in connection with a high multi-user selection diversity order delivers less and less benefit.

The SINR cdfs as well as the means of all multiple antenna schemes that will in the following be considered in link and network simulations have been presented in a flat Rayleigh fading environment with AWGN other-sector interference. It was found that 2×2 CLM1 SINR statistics are superior to all other single stream schemes, closely followed by 2×2 SMP$_{sel}$. The 2×2 SMP$_{dual}$-OPC SINR statistics appear even worse than those of the simple 1×1 SISO reference case. However, 2×2 SMP$_{dual}$-OPC delivers simultaneously two data streams at the price of additional co-stream interference. It was shown that the amount of co-stream interference is upper bounded. Priced in terms of mean SINR the cost of 2×2

SMP$_{dual}$-OPC co-stream transmission, for example with respect to the mean SINR of 2×2 SMP$_{sel}$, does not exceed 7.4 dB.

In addition to more details on the presented analytical results, Appendix A covers mean SINR performance of 1×1 SISO and 1×2 SIMO-MRC in the presence of one dominant interferer, 1×2 SIMO-MRC performance with correlated interference experienced at the antenna elements, 2×1 CLM1-MRC mean SINR performance in frequency selective fading, and 2×2 branch MRC with correlation between the antenna elements. Instead of presenting the obtained bounds here they are introduced at their first use when validating and interpreting the obtained simulation results.

Chapter 3

MIMO DS-CDMA SINR Formulation

This chapter introduces a general downlink MIMO DS-CDMA SINR formulation that describes the symbol level SINR at the output of a linear space-time RAKE or a linear space-time MMSE receiver. Derivations are based on the SISO DS-CDMA SINR derivations in [Fran02]. The presented formulations are, however, more general as they allow to incorporate different multiple antenna transmission schemes that employ a finite number of tx weight sets, as well as different kinds of potentially simultaneously deployed spreading strategies, *i.e.* orthogonal spreading, pseudo random spreading, or identical spread spatial multiplexing. This flexibility is achieved through the introduction of a novel virtual channel concept. The developed SINR formulations are the basis of all tx-rx-scheme SINR performance simulations presented throughout this dissertation.

3.1 Introduction

The following uses a time discrete block signal processing approach to derive the symbol level SINR at the output of either a linear space-time RAKE or a linear space-time MMSE receiver. Besides accounting for the desired signal, the SINR formulation needs to account for interfering signals transmitted within the same sector as well as interfering signals transmitted in other sectors. With respect to the desired signal all other signals can either appear as

- orthogonal spread interference,
- pseudo random spread interference, or
- identical spread interference with different spatial signatures.

The MIMO DS-CDMA SINR formulation should be general enough to be applicable to various tx antenna processing schemes with the additional condition that different antenna processing schemes can be used simultaneously in the same sector. If the formulation is able to write the received signal in the form of a standard linear equation, then known RAKE and MMSE filter solutions as in [Klei97], [Fran02] can be applied. The MMSE optimisation criterion is to minimise the mean of the square error between estimated and actual symbol. This maximises the symbol level SINR at the output of the MMSE receiver. The solution is the standard solution to the discrete time representation of the Wiener-Hopf equations [Hayk96, p. 206], [Moon00, pp. 169-179]. It is based on the inverse of the received signal covariance matrix and the received signal mean vector, *i.e.* the covariance of the received signal with the desired filter output. Similarly the RAKE receiver can be seen as a matched filter, whose formulation only involves the received signal mean vector [Klei97], [Fran02]. The difficulty is therefore not to find the receiver formulation itself, but rather to account for all the signal components contributing to the received signal covariance matrix and the received signal mean vector.

To come to a general formulation of the received signal covariance matrix and the received signal mean vector independent of potential tx weights, a virtual channel formulation is introduced, where the virtual channel represents the radio propagation channel *after* transmit weight application. The virtual channel concept is depicted in Figure 3.1. The upper part displays the standard transmit weight transmission in the physical domain, as for example introduced in Figure 2.7. Different sectors are indexed with a sector index i. Sector i transmits a chip sequence using transmit weight set m. After tx weight application the chip sequence is transmitted from the physical transmit antennas. The radio propagation channel between the physical tx antennas and the physical rx antennas is described through physical channel impulse response vectors $\underline{\mathbf{h}}$. All other chip sequences transmitted with different weight sets are additionally transmitted over the same physical antennas.

In the lower part of Figure 3.1 the physical channel impulse responses are combined with the transmit weights to form a virtual channel impulse response, *i.e.*

$$\mathbf{h}^i_{n,m} = \underline{\mathbf{h}}^i_{n,1} \cdot w^i_{1,m} + \underline{\mathbf{h}}^i_{n,2} \cdot w^i_{2,m} \quad , \tag{3.1}$$

where n is the receive antenna index and in the presented example $n \in [1, 2]$. The number of virtual channels in a sector is denoted N_{vir}. It is constant and identical to the number of possible tx weight sets. The problem of accounting for own sector interference is thus transformed into the problem of accounting for the received powers, P^i_m, over the different virtual channels. Similarly the interference received from N_{sec} other sectors is described by the received power over their virtual channels. The total received signal vector $\mathbf{r}$ can through the virtual channel concept be written as

$$\mathbf{r} = \sum_{i=1}^{N_{\text{sec}}} \sum_{m=1}^{N_{vir}} \mathbf{H}^i_m \cdot \mathbf{s}^i_m + \boldsymbol{\psi} \quad , \tag{3.2}$$

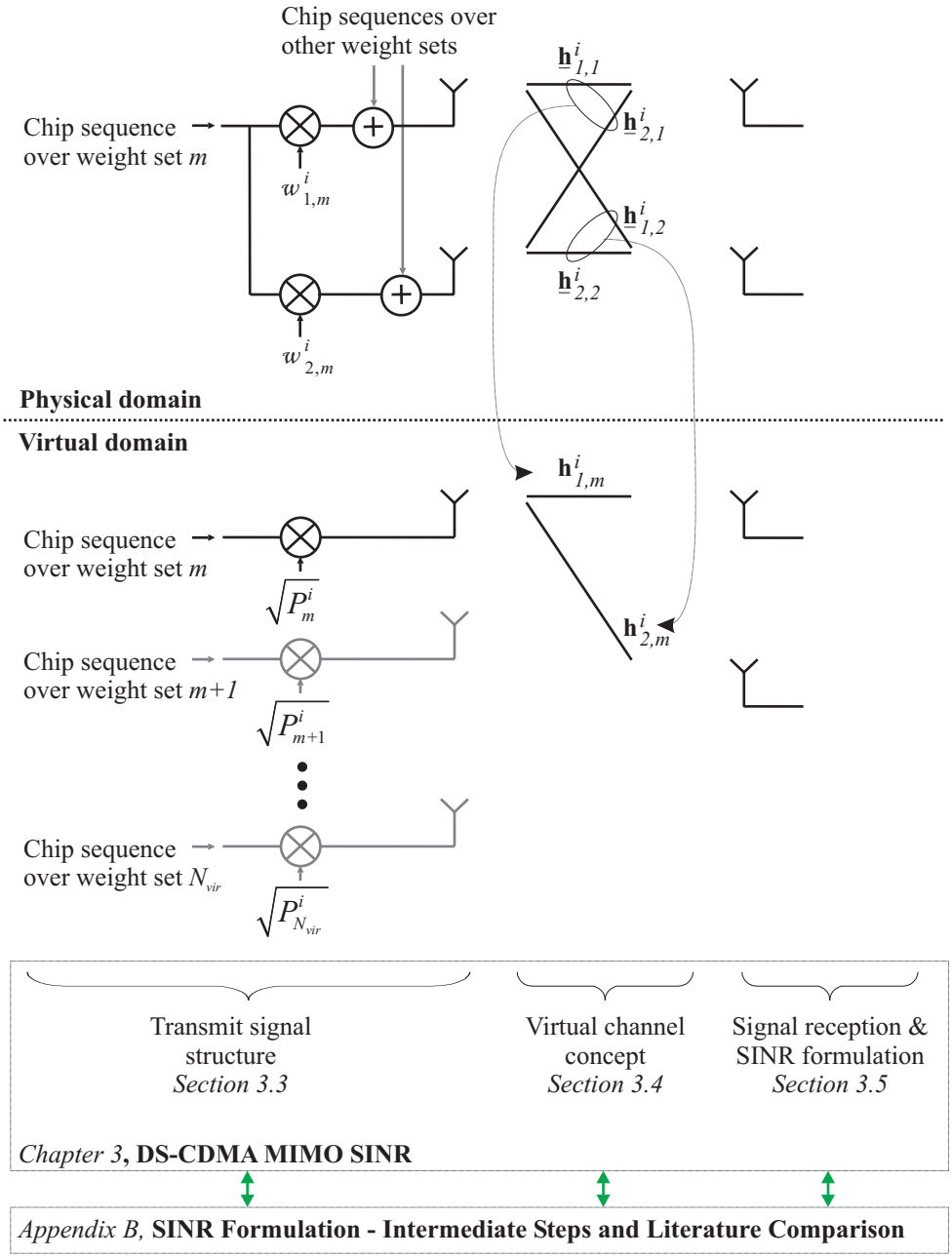

Figure 3.1: Virtual channel representation and chapter outline.

where $\mathbf{H}_m^i$ is a convolution matrix [Rale98], [Fran02] constructed from the virtual channel impulse responses corresponding to virtual channel m and sector i. Further, $\mathbf{s}_m^i$ represents the combined chip sequence vector form sector i over virtual channel m, and $\boldsymbol{\psi}$ represents thermal noise. Thus the virtual channel concept allows to describe different multiple antenna schemes in the form of a standard linear equation for which the RAKE and MMSE filter solutions are known [Klei97], [Fran02]. The disadvantages are that the virtual channel concept is only applicable if the tx schemes can be described with a finite number of tx weight sets. Further, it makes it necessary to account for the time variant powers of the different chip sequence vectors.

Figure 3.1 not only introduces the virtual channel concept, but also gives an overview of the main sections within this chapter. After presenting the underlying assumptions in Section 3.2, details on the transmit signal structure are presented in Section 3.3. Among others it will be shown how to separately account for the received powers from orthogonal spread interfering signals, pseudo random spread interfering signals, and identical spread interfering signals with different spatial signatures. The details on the virtual channel concept are given in Section 3.4, while signal reception is outlined in Section 3.5. Special emphasis is in Section 3.5 put on deriving the symbol level SINR formulation for the space-time RAKE and the space-time MMSE receiver. More involved and lengthy mathematical derivations are carried out in Appendix B. Moreover, Appendix B compares the obtained SINR formulations to a less general formulation available in the public literature.

3.2 Assumptions

To simplify the derivations the following assumptions are made:

- 3G systems commonly use root raised cosine tx filters [3GPP04a], [Koro04]. When receiving with corresponding root raised cosine rx filters there is ideally no inter chip interference in frequency flat fading propagation channels [Hayk94, pp. 427-434]. Further, the rx filters output is usually over-sampled at several times the chip rate, allowing, for example, RAKE finger placement at fractional chip times [Holm04, p. 54]. For simplicity the following is, however, based on a discrete time model with chip rate sampling. This detaches the derivations from a specific physical implementation. It is, however, in line with other derivations that present basic principles rather than detailed implementations, *e.g.* [Klei97], [Wern99], [Fran02].
- The radio propagation channel is assumed stationary over a single block-processing operation. This assumption is justified by the fact that in the following a block-processing operation will relate to less than three HS-DSCH symbol intervals. Thus it is in the order of 12 μs. In the frequency range

of importance to 3G, *i.e.* around 1 GHz to 3 GHz [Holm04, Chp. 1], the radio propagation channel coherence time is even for fast moving mobiles in the ms range [Rapp99, pp. 165-166]. To apply the following derivations to other systems, it is necessary to assure that this stationery assumption remains valid.

- The transmitted data symbols as well as the Gold Scrambling code chips are assumed aperiodic i.i.d, which follows the approach in [Fran02].

- The excess delay spread of the radio propagation channel [Rapp99, p. 160] stays within N_L chip periods. The receive filter chip length is $N_{FIR} = 2 \cdot N_L - 1$. This assures that all IPI components before and after the chip of interest can be represented [Ahme01]. In real implementations, only a limited amount of hardware will be available. *E.g.* the number of available RAKE fingers might be limited to six [3GPP03a]. The above assumption of the availability of N_{FIR} receive filter weights, similarly to the one taken in [Fran02], is therefore ideal and detached from implementation specific considerations.

3.3 Transmit Signal Structure

The transmit signal structure is presented. The selected notation targets the description of all signal chips that play a roll in recovering a transmitted symbol at the receiver.

In standard DS-CDMA downlink transmission [Tann04], [Koro04] a *channelisation code* and a *scrambling code* sequence are jointly applied to perform direct sequence spreading of the data symbols. Real valued channelisation codes are obtained from a Walsh-Hadamard code tree and are reused in different sectors of the cellular system. Time aligned channelisation codes from this tree are orthogonal. Let the chip length of the channelisation code of interest be N_{sf}. Channelisation code chips can take the values ± 1. Every orthogonal code resource is associated with an index k and exactly N_{sf} equal length orthogonal channelisation code resources exist. Different sectors i use different pseudo random scrambling codes. As in [Fran02] it is assumed that the scrambling code sequences are aperiodic i.i.d. They have zero mean, variance one, and their chips take on the values $\pm\frac{1}{\sqrt{2}} \pm \frac{1}{\sqrt{2}}j$.

A *spreading code* is defined through chip-by-chip multiplication of a channelisation code with index k and an N_{sf} chip long fraction of the scrambling code with index i. Hence it carries a joint index k, i. A symbol $d_m^{k,i}[p]$ with symbol index p, to be transmitted over virtual channel m, is spread with this N_{sf} chip long

spreading code. The corresponding spreading code vector $\mathbf{c}^{k,i}[p]$ is given by

$$\mathbf{c}^{k,i}[p] = \mathbf{c}^{k,i}\left[\left\lceil \frac{q}{N_{sf}} \right\rceil\right] = \left[\begin{array}{cccc} c^{k,i}[q] & c^{k,i}[q+1] & \ldots & c^{k,i}[q+N_{sf}-1] \end{array}\right]^T \quad , \tag{3.3}$$

where (3.3) q is introduced as the discrete chip time index. It relates to the symbol index p via

$$p = \left\lceil \frac{q}{N_{sf}} \right\rceil \quad , \tag{3.4}$$

where $\lceil \cdot \rceil$ represents the rounding up operation to the nearest integer. This operation, for example, indicates that the code chip $c^{k,i}[0]$ corresponds to a different symbol than the code chips $c^{k,i}[1]$ to $c^{k,i}[N_{sf}]$.

The symbols of data sequence $\left\{d_m^{k,i}\right\}$ are assumed i.i.d between the points of a complex and origin symmetric constellation diagram. *E.g.* they might be QPSK or 16 QAM modulated. The mean symbol power is one. Statistical properties of spreading codes and data sequences are detailed in Appendix B.1.1.

Attributing a power $P_m^{k,i}$ to the data sequence $\left\{d_m^{k,i}\right\}$ a single chip of the spread signal is given by

$$s_m^{k,i}[q] = \sqrt{P_m^{k,i}} \cdot c^{k,i}[q] \cdot d_m^{k,i}\left[\left\lceil \frac{q}{N_{sf}} \right\rceil\right] \quad , \tag{3.5}$$

For notational convenience, the power $P_m^{k,i}$ not only relates to the sector's transmit power, but also incorporates all mean power effects, *e.g.* caused by path loss and shadow fading between the sector antennas and the mobile terminal [Rapp99, Chp. 3]. Thus $P_m^{k,i}$ represents the small area mean received power, where *small area mean* indicates that it is the power obtained when averaging out the effect of multipath fading.

Stacking $N_{FIR} + N_L - 1$ chips into a vector delivers the spread signal vector

$$\mathbf{s}_m^{k,i}[q] = \left[\begin{array}{l} s_m^{k,i}\left[q - \dfrac{N_{FIR}-1}{2}\right] \\ \vdots \\ s_m^{k,i}[q] \\ \vdots \\ s_m^{k,i}\left[q + \dfrac{N_{FIR}-1}{2} + N_L - 1\right] \end{array}\right] \quad . \tag{3.6}$$

Further, the matrix $\mathbf{S}_m^{k,i}[p]$ is defined as

$$\mathbf{S}_m^{k,i}[p] = \left[\begin{array}{cccc} \mathbf{s}_m^{k,i}[q] & \mathbf{s}_m^{k,i}[q+1] & \ldots & \mathbf{s}_m^{k,i}[q+N_{sf}-1] \end{array}\right] \quad , \tag{3.7}$$

with the dimensions $(N_{FIR}+N_L-1)\times N_{sf}$. This matrix will play a central role when estimating the original data symbol $d_m^{k,i}[p]$. Its row dimension accounts for IPI components before and after the chip of interest, while its column dimension accounts for the fact that the symbol $d_m^{k,i}[p]$ is spread over N_{sf} chips.

Summing the spread signal vectors from all channelisation code resources delivers

$$\mathbf{s}_m^i[q]=\sum_{k=1}^{N_{sf}}\mathbf{s}_m^{k,i}[q] \quad , \tag{3.8}$$

which is the combined chip sequence vector to be transmitted in sector i using virtual channel m. Similarly the matrix $\mathbf{S}_m^i[p]$ is defined as

$$\mathbf{S}_m^i[p]=\sum_{k=1}^{N_{sf}}\mathbf{S}_m^{k,i}[p] \quad , \tag{3.9}$$

and the small area mean received power sum is defined as

$$P_m^i=\sum_{k=1}^{N_{sf}}P_m^{k,i} \quad . \tag{3.10}$$

It represents the total small area mean received power from sector i over virtual channel m.

To implement various tx-schemes, like for example CLM1 or SMP$_x$, the virtual channel concept requires a virtual channel power mapping strategy, as indicated in the lower part of Figure 3.1. This power mapping strategy determines the power $P_m^{k,i}$ of the spread signal sequence $\left\{s_m^{k,i}\right\}$. Besides large scale mean power effects, that for notational simplicity have been absorbed in $P_m^{k,i}$, the virtual channel power is dependent on a constant fractional sector power allocation, denoted $\eta^{k,i}$, and a time dependent virtual channel mapping function $\omega_m^{k,i}$, *i.e.*

$$P_m^{k,i}=\omega_m^{k,i}\cdot\eta^{k,i}\cdot\overline{P}^i \quad , \tag{3.11}$$

where $\overline{P}^i$ represents the *full load*, small area mean received power from sector i. In other words, $\overline{P}^i$ corresponds to the total multipath averaged SISO link received power from sector i, if this sector was permanently transmitting with constant power. For organisational purposes the small area mean received power from all virtual channels of sector i is expressed as a virtual channel power vector $\mathbf{P}^{k,i}$

$$\mathbf{P}^{k,i}=\begin{bmatrix}P_1^{k,i}\\P_2^{k,i}\\\vdots\\P_{N_{vir}}^{k,i}\end{bmatrix}=\underbrace{\begin{bmatrix}\omega_1^{k,i}\\\omega_2^{k,i}\\\vdots\\\omega_{N_{vir}}^{k,i}\end{bmatrix}}_{\boldsymbol{\omega}^{k,i}}\cdot\eta^{k,i}\cdot\overline{P}^i \quad , \tag{3.12}$$

where the vector $\boldsymbol{\omega}^{k,i}$ is implicitly defined through stacking all N_{vir} virtual channel mapping functions. It is restricted to $\left|\boldsymbol{\omega}^{k,i}\right|_1 \leqslant 1$.

The following considers an example where only the HS-DSCH channel is transmitted in sector i using CLM1: As introduced in Table 2.2, with CLM1 the HS-DSCH channel can be transmitted with four different transmit weights. In this case the virtual channel power vector $\mathbf{P}^{k,i}$ writes

$$\mathbf{P}^{HSDSCH,i} = \begin{bmatrix} P_1^{HSDSCH,i} \\ P_2^{HSDSCH,i} \\ P_3^{HSDSCH,i} \\ P_4^{HSDSCH,i} \end{bmatrix} = \underbrace{\begin{bmatrix} \omega_1^{HSDSCH,i} \\ \omega_2^{HSDSCH,i} \\ \omega_3^{HSDSCH,i} \\ \omega_4^{HSDSCH,i} \end{bmatrix}}_{\boldsymbol{\omega}^{HSDSCH,i}} \cdot \eta^{HSDSCH,i} \cdot \overline{P}^i \quad . \tag{3.13}$$

The HS-DSCH is using the orthogonal channelisation code resource k. In case of $\eta^{HSDSCH,i} = 1$, this means the entire full load, small area mean received power from sector i is due to the HS-DSCH transmission. The time variant vector

$$\boldsymbol{\omega}^{HSDSCH,i} = \begin{bmatrix} \omega_1^{HSDSCH,i} \\ \omega_2^{HSDSCH,i} \\ \omega_3^{HSDSCH,i} \\ \omega_4^{HSDSCH,i} \end{bmatrix} \quad , \tag{3.14}$$

determines over which virtual channel the HS-DSCH power is actually transmitted. One of its elements is one, while the others are zero, *e.g.*

$$\boldsymbol{\omega}^{HSDSCH,i} = \begin{bmatrix} 0 \\ 1 \\ 0 \\ 0 \end{bmatrix} \quad , \tag{3.15}$$

in which case the HS-DSCH power would be temporarily received over the virtual channel corresponding to tx weight set two.

Returning to the definition of the virtual channel power vector $\mathbf{P}^{k,i}$, further stacking operations with respect to the code resources k enables an extended version of (3.10), *i.e.*

$$\mathbf{P}^i = \underbrace{\begin{bmatrix} \boldsymbol{\omega}^{1,i} & \boldsymbol{\omega}^{2,i} & \dots & \boldsymbol{\omega}^{N_{sf},i} \end{bmatrix}}_{\boldsymbol{\omega}^i} \cdot \underbrace{\begin{bmatrix} \eta^{1,i} \\ \eta^{2,i} \\ \vdots \\ \eta^{N_{sf},i} \end{bmatrix}}_{\boldsymbol{\eta}^i} \cdot \overline{P}^i \quad , \tag{3.16}$$

where the virtual channel power mapping matrix $\boldsymbol{\omega}^i$ and the sector power allocation vector $\boldsymbol{\eta}^i$ are defined implicitly, and $\boldsymbol{\eta}^i$ is restricted to $\left|\boldsymbol{\eta}^i\right|_1 = 1$.

The implementation of the virtual channel power mapping matrix $\boldsymbol{\omega}^j$ is tx-scheme specific. In Chapter 4 it will be shown how every column vector of $\boldsymbol{\omega}^j$ implements the tx scheme of a certain transmission group, *i.e.* a group of code resources that are simultaneously transmitted using the same tx weight set. Further, the elements of $\boldsymbol{\eta}^j$ will be shown to distribute the total sector transmit power between the transmission groups. Thus $\boldsymbol{\omega}^j$ and $\boldsymbol{\eta}^j$ are placeholders to allow the organisation and implementation of different simultaneously used tx schemes as for example specified in Table 1.2. The remainder of this chapter will proceed with the general SINR formulation independent of these very set-up specific considerations.

Throughout this section an indexing notation, $^{k,i}_{m}$, has been defined. k was introduced as the channelisation code index. i was introduced with a double meaning, firstly indicating sector i, and secondly indicating scrambling code i. This double definition eases the notation and is unambiguous as long as only one scrambling code is used per sector. This will be the case throughout all studied scenarios. However, to obtain a more general formulation that allows the usage of several scrambling codes per sector an additional index is introduced in Appendix B.3. This additional index clearly distinguishes different scrambling codes within sector i. Finally m was introduced as the virtual channel index. With this indexing notation it is possible to distinguish orthogonal spread interfering signals, pseudo random spread interfering signals, and identically spread interfering signals with different spatial signatures. This can be seen in the following example: Let the capital letters K, I, M denote the *desired* signal's channelisation code index, scrambling code index, and virtual channel (spatial signature) index respectively. The desired spread signal vector corresponding to a chip q_1 therefore writes $\mathbf{s}^{K,I}_{M}[q_1]$. Further, $\mathbf{s}^{k,i}_{m}[q_2]$ is any spread signal vector at chip q_2. If $\mathbf{s}^{k,i}_{m}[q_2] \wedge (i \neq I \vee q_2 \neq q_1)$ the signal contribution appears as pseudo random spread with respect to the desired spread signal vector. If $\mathbf{s}^{k,i}_{m}[q_2] \wedge i = I \wedge q_2 = q_1 \wedge k \neq K$, the signal appears as orthogonal spread, *i.e.* zero interference. Finally if $\mathbf{s}^{k,i}_{m}[q_2] \wedge i = I \wedge q_2 = q_1 \wedge k = K \wedge m \neq M$, the signal is identically spread, but has experienced a different virtual radio propagation channel. It therefore carries a different spatial signature. Details on the virtual channel propagation are presented in the following section.

3.4 Virtual Channel Propagation

N_L was introduced as the number of chips higher or equal to the chip length of the excess delay spread of the radio propagation channel. In sector i an N_{FIR} chip long channel impulse response vector $\underline{\mathbf{h}}^{i}_{n,z}$, is defined between physical tx antenna[1]

[1]The index z is in Chapter 2 used to index MCS-multicode combinations. The intended meaning of z will, however, always be clear from the context.

z and physical rx antenna n, *i.e.*

$$\underline{\mathbf{h}}^i_{n,z} = \left[\begin{array}{cccccccc} \underline{h}^i_{n,z}[1] & \underline{h}^i_{n,z}[2] & \dots & \underline{h}^i_{n,z}[N_L] & 0 & \dots & 0 \end{array} \right]^T \quad . \tag{3.17}$$

where the elements $\underline{h}^i_{n,z}$ represent complex multipath channel transfer functions, at the discrete chip delays 1 to N_L. Further, N_{FIR} was defined as $2 \cdot N_L - 1$. The channel impulse response vectors are hence zero padded using $N_L - 1$ zeros. The channel impulse response vectors are time variant. However, the discrete chip time index q is dropped in (3.17) and throughout the following to simplify the notation. If one or more antennas transmit a weighted version of the same signal, the corresponding combined channel is referred to as *virtual channel*, and the impulse responses relating to a specific rx antenna n are referred to as virtual channel impulse responses. They are defined as

$$\mathbf{h}^i_{n,m} = \sum_{z=1}^{N_{tx}} \underline{\mathbf{h}}^i_{n,z} \cdot w^i_{z,m} \quad , \tag{3.18}$$

which is a generalised form of (3.1). $w^i_{z,m}$ represents the tx weight applied to physical tx-antenna z. The weights are normalised so that

$$\sum_{z=1}^{N_{tx}} \left| w^i_{z,m} \right|^2 = 1 \quad . \tag{3.19}$$

This means that the power of any applicable weight set is one.

As small area mean received power effects are absorbed in the definition of the spread signal vector, the mean power of the channel impulse responses, and with (3.19) also the mean power of the virtual channel impulse responses, are normalised to one, *i.e.*

$$\mathrm{E}_{mf} \left\{ \left(\underline{\mathbf{h}}^i_{n,z} \right)^H \underline{\mathbf{h}}^i_{n,z} \right\} = \mathrm{E}_{mf} \left\{ \left(\mathbf{h}^i_{n,m} \right)^H \mathbf{h}^i_{n,m} \right\} = 1 \quad , \tag{3.20}$$

where $\mathrm{E}_{mf} \{ \cdot \}$ indicates expectation with respect to multipath fading.

Multipath propagation is described as convolution of the combined chip sequence vector $\mathbf{s}^i_m$ with the virtual channel impulse responses. For this purpose the $N_{FIR} \times (N_{FIR} + N_L - 1)$ convolution matrix of vector $\mathbf{h}^i_{n,m}$ is defined as

$$\mathbf{H}^i_{n,m} = \left[\begin{array}{ccccccccc} h^i_{n,m}[N_L] & h^i_{n,m}[N_L-1] & \cdots & h^i_{n,m}[1] & & & & & \\ & h^i_{n,m}[N_L] & \cdots & h^i_{n,m}[2] & h^i_{n,m}[1] & & & & \\ & & & \vdots & \vdots & & & & \\ & & & h^i_{n,m}[N_L] & h^i_{n,m}[N_L-1] & \cdots & h^i_{n,m}[2] & h^i_{n,m}[1] & \\ & & & & & & \vdots & \vdots & \\ & & & & & & h^i_{n,m}[N_L] & h^i_{n,m}[N_L-1] & \cdots \; h^i_{n,m}[1] \\ & & & & & & & h^i_{n,m}[N_L] & \cdots \; h^i_{n,m}[2] \; h^i_{n,m}[1] \end{array} \right] , \tag{3.21}$$

where vector $\mathbf{h}^i_{n,m}$ corresponds to the N_L-th column of $\mathbf{H}^i_{n,m}$

Stacking all virtual channel matrices corresponding to a mobile's N_{rx} physical receive antennas delivers the virtual channel matrix $\mathbf{H}^i_m$, *i.e.*

$$\mathbf{H}^i_m = \begin{bmatrix} \mathbf{H}^i_{1,m} \\ \mathbf{H}^i_{2,m} \\ \vdots \\ \mathbf{H}^i_{N_{rx},m} \end{bmatrix} \quad . \tag{3.22}$$

For further developments, it should be noted that the N_L-th column of $\mathbf{H}^i_m$ is given by

$$\left(\mathbf{H}^i_m\right)_{[:,N_L]} = \underbrace{\begin{bmatrix} \mathbf{h}^i_{1,m} \\ \mathbf{h}^i_{2,m} \\ \vdots \\ \mathbf{h}^i_{N_{rx},m} \end{bmatrix}}_{\mathbf{h}^i_m} \quad , \tag{3.23}$$

where $\mathbf{h}^i_m$, as representation of all stacked $\mathbf{h}^i_{n,m}$, is defined implicitly.

Additionally to the serving and all interfering sectors' signal power, thermal noise will be present at the rx antennas. Thermal noise is represented by vector $\boldsymbol{\psi}[q]$ containing $N_{FIR} \cdot N_{rx}$ AWGN samples with variance P^{th}, *i.e.*

$$\mathrm{E}\left\{\boldsymbol{\psi}[q] \cdot (\boldsymbol{\psi}[q])^H\right\} = P^{th} \cdot \mathbf{I}_{(N_{FIR} \cdot N_{rx})} \quad , \tag{3.24}$$

where P^{th} denotes thermal noise power.

3.5 Signal Reception and SINR Formulation

As introduced in (3.2) the received signal vector writes

$$\mathbf{r}[q] = \sum_{i=1}^{N_{\mathrm{sec}}} \sum_{m=1}^{N_{vir}} \mathbf{H}^i_m \cdot \mathbf{s}^i_m[q] + \boldsymbol{\psi}[q] \quad . \tag{3.25}$$

Like in [Fran02] a chip spaced post despreading receive filter implementation is considered and a conceptual diagram of despreader and receive filter implementation is displayed in Figure 3.2. It can be seen that N_{sf} consecutive observations of the received signal vector $\mathbf{r}[q]$ are despread with the complex conjugate of the desired symbol's spreading code vector $\mathbf{c}^{K,I}[p]$, forming the post despreading receive filter input vector $\mathbf{z}^{K,I}_M[p]$. Recall that the upper case indices are introduced to distinguish the desired spreading code resource K, I, and the desired virtual

channel M from any code resource k, i, and any virtual channel m. Further, it can be observed that the post despreading receive filter coefficients $\overline{g}_{n,M}^{K,I}$ at each receive antenna n span an N_{FIR} chip long interval, *i.e.* from $-\frac{N_{FIR}-1}{2}$ to $\frac{N_{FIR}-1}{2}$. The structure of $\mathbf{z}_M^{K,I}[p]$ is, additionally to the visual representation in Figure 3.2, also given in Appendix B.1.2. RAKE and MMSE receiver distinguish themselves through different receive filter weights.

The post despreading MMSE receive filter weights can be calculated based on a standard solution to the Wiener-Hopf equations [Hayk96, p. 206]. The optimisation criterion is to minimise the mean of the square error between estimated and actual symbols and thus to maximise the output SINR. Following the approach in [Madh94], [Fran02] they are in matrix vector notation given by

$$\mathbf{g}_M^{K,I}\Big|_{\ MMSE}\ [p] = \left(\underbrace{\mathrm{E}_{d,\psi}\left\{ \mathbf{z}_M^{K,I}[p] \cdot \left(\mathbf{z}_M^{K,I}[p] \right)^H \right\}}_{\mathbf{\Gamma}_M^{K,I}[p]} \right)^{-1} \cdot \underbrace{\mathrm{E}_{d,\psi}\left\{ \mathbf{z}_M^{K,I}[p] \cdot \left(d_M^{K,I}[p] \right)^* \right\}}_{\boldsymbol{\nu}_M^{K,I}[p]} \quad , \tag{3.26}$$

where the expectation $\mathrm{E}_{d,\psi}\{\ \cdot\ \}$ is taken over the user's symbols and thermal noise. Details on the structure of the implicitly introduced received signal mean vector $\boldsymbol{\nu}_M^{K,I}[p]$ and the received signal covariance matrix $\mathbf{\Gamma}_M^{K,I}[p]$ can be found in Appendix B.1.3 and B.1.4 respectively.

Using these receive filter weights the soft symbol estimates are obtained as

$$\hat{d}_M^{K,I}[p] = \left(\mathbf{g}_M^{K,I}\Big|_{\ MMSE}\ [p] \right)^H \cdot \mathbf{z}_M^{K,I}[p] \quad . \tag{3.27}$$

However, $\mathbf{g}_M^{K,I}$, depending on the exact spreading code chips, needs to be updated on a chip-to-chip basis, which, although optimum, is highly undesirable from a computation complexity point of view. Following the approach in [Fran02] the average symbol level equaliser $\overline{\mathbf{g}}_M^{K,I}$ is therefore obtained by additional averaging

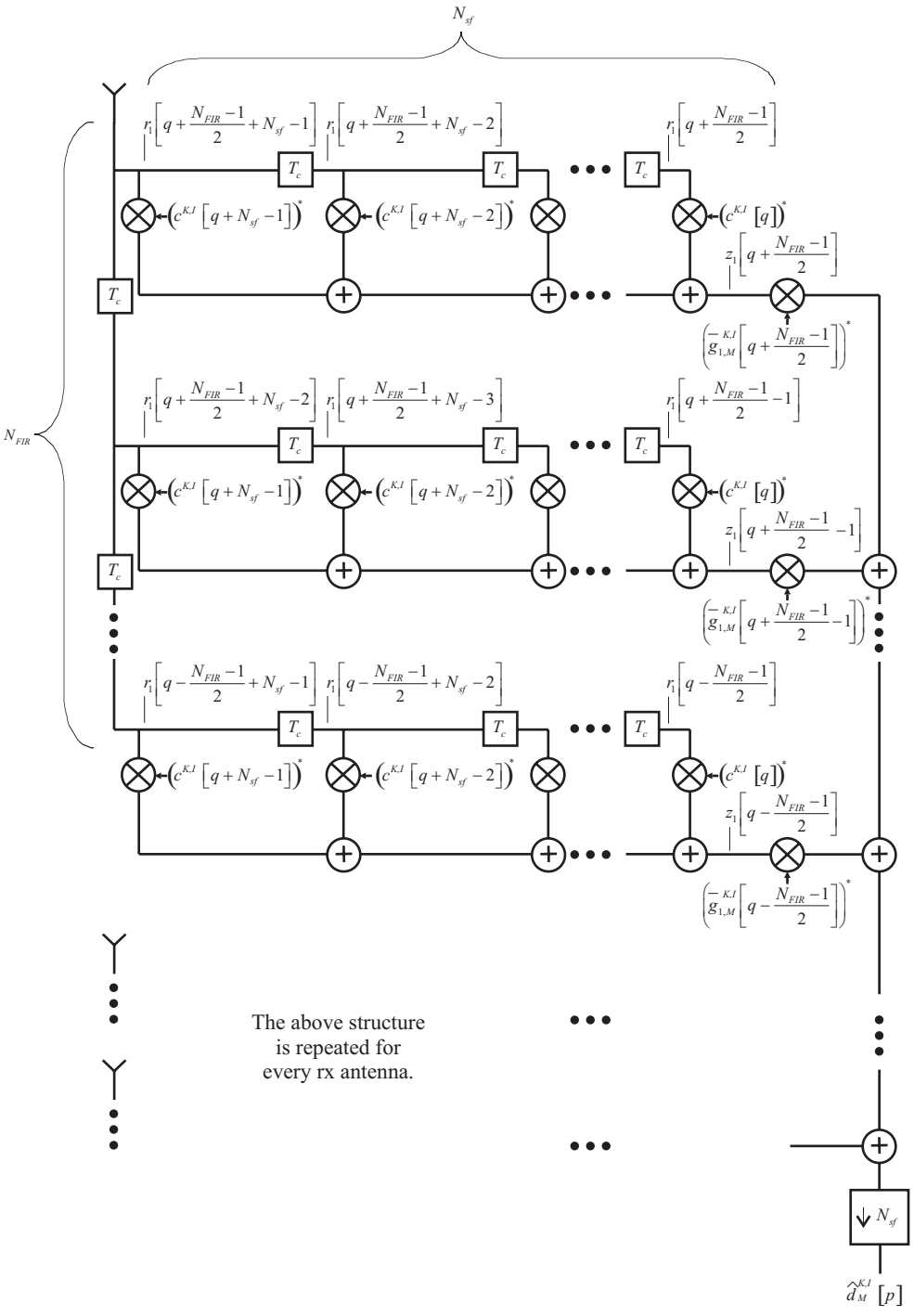

Figure 3.2: Conceptual despreader and receive filter diagram.

over the spreading code chips, *i.e.*

$$\overline{\mathbf{g}}_M^{K,I}\Big|_{MMSE} = \left(\underbrace{\mathrm{E}_c\left\{\mathrm{E}_{d,\psi}\left\{\mathbf{z}_M^{K,I}[p]\cdot\left[\mathbf{z}_M^{K,I}[p]\right]^H\right\}\right\}}_{\overline{\mathbf{\Gamma}}_M^{K,I}}\right)^{-1} \cdot \underbrace{\mathrm{E}_c\left\{E_{d,\psi}\left\{\mathbf{z}_M^{K,I}[p]\cdot\left[d_M^{K,I}[p]\right]^*\right\}\right\}}_{\overline{\boldsymbol{\nu}}_M^{K,I}} \quad . \tag{3.28}$$

The same equaliser weights can now be used for the reception of several symbols, where the required weight update rate relates, among others, to the channel's coherence time. As the weight vector is therefore no longer a direct function of just a single symbol time instant p, the index is dropped in (3.28) and throughout the following. Every further mentioning of the MMSE receiver relates to the chip averaged MMSE receiver definition of (3.28).

Furthermore, the RAKE receiver can under the introduced post despreading receiver formulation be described as matched filter, *i.e.* [Fran02]

$$\overline{\mathbf{g}}_M^{K,I}\Big|_{RAKE} = \underbrace{\mathrm{E}_c\left\{E_{d,\psi}\left\{\mathbf{z}_M^{K,I}[p]\cdot\left[d_M^{K,I}[p]\right]^*\right\}\right\}}_{\overline{\boldsymbol{\nu}}_M^{K,I}} \quad . \tag{3.29}$$

It can be seen that the matched filter part $\overline{\boldsymbol{\nu}}_M^{K,I}$ is identical in the RAKE and the MMSE receiver formulation. However, the MMSE receiver in (3.28) additionally involves the inverse of the chip averaged received signal covariance matrix.

As shown in Appendix B.1.5 the matched filter part, *i.e.* the chip averaged mean vector is given as

$$\overline{\boldsymbol{\nu}}_M^{K,I} = N_{sf}\cdot\sqrt{P_M^{K,I}}\cdot\mathbf{h}_M^I \quad , \tag{3.30}$$

which can be seen as a simple matched filter to the virtual channel impulse responses scaled by the spreading factor N_{sf} and the square root of the small area mean received power corresponding to the desired code resource K, I and the desired virtual channel M. Moreover, as derived in Appendix B.1.6, the chip aver-

aged received signal covariance matrix is given by

$$\begin{aligned}\overline{\mathbf{\Gamma}}_M^{K,I} = & N_{sf} \sum_{i=1}^{N_{\text{sec}}} \sum_{m=1}^{N_{vir}} P_m^i \cdot \mathbf{H}_m^i \left(\mathbf{H}_m^i\right)^H \\ & - N_{sf} \sum_{m=1}^{N_{vir}} P_m^I \cdot \mathbf{h}_m^I \left(\mathbf{h}_m^I\right)^H \\ & + \left(N_{sf}\right)^2 \sum_{m=1}^{N_{vir}} P_m^{K,I} \cdot \mathbf{h}_m^I \left(\mathbf{h}_m^I\right)^H \\ & + N_{sf}\, P^{\text{th}} \cdot \mathbf{I}_{(N_{rx} \cdot N_{FIR})} \quad . \end{aligned} \tag{3.31}$$

The different terms constituting the chip averaged received signal covariance matrix can intuitively be associated with:

Line 1: All power from all sectors and all virtual channels.

Line 2: Minus the power of chip aligned code resources under the desired scrambling code I.

Line 3: Plus the power of the chip aligned wanted channelisation code resource K, which includes the desired signal power but also interfering signal power from spatial multiplexed signals using the same channelisation code resource K as the desired signal. They all experience a coherent despreading gain of N_{sf}. In this special situation there is thus no processing gain with respect to spatial multiplexed interfering signals.

Line 4: Plus thermal noise contribution.

Separating the desired signal contribution, *i.e.* uniquely identified by desired code resource K, I and wanted virtual broadcast channel M, the chip averaged covari-

ance matrix is rewritten as

$$\overline{\mathbf{\Gamma}}_M^{K,I} = N_{sf} P_M^I \cdot \underbrace{\left(\begin{array}{l} \sum_{i=1}^{N_{\text{sec}}} \sum_{m=1}^{N_{vir}} \frac{P_m^i}{P_M^I} \cdot \mathbf{H}_m^i \left(\mathbf{H}_m^i\right)^H \\ - \sum_{m=1}^{N_{vir}} \frac{P_m^I}{P_M^I} \cdot \mathbf{h}_m^I \left(\mathbf{h}_m^I\right)^H \\ + N_{sf} \cdot \sum_{\substack{m=1 \\ m \neq M}}^{N_{vir}} \frac{P_m^{K,I}}{P_M^I} \cdot \mathbf{h}_m^I \left(\mathbf{h}_m^I\right)^H \\ + \frac{P^{th}}{P_M^I} \cdot \mathbf{I}_{(N_{rx} \cdot N_{FIR})} \end{array} \right)}_{\mathbf{\Omega}_M^{K,I}} + (N_{sf})^2 \cdot P_M^{K,I} \cdot \mathbf{h}_M^I \left(\mathbf{h}_M^I\right)^H \quad . \tag{3.32}$$

The implicitly defined $\mathbf{\Omega}_M^{K,I}$ represents the pure interference plus noise received signal covariance matrix.

Independent of the receiver type, *e.g.* RAKE or MMSE receiver, the desired signal power is captured by $\left| \left(\overline{\mathbf{g}}_M^{K,I}\right)^H \cdot \overline{\boldsymbol{\nu}}_M^{K,I} \right|^2$, and the total received power including desired power, interference power, and noise power is given by $\left(\overline{\mathbf{g}}_M^{K,I}\right)^H \cdot \overline{\mathbf{\Gamma}}_M^{K,I} \cdot \overline{\mathbf{g}}_M^{K,I}$, so that the symbol level SINR is

$$SINR_M^{K,I} = \frac{\left| \left(\widehat{\overline{\mathbf{g}}}_M^{K,I}\right)^H \cdot \overline{\boldsymbol{\nu}}_M^{K,I} \right|^2}{\left(\widehat{\overline{\mathbf{g}}}_M^{K,I}\right)^H \cdot \overline{\mathbf{\Gamma}}_M^{K,I} \cdot \widehat{\overline{\mathbf{g}}}_M^{K,I} - \left| \left(\widehat{\overline{\mathbf{g}}}_M^{K,I}\right)^H \cdot \overline{\boldsymbol{\nu}}_M^{K,I} \right|^2} \quad , \tag{3.33}$$

where $[\widehat{\cdot}]$ indicates the estimate of the true value.

As shown in Appendix B.2.2 the symbol level SINR for the post despreading chip averaged MMSE receiver can be derived from (3.33) and is given by

$$\begin{aligned} & SINR_M^{K,I} \Big|_{MMSE} \\ & = N_{sf} \frac{P_M^{K,I}}{P_M^I} \cdot \frac{\left| \left(\left(\widehat{\mathbf{h}}_M^I\right)^H \left(\widehat{\mathbf{\Omega}}_M^{K,I}\right)^{-1} \mathbf{h}_M^I \right) \right|^2}{\left(\widehat{\mathbf{h}}_M^I\right)^H \left(\widehat{\mathbf{\Omega}}_M^{K,I}\right)^{-1} \mathbf{\Omega}_M^{K,I} \left(\widehat{\mathbf{\Omega}}_M^{K,I}\right)^{-1} \left(\widehat{\mathbf{h}}_M^I\right)} \quad . \end{aligned} \tag{3.34}$$

Furthermore, as shown in Appendix B.2.3, the post despreading RAKE receiver delivers a symbol level SINR expressed by

$$SINR_M^{K,I}\Big|_{RAKE} = N_{sf}\frac{P_M^{K,I}}{P_M^I}\cdot\frac{\left|\left(\widehat{\mathbf{h}}_M^I\right)^H\left(\mathbf{h}_M^I\right)\right|^2}{\left(\widehat{\mathbf{h}}_M^I\right)^H\boldsymbol{\Omega}_M^{K,I}\widehat{\mathbf{h}}_M^I} \quad . \tag{3.35}$$

Validation of the developed expressions is performed in Appendix C. In the validation process the developed SINR formulations are used to generate SINR statistics in special test cases. The collected statistics are compared with the closed form SINR cdfs presented in Chapter 2. Additionally they are for the RAKE receiver case compared with SINR statistics generated with an independently developed Nokia internal link level simulator. In all tested cases it is found that the developed SINR expressions are able to reproduce the reference SINR statistics. This is seen as a validation, not only of the derivations, but also of their simulator implementation.

3.6 SINR Formulation - Additional Perspective

The following looks at the SINR formulation assuming ideal channel and received signal covariance estimation. Further, the *singular value decomposition* (SVD) [Moon00, Chp. 7] of $\boldsymbol{\Omega}_M^{I,K}$ is used to see the SINR formulations from a different perspective.

In case of ideal channel and noise covariance estimation, *i.e.* $\widehat{\mathbf{h}}_M^I = \mathbf{h}_M^I$ and $\widehat{\boldsymbol{\Omega}}_M^{K,I} = \boldsymbol{\Omega}_M^{K,I}$, the SINR expression in (3.34) can be simplified to deliver

$$\begin{aligned}
&SINR_M^{K,I}\Big|_{MMSE}^{idealest} \\
&= N_{sf}\frac{P_M^{K,I}}{P_M^I}\cdot\frac{\left|\left(\left(\mathbf{h}_M^I\right)^H\left(\boldsymbol{\Omega}_M^{K,I}\right)^{-1}\mathbf{h}_M^I\right)\right|^2}{\left(\mathbf{h}_M^I\right)^H\left(\boldsymbol{\Omega}_M^{K,I}\right)^{-1}\boldsymbol{\Omega}_M^{K,I}\left(\boldsymbol{\Omega}_M^{K,I}\right)^{-1}\left(\mathbf{h}_M^I\right)} \\
&= N_{sf}\frac{P_M^{K,I}}{P_M^I}\cdot\frac{\left|\left(\left(\mathbf{h}_M^I\right)^H\left(\boldsymbol{\Omega}_M^{K,I}\right)^{-1}\mathbf{h}_M^I\right)\right|^2}{\left(\mathbf{h}_M^I\right)^H\left(\boldsymbol{\Omega}_M^{K,I}\right)^{-1}\left(\mathbf{h}_M^I\right)} \\
&= N_{sf}\frac{P_M^{K,I}}{P_M^I}\cdot\left(\mathbf{h}_M^I\right)^H\left(\boldsymbol{\Omega}_M^{K,I}\right)^{-1}\mathbf{h}_M^I
\end{aligned} \quad . \tag{3.36}$$

Similarly the RAKE receiver SINR expression from (3.35) turns into

$$SINR_M^{K,I}\left|\begin{array}{c} idealest \\ RAKE \end{array}\right. = N_{sf}\frac{P_M^{K,I}}{P_M^I}\cdot\frac{\left|\left(\mathbf{h}_M^I\right)^H\left(\mathbf{h}_M^I\right)\right|^2}{\left(\mathbf{h}_M^I\right)^H\mathbf{\Omega}_M^{K,I}\mathbf{h}_M^I} \quad . \tag{3.37}$$

Using the SVD the square symmetric interference plus noise covariance matrix $\mathbf{\Omega}_M^{I,K}$ can be decomposed in the unitary matrix $\mathbf{U}$, carrying its eigenvectors, and the diagonal matrix $\mathbf{\Lambda}$ carrying its eigenvalues, *i.e.*

$$\mathbf{\Omega}_M^{I,K} = \mathbf{U}\mathbf{\Lambda}\mathbf{U}^H \quad , \tag{3.38}$$

and

$$\left(\mathbf{\Omega}_M^{I,K}\right)^{-1} = \mathbf{U}\mathbf{\Lambda}^{-1}\mathbf{U}^H \quad . \tag{3.39}$$

Combining further the channel impulse response vector with the unitary matrix $\mathbf{U}$ into vector $\mathbf{u}$ with interchangeable statistical characteristics, *i.e.*

$$\mathbf{u}^H = \left(\mathbf{h}_M^I\right)^H\mathbf{U} \quad , \tag{3.40}$$

the SINR expressions from (3.36) and (3.37) can be rewritten as

$$\begin{aligned} \frac{SINR_M^{K,I}\left|\begin{array}{c} idealest \\ MMSE \end{array}\right.}{N_{sf}\frac{P_M^{K,I}}{P_M^I}} &= \left(\mathbf{h}_M^I\right)^H\left(\mathbf{\Omega}_M^{I,K}\right)^{-1}\mathbf{h}_M^I \\ &= \left(\mathbf{h}_M^I\right)^H\mathbf{U}\mathbf{\Lambda}^{-1}\mathbf{U}^H\mathbf{h}_M^I \\ &= \mathbf{u}^H\mathbf{\Lambda}^{-1}\mathbf{u} \\ &= \sum_{e=1}^{N_{FIR}\cdot N_{rx}}\frac{|u_e|^2}{\lambda_e} \end{aligned} \quad , \tag{3.41}$$

and as

$$\begin{aligned}\frac{SINR_M^{K,I}\left|\begin{array}{c} idealest \\ RAKE \end{array}\right.}{N_{sf}\frac{P_M^{K,I}}{P_M^I}} &= \frac{\left|\left(\mathbf{h}_M^I\right)^H\left(\mathbf{h}_M^I\right)\right|^2}{\left(\mathbf{h}_M^I\right)^H\mathbf{\Omega}_M^{I,K}\mathbf{h}_M^I} \\ &= \frac{\left|\left(\mathbf{h}_M^I\right)^H\left(\mathbf{h}_M^I\right)\right|^2}{\left(\mathbf{h}_M^I\right)^H\mathbf{U}\mathbf{\Lambda}\mathbf{U}^H\mathbf{h}_M^I} \\ &= \frac{\mathbf{u}^H\mathbf{u}\mathbf{u}^H\mathbf{u}}{\mathbf{u}^H\mathbf{\Lambda}\boldsymbol{u}} \\ &= \frac{\left(\sum\limits_{e=1}^{N_{FIR}\cdot N_{rx}}|u_e|^2\right)^2}{\sum\limits_{e=1}^{N_{FIR}\cdot N_{rx}}|u_e|^2\cdot\lambda_e}\end{aligned} . \tag{3.42}$$

Interpreting the $|u_e|^2$ as signal power components and the λ_e as the interference plus noise power components, the RAKE receiver can be seen to *rake* in all signal power in a maximum ratio sense, however, without considering the interference power that is *raked* in with it. On the contrary, the MMSE receiver considers the interference power that comes in connection with the signal power and performs OPC. Its SINR is therefore the sum over the individual SINRs. To come to an exact expression or to approximations of the SINR distribution after OPC, a similar decomposition as in (3.41) is frequently used, *e.g.* [Boga80], [Vill99], [Pham99], [Tokg04]. Should the interference covariance matrix $\mathbf{\Omega}_M^{I,K}$ turn into a weighted identity matrix, the SINRs of the RAKE and the MMSE receiver become identical, which can either directly be seen from (3.34) and (3.35) or indirectly from the fact that all eigenvalues of the received signal covariance matrix become identical. For identical λ_e (3.42) can be simplified as

$$\begin{aligned}\frac{SINR_M^{K,I}\left|\begin{array}{c} idealest, AWGN\_int \\ RAKE \end{array}\right.}{N_{sf}\frac{P_M^{K,I}}{P_M^I}} &= \frac{\left(\sum\limits_{e=1}^{N_{FIR}\cdot N_{rx}}|u_e|^2\right)^2}{\sum\limits_{e=1}^{N_{FIR}\cdot N_{rx}}|u_e|^2\cdot\lambda_e} \\ &= \frac{\left(\sum\limits_{e=1}^{N_{FIR}\cdot N_{rx}}|u_e|^2\right)^2}{\lambda_e\cdot\sum\limits_{e=1}^{N_{FIR}\cdot N_{rx}}|u_e|^2} \\ &= \sum_{e=1}^{N_{FIR}\cdot N_{rx}}\frac{|u_e|^2}{\lambda_e}\end{aligned} , \tag{3.43}$$

which can be related to the standard result of the MRC with equal noise power on every MRC branch, *e.g.* [Jake94, p. 318].

For a two sector SISO situation (3.36) and (3.37) are equivalent to the SINR expressions in [Fran02, p.19] and [Fran02, p.20] respectively. For a MISO set-up (3.37) is equivalent to the RAKE receiver SINR formulations in [Hara01, (10)]. In Appendix B.4 (3.37) is additionally related to the RAKE receiver MIMO DS-CDMA SINR formulations of [Rami03a], [Rami03b].

3.7 Summary

A mathematical framework to describe the symbol level SINR in the downlink of a DS-CDMA MIMO systems has been derived for linear space-time MMSE and linear space-time RAKE receivers. Derivations are based on the SISO SINR derivations in [Fran02]. The outer structure of the derived SINR expressions in (3.34) and (3.35) can be found in numerous other publications, *e.g.* [Wint84], [Fran02], [Moto02], [Luce02]. However, the internal structure of the received interference plus noise covariance matrix $\mathbf{\Omega}_M^{K,I}$ as presented in this chapter is kept very general. Its internal structure, given in (3.32), is built on a virtual channel concept, where a virtual channel is defined as radio propagation channel after tx weight combining. This virtual channel concept allows integration of various multiple antenna transmission, spreading code, and sector power allocation schemes in a unified framework. Example implementations for CLM1 and SMP, accounting also for other channels transmitted within the same sector, can be found in Chapter 4. Analytical and simulation based validation is performed in Appendix C. In all tested cases the developed SINR formulations are able to reproduce reference SINR statistics. Due to their generality the developed MIMO DS-CDMA SINR formulations constitute a powerful tool for link and network performance assessment.

Chapter 4

Modelling Framework

The following introduces modelling and simulation aspects used to generate link and network performance results. It is shown how the virtual channel concept introduced in Chapter 3 can be used to implement CLM1 as well as SMP on the HS-DSCH channel, while at the same time accounting for other channel transmission. All simulation models are tailored to fit the decoupled quasi-static simulation approach introduced in Chapter 1. Specifically a novel other-sector interference model is developed that allows to account for other-sector interference properties already on *link level*. Main interference modelling details have been published in [Berg04b].

4.1 Introduction

The main performance differences between advanced tx and rx schemes surface when observing the different SINR statistics the schemes deliver. To estimate which effects different SINR statistics have on the network level and thus on the sector throughput, link and network level simulations are necessary. The following outlines the simulation models as well as the simulation parameters selected to generate link and network level HSDPA performance results. The decoupled, quasi-static simulation approach, originally introduced in Subsection 1.5.3, is displayed in Figure 4.1. It incorporates an existing HSDPA network level simulator and an existing MIMO channel simulator marked with dotted boxes.

To enable link and network decoupled simulations, where the existing network simulator reads every user's link performance from a database, it is essential to find a small set of user-parameters that can be used in the lookup process. Through a study of the regular grid cellular simulation scenario displayed in Figure 1.8, [SCM 03], [3GPP03a], [3GPP04d] a user's *line of sight angle of connection* (AoC) and a

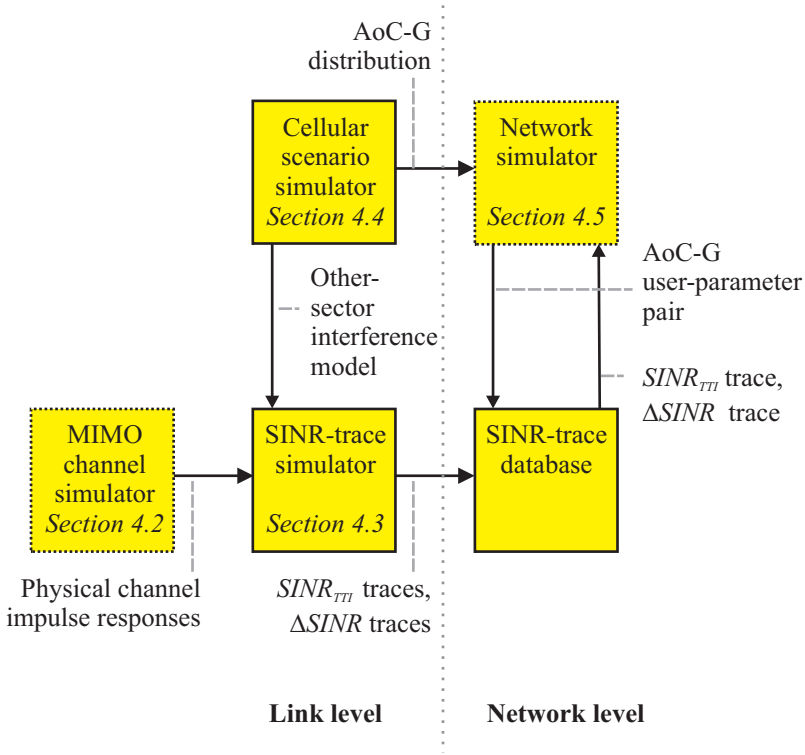

Figure 4.1: Overview of simulation concept and chapter outline. The dotted boxes mark sub simulators that are merely adapted to fit into the overall concept. The solid boxes mark newly developed simulator components.

user's own-to-other-sector received power ratio, also known as *cell geometry factor* (G-factor), are identified as two parameters that can describe the users' average interference situations. For every AoC-G user-parameter pair, SINR-traces and SINR variability traces, called ΔSINR -traces, are pre-computed. On the basis of a two-dimensional AoC-G distribution the network simulator then picks AoC-G user-parameter pairs that are used to look up the link performance of every new user. This way a user population is generated that is similar to a user population obtained from dropping users uniformly distributed in the centre target cell.

The remainder of the chapter is structured as indicated in Figure 4.1. Section 4.2 outlines the correlation based stochastic multipath fading channel model used to generate spatially correlated MIMO channel impulse responses. Section 4.3 shows how the MIMO DS-CDMA SINR formulation developed in Chapter 3 can be employed to describe the SINR experienced on the HS-DSCH when either CLM1 or SMP transmission are used. It will further be shown how to account for the other channels transmitted in the same sector, which are using the transmission strategies of Table 1.2. Specifically, models for $SINR_{TTI}$ and ΔSINR , which were first introduced in (2.2) and (1.1), are presented. Section 4.4 develops two

other-sector interference models that allow pre-computation of SINR performance results, *i.e.* $SINR_{TTI}$ and ΔSINR traces, to be stored in the user performance database. The simulation models of the network level simulator are outlined in Section 4.5. Supporting material and simulator validation results are presented in Appendix C.

4.2 MIMO Multipath Fading

Numerous ways to model and simulate correlated multipath fading MIMO channels exist, and are among others reviewed in [Schu04]. The multipath fading MIMO channel model used throughout is a correlation based stochastic model, presented in [Pede00], [Kerm02]. It was proposed to 3GPP in [Luce01] and was finally accepted as one way to implement the 3GPP MIMO channel link level test cases [SCM 03]. A software implementation of the model evolved from the European IST METRA and I-METRA projects [Schu00], [Schu02a] and has been adapted to satisfy the network level simulation needs within this dissertation. The main features related to the description of the *power delay profile*s (PDPs) as well as spatial correlation at both ends are outlined in the following subsections.

4.2.1 Power Delay Profile and Chip Alignment Procedure

In SISO channel simulations one of the main ways to distinguish between different multipath channels is to separate them according to their PDPs. In 1997 the *International Telecommunication Union* (ITU) issued a recommendation [ITU97] that specifies a set of channels generally referred to as *Pedestrian A*, *Pedestrian B*, *Vehicular A*, and *Vehicular B*. These names are originally chosen considering the mobility situation of a user. In the following the PDPs of the Pedestrian A channel and the Vehicular A channel are considered. Using the coherence bandwidth approximation of [Rapp99, p. 163], where the coherence bandwidth is the frequency separation for which the frequency correlation function exhibits values $\geqslant 0.9$, the coherence bandwidth of the Pedestrian A and the Vehicular A PDP are estimated to be 0.43 MHz and 0.05 MHz respectively. Over a bandwidth of 5 MHz the Pedestrian A channel can thus be regarded as weakly frequency selective, very close to a flat fading channel, whereas the Vehicular A channel is frequency selective.

As stated in Chapter 3, chip oversampling is omitted, so that the smallest time entity for simulations is the duration of a code chip, denoted T_c. The path delays of the channel impulse responses defined in [ITU97] are, however, not chip aligned, and energy received with these delays will have to be related to chip spaced channel impulse response. The default implementation in the MIMO channel modelling software follows [3GPP01b, p. 22], where the path energy is split between the clos-

est chip sampling points [Schu02a]. Another strategy moves the entire path energy to the closest chip sampling point. As displayed in Table 4.1 the chip alignment procedure alters coherence bandwidth and *root mean square* (rms) delay spread [Rapp99, p. 160]. As shown in Appendix C.1.4 it thus also affects the obtainable SINR statistics. The aim in the following is to use two chip aligned PDPs that represent a weakly frequency selective (nearly frequency flat) fading channel and a frequency selective fading channel. Both alignment procedures are suitable, but for comparability reasons with [Rami03b], [Rami03a], as well as with a Nokia internal link simulation tool the closest chip alignment procedure is selected.

	PeA			**VhA**		
	ITU	**Closest**	**Split**	**ITU**	**Closest**	**Split**
Rms delay spread, [ns]	45.99	35.39	68.75	370.39	362.38	371.28
Coh. bandwidth, [MHz]	0.43	0.57	0.29	0.05	0.06	0.05

Table 4.1: Effects of different chip alignment procedures on the rms delay spread and the 0.9 coherence bandwidth.

4.2.2 Tx Correlation

In the assessment of MIMO scheme performance the frequency selectivity is just one important channel characteristic. Additionally the correlation properties at the tx and the rx side are known to significantly influence the MIMO channel capacity [Chua02], [Oyma03], [Mart04]. Correlation properties depend on the antenna deployment, *e.g.* co or cross polarised with a certain element separation, as well as on the angular power spectra at both ends. Based on measurements [Pede97], [Pede98] the *power azimuth spectrum* (PAS) at the base station is selected to be truncated Laplacian distributed around the AoC with an *rms angle spread* (AS), of 5^o[SCM 03, p. 44]. Assuming additionally that all radio waves travel in the horizontal plane, the correlation coefficient between co-polarised, horizontally deployed tx antenna elements is a function of tx antenna spacing and AoC [Schu02c].

To obtain a *highly correlated* (hc) and a *weakly correlated* (wc) tx antenna deployment scenario two reference tx antenna spacings of 0.5 wavelength and 10 wavelengths have been chosen, and the envelop tx correlation coefficient, $|\rho_{tx}|^2$, is plotted in Figure 4.2 as a function of AoC.

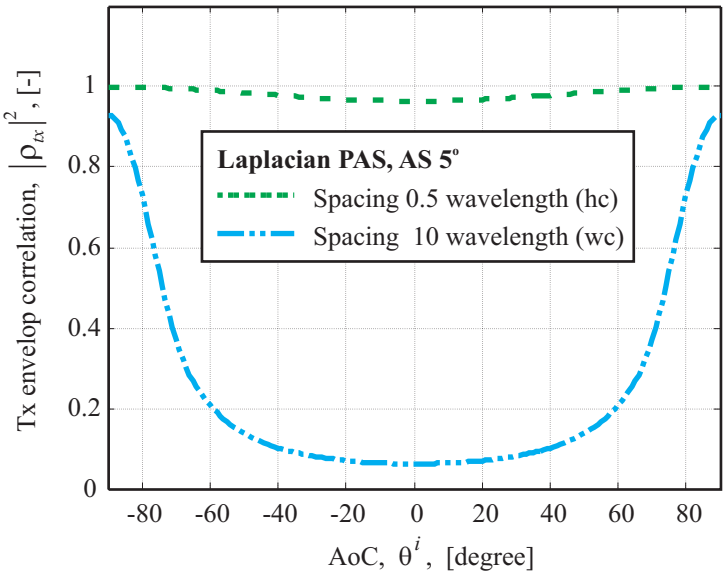

Figure 4.2: Tx envelop correlation as a function of AoC.

4.2.3 Rx Correlation and Doppler Spectrum

Similarly, the spatial characteristics at the rx side are described via a PAS, and an *angle of arrival* (AoA). A standard approach assumes that the UE are surrounded by scatterers, and their PASs are uniformly distributed over 360°[Rapp99, pp. 179-181]. Although some measurement campaigns have shown that radio wave propagation is often following the direction of street canyons AoA [Fuhl97], [Kuch00], the simple uniform scattering approach is used for all simulations to confine the amount of required link level simulations. The horizontally deployed rx antennas are selected to be separated by 0.5 wavelength. This selection follows one possible setting in [SCM 03], for which the rx magnitude correlation reference is given as $|\rho_{rx}| = 0.3042$. In case of terminal movement, the selected spatial characteristics do not only relate to the rx correlation, but also influence the temporal channel variation reflected in the Doppler spectrum [Rapp99, Chp. 4]. For the uniform scattering model the classical Clarke's type Doppler spectrum [Clar68] is obtained and plotted in Appendix C.1.3.

4.2.4 MIMO Multipath Fading Model Summary

A stochastic correlation based multipath fading MIMO channel model is used. Four different propagation channel cases are specified throughout. Their main pa-

rameters are summarised in Table 4.2. The selection includes the SCM link level test Case II.2 [SCM 03, pp. 6-7], which can be obtained from VhA wc or VhA hc by fixing the AoC to 20°. MIMO channel simulations are performed with an adapted version of the I-METRA channel model simulation software [I ME03]. Adaptation is confined to the set-up of the four channel cases of Table 4.2 and to smaller modifications of the MIMO channel simulator's interfaces. Validation of the adapted MIMO channel simulator is presented in Appendix C.1.

	PeA wc	**PeA hc**	**VhA wc**	**VhA hc**
Tx spacing, [wave]	10	0.5	10	0.5
PDP [1]	ITU-Pedestrian A		ITU-Vehicular A	
Tx PAS	Laplacian with of AS 5°			
Rx PAS	360° uniform			
Rx spacing, [wave]	0.5			

Table 4.2: Overview of the four different MIMO multipath fading cases used throughout. [1]The energy of the ITU PDPs is chip aligned to the closest chip sampling instances.

4.3 $\mathbf{SINR_{TTI}}$ and ΔSINR Traces

The following subsections show how the virtual cannel concept can be used to implement single antenna transmission, CLM1 and SMP. With these implementations the link level SINR trace simulator calculates the user performance metrics $SINR_{TTI}$ and ΔSINR .

4.3.1 Transmission Group Sector Power Allocation

The power received over the different virtual channels is in (3.16) represented through the virtual channel power vector $\mathbf{P}^i$, with one entry per channelisation code resource k. UTRAN uses different spreading factors on the different data and signalling channels. Moreover, multicode link adaptation is used on the HS-DSCH channel. From an organisational point of view it is thus convenient to combine the different elements constituting $\mathbf{P}^i$ into transmission groups. A transmission group is throughout defined as a collection of signalling or data channels that is modelled using a single virtual channel power mapping vector. As introduced in Table 1.2 the HS-DSCH, the PCPICH, the HS-SCCH, and the DCH are modelled. The virtual channel power vector $\mathbf{P}^i$, using four transmission groups, is redefined

as

$$\mathbf{P}^i = \underbrace{\left[\begin{array}{cccc} \boldsymbol{\omega}^{PCPICH,i} & \boldsymbol{\omega}^{HSSCCH,i} & \boldsymbol{\omega}^{HSDSCH,i} & \boldsymbol{\omega}^{DCH,i} \end{array}\right]}_{\boldsymbol{\omega}^i} \cdot \underbrace{\left[\begin{array}{c} \eta^{PCPICH,i} \\ \eta^{HSSCCH,i} \\ \eta^{HSDSCH,i} \\ \eta^{DCH,i} \end{array}\right]}_{\boldsymbol{\eta}^i} \cdot \overline{P}^i \quad . \tag{4.1}$$

$\boldsymbol{\eta}^i$ is a vector containing the sector power allocation to the different transmission groups. The column vectors in $\boldsymbol{\omega}^i$ are responsible to implement the potentially time variant virtual channel power mapping processes for the different transmission groups. $\overline{P}^i$ is recalled as the full load small area mean received power from sector i.

To obtain the received signal covariance matrix it is important to note that P_m^i formally defined in (3.10) is given as the m^{th} element of $\mathbf{P}^i$. Further, with respect to multicode operation it is important that the power formerly related to desired code resource K, I and desired virtual channel M is now expressed by

$$\begin{aligned} P_M^{K,I} &= \frac{1}{\tilde{N}_{code}} P_M^{HSDSCH,I} \\ &= \frac{1}{\tilde{N}_{code}} \cdot \omega_M^{HSDSCH,I} \cdot \eta^{HSDSCH,I} \cdot \overline{P}^I \end{aligned} \quad , \tag{4.2}$$

which shows that the HS-DSCH power is equally split between all multicode resources used within one TTI.

For dual stream transmission it is assumed that the co-stream transmits over all code resources set aside for HS-DSCH transmission. From the information theoretic results in [Fosc98] it is known that dual stream transmission can at best double single stream capacity. On the other hand, multicodes can be used to map stream SINR linearly to sector throughput. It is therefore spectrally more efficient to use all available code resources before enabling co-stream transmission. The power over the co-stream writes

$$\begin{aligned} P_m^{K,I} &= \frac{1}{\tilde{N}_{codeco}} P_m^{HSDSCH,I} \ \wedge \ m \neq M \\ &= \frac{1}{\tilde{N}_{codeco}} \cdot \omega_m^{HSDSCH,I} \cdot \eta^{HSDSCH,I} \cdot \overline{P}^I \end{aligned} \quad . \tag{4.3}$$

Thus the received signal covariance matrix from (3.32) rewrites

$$\overline{\mathbf{\Gamma}}_M^{HSDSCH,I} = N_{sf} P_M^I \cdot \underbrace{\left(\begin{array}{l} \sum\limits_{i=1}^{N_{\text{sec}}} \sum\limits_{m=1}^{N_{vir}} \frac{P_m^i}{P_M^I} \cdot \mathbf{H}_m^i \left(\mathbf{H}_m^i\right)^H \\ - \sum\limits_{m=1}^{N_{vir}} \frac{P_m^I}{P_M^I} \cdot \mathbf{h}_m^I \left(\mathbf{h}_m^I\right)^H \\ + N_{sf} \cdot \sum\limits_{\substack{m=1 \\ m \neq M}}^{N_{vir}} \frac{P_m^{HSDSCH,I}}{\tilde{N}_{codeco} \cdot P_M^I} \cdot \mathbf{h}_m^I \left(\mathbf{h}_m^I\right)^H \\ + \frac{P^{th}}{P_M^I} \cdot \mathbf{I}_{(N_{rx} \cdot N_{FIR})} \end{array} \right)}_{\mathbf{\Omega}_M^{HSDSCH,I}} \cdot$$
$$+ \frac{(N_{sf})^2}{\tilde{N}_{code}} \cdot P_M^{HSDSCH,I} \cdot \mathbf{h}_M^I \left(\mathbf{h}_M^I\right)^H \tag{4.4}$$

It can be seen that the received signal covariance matrix and hence also the interference covariance matrix corresponding to the desired HS-DSCH stream are a function of the multicode link adaptation decisions on the interfering co-stream. As a consequence the SINR on the desired stream is a function of the link adaptation decisions on the co-stream.

4.3.2 Single Antenna Transmission

In those cases where only a single transmit antenna is used, *i.e.* 1×1 SISO and 1×2 SIMO, only one virtual channel exists per sector. This virtual channel is identical to the physical radio propagation channel. Further, it is assumed that PCPICH, HS-SCCH, and DCH channels are transmitted with constant tx power. $\mathbf{P}^i$ therefore simplifies to

$$\mathbf{P}^i = \underbrace{\left[\begin{array}{cccc} \boldsymbol{\omega}^{PCPICH,i} & \boldsymbol{\omega}^{HSSCCH,i} & \boldsymbol{\omega}^{HSDSCH,i} & \boldsymbol{\omega}^{DCH,i} \end{array} \right]}_{\boldsymbol{\omega}^i} \cdot \underbrace{\left[\begin{array}{c} \eta^{PCPICH,i} \\ \eta^{HSSCCH,i} \\ \eta^{HSDSCH,i} \\ \eta^{DCH,i} \end{array} \right]}_{\boldsymbol{\eta}^i} \cdot \overline{P}^i$$
$$= \underbrace{\left[\begin{array}{cccc} 1 & 1 & 1 \cdot p_{activity}^{HSDSCH,i} & 1 \end{array} \right]}_{\boldsymbol{\omega}^i} \cdot \underbrace{\left[\begin{array}{c} \eta^{PCPICH,i} \\ \eta^{HSSCCH,i} \\ \eta^{HSDSCH,i} \\ \eta^{DCH,i} \end{array} \right]}_{\boldsymbol{\eta}^i} \cdot \overline{P}^i \tag{4.5}$$

(4.6)

where $p_{activity}^{HSDSCH,i}$ takes either the values 0 or 1, indicating whether the HS-DSCH power is on or off. The HS-DSCH power of the serving sector is always on, *i.e.*

$$p_{activity}^{HSDSCH,I} = 1 \quad . \tag{4.7}$$

For every interfering sector $p_{activity}^{HSDSCH,i}$ is updated once per TTI, following the Bernoulli distribution [Moon00, p. 447],

$$\mathrm{pr}\left(p_{activity}^{HSDSCH,i}\right) = \begin{cases} \alpha, & \text{for } p_{activity}^{HSDSCH,i} = 1 \\ & \\ 1-\alpha, & \text{for } p_{activity}^{HSDSCH,i} = 0 \end{cases} \quad ,\forall\, i \neq I \quad , \tag{4.8}$$

where the HS-DSCH activity factor α is introduced as the average fraction of time the interfering sectors are transmitting HS-DSCH power. *E.g.* $\alpha = 1$ describes a network with constant HS-DSCH transmission, whereas $\alpha = 0.5$ describes a network where the interfering sectors transmit the HS-DSCH only 50% of the time. The remaining time no HS-DSCH power is transmitted.

4.3.3 CLM1 and Other Channel Transmission

In CLM1 six different transmit weight sets are required, which can be ordered as indicated in Table 4.3. The first two weight sets simply correspond to a transmission from physical tx antenna one and two respectively. The remaining weight sets correspond to the four potential CLM1 weight states as introduced in Chapter 2, [Rami04b], [Hott03]. As indicated in Table 1.2 (a) every sector broadcasts two orthogonal pilot signals over the two physical transmit antennas. Furthermore, the HS-SCCH is transmitted from these antennas using STTD [3GPP04f], [Rami04b], [Hott03, p. 63]. The HS-DSCH is transmitted using one of the virtual channels $m \in [3,4,5,6]$. Further, it is assumed that all DCH channels are transmitted with

Virtual channel index, m	**Tx antenna weight set** $w_{1,m}^i$	$w_{2,m}^i$
1	1	0
2	0	1
3	$\frac{1}{\sqrt{2}}$	$\frac{1}{\sqrt{2}} \cdot e^{j\frac{1}{4}\pi}$
4	$\frac{1}{\sqrt{2}}$	$\frac{1}{\sqrt{2}} \cdot e^{j\frac{3}{4}\pi}$
5	$\frac{1}{\sqrt{2}}$	$\frac{1}{\sqrt{2}} \cdot e^{j\frac{5}{4}\pi}$
6	$\frac{1}{\sqrt{2}}$	$\frac{1}{\sqrt{2}} \cdot e^{j\frac{7}{4}\pi}$

Table 4.3: Virtual channel weight sets in case the HS-DSCH channel uses CLM1.

equally distributed power over the virtual channels 3 to 6. These settings, combined with the HS-DSCH activity model introduced in the previous subsection, lead to a virtual channel power vector given by

$$\mathbf{P}^i = \underbrace{\begin{bmatrix} 0.5 & 0.5 & 0 & 0 \\ 0.5 & 0.5 & 0 & 0 \\ 0 & 0 & \left(\delta\left(3-o^i\right)\cdot p_{activity}^{HSDSCH,i}\right) & 0.25 \\ 0 & 0 & \left(\delta\left(4-o^i\right)\cdot p_{activity}^{HSDSCH,i}\right) & 0.25 \\ 0 & 0 & \left(\delta\left(5-o^i\right)\cdot p_{activity}^{HSDSCH,i}\right) & 0.25 \\ 0 & 0 & \left(\delta\left(6-o^i\right)\cdot p_{activity}^{HSDSCH,i}\right) & 0.25 \end{bmatrix}}_{\boldsymbol{\omega}^i} \cdot \underbrace{\begin{bmatrix} \eta^{PCPICH,i} \\ \eta^{HSSCCH,i} \\ \eta^{HSDSCH,i} \\ \eta^{DCH,i} \end{bmatrix}}_{\boldsymbol{\eta}^i} \cdot \overline{P}^i \quad , \tag{4.9}$$

where the Dirac term is introduced to indicate over which virtual channel the HS-DSCH power is actually transmitted. The option indicator $o^i \in [3,4,5,6]$, is updated on a slot-to-slot basis. For the serving sector it is determined as

$$o^I = \underset{m\in[3,4,5,6]}{\arg\max} \left\{ \left(\widehat{\boldsymbol{h}}_m^{\,I} \right)^H \cdot \widehat{\boldsymbol{h}}_m^{\,I} \right\} \quad , \tag{4.10}$$

where the $\widehat{\boldsymbol{h}}_m^{\,I}$ represents the ensemble average over the virtual channel impulse responses taken over all chips within one slot, *i.e.*

$$\widehat{\boldsymbol{h}}_m^{\,I} = E\left\langle \mathbf{h}_m^I \right\rangle_{2560} \quad . \tag{4.11}$$

The virtual channel decision in (4.10) is thus taken to maximise the received signal power at the UE [3GPP04g]. To account for uplink signalling and weight processing, the decision is applied with a two-slot delay as in [Rami03a, p. 122]. Further, the feedback is assumed error free. The effects of feedback delay and feedback errors are analysed in [Hama01b]. Analytical and simulation results for a feedback delay of 1.5 slots and a feedback error rate of 4% are presented. It is found that at low mobile speeds up to 20 km/h there is hardly any negative effect of feedback delay, *i.e.* < 0.1 dB SINR loss. The 4% error probability is found to cause around 0.1 dB SINR loss. In [Gerl02] it is concluded that even a feedback error rate of 10% only causes marginal SINR degradation. To assume error free feedback can therefore be seen as slightly optimistic.

In a system deploying CLM1 the HS-DSCH power allocation of the interfering sectors depends on the virtual channel conditions towards the interfering users. The power allocation updates are therefore dependent on the speeds of these users. For simplicity it is, however, assumed throughout that all $o^i\big|_{i\neq I}$ are asynchronously

updated once per TTI following the distribution, *i.e.*

$$\mathrm{pr}\left(o^i\right) = \begin{cases} 0.25\ , \text{ for } o^i = 3 \\ 0.25\ , \text{ for } o^i = 4 \\ 0.25\ , \text{ for } o^i = 5 \\ 0.25\ , \text{ for } o^i = 6 \end{cases} ,\forall\, i \neq I \quad , \tag{4.12}$$

which reflects a low mobility situation where CLM1 weight updates are mainly due to scheduling different uniformly distributed interfering users during consecutive TTIs.

4.3.4 SMP and Other Channel Transmission

Shifting the focus to SMP_x transmission, all but the HS-DSCH power is split evenly between the two physical tx antennas, each one corresponding to one virtual channel. The other channel transmission strategies are summarised in Table 1.2 (b). As outlined in Subsection 2.3.3, ideally a smart packet scheduler would decide among three HS-DSCH transmission options as given in Table 4.4. For this general SMP_x case the virtual channel power vector writes

$$\mathbf{P}^i = \underbrace{\begin{bmatrix} 0.5 & 0.5 & \left(\left(0.5\cdot\delta\left(1-o^i\right)+\delta\left(2-o^i\right)\right)\cdot p_{activity}^{HSDSCH,i}\right) & 0.5 \\ 0.5 & 0.5 & \left(\left(0.5\cdot\delta\left(1-o^i\right)+\delta\left(3-o^i\right)\right)\cdot p_{activity}^{HSDSCH,i}\right) & 0.5 \end{bmatrix}}_{\boldsymbol{\omega}^i} \cdot \underbrace{\begin{bmatrix} \eta^{PCPICH,i} \\ \eta^{HSSCCH,i} \\ \eta^{HSDSCH,i} \\ \eta^{DCH,i} \end{bmatrix}}_{\boldsymbol{\eta}^i} \cdot \overline{P}^i \quad , \tag{4.13}$$

As shown in [Fern04], the transmission option selection probability of such SMP_x scheduler depends on the multipath environment, the encountered antenna correlations and the multi-user diversity order. As such smart multi stream MIMO packet scheduler is not available in the network simulator implementation, the two sub cases SMP_{sel} and SMP_{dual} are introduced.

In SMP_{sel} dual stream transmission is disabled in the serving sector. This means $o^I \neq 1$. The HS-DSCH transmission is scheduled selecting the $o^I \in [2,3]$ that delivers the higher TTI level SINR. A feedback delay of three TTI, *i.e.* 6 ms, is

Value of option indicator, o^i	**Option description**
1	Dual stream
2	Single stream from antenna 1
3	Single stream from antenna 2

Table 4.4: SMP_x tx options.

used in line with [3GPP04d] where the round trip feedback delay is given as seven slots. The feedback delay is selected higher than for CLM1, as it is assumed that the SMP$_x$ feedback will be combined into the CQI feedback words used for link adaptation and packet scheduling decisions.

In SMP$_{dual}$ dual stream transmission is always used in the serving sector, *i.e.* $o^I = 1$, and HS-DSCH packet scheduling decisions are taken independently for each stream.

For simplicity, common other-sector interference behaviour is implemented for SMP$_{sel}$ and SMP$_{dual}$. It is based on a uniformly distributed discrete random process given by

$$\mathrm{pr}\left(o^i\right) = \begin{cases} \frac{1}{3}\,, \text{ for } o^i = 1 \\ \frac{1}{3}\,, \text{ for } o^i = 2 \\ \frac{1}{3}\,, \text{ for } o^i = 3 \end{cases} \quad ,\forall\, i \neq I \quad , \tag{4.14}$$

where o^i is asynchronously updated once per TTI.

4.3.5 Channel and Received Signal Covariance Model

The RAKE receiver implementation in (3.29) only requires knowledge of the averaged mean vector. The MMSE receiver implementation in (3.28) requires knowledge of the averaged mean vector and the chip averaged received signal covariance matrix. In UTRAN both can be estimated with the help of the continuously broadcast pilot sequences over the PCPICHs for all sectors in the active set. Moreover, estimation can be assisted by dedicated pilot symbols transmitted on the DCH [3GPP04f], [Usud00]. In case of signal transmission from two tx antennas, two orthogonal pilot symbol sequences are broadcast from each antenna. They are scrambled with the primary scrambling code and spread with a Walsh-Hadamard code of $N_{sf} = 256$ [3GPP04f], allowing the transmission of 10 pilot symbols per slot and per tx antenna. In general, channel estimation and adaptive equaliser implementation is a broad field of research, treated among others in [Bora92], [Fran98], [Heik99], [Wern99], [Weis99], [Hool01], [Heik02], [Fran02], [Deng03]. However, this dissertation aims at the evaluation of advanced tx and rx concepts independent of a specific adaptive receiver implementation. Ideal channel and received signal covariance estimation is therefore used throughout the following. In [McBe03] a similar ideal channel and received signal covariance estimation approach is compared against linear pilot based estimation. Using comparable HSDPA system parameter settings it is found that real linear estimation in a dual transmit antenna system degrades sector throughput performance by around 5% to 11% percent for

a Pedestrian A PDP and by around 13% to 17% percent for a Vehicular A PDP. It can therefore be expected that real channel estimation procedures would have similar effects for the dual tx antenna schemes CLM1 and SMP_x throughout the following. In case of single antenna transmission only one pilot signal is transmitted, which is likely to improve SISO and SIMO channel and received signal covariance estimation, leading to a less significant loss for these single tx antenna schemes.

4.3.6 $SINR_{TTI}$ and ΔSINR Metric

On the assumption of ideal channel and received signal covariance estimation, and under additional consideration of the transmission group notation, *i.e.* (4.2) to (4.4), the SINR expressions from (3.34) and (3.35) rewrite

$$SINR_M^{HSDSCH,I} \left| \begin{array}{l} idealest \\ MMSE \end{array} \right.$$

$$= \frac{N_{sf}}{\tilde{N}_{code}} \cdot \frac{P_M^{HSDSCH,I}}{P_M^I} \cdot \left(\mathbf{h}_M^I\right)^H \left(\mathbf{\Omega}_M^{HSDSCH,I}\right)^{-1} \mathbf{h}_M^I \quad , \tag{4.15}$$

and

$$SINR_M^{HSDSCH,I} \left| \begin{array}{l} idealest \\ RAKE \end{array} \right.$$

$$= \frac{N_{sf}}{\tilde{N}_{code}} \cdot \frac{P_M^{HSDSCH,I}}{P_M^I} \cdot \frac{\left|\left(\mathbf{h}_M^I\right)^H \left(\mathbf{h}_M^I\right)\right|^2}{\left(\mathbf{h}_M^I\right)^H \mathbf{\Omega}_M^{HSDSCH,I} \mathbf{h}_M^I} \quad . \tag{4.16}$$

These expressions are used to determine the symbol level SINR experienced on the desired stream of the HS-DSCH channel.

The reference value $SINR_{TTI}$ is in (2.2) defined as the ensemble average over all symbols within one TTI if only one multicode was used on the HS-DSCH channel. This would, however, require the calculation of 480 symbol level SINRs per 2 ms. To ease the simulation load only 24 evenly separated symbol level SINRs are calculated per TTI so that the reference $SINR_{TTI}$ is approximated as

$$SINR_{TTI} \approx \mathrm{E}\left\langle SINR_M^{HSDSCH,I} \left| \begin{array}{l} idealest \end{array} \right. \right\rangle_{\text{24, evenly spaced over 2 ms}} \quad . \tag{4.17}$$

$SINR_M^{HSDSCH,I} \left| \begin{array}{l} idealest \end{array} \right.$ is calculated as given in (4.15) or (4.16) for a single multicode used on the desired HS-DSCH channel. Further, if an interfering co-channel

is present, *i.e.* for SMP_{dual}, all multicodes allocated to HS-DSCH operation are assumed to be used on this interfering HS-DSCH co-channel.

To obtain a metric for the SINR variability within a TTI, SINR estimates for each of the three slots within a TTI are defined as [1]

$$SINR_{slot} = \mathrm{E}\left\langle SINR_M^{HSDSCH,I} \,\middle|\, idealest \right\rangle_{\text{8, evenly spaced over 2/3 ms}} . \tag{4.18}$$

Using the three slot level estimates a metric for the SINR variability within a TTI is defined as

$$\Delta SINR = \frac{\max\limits_{slot\in[1,2,3]} \{SINR_{slot}\}}{\min\limits_{slot\in[1,2,3]} \{SINR_{slot}\}} . \tag{4.19}$$

$SINR_{TTI}$ and $\Delta SINR$ will be used for an advanced turbo decoder performance description, and their time traces are stored in the user performance database.

4.3.7 SINR_{TTI} and ΔSINR Modelling Summary

In this section it was shown how the virtual channel concept and the MIMO DS-CDMA SINR formulations from Chapter 3 can be used to obtain the symbol level SINR for SISO/SIMO, CLM1 and SMP. To account for other channel transmissions as well as for the desired HS-DSCH channel, transmission groups have been defined. Each transmission group is modelled with a single virtual channel power mapping vector. Specifically with respect to the HS-DSCH transmission group an activity model is included in the definition of $\boldsymbol{\omega}^{HSDSCH,i}$. This model will be used to simulate discontinuous transmission of interfering other-sector HS-DSCHs. Besides, the SINR performance metrics $SINR_{TTI}$ and ΔSINR have been defined. Time evolving $SINR_{TTI}$ and ΔSINR traces are used to build up the user-performance database. The link simulator implementation is validated in Appendix C.2. In the validation process the obtained $SINR_{TTI}$ statistics are compared against analytical bounds from Chapter 2 and against $SINR_{TTI}$ statistics from a Nokia internal link simulator. All tests show a good match between the SINR trace link simulator output and the references.

4.4 Other-Sector Interference

The interference situation in the standard regular grid cellular scenario set-up from Figure 1.8, [SCM 03], [3GPP03a], [3GPP04d] is to be modelled using a decou-

[1] As geometric averaging of symbol level SINRs is also a commonly used procedure, *e.g.* [Rami04b], it is recalled that throughout this dissertation calculations are presented in linear values.

pled link network simulation approach as indicated in Figure 1.9 and Figure 4.1. In a decoupled link and network level simulation approach the link performance needs to be *pre-computed*. This requires an other-sector interference model that describes every user's average interference situation. The following specifically looks at ways to describe the other-sector interference *powers* and the other-sector antenna array *tx correlations*. Powers as well as tx correlations can influence the SINR distribution and the SINR variability distribution of a user. *E.g.* if an interfering sector switches its HS-DSCH power from on to off, the severity of the resulting SINR variation depends on the sector's share of the overall interference power contribution. Similarly the other-sector tx correlation can influence how drastically a transmit weight set update affects the received interference power. If the propagation channel transfer functions from an interfering sector have similar amplitudes, in phase and anti phase addition of the interfering sector's signal have a similar effect as switching the interfering sector's tx power from on to off. This effect is less severe if the interfering sector's transfer functions have different amplitudes. The probability of having similar or different amplitudes is, however, related to the tx correlation, and one can think of the whole aspect as a form of *interference transmit diversity*, *i.e.* in one case the interference contribution is more stable than in the other. Besides accounting for interfering powers and tx correlations, the model in [SCM 03] also accounts for various other-sector time dispersion situations. For simplicity, however, the following uses a uniform time dispersion description for all explicitly modelled sectors in the cellular set-up. This means that all explicitly modelled interfering sectors use the same MIMO multipath fading case description as the serving sector. The four selected MIMO multipath fading cases have been summarised in Table 4.2.

A decoupled look-up approach requires that the link performance database has a finite size. Geometrically-based stochastic models [Schu04, pp. 382-384], like the one used in the 3GPP MIMO scheme performance evaluation [SCM 03], [3GPP04d], produce an infinite amount of other-sector interference situations. The task is therefore to find user-parameter dimensions that well describe a user's average performance situation. Secondly, it needs to be investigated which sampling resolution is required per user-parameter dimension to come close to the power and tx correlation modelling performance of infinite models. A physical location approach could pre-compute user performance traces for every point on a regular grid within the centre target cell. Such a grid is indicated in Figure 4.3 (a). Further, for every location several shadow fading realisations [Rapp99, pp. 104-105] could be pre-computed. The three user-parameter dimensions of such a physical location sampling approach are depicted in Figure 4.3 (b).

Placing a user at a geometrical position in the centre target cell allows the precomputation of path loss [Rapp99, p. 102-104] and the AoC to all sectors. This information, together with a random process to account for different shadow fading realisations, can be used to calculate the serving sector's and the interfering

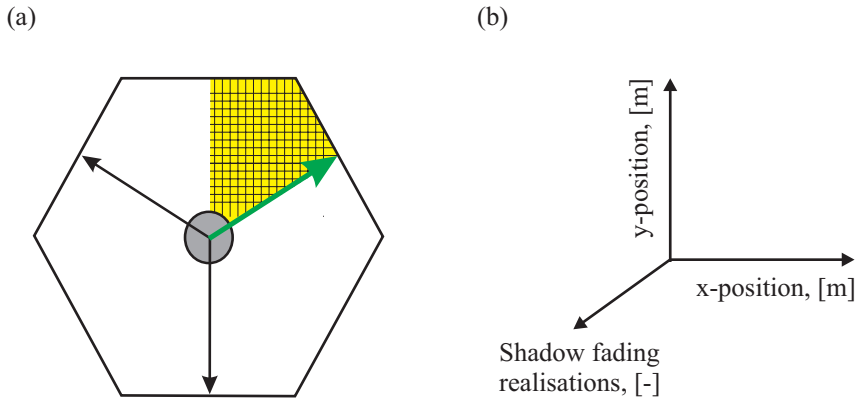

Figure 4.3: Sketch of a physical location sampling approach and its corresponding user performance database dimensions.

sectors' received powers. Further, as displayed in Figure 4.2, the AoC relates for the four selected MIMO multipath fading cases directly to the tx correlation of the serving and the interfering sectors. The disadvantage of a physical location sampling approach is that it leads to a large user-parameter database size. This can be seen on the example of a hexagonal cell who's dimensions are based on a site-to-site distance of 2800 m. This corresponds to a standard macrocellular set-up [3GPP03a], [3GPP04d]. Covering this cell with a rectangular grid of points with a step size in x and y direction of 75 m leads to around 1200 points (physical locations in the cell). Exploiting symmetries this number can be reduced to around 200 points. Considering 10 shadow fading realisations per point leads to a situation where 2000 link level performance traces would have to be pre-computed and stored in the user performance database. Considering that every point corresponds to a single link simulation, it is desirable to find a model that requires less points while achieving a similar simulation accuracy.

To investigate which user-parameters can describe a user's average interference situation a cellular scenario simulator implementing path loss models, shadow fading models, and sector antenna array patterns, has been built, and will be described in detail in Subsection 4.4.1. As indicated in Figure 4.4 this cellular scenario simulator is used to extract two other-sector interference models. The AWGN interference model accounts for the serving sector's tx correlation, but models other-sector interference as one AWGN source. Details on the AWGN other-sector interference model are provided in Section 4.4.2. Further, an *own site plus 2 other sector interference model* (OWNP2) is extracted. It models the multipath fading powers from the sectors at the own site plus the multipath fading powers from the two strongest other site sectors. This OWNP2 approach is presented in Section 4.4.3. The FULL cellular set-up, as implemented in the cellular scenario simulator, serves as a reference to assess the performance of both models. This performance depends among others on the oversampling granularity of the user-parameters. The

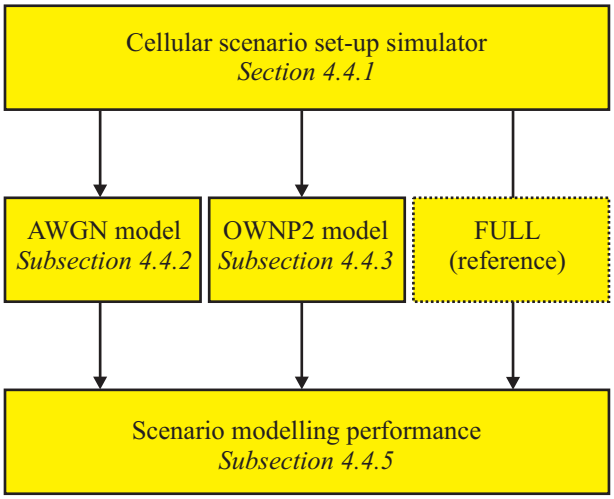

Figure 4.4: Section outline.

user-parameter sampling space and its oversampling granularity is for the AWGN and OWNP2 model outlined in Subsection 4.4.4. Performance comparison with the FULL cellular scenario set-up is thereafter presented in Section 4.4.5. The core results presented throughout the following subsections were previously published in [Berg04b].

4.4.1 FULL Cellular Scenario Set-Up

The three sector site regular grid cellular scenario set-up from [SCM 03], [3GPP03a], [3GPP04d], as introduced in Figure 1.8 is used. A zoom of the centre target cell is displayed in Figure 4.5. Three sectors per site lead to a total of 57 sectors, where the main lobes of the directional sector antenna elements are oriented as indicated by the solid arrows. A user, irrespective of its location, is only connected to the sector from which it receives the strongest small area mean power. Soft handover is not specified for the HS-DSCH channel. As detailed in Section 4.3, to construct the virtual channel power vector $\mathbf{P}^i$, knowledge of the full load small area mean received power $\overline{P}^i$ is required. The i-th sector's full load small area mean received power is calculated as

$$\overline{P}^i = \overline{L}^i_{ant} \cdot L^i_{ant} \cdot L^i_{path} \cdot L^i_{sh} \cdot \overline{P}^i_{tx} \quad , \tag{4.20}$$

where $\overline{L}^i_{ant}$, L^i_{ant}, L^i_{path}, L^i_{sh} and $\overline{P}^i_{tx}$ represent tx antenna mean gain, mean normalised antenna pattern gain, path gain, shadow fading gain and the i^{th} sector's full load transmit power respectively.

The antenna mean gain $\overline{L}^i_{ant}$ amounts to 14 dBi. The i-th sector's normalised

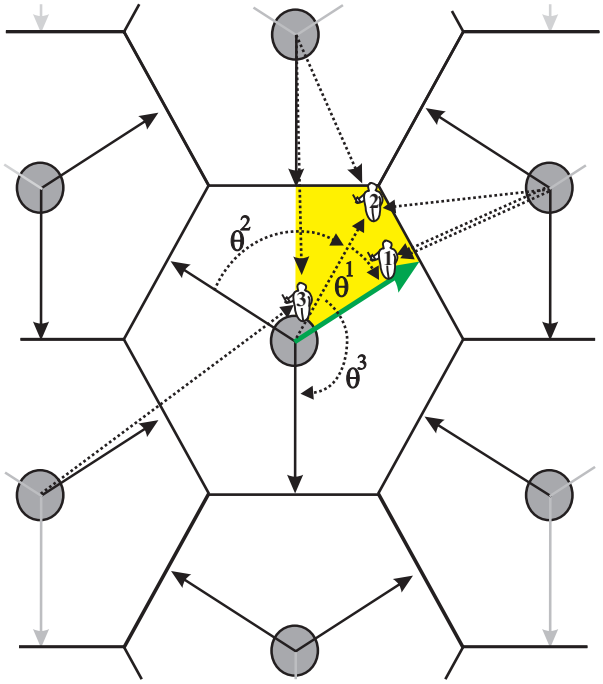

Figure 4.5: Zoom of the centre target cell, with the first tier of surrounding base station sites. The mobile users, numbered one, two and three will serve to describe example interference situations.

antenna pattern gain L^i_{ant} towards a mobile user is a function of the user's AoC, denoted θ^i. It is measured clockwise from the sector antenna broadside. The pattern is given as [SCM 03], [3GPP03a]

$$L^i_{ant}\left[\theta^i\right] = 10^{\left(-\frac{1}{10}\cdot\min\left\{12\cdot\left(\frac{\theta^i}{70^o}\right)^2,\,20\right\}\right)} \quad . \tag{4.21}$$

It is sketched in Figure 4.6 for all three sectors at one site, where the AoC of the individual antenna patterns is related to the *angle of departure* (AoD) measured anticlockwise from the horizontal axis. Path gain is calculated in the same way as in the *COST 231-Walfisch-Ikegami Model* [Ikeg84], [Walf88], [COST91], using the parameters as in [ETSI98], [3GPP03a]. For a carrier frequency of 2 GHz and a sector antenna height of 15 m above the average rooftop level $L^i_{path}\left[s\right]$ is given as

$$L^i_{path}\left[s\right] = (10)^{-1.53}\cdot\left(\frac{s}{\mathrm{m}}\right)^{-3.76} \quad , \tag{4.22}$$

where s denotes the distance between the sector antenna and the mobile user measured in meters. Shadow fading gain L^i_{sh} is modelled log-normal distributed. It is identical for all sectors at one site and correlated between all 19 sites [Sore99], [SCM 03], [3GPP03a]. Shadow fading correlation is introduced using a Cholesky decomposition approach as given in [Klin99]. All main cellular scenario set-up parameters are summarised in Table 4.5. Checks on the simulator implementation

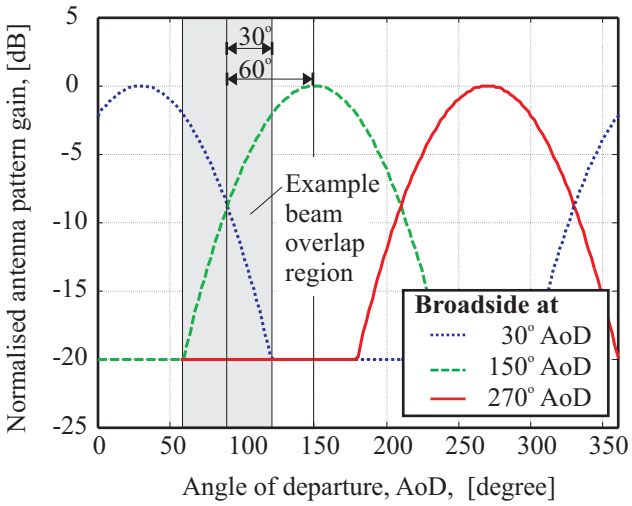

Figure 4.6: Standard sector antenna patterns for three sector sites [SCM 03], [3GPP03a]. If several tx antenna elements exist in each sector, every element follows the directional antenna pattern.

Parameter	**Setting**
Total number of sectors, N_{sec}	57
Sectors per site, $N_{secpsite}$	3
Site-to-site distance	2800 m
Antenna pattern gain, $L^i_{ant}\left[\theta^i\right]$	$-\min\left\{12\cdot\left(\frac{\theta^i}{70^o}\right)^2, 20\right\}$ dB
Antenna pattern mean gain, $\overline{L}^i_{ant}$	14 dBi
Path Gain, $L^i_{path}\left[s\right]$, s in m	$-15.3-37.6\cdot\log_{10}\left(\frac{s}{\mathrm{m}}\right)$ dB
Shadow fading standard deviation	8 dB
Shadow fading correlation (same site)	1
Shadow fading correlation (between sites)	0.5
Full load sector transmit power, $\overline{P}^i_{tx}$	43 dBm
Thermal noise spectral density	-174 dBm/Hz
System bandwidth	5 MHz
UE noise figure	9 dB

Table 4.5: Cellular scenario parameters.

are performed against results from a Nokia internal dynamic network simulator. They are presented in Appendix C.3.

4.4.2 AWGN Model

Looking at existing other-sector interference models it is found that approximating other-sector interference as AWGN is, due to its simplicity, a frequently used strategy, *e.g.* [3GPP04h], [Rant01], [Kold02]. For single transmit antenna schemes the only required user-parameter needs to describe the amount of other-sector interference power that a user experiences. A distribution of this power could be extracted from the cellular scenario set-up. However, a commonly used approach is not directly based on the other-sector interference power, but rather on the ratio of multipath averaged own sector received power to the power sum of all other sectors' multipath averaged received powers. This ratio is known as the G-factor and is, for example, used in [Huan03], [Fono02]. It is given by

$$G = \frac{\overline{P}^I}{\sum_{i=2}^{N_{sec}} \overline{P}^i} \quad , \tag{4.23}$$

where $\overline{P}^I$ represents the total small area mean received power from the serving sector I. Without loss of generality all remaining sectors are indexed from 2 to N_{sec}. Some authors also add a thermal noise contribution to the denominator of (4.23) [Holm04, p.361]. Using a bandwidth of 5 MHz, a noise spectral density of -174 dBm, and a UE noise figure of 9 dB the thermal noise floor lies around -98 dBm. With the help of the cellular scenario simulator the minimum other-sector interference level is, on the other hand, found to lie around -80 dBm. This shows that the thermal noise floor lies significantly below the other-sector interference level, *i.e.*

$$P^{th} \ll \sum_{i=2}^{N_{sec}} \overline{P}^i \quad . \tag{4.24}$$

Thus the investigated macrocellular scenario is interference limited, and for simplicity the thermal noise contribution it neglected throughout. The G-factor averaged over 400 shadow fading realisations is plotted in Figure 4.7 (a) and its distribution is given in Figure 4.7 (b). Its mean lies around 8 dB.

To perform decoupled link and network level simulations SINR traces for a finite set of G-factors can be pre-computed and stored in the user performance database. The network level simulator would then pick new users on the basis of the G-factor distribution. This is the approach implemented in the Nokia internal simulator used in [Kold02], [Kold03a].

When multiple tx antennas are present, the tx correlation needs to be described additionally. Some approaches simply assume a certain tx correlation magnitude. A tx correlation magnitude of zero, which relates to uncorrelated tx antenna elements is for example assumed in [Ahme01], [Rami03b], while tx correlation

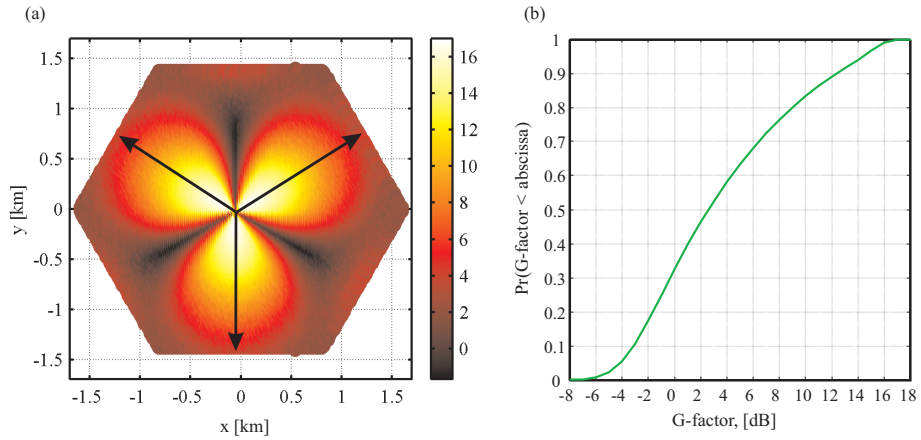

Figure 4.7: (a) G-factor as experienced over the centre cell area, when averaged over 400 shadow fading realisations. (b) G-factor distribution in the centre cell.

magnitudes fixed to a certain value different from zero are assumed in [Poll04], [Fern04]. For the MIMO multipath fading cases introduced in Section 4.2, tx correlation is a function of AoC. Thus the AoC is chosen as a second user-parameter to indirectly model the tx correlation in the AWGN model. In a decoupled link network simulation approach multiple SINR user performance traces are generated for a selection of AoC-G user-parameter pairs. The user performance database has the G-factor and the AoC as look-up dimensions. As can be seen in Figure 4.7 (a), the G-factor distribution and the AoC distribution are not independent. Their joint probabilities have been collected for the centre target cell. The network level simulator has now to use a joint AoC-G distribution to look up a user's performance. The probability that a user is served under a specific AoC is given in Figure 4.8 (a) and selected AoC conditioned G-factor cdfs are given in Figure 4.8 (b).

The AWGN interference model can be used to describe the own-to-other-sector multipath averaged received power ratios, as well as own-sector tx correlation. For single tx antenna schemes one user-parameter suffices to model a user's interference situation. For multiple tx antenna schemes two user-parameters, the AoC and the G-factor, are needed. Revisiting Figure 4.3 it can be seen that the AWGN other-sector interference model hence copes with one less look-up dimension than the physical location sampling approach. This is due to the fact that the effect of different shadow fading realisations is inherent to the G-factor distribution. However, the AWGN model neither accounts for temporal other-sector interference variation nor for spatial interference properties that play an important role when using multiple antenna terminals with interference suppression capabilities [Vill99]. To overcome these restrictions the OWNP2 interference model is developed in the following subsection.

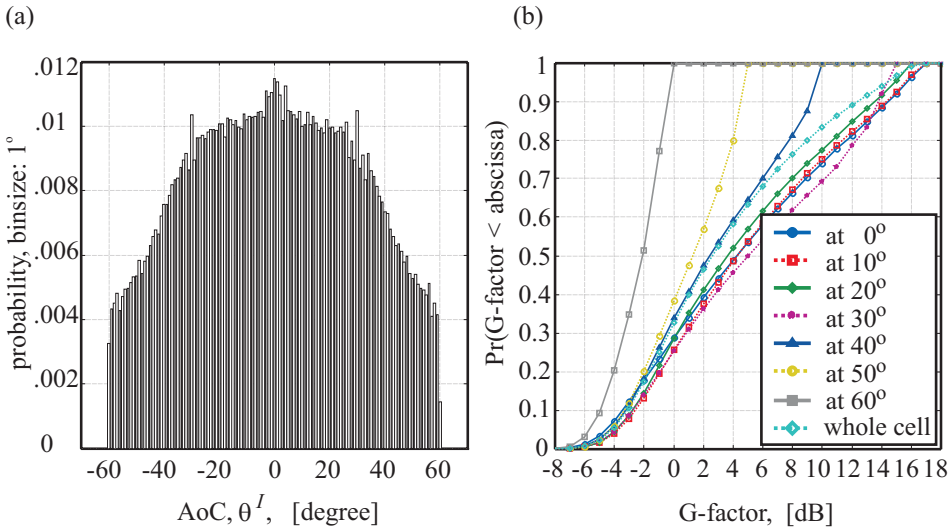

Figure 4.8: (a) AoC distribution histogram, (b) conditional G-distribution cdfs.

4.4.3 OWNP2 Model

The N_{sec} sectors are divided into two groups, the group of sectors at the same site as the serving sector, and the group of all other site sectors. Within each group the sectors are ordered corresponding to their small area mean received power so that the ordering of the own site sectors is $\overline{P}^I > \overline{P}^2 > \ldots \overline{P}^{N_{secpsite}}$, and the ordering of the other site sectors is $\overline{P}^{N_{secpsite}+1} > \overline{P}^{N_{secpsite}+2} \ldots > \overline{P}^{N_{\text{sec}}}$, where $N_{secpsite}$ indicates the number of sectors per site.

To model the occurrence of dominant other-sector interference [Vent03] and [Pukk03], for example, use a *dominant interference ratio* (DIR). An identical concept is also used in [Fran02]. The DIR is defined as

$$DIR = \frac{\max\limits_{i\in[2,\ldots N_{\text{sec}}]} \left\{\overline{P}^i\right\}}{\sum\limits_{i=2}^{N_{sec}} \overline{P}^i - \max\limits_{i\in[2,\ldots N_{\text{sec}}]} \left\{\overline{P}^i\right\}} \quad . \tag{4.25}$$

In words, it is the ratio of the interfering sector with the strongest small area mean received power to the sum of all other sectors' small area mean received power. The definition does not distinguish between the aforementioned own and other site sector groups. The DIR encountered over the centre cell area when averaged over 400 shadow facing realisations, as well as the DIR distribution are displayed in Figure 4.9 (a) and (b) respectively. The DIR will in Chapter 5 be used to characterise a user's interference situation. However, with respect to the envisaged decoupled interference modelling approach the introduction of DIR as a user-parameter has two main deficiencies:

- As can be seen through a comparison between Figure 4.7 (a) and Figure 4.9 (a), there is a strong dependency between AoC-G and DIR. Picking the DIR from an independent probability density functions can lead to unrealistic AoC-G-DIR combinations. The network simulator would therefore have to pick the user-parameter triple from a joint AoC-G-DIR distribution. Moreover, introducing the DIR as a user-parameter extends the two-dimensional user parameter look-up space into the third dimension, which is undesirable from a database size point of view.
- Further, the DIR falls short of describing more complex interference situations, *e.g.* situations where two or three dominant interferers are present. Especially to simulate the performance of advanced multiple antenna terminals with $N_{rx} > 2$ the interference power of further dominant interferers is important as up to $N_{rx} - 1$ interferers might be spatially suppressed [Vill99]. This implies that similar ratios would have to be sought to describe the power of additional dominant interferers. Such an approach therefore drastically increases the size of the user-parameter database.

Instead of using DIR as a user-parameter the OWNP2 interference modelling approach is based on the fact that there is a very strong relationship between the parameters AoC, G and DIR. Figure 4.7 (a) and Figure 4.9 (a) suggest that particularly strong dominant interference is coming from the neighbouring sectors at the same site. High DIRs up to approximately 11 dB can occur. A comparison with Figure 4.6 shows that this is the case right at the centre of the beam overlap regions. In fact, using the standard assumption that path and shadow fading gain from all sectors at one site are identical [SCM 03], [3GPP03a], [3GPP04d], the full load small area mean received powers of the neighbouring sectors at the same site, *i.e.* $i \in [2, 3]$, can be related to the full load small area mean received power from

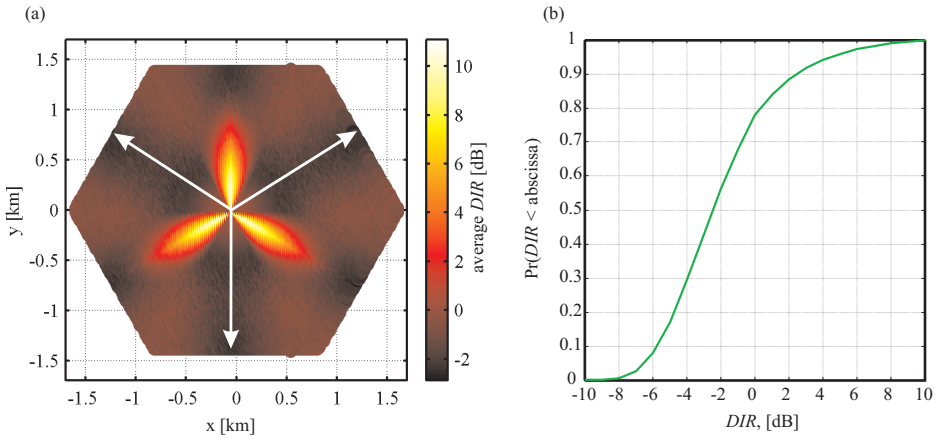

Figure 4.9: (a) DIR as experienced over the centre cell area, when averaged over 400 shadow fading realisations. (b) DIR distribution in the centre cell.

the serving sector as

$$\frac{\overline{P}^i}{\overline{P}^I} = \frac{L^i_{ant}\left[\theta^i\right]}{L^I_{ant}\left[\theta^I\right]} \quad . \tag{4.26}$$

For the investigated three-sector site set-up the relationship between the AoCs is given by

$$\theta^2 = \begin{cases} \theta^I + 120^{\text{o}}, \text{ for } \theta^I \leqslant 0^{\text{o}} \\ \theta^I - 120^{\text{o}}, \text{ for } \theta^I > 0^{\text{o}} \end{cases}$$
$$\theta^3 = \begin{cases} \theta^I - 120^{\text{o}}, \text{ for } \theta^I \leqslant 0^{\text{o}} \\ \theta^I + 120^{\text{o}}, \text{ for } \theta^I > 0^{\text{o}} \end{cases} \quad . \tag{4.27}$$

On the basis of cellular scenarios simulations it is found that other site interference, *i.e.* from the group of sectors indexed $(N_{secpsite}+1)$ to N_{sec}, plays an increasingly dominant role towards the cell borders. The total small area mean received power sum from all other site sectors can on the basis of (4.26), (4.27) and (4.23) be expressed as

$$\sum_{i=N_{secpsite}+1}^{N_{\text{sec}}} \overline{P}^i = \left(\frac{1}{G} - \sum_{i=2}^{N_{secpsite}} \frac{L^i_{ant}\left[\theta^i\right]}{L^I_{ant}\left[\theta^I\right]}\right) \cdot \overline{P}^I \quad , \tag{4.28}$$

The average contributions of the first and second strongest other site interferer, $i \in [4, 5]$, to the total other site full load small area mean received power sum, *i.e.*

$$\overline{\mu}^i = E\left\{\frac{\overline{P}^i}{\sum_{j=N_{secpsite}+1}^{N_{\text{sec}}} \overline{P}^j}\right\} \quad , \tag{4.29}$$

were found to be 0.42 and 0.18 respectively. Their full load small area mean received powers can thus be approximated as

$$\overline{P}^i \approx \overline{\mu}^i \cdot \left(\frac{1}{G} - \sum_{i=2}^{N_{secpersite}} \frac{L^i_{ant}\left[\theta^i\right]}{L^I_{ant}\left[\theta^I\right]}\right) \cdot \overline{P}^I \quad . \tag{4.30}$$

A similar modelling process could be continued up to the total of N_{sec} sectors. However, the OWNP2 model stops at the power modelling of the *own site plus two other site sectors*. The remaining full load small area mean received sector power sum is approximated as

$$\sum_{i=N_{secpersite+3}}^{N_{\text{sec}}} \overline{P}^i \approx \left(1 - \sum_{i=N_{secpersite}+1}^{N_{secpersite}+2} \overline{\mu}^i\right) \cdot \left(\frac{1}{G} - \sum_{i=2}^{N_{secpersite}} \frac{L^i_{ant}\left[\theta^i\right]}{L^I_{ant}\left[\theta^I\right]}\right) \cdot \overline{P}^I \quad . \tag{4.31}$$

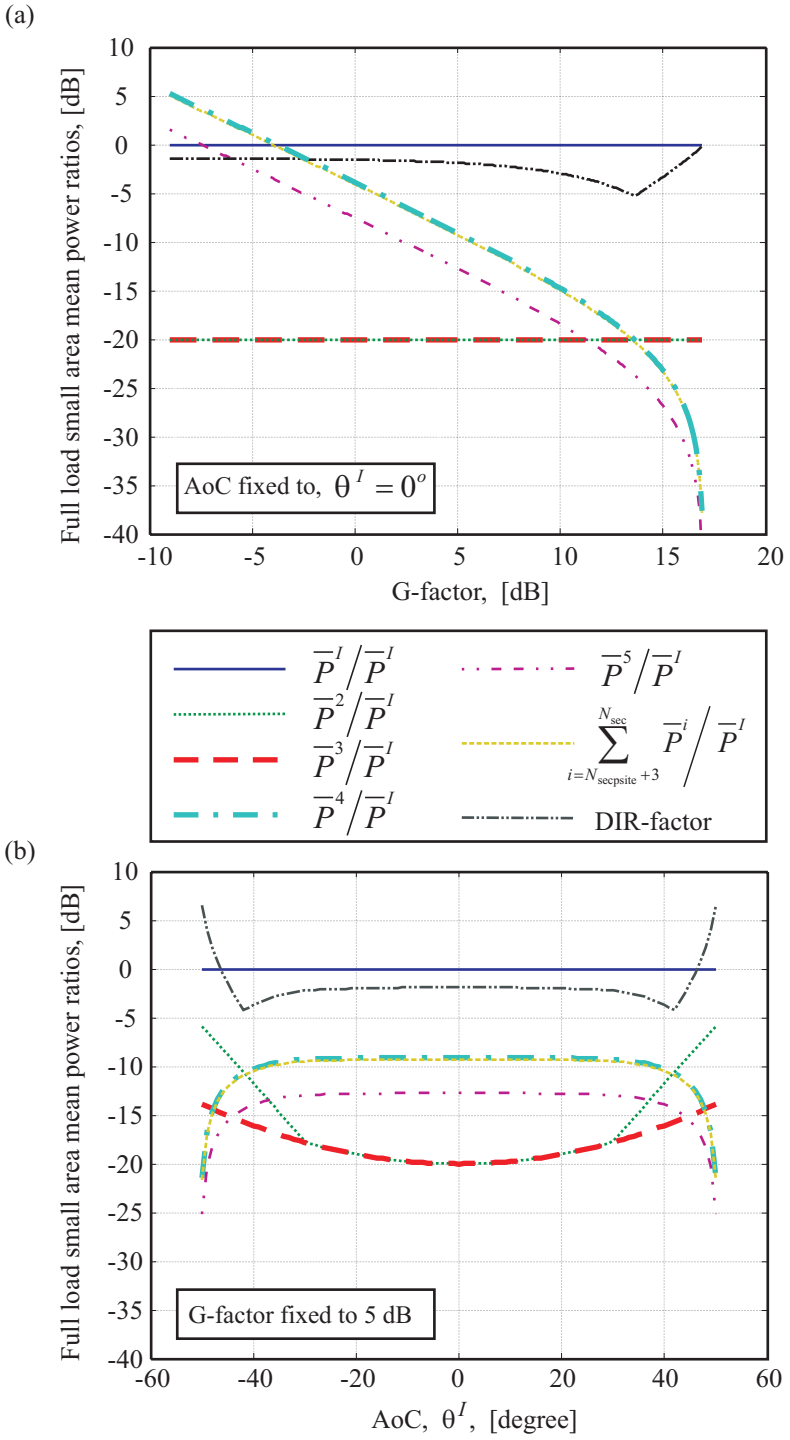

Figure 4.10: Examples of the OWNP2 power relations.

The power modelling part of the OWNP2 model hence describes the small area mean received power of four interfering sectors on the basis of the two user-parameters AoC and G. The DIR can be calculated as a function of AoC-G. Figure 4.10 visualises the power modelling relations within the OWNP2 model. It plots all modelled small area mean received powers with respect to the serving sector's small area mean received power. Figure 4.10 (a) presents the power model at the serving sector's broadside, *i.e.* $\theta^I = 0^{\text{o}}$. The power ratios are plotted over the G-factor dimension. Figure 4.10 (b) displays the power model at a fixed G-factor of 5 dB. The power ratios are plotted over the serving sector's AoC dimension.

Relating all other-sector powers to just the two user-parameters AoC and G conflicts for a small part of the model with the original definition that the serving sector is the sector with the strongest small area mean received power. With this definition no single other sector's small area mean received power can exceed the small area mean received power of the serving sector. Looking at Figure 4.10 (a) it can be seen that for G-factors ≤ -4 dB the strongest other site sector exceeds the small area mean received power of the serving sector. Relating this to the G-factor distribution of Figure 4.7 (b), it means that in 5 % of the cases the strongest interfering sector is modelled as too strong with respect to the overall interference contribution. However, the total overall other-sector interference power sum is still modelled correctly. As a consequence, a dual antenna MMSE receiver could deliver slightly optimistic results in 5% of the cases, as it can obtain increased interference suppression benefit when there is a dominant interferer. In general, the interference suppression benefit will be shown to be marginal at low G-factors. Thus modelling the strongest other-sector interferer in 5% of the cases as too strong has marginal effects.

Besides interference power modelling, the other-sector interference model is supposed to account for the other-sectors tx correlations. The tx correlation as a function of AoC can for the interfering sectors at the same site be directly obtained with the help of (4.27). To determine the tx correlation of the two strongest other site sectors a simple relation between their AoCs, *i.e.* $\left|\theta^i\right|, i \in [4,5]$, and the absolute of the serving sector's AoC, $\left|\theta^I\right|$, is sought. Therefore the joint AoC probability densities have been collected and are displayed in Figure 4.11.

On the basis of these joint probability densities the linear regression models displayed in Figure 4.11 (a) and (b) have been extracted by (i) identification of points with the highest probability ('maxima' & 'outlier'), (ii) selection of linear regression intervals by inspection, (iii) identification of points ('outlier') who's $\left|\theta^i\right|$ deviates by more than the estimated standard deviation from the estimated mean over an interval, and (iv) linear least square curve fit through the 'maxima' only. The absolute AoC relationships of Figure 4.11 can be interpreted revisiting the three example mobile positions in Figure 4.5. The serving sector's broadside is marked by the bold arrow. In position 1, $\left|\theta^I\right|$ is close to 0°, while there is a high

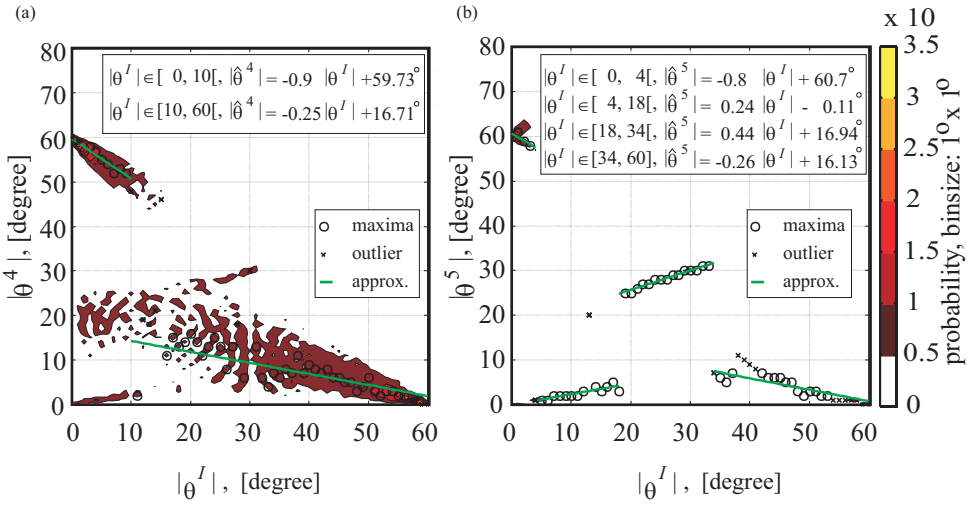

Figure 4.11: Other site sector AoC approximation.

probability that the strongest other site interferers are received with $|\theta^4|$ and $|\theta^5|$ close to 60°, as indicated by the dotted arrows pointing at mobile position 1. In position 2, $|\theta^I|$ is close to 30°, while there is a high probability that the other site interferers are received with $|\theta^4|$ and $|\theta^5|$ also close to 30°. This is indicated by the dotted arrows pointing at mobile position 2. In position 3, $|\theta^I|$ is close to 60°, while there is a high probability that the other site interferers are received with $|\theta^4|$ and $|\theta^5|$ close to 0°. This is indicated by the dotted arrows pointing at mobile position 3.

With this additional AoC modelling component the OWNP2 interference model not only accounts for the small area mean received powers, but indirectly also for the tx correlations of the serving as well as four interfering sectors.

4.4.4 User-Parameter Sampling Space

Under a physical location sampling approach the sampling space can be limited to the shaded area in Figure 4.5. All other areas inside the centre target cell have similar geometrical properties. With a physical location sampling grid the question would be which step size to choose in x and y direction and how many shadow fading realisations to consider to achieve reproducible statistical representations of the FULL scenario. Instead of representing physical locations in the centre target cell, the AWGN and the OWNP2 interference model are both based on the user-parameters AoC and G. In the same way as the physical location sampling space is tightly confined, the AoC-G parameter space can be confined. From (4.26) it can

be shown that the obtainable G-factor as a function of AoC is upper bounded by

$$G\left[\theta^I\right] < \frac{L^I_{ant}\left[\theta^I\right]}{\sum_{i=2}^{N_{secpsite}} L^i_{ant}\left[\theta^i\right]} \quad , \tag{4.32}$$

which for the investigated three sector site deployment and an antenna pattern front to back ratio of 20 dB means that G-factors > 17 dB cannot occur. Further, from Figure 4.7 (b) it can be seen that G-factors below -8 dB are highly unlikely. Moreover, due to the fact that path and shadow fading gain are assumed identical for different sectors at one site, and due to the fact that the sector with the strongest small area mean received power is defined as the serving sector, also the serving sector's AoC is bounded by

$$\left|\theta^I\right| \leqslant \frac{360^o}{2 \cdot N_{secpsite}} \quad . \tag{4.33}$$

Thus for the investigated three sector site deployment a user is never connected at $\left|\theta^I\right| > 60^o$. At higher AoCs the user is connected to the neighbouring sector as that sector has a higher antenna pattern gain. The situation can be visualised through Figure 4.6 and is confirmed through Figure 4.8 (a).

Figure 4.12 (a) displays this confined user-parameter space in the form of a histogram. It relates to the same statistical information as displayed in Figure 4.8. Darker shades indicate less probability that an AoC-G pair occurs. Further, a potential AoC-G based sampling grid is indicated. Figure 4.12 (b) presents the corresponding user performance database dimensions. Through comparison with Figure 4.3 (b) it can be seen that one less dimension is needed than in the physical location based sampling approach. This is due to the fact that shadow fading

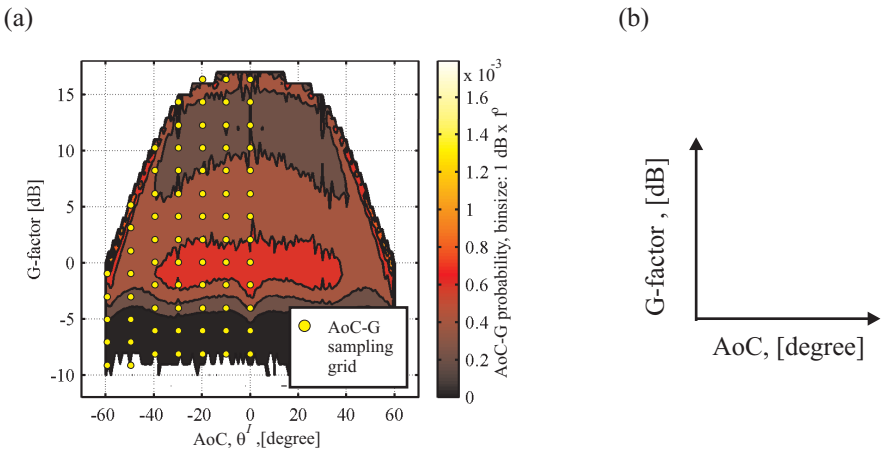

Figure 4.12: (a) AoC-G occurrence histogram, including a potential AoC-G sampling grid. (b) Sketch of AoC-G user-parameter database dimensions.

processes are integrated into the definition of the G-factor. The questions of the required AoC-G step-size is in the following subsection answered with the help of cellular scenario simulations.

4.4.5 AWGN and OWNP2 Performance

As indicated in Figure 4.4, the FULL cellular scenario serves as a reference to assess the AWGN and OWNP2 model performance. Operation of the cellular scenario simulator in itself is validated in Appendix C.3. Assessment of the interference models is performed in two steps. In the first step no constraints are put on the sampling resolution of the user-parameters AoC and G. It is investigated how well the interference models can represent the multipath fading situation and the tx correlation distribution of the FULL set-up. The second step constraints both interference models to work on a fixed AoC-G grid as displayed in Figure 4.12 (a). It is investigated how well the interference models can represent the SINR statistics of the FULL set-up.

For comparison purposes flat Rayleigh multipath fading channels are used. Their virtual channel transfer functions are given as $h^i_{n,m}$. Their tx correlation is determined as outlined in Subsection 4.2.2. As one quality measure of the other-sector interference model the *interference error ratio* (IER) is defined as

$$IER = \frac{P_{FULL}}{P_{model}} \quad , \tag{4.34}$$

where

$$P_{FULL} = \sum_{i=2}^{N_{\text{sec}}} \sum_{m=1}^{N_{vir}} \left| h^i_{n,m} \right|^2 \cdot \overline{P}^i \quad . \tag{4.35}$$

P_{FULL} hence represents the sum of all multipath fading power contributions from all interfering sectors and virtual channels m as experienced at a single rx antenna n. Further, P_{model} is either a placeholder for P_{AWGN}, given as

$$P_{AWGN} = \frac{1}{G} \cdot \overline{P}^I \quad , \tag{4.36}$$

or a placeholder for P_{OWNP2} defined on the basis of (4.26), (4.30) and (4.31) as

$$P_{OWNP2} = \left(\begin{array}{l} \sum_{i=2}^{N_{secpsite}} \sum_{m=1}^{N_{vir}} \left|h_{n,m}^{i}\right|^2 \frac{L_{ant}^{i}\left(\theta^{i}\right)}{L_{ant}^{I}\left(\theta^{I}\right)} \\ + \sum_{i=N_{secpsite}+1}^{N_{secpsite}+2} \sum_{m=1}^{N_{vir}} \left|h_{n,m}^{i}\right|^2 \overline{\mu}^{i} \cdot \left(\frac{1}{G} - \sum_{i=2}^{N_{secpcell}} \frac{L_{ant}^{i}\left(\theta^{i}\right)}{L_{ant}^{I}\left(\theta^{I}\right)} \right) \\ + \left(1 - \sum_{i=N_{secpsite}+1}^{N_{secpsite}+2} \overline{\mu}^{i} \right) \cdot \left(\frac{1}{G} - \sum_{i=2}^{N_{secpcell}} \frac{L_{ant}^{i}\left(\theta^{i}\right)}{L_{ant}^{I}\left(\theta^{I}\right)} \right) \end{array} \right) \cdot \overline{P}^{I} \quad \cdot \tag{4.37}$$

P_{AWGN} and P_{OWNP2} are thus the multipath fading interference power sums of all interfering sectors when modelled with the AWGN or the OWNP2 interference model respectively. In the ideal caseP_{FULL} would equal P_{model}, so that $IER = 1$. Figure 4.13 (a) and (b) show the absolute of the IER at the 95^{th} percentile as encountered over the centre cell area. It can be seen that the AWGN other-sector interference model introduces significant errors in the sector beam overlap regions. On the contrary the OWNP2 model performs well in those regions due to the fact that these high DIR areas are accurately modelled through the relation of serving and interfering sectors at the same site. Moving towards the cell boarders the OWNP2 model still shows considerable benefits when compared to the simple AWGN interference model. A different perspective of these IER-results is given in Figure 4.13 (c), where IER cdfs for the whole centre cell area are displayed. It is found that the absolute of the 95^{th} percentile is for the AWGN model given by 5.3 dB and can with the OWNP2 model be reduced to 2.1 dB.

Besides power modelling the OWNP2 model also approximates the AoCs of the strongest other site sectors using the linear regression models from Figure 4.11. To get a feeling which impact these AoC relationships can have on tx antenna correlation, for example considering a Laplacian distributed PAS with an rms angle spread of 5°and a tx antenna spacing of 10 wavelengths, the tx magnitude correlation cdfs are plotted in Figure 4.13 (d) for sector 4 and 5. It can be seen that the simple linear relations between serving sector AoC and the strongest other site AoCs cannot fully achieve the same tx correlation distribution. While the model for sector 4 overestimates tx correlation, the model for sector 5 underestimates it.

In general the performance results from Figure 4.13 give insight into some of the modelling effects. However, the link parameters that finally influence network level performance are the $SINR_{TTI}$ and the ΔSINR . As introduced in Subsection 1.3.3 variability cannot only come from Doppler effects, but might be caused by HS-DSCH power or tx weight switching. To describe the on/off switching of the

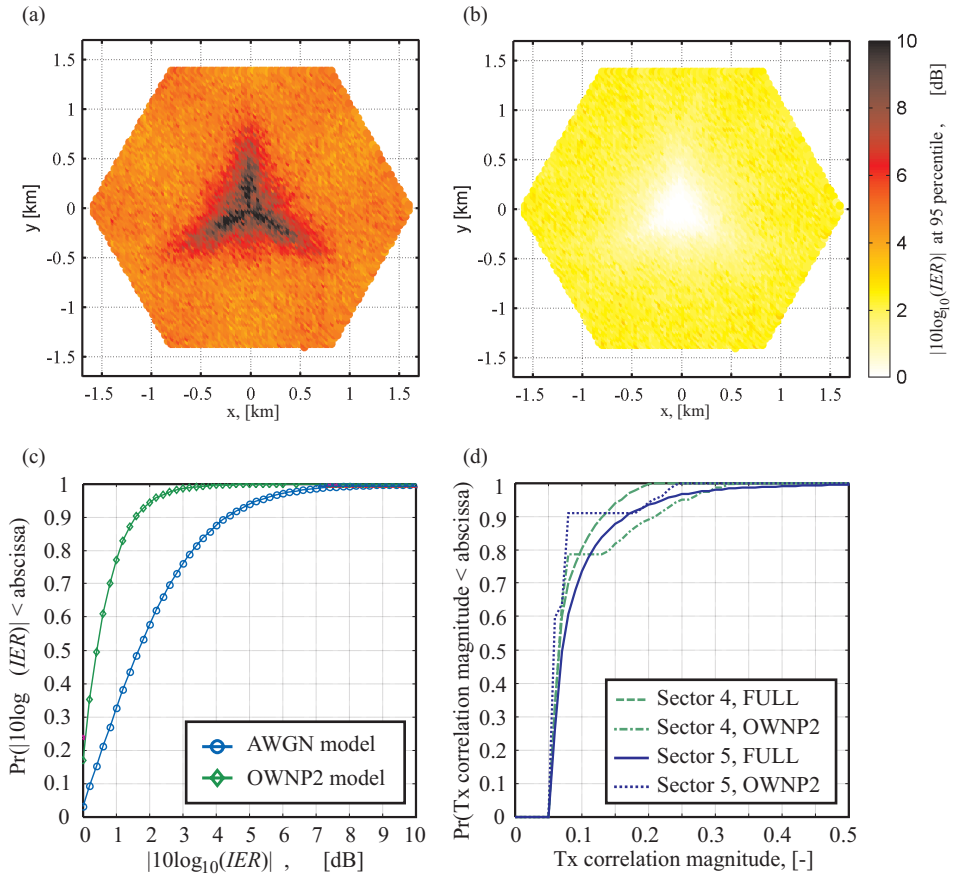

Figure 4.13: $|10 \cdot \log_{10}(IER)|$ at the 95^{th} percentile, (a) under the AWGN model, (b) under the OWNP2 model. (c) IER cdfs, (d) tx correlation cdfs.

interfering HS-DSCH power the HS-DSCH activity factor α has been introduced in Subsection 4.3.2. To answer the question if the developed interference models delivers a sufficient trade-off between simulation accuracy and simulation complexity the SINR and ΔSINR statistics for a 1×1 SISO and a 2×1 CLM1 scheme are collected. The employed simulation parameters are summarised in Table 4.6. The simulation results are displayed in Figure 4.14.

Figure 4.14 (a) displays the collected SINR cdfs for all three set-ups in a SISO and a CLM1 configuration. Figure 4.14 (b) displays the corresponding ΔSINR cdfs. A zoom on Figure 4.14 (a) would reveal that the SINR_{TTI} cdfs differ by up to 0.6 dB. Bearing in mind that link and system performance simulations will be performed with the aim of comparing different schemes within an identical simulation set-up, it is concluded that the SINR_{TTI} cdfs can be represented by both the AWGN and the OWNP2 interference model.

When looking at the ΔSINR statistics in Figure 4.14 (b) it is found that the

Parameter	Setting
MIMO channel test case	Flat Rayleigh fading, Laplacian tx PAS, tx AS of 5°, tx antenna spacing of 10 wavelengths
Spreading factor, N_{sf}	16
Sector power allocation, $\boldsymbol{\eta}^i$	$\left[\begin{array}{cccc} 0.1 & 0.1 & 0.7 & 0.1 \end{array}\right]^T$
Sampling grid:	
FULL	20 m x-y step size, $N_{shadow} = 400$
AWGN & OWNP2	$10^\circ \times 2$ dB
UE speed	0 km/h (no variation due to Doppler)
Number of simulated TTI	1000 per sampling point, multipath fading identical for all symbols inside a TTI, but independent between TTIs
HS-DSCH activity factor α:	
1×1 SISO case	0.5 (variation due to on/off switching)
2×1 CLM1 case	1 (variation due to weight switching)

Table 4.6: Parameter settings used to assess the SINR modelling performance of the OWNP2 and the AWGN model.

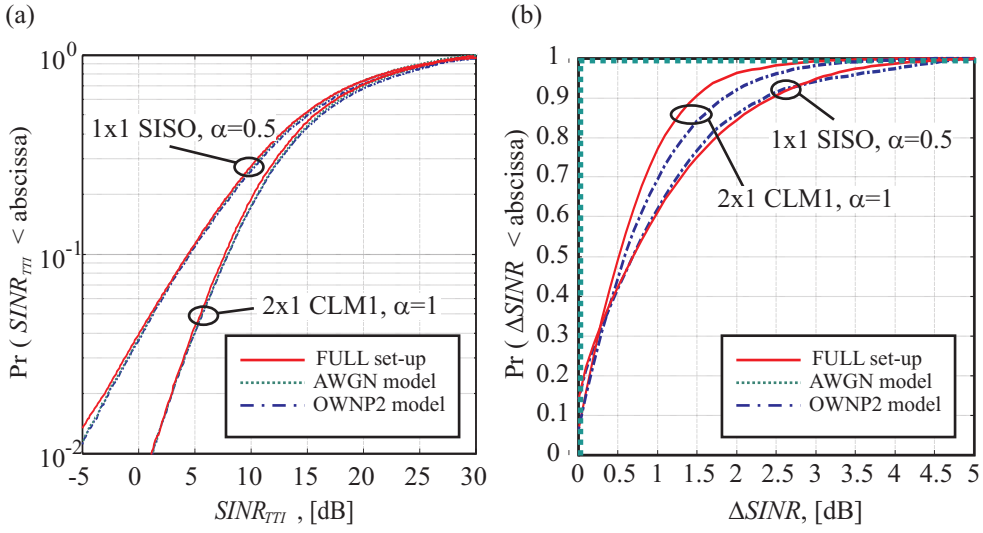

Figure 4.14: (a) $SINR_{TTI}$ cdfs, (b) ΔSINR cdfs. Both generated from the FULL cellular scenario set-up and the AWGN as well as the OWNP2 interference models.

SINR variations due to on/off switching in the SISO case can be well represented by the OWNP2 model. For the CLM1 case, where variation is caused purely by other-sector tx weight updates, higher discrepancies are obtained. At the 90^{th} percentile the OWNP2 model produces a SINR variability that is 0.3 dB higher than the variability encountered in the FULL set-up. This level of discrepancy is due to a coarse 10° oversampling in the AoC-domain and also due to the linear regression based other site sector AoC approximation as given in Figure 4.11. As will be shown in Section 4.5.5 the ΔSINR is considered as it influences turbo decoder performance. However, a 0.3 dB ΔSINR discrepancy has minimal impact on turbo decoder performance [Berg04a]. It is therefore concluded that the OWNP2 model can represent the ΔSINR statistics accurately enough. It can further be seen that no ΔSINR variations occur under the AWGN model as it models other-sector interference as a time invariant AWGN source.

4.4.6 Other-Sector Interference Modelling Summary

Based on a standard regular grid cellular scenario set-up from [SCM 03], [3GPP03a], [3GPP04d], two other-sector interference models have been extracted with the aim of allowing the pre-computation of $SINR_{TTI}$ as well as ΔSINR traces. Pre-computation is desirable as it allows run-time efficient network simulations and reusability of link level results to perform, for example, sweeps over a range of different network level parameter settings.

Instead of placing users at physical locations within the centre target cell, both models are based on AoC-G user-parameter pairs. With the help of these pairs the AWGN model indirectly accounts for a user's tx correlation with respect to the serving sector. Further, it describes a user's mean signal power relative to AWGN other-sector interference.

The OWNP2 model additionally accounts individually for the small area mean received power of the own site sectors as well as the small area mean received power of the strongest two other site sectors. Further their tx correlation is modelled. The remaining sectors are modelled as a single time invariant AWGN source. Thus especially the very high DIR situations are accurately modelled. This is due to the fact that high DIR situations are caused by the neighbouring sectors at the same site, for which the OWNP2 model does not approximate the received power, but calculates its exact value. This calculation is possible due to the standard assumption that path loss and shadow fading are identical for all sectors at the same site.

The AoC-G user parameter space was confined to realisable values, and an AoC-G user-parameter sampling grid of $10^{\circ} \times 2$ dB was chosen. It was found that the grid's step size delivers a good trade-off between simulation accuracy and link

level simulation load. If AoC symmetry is exploited, 74 user-parameter traces are to be pre-computed. This is considerably less than what would be required when using physical location based sampling.

4.5 Network Level Processes

The network level simulator is with minor adjustments identical to the simulator described in [Kold02], [Fred02] and [Kold03a]. It implements models for the basic HSDPA mechanisms introduced in Chapter 2. An overview of the models is given in Figure 4.15. These models are briefly outlined in the following subsections following the order indicated in Figure 4.15. More time is spent on the turbo decoder performance model as it is novel and was not yet described in the above references.

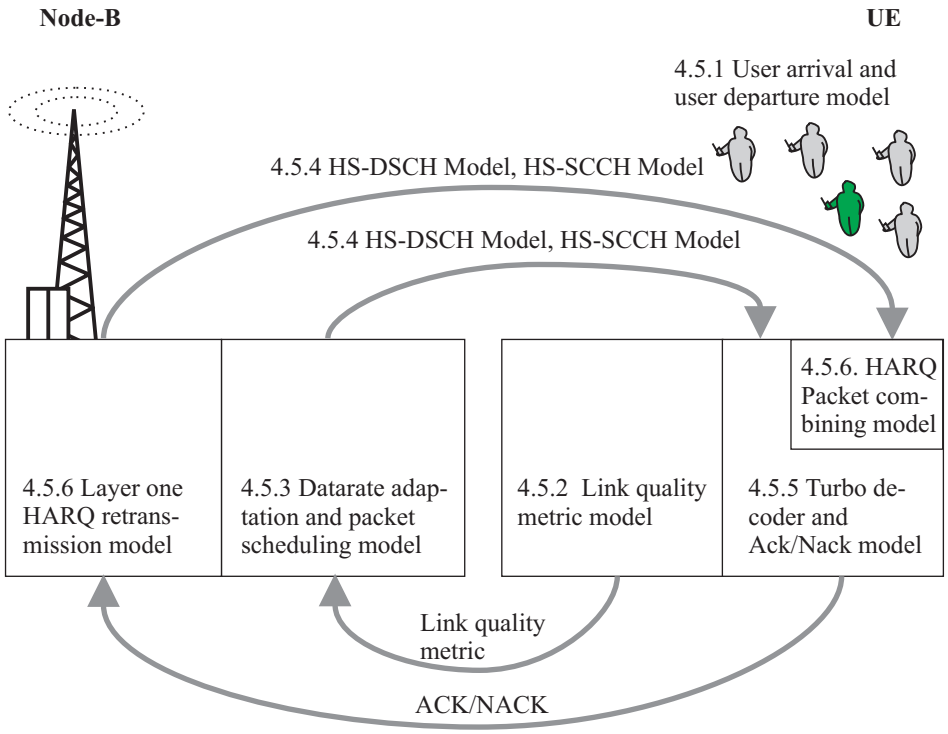

Figure 4.15: Overview of the main network simulator models and section outline.

4.5.1 User Arrival and Departure Model

Packet calls are generated according to a homogeneous Poisson process, which means that the call inter-arrival times are independent and negative exponentially distributed. Process configuration, however, is such as to effectively obtain a full transmit buffer model. Every new user requests 800 kbit of data and either leaves the network once the download is completed, or it is dropped when the data rate falls below 8 kbps over a 2 s long interval. This model thus corresponds to the 'FIXED' traffic model introduced in [Kold03a]. New user admission is upper bounded by N_{queued_max}, which means that no more than N_{queued_max} users are allowed in the queue, and excess users are blocked. In the 'FIXED' traffic model N_{queued_max} indirectly sets the multi user selection diversity order that can be exploited by channel quality dependent packet schedulers. For the PF scheduler $N_{queued} \approx N_{queued\_max}$. The RR scheduler cannot benefit from multi user selection diversity. Even though there are up to N_{queued_max} users in the system, its exploitable multi user selection diversity order is $N_{queued} = 1$. The 'FIXED' full buffer model was selected to investigate the maximum sector throughput that can be obtained with the different advanced transmission and reception schemes without encountering significant constraints imposed by higher layer data traffic aspects.

Upon arrival an AoC-G user-parameter-pair is assigned to every new user. The AoC-G parameter pair selection process is based on the AoC-G distribution displayed in Figure 4.12 (a) (Figure 4.8). With this AoC-G user-parameter-pair the user's time evolving $SINR_{TTI}$ and ΔSINR traces are retrieved from the user performance database.

4.5.2 Link Quality Metric Model

In reality the Node-B can extract channel quality information form TPC and CQI uplink signalling. The link quality metric is in the following modelled by perturbing the TTI level SINR by a lognormal distributed error ε with 0 dB mean, and a standard deviation of 1 dB, *i.e.*

$$\varepsilon \cdot SINR_{TTI} \quad , \tag{4.38}$$

This model is applied to account for SINR measurement inaccuracies at the UE [3GPP04i], and for the finite granularity of the CQI feedback words that relate to SINR values with approximately 1 dB spacing [3GPP04g, pp. 38-43]. The perturbed SINR information is used for link adaptation and packet scheduling decisions in connection with a three TTI feedback delay. This delay is selected on the basis of the seven slot minimum feedback delay specified in [3GPP04d] rounded up to the next full TTI boundary.

4.5.3 Data Rate Adaptation and Packet Scheduling Model

The MCS-multicode option is selected according to the 10% first transmission PEP link adaptation strategy outline in Subsection 2.2.3. The perturbed and delayed TTI level SINR from the previous subsection is used to determine the 10% PEP on the turbo decoder performance curves in Figure 2.4.

In case of RR scheduling all users with data in their Node-B buffers are scheduled sequentially. The PF scheduling algorithm is implemented as described in [Kold03a]. The PF filter length is set to 100. This selection is based on the PF algorithm convergence study in [Kold03a]. For a user diversity order of 10 and a mobile speed of 3 km/h this selection leads to throughput averaging over approximately 2 wavelengths. For every new user the average throughput value is initialised with 128 kb/s.

4.5.4 HS-DSCH and HS-SCCH Model

The HS-SCCH signalling channel is not explicitly modelled, but its interference power is included in the SINR calculations as outlined in Section 4.3.

The SINR performance over the HS-DSCH channel is read from the user performance database, where the two SINR performance measures $SINR_{TTI}$ and ΔSINR are stored as time traces.

4.5.5 Turbo Decoder Performance and ACK/NACK Model

Once a downlink HS-DSCH packet has been transmitted to user U, it needs to be determined whether the packet can be detected error free. To model this process a turbo decoder performance description is required. The underlying turbo decoder uses a maximum a-posteriori probability algorithm with soft decisions based on log-likelihood ratios [Proa01, pp. 519-520]. Eight decoding iterations are used. The turbo coder's performance depends on the SINR statistics experienced by the symbols within a packet. These SINR statistics change, for example, when at higher mobile speeds transmitting a packet in a frequency selective VhA channel or a relatively flat fading PeA channel [Rata02]. Different degrees of frequency diversity lead to either very similar symbol level SINRs or to a wider spread of experienced symbol level SINRs. For SISO network simulations it is therefore a standard approach to use different turbo decoder performance descriptions (performance curves) for different propagation channels and mobile speeds [3GPP01a].

Considering multiple antenna systems, different degrees of antenna diversity order would also call for different turbo decoder performance curves [Heik03, pp.

27-41]. Taking, for example, the ten multiple antenna processing options of Table 1.1, considering the PeA and the VhA PDP, and accounting for the fact that for every of the 12 MCS a different turbo decoder performance curve is needed, the task would be to generate 240 turbo decoder performance curves. In this example it was not even considered that curves for different tx correlations and other sector interference situations might additionally be required. It can be seen that the number of different performance curves that need to be pre-computed grows rapidly when one wants to account for the different SINR statistics experienced by the symbols within a packet.

The goal is therefore to find a turbo decoder performance description that relates the SINR statistics of the different physical set-ups to simple parameters that allow for a common turbo decoder performance look-up. As one parameter the average SINR of a packet is selected, since it corresponds to the standard look up parameter in the open literature [Park01], [Love01], [Lao03], [Chiu04]. It is further noted that especially the SINR variability within a TTI influences the turbo decoder performance. The ΔSINR metric defined in (4.19) is therefore used as the second lookup parameter to describe turbo decoder performance. With a Nokia internal turbo decoder performance simulator[2] the PEP performance is obtained as a function of

$$PEP = f\left(SINR_{eff},\, \Delta SINR,\, MCS\right) \quad , \tag{4.39}$$

where for the first transmission of a packet $SINR_{eff}$ is obtained from $SINR_{TTI}$ by dividing through the number of multicodes used within the packet, as introduced in (2.3). Two examples of these turbo decoder performance look up curves are given in Figure 4.16 for the modulation and coding schemes QPSK, 0.5 (MCS 4) and 16 QAM, 0.5 (MCS 8). Darker shades indicate higher PEP. It can be seen that besides different absolute areas of operation the characteristics of the two modulation and coding schemes are similar. For lower ΔSINR the transition regions from a PEP of 1 to a PEP of 0 are steeper than the transition regions encountered at higher ΔSINR . Generally, with increasing ΔSINR more SINR is required to maintain the same PEP performance. A more conventional way of displaying these performance results is given in Figure 4.17, where the turbo decoder performance is plotted for a range of ΔSINR using MCS 8 only. Seeing Doppler as one potential source of ΔSINR , the Doppler penalty results in [Rata02, Table 3] can be used to confirm the trend that with increasing ΔSINR a higher SINR is required to maintain a certain PEP performance. For a ΔSINR of 0 dB, there is no variability of the slot level SINRs within a TTI. The obtained curves are in this case identical to the curves obtained in an AWGN channel. This is shown in Appendix C.4.1 via comparison to the AWGN results in [Lao03] and [Chiu04].

[2]Troels E. Kolding inspired the usage of the ΔSINR performance metric. Frank Frederiksen generated the turbo decoder performance curves. Both are with Nokia Networks Aalborg R&D, Denmark.

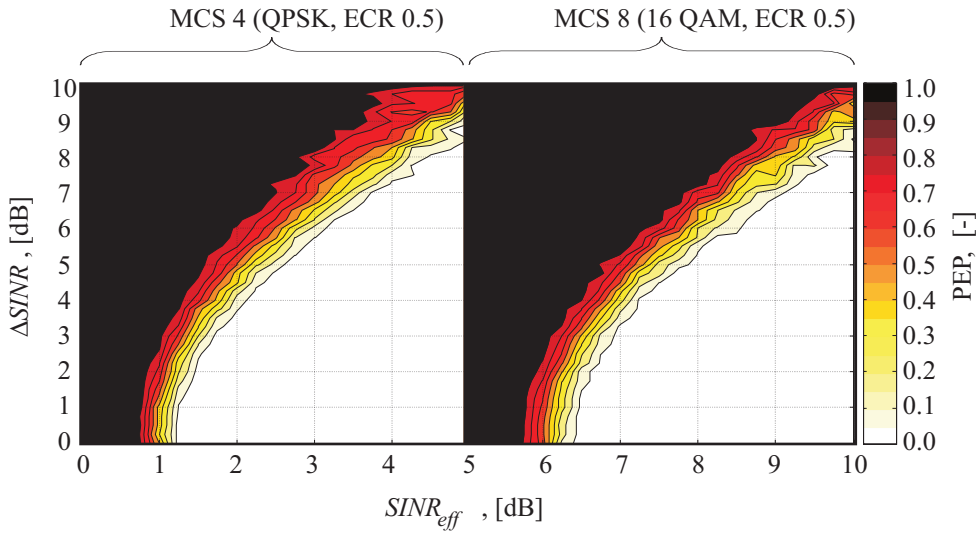

Figure 4.16: Turbo decoder performance contour plots for QPSK and 16 QAM, both with an ECR of 0.5.

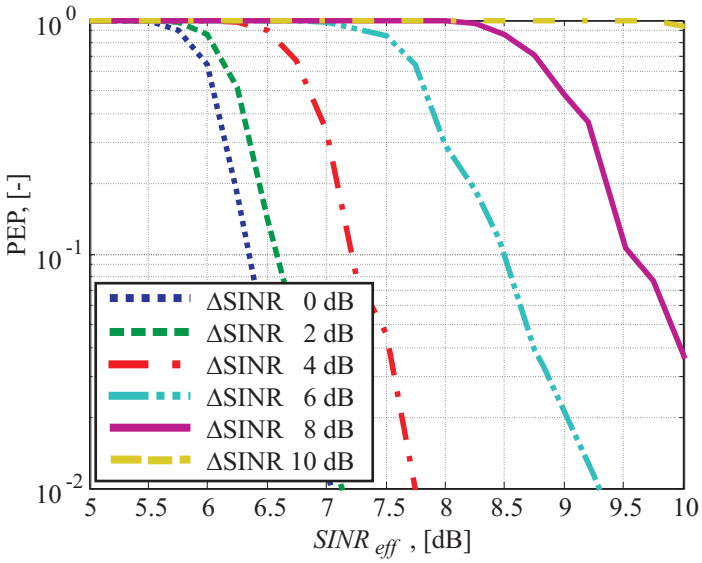

Figure 4.17: Turbo decoder performance using 16 QAM and an ECR of 0.5

Turbo decoder performance curves are produced for every MCS given in Table 2.1. On the basis of these curves a Bernoulli experiment [Moon00, p. 447] with probability distribution

$$\mathrm{pr}\left(PE_{indicator}\right) = \begin{cases} PEP, \text{ for } PE_{indicator} = 1 \\ 1 - PEP, \text{ for } PE_{indicator} = 0 \end{cases}, \tag{4.40}$$

is executed to determine whether the packet sent to user U is decoded correctly. In case of a packet error, *i.e.* $PE_{indicator} = 1$, a NACK is signal. In case of no error an ACK is signalled. ACK and NACK signalling is modelled error free.

4.5.6 Layer One HARQ Retransmission Model

To assure a smooth data packet flow a SAW protocol [Lin84], [Tann89, pp.217-219] with six simultaneously active SAW processes like in [3GPP01a], [Kold03b] is used. Upon reception of a NACK the erroneously received data packet is put into the queue for retransmission. It can at the fastest be retransmitted after 5 T_{TTI}, *i.e.* 10 ms, once the transmission of the remaining SAW processes is completed. The packet thus does not get a different scheduling priority than packets awaiting their first transmission. This selection is taken not to constrain potentially achievable multi user diversity effects. Once a retransmission is received by user U the effective SINR of the combined packet is calculated using the incremental redundancy model outlined in [Fred02]. Averaging is used to calculate the new ΔSINR . These post packet combining parameters are then again used to look up a user's turbo decoder performance as outlined in the previous subsection. Like in [Fred02] the maximum number of packet retransmissions is set to four.

4.5.7 Network Modelling Summary

Network simulations are performed with an existing network level simulator. Modelling details can be found in [Kold01], [Kold02], [Fred02] and [Kold03a]. The basic processes including a novel turbo decoder performance description have been outlined within this section. By comparison with open literature results basic network level simulator operation is validated in Appendix C.4.

4.6 Modelling Framework Summary

The sections of this chapter outlined MIMO multipath channel modelling, SINR user performance modelling, cellular scenario and other-sector interference modelling, as well as the models for the network level processes. Several simulation

parameter selections have been made and will for the sake of convenience be revisited in Chapter 5. Simulator validation has been performed analytically, through comparison with public literature, and through comparison with Nokia internal simulation results. All tests indicate expected simulator operation. Details on the different validation procedures are provided in Appendix C.

Chapter 5

Performance Results

The chapter presents selected simulation results and benchmarks the obtained SINR performance against analytical bounds. Among others it is found that:

- The AWGN model underestimates link and network performance. In PeA the SINR underestimation is accurately predicted through a novel analytical bound.
- In the investigated macrocellular scenario, there is little negative impact from partial HS-DSCH activity-induced interference variation.
- In PeA the 1×2 SIMO MMSE spatial interference suppression mean SINR benefit is accurately predicted through a novel analytical bound.
- CLM1 performance is positively impacted by tx correlation. From all investigated schemes 2×2 CLM1 MMSE with high tx correlation delivers the highest sector throughput.
- In PeA the cost of dual stream SMP in terms of mean SINR degradation per stream is accurately predicted through a novel analytical bound. SMP_x extends the system's dynamic range and has the potential to improve SIMO system performance.

5.1 Introduction

The following sections present selected single and multiple antenna scheme simulation results, highlighting effects with respect to other-sector interference properties, rx and tx correlation, as well as co-stream interference. The chapter is structured and interconnected to other parts of the dissertation as indicated in Figure 5.1.

After introducing prerequisites important for the general understanding throughout, the performance of every antenna scheme is analysed by looking at two selected topics per scheme. The individual sections are not self-contained, *i.e.* results from earlier sections are assumed known to build the line of argumentation in later sections. After the individual assessment the network sector throughput performance of all schemes is compared. As the individual antenna scheme discussions are limited to the presentation of selected results, the entire main simulation results are available in the corresponding tables of Annex I.

The results are based on a variety of different Monte Carlo simulations as depicted in Figure 4.1. Thus they are random by nature, but are reproducible with a certain accuracy. Repeatability, as achieved at different levels of the simulation framework, is analysed and presented in Appendix D. It is found that with 99% confidence the mean multipath fading channel power, the sector mean SINR results, and the sector throughput results can be reproduced with an accuracy of 4.5%, 3.5%, and 6% respectively.

5.2 Prerequisites

The simulation results are based on the modelling framework introduced in Chapter 4. Throughout Chapter 4 numerous parameter selections have been made. As a single source of reference *MIMO Channel*, *SINR-Trace Link*, *Scenario*, and *Network* simulator parameters are summarised in Table 5.1.

SINR traces are obtained for every point on the AoC-G sampling grid. To present sector level SINR statistics the individual trace statistics are combined, weighted by their AoC-G probability. The AoC-G sampling grid as well as the AoC-G histogram is re-plotted in Figure 5.2 (a).

The trace based simulation approach does not only allow to assess the SINR statistics, $\mathrm{SINR}_{\mathrm{TTI}}$ and $\Delta\mathrm{SINR}$, on sector level, but it also gives the opportunity to assess specifically effects that occur at high and low DIR as well as at high and low G. Thus four individual AoC-G positions are selected for which the individual SINR-trace statistics will be analysed. These four positions are plotted in Figure 5.2 (b) on top of a contour plot showing DIR as a function of AoC-G. Darker shading marks a higher DIR. The high and low DIR positions, labelled hDIR and lDIR, can be thought of as locations inside and outside the neighbouring sector beam overlap region respectively. At hDIR the neighbouring sector at the same site is received as the strongest interferer, roughly 6 dB below the small area mean received power of the serving sector. All other sectors are received with far less small area mean power. This relates hDIR not only to a physical location in the beam overlap region, but also to a physical location close to the serving base station site. In lDIR both interfering sectors at the same site are received over their

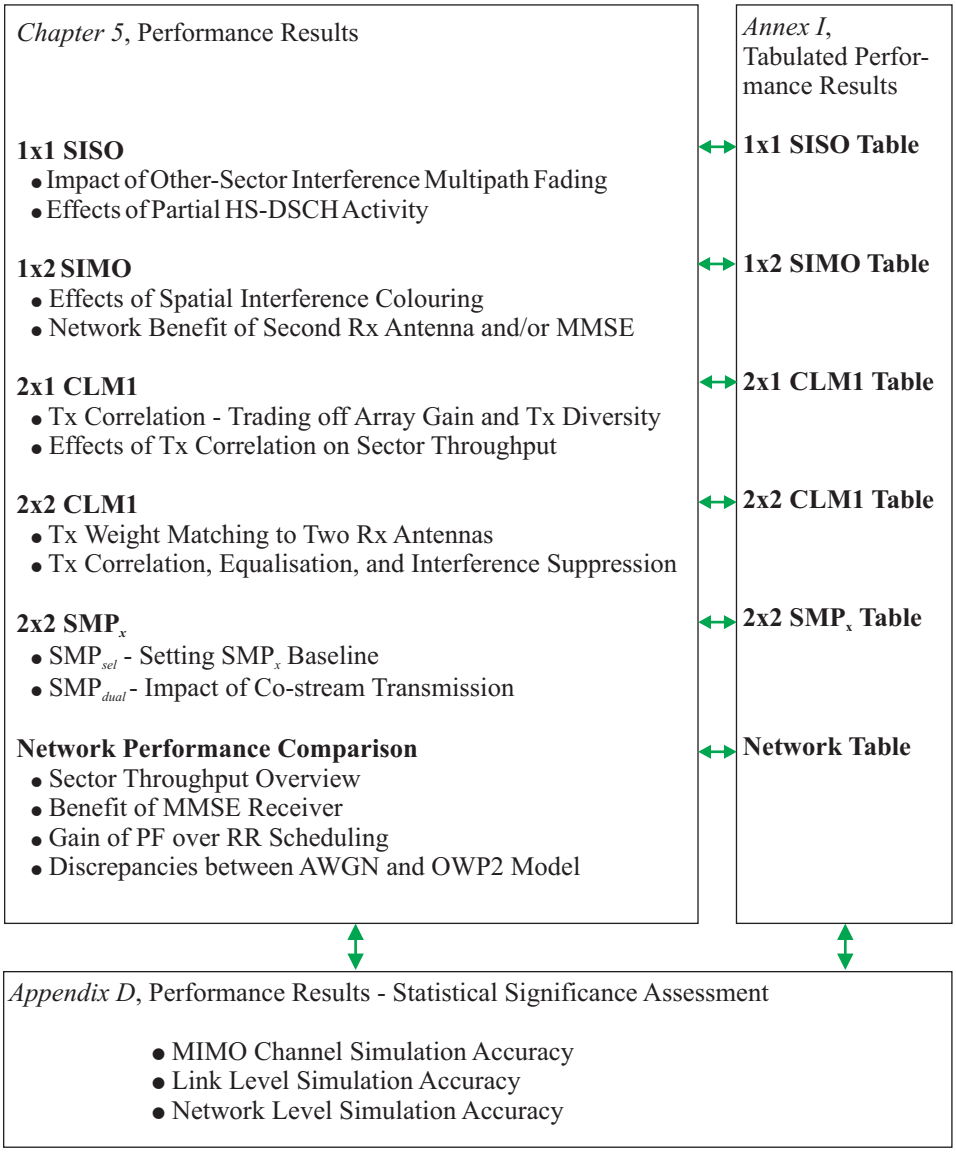

Figure 5.1: Structure of Chapter 5, and its interrelation to Annex I as well as Appendix D.

Parameter	Setting
MIMO channel simulation	
PDP (chip aligned)	ITU-Pedestrian A, ITU-Vehicular A
Tx PAS	Laplacian, AS 5°
Tx spacing	10 or 0.5 wavelength, (wc or hc)
Rx PAS	360° uniform
Rx spacing	0.5 wavelength
SINR-trace simulation	
Carrier frequency	2 GHz
Chip rate	3.84 Mc/s
Other sector interference model	AWGN or OWNP2
HSDPA activity factor, α	1 or 0.5
HS-DSCH sector power ratio, $\eta^{HSDSCH,i}$	0.7
Spreading factor, N_{sf}	16
UE speed	3 km/h
Receiver type	RAKE or MMSE
Tx-rx configurations	SISO, SIMO, CLM1, SMP$_{sel}$, SMP$_{dual}$
Channel and rx-covariance estimation	Ideal
CLM1 weight feedback	Error free, delayed by 2 slots, *i.e.* ≈ 1.33 ms
SMP$_x$ weight feedback	Error free, delayed by 3 T_{TTI}, *i.e.* 6 ms
Cellular scenario simulation	
Total number of sectors, N_{sec}	57
Sectors per site, $N_{secpsite}$	3
Site-to-site distance	2800 m
Antenna pattern gain, $L^i_{ant}\left[\theta^i\right]$	$-\min\left\{12\cdot\left(\frac{\theta^i}{70^o}\right)^2, 20\right\}$ dB
Antenna pattern mean gain, $\overline{L}^i_{ant}$	14 dBi
Path Gain, $L^i_{path}\left[s\right]$, s in m	$-15.3-37.6\cdot\log_{10}\left(\frac{s}{\mathrm{m}}\right)$ dB
Shadow fading standard deviation	8 dB
Shadow fading correlation (same site)	1
Shadow fading correlation (between sites)	0.5
Full load sector transmit power, $\overline{P}^i_{tx}$	43 dBm
Thermal noise spectral density	-174 dBm/Hz
System bandwidth	5 MHz
UE noise figure	9 dB
Network simulation	
Number of multicodes available to HS-DSCH	15
Traffic model	FIXED, 800 kbits
Max. number of users in sector, N_{queued_max}	10
Modulation schemes	QPSK, 16 QAM
Effective code rate	0.2 to 0.9 in 0.1 steps
Link adaptation criterion	10% first transmission PEP
Link adaptation and scheduling delay,	3 T_{TTI}, *i.e.* 6 ms
Packet scheduling algorithms	RR, PF (PF filter length 100, init. 128 kb/s)
HARQ algorithm	Incremental redundancy, 6 SAW channels
Maximum number of retranmissions	4

Table 5.1: Simulation parameter overview.

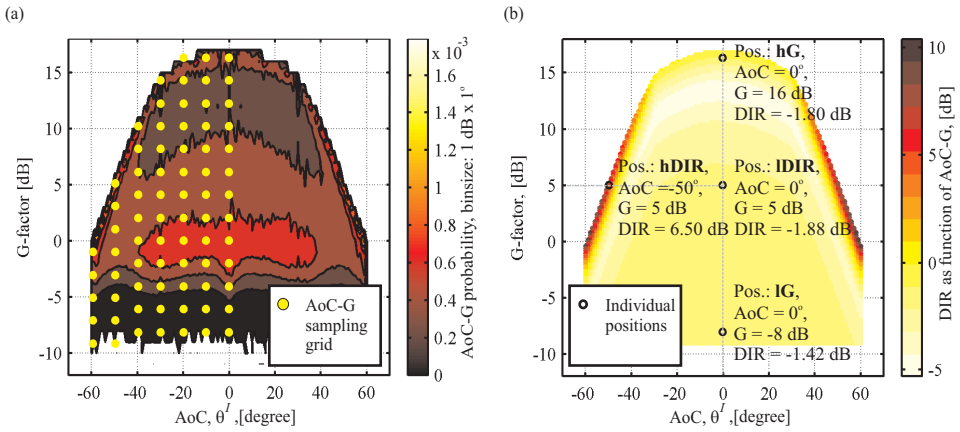

Figure 5.2: (a) whole sector sampling grid and (b) selected high and low G and DIR positions.

side lobes, 20 dB below the small area mean received power of the serving sector. lDIR is physically located further away from the serving sector's site, in a location where a group of interfering sectors accounts for the majority of the interference. The exact sector power settings used in hDIR and lDIR can be found when revisiting Figure 4.10 (b). While, for example, a high DIR as encountered in hDIR can have significant impact on the statistics of an individual SINR trace, the occurrence probability of such high DIR on sector level is relatively low. This can be seen in Figure 5.2 (a), where darker colours indicate lower AoC-G probability. The hDIR position is not the most frequently encountered. It is much more likely to encounter a DIR of 0 dB, which is in fact the average DIR extracted from the full cellular scenario set-up.

The lG and hG positions are like the lDIR position related to the serving sector's broadside. hG can be interpreted as being close to the serving base station site. lG relates to a physical location much further out into the sector, approximately located in the middle between two sites. There the serving base station's signal and several other-sector interferers are received with comparable small area mean power. The exact power settings used in lG and hG can be found when revisiting Figure 4.10 (a).

Additionally, the different AoCs in hDIR and (lDIR, lG, hG) correspond to different tx correlations as presented in Figure 4.2. The serving sector's tx correlation magnitude at -50° is $|\rho_{tx,hc}| = 0.985$, $|\rho_{tx,wc}| = 0.138$ for the hc and wc antenna spacing respectively. At 0° it is $|\rho_{tx,hc}| = 0.964$, $|\rho_{tx,wc}| = 0.062$ for the hc and wc antenna spacing respectively. Hence no significant effect is expected when changing the tx correlation between hDIR and (lDIR, lG, hG). Only changing between the narrow antenna spacing of 0.5 wavelength, *i.e.* hc, and the 10 wavelengths spacing, *i.e.* wc, has a significant impact on the tx correlation.

5.3 1×1 SISO

Effects of other-sector interference variability are investigated throughout this section. From a network perspective trackable variability can come from Doppler effects on the other sector's multipath fading interfering signals. The impact is mainly seen when looking at the SINR cdfs, their mean and their standard deviation, as performed in Subsection 5.3.1. For link adaptation and packet scheduling untrackable interference variation may occur due to on/off switching of other sector's HS-DSCH power. Link and system level effects of this partial HS-DSCH activity are investigated in Subsection 5.3.2.

5.3.1 Impact of Other-Sector Multipath Fading

To point out the effect of other-sector multipath fading the SINR statistics for the hDIR and the lDIR position are collected and displayed in Figure 5.3. Under the AWGN model other-sector interference is approximated by its mean. Thus the same cdf is obtained at hDIR and lDIR.

Despite the fact that in all three situations the mean other-sector interference power is identical, it can be seen that the hDIR causes a higher SINR mean. Further, the SINR mean under the OWNP2 model is generally higher than the mean under the AWGN model.

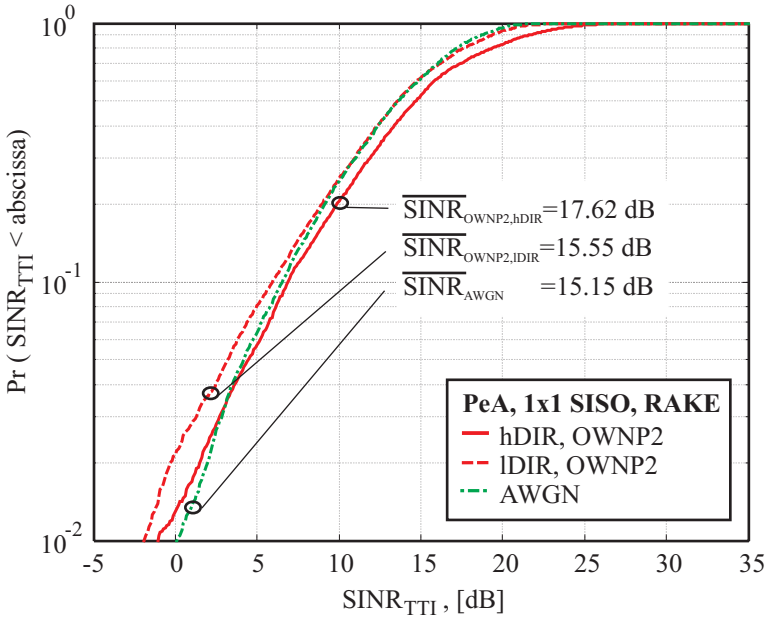

Figure 5.3: Influence of DIR on SINR distribution.

To explain this observation analytically the PeA channel is approximated as a flat Rayleigh fading channel. Further, it is assumed that all but the strongest other-sector interferer are experienced as AWGN. In this case[1] the DIR is identical to the dominant interference power to noise ratio, $\overline{INR}$. Analytical SINR statistics in flat Rayleigh fading with a single dominant interferer are detailed in Appendix A.2. Using the analytical derivations from (A.47) it can be shown that the SINR mean under the OWNP2 model is by the factor

$$\left(\frac{DIR}{DIR+1}\right)^2 + 1 \quad , \tag{5.1}$$

higher than the SINR mean under the AWGN model. It can be seen that this factor asymptotically approaches 1 for a DIR going to 0. Further, it approaches 2 for a DIR going towards infinity. Similarly the ratio of SINR mean in the hDIR and lDIR position can be derived as

$$\frac{\left(\frac{hDIR}{hDIR+1}\right)^2 + 1}{\left(\frac{lDIR}{lDIR+1}\right)^2 + 1} \quad , \tag{5.2}$$

where $hDIR$ and $lDIR$ are used to represent the actual DIR values at position hDIR and lDIR respectively. To show that this simple flat fading example gives quite accurate indications of the expected SINR mean discrepancies, the mean SINR ratios as well as their analytical approximation on the basis of (5.1) and (5.2) are displayed in Table 5.2. As can be seen, the simulation results match roughly the analytical approximation.

The SINR means and SINR standard deviations for the whole sector area are given in Table 5.3. It can be seen that over the whole sector OWNP2 and AWGN results become similar. This can be explained by the fact that on sector level high DIR situations are rare. Further, in the VhA environment frequency diversity causes the other-sector interference to appear more stable. In this case approximating it as AWGN, as done by the AWGN model, is not such a drastic approximation.

To conclude, modelling other-sector interference as AWGN leads to a reduced SINR mean and to a reduced SINR standard deviation. Underestimation is pronounced in frequency flat fading situations in the presence of a single dominant

SINR ratios	**Sim., [dB]**	**Analy., [dB]**
(hDIR, OWNP2) over (AWGN)	2.47	2.22
(lDIR, OWNP2) over (AWGN)	0.40	0.63
(hDIR, OWNP2) over (lDIR, OWNP2)	2.07	1.6

Table 5.2: Simulated SINR mean ratios and analytical approximation.

[1]DIR and $\overline{INR}$ are not always identical. The $\overline{INR}$ might also be used to describe dominant co-stream interference.

PDP	Model	SINR mean, [dB]	SINR std, [dB]
PeA	OWNP2	17.78	21.00
PeA	AWGN	17.06	19.94
VhA	OWNP2	11.00	9.81
VhA	AWGN	10.87	9.83

Table 5.3: Influence of other-sector interference properties on mean and standard deviation of the experienced SINR distributions.

interferer. In those situations the SINR underestimation can be predicted on the basis of (5.1). Seen over the whole sector the AWGN model in the PeA environment underestimates the mean SINR by 0.72 dB. In the VhA environment underestimation is reduced to 0.13 dB and thus becomes negligible. Slightly higher sector level mean SINR discrepancies, *i.e.* 0.88 dB and 0.35 dB, are encountered in connection with MMSE reception. The assessment was carried out for the 1×1 SISO situation to avoid that spatial colouring effects overlap with effects from multipath fading interference power variation.

5.3.2 Effects of Partial HS-DSCH Activity

The effect of partial other-sector HS-DSCH activity, as introduced in Subsection 1.3.3, is analysed. Simulation results are presented for the PeA environment as there the variability effects due to a lack of frequency diversity are more pronounced. Variability effects are analysed via comparison to a static reference set-up. The parameter settings related to variability modelling are summarised in Table 5.4. In case of partial other-sector HS-DSCH activity, the entire mean interference level is reduced. The mean power reduction per sector is calculated as

$$\mathrm{E}\left\{\boldsymbol{\omega}^i \cdot \boldsymbol{\eta}^i\right\} = \left(1 - \eta^{HSDSCH,i} \cdot (1-\alpha)\right) \quad , \tag{5.3}$$

where the expectation is taken with respect to the Bernoulli HS-DSCH activity distribution from (4.8). As can be seen from Table 5.4, under the *variability* set-up,

	Variability	Static reference
Interference model	OWNP2	
Activity factor, α	0.5	
Sector I	Always on	
Sector 6 to 57	Received power scaled by $\left(1 - \eta^{HSDSCH,i} \cdot (1-\alpha)\right)$	
Sector 2 to 5	HS-DSCH on/off switching as defined in Section 4.3.2	Received power scaled by $\left(1 - \eta^{HSDSCH,i} \cdot (1-\alpha)\right)$

Table 5.4: Parameter settings used to compare a situation with HS-DSCH power *Variability* against a *Static reference*.

the power from all individually modelled interfering sectors, *i.e.* $i \in [2, 3, 4, 5]$, undergoes the on/off switching process specified in Subsection 4.3.2. All remaining interfering sectors, that under the OWNP2 model are represented by a single AWGN contribution, are downscaled in accordance with (5.3). In the *static reference* set-up the individually modelled sectors do not follow the on/off switching process. Their powers are, like the powers of all other interfering sectors, downscaled in accordance with (5.3).

The ΔSINR statistics for the variability set-up and the static reference set-up, collected over the whole sector area, are presented in Figure 5.4. Further, the obtained SINR and ΔSINR means are given in Table 5.5. From Figure 5.4 it can be seen that pure Doppler effects cause a ΔSINR that for approximately 90% of the cases lies below 0.5 dB. In case of partial HS-DSCH activity, ΔSINR generally increases, but remains for 90% of the cases well below 2 dB. Thus it also stays substantially below the upper bound of 5.3 dB presented in Figure 1.5 (b). Relating the ΔSINR statistics from Figure 5.4 to the turbo decoder performance of Figure 4.16

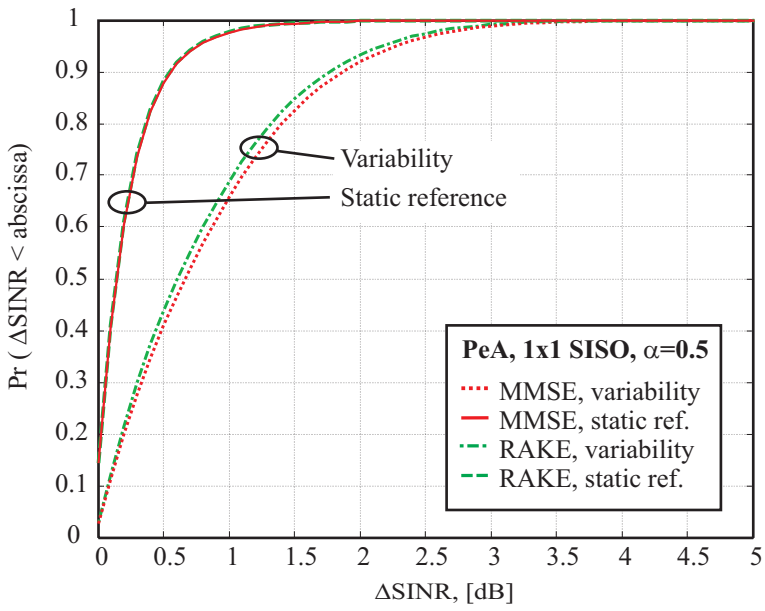

Figure 5.4: Comparison of ΔSINR cdfs for the variability and the static reference set-up.

	Receiver	SINR mean, [dB]	ΔSINR mean, [dB]
Variability	MMSE	20.17	0.88
Static ref.	MMSE	19.92	0.23
Variability	RAKE	19.23	0.82
Static ref.	RAKE	19.03	0.23

Table 5.5: SINR mean and ΔSINR mean under the variability and the static reference set-up.

and Figure 4.17, it can be concluded that for 90% of the cases the turbo decoder performance loss due to partial HS-DSCH activity is below 0.25 dB. Looking at the encountered SINR mean values in Table 5.5, it is found that HS-DSCH on/off switching causes a slight mean SINR benefit of around 0.2 dB with respect to the static reference. Similarly to the derivations in the previous subsection this mean benefit can directly be related to the increased interference variability. As slight turbo decoder performance degradations and slightly improved mean values are counteracting effects, a final conclusion on the effects of other-sector interference variability can only be drawn with additional consideration of the network level performance.

To investigate the impact of other-sector interference variability on link adaptation only, sector throughput results have been obtained in connection with the link quality independent RR scheduler. The joint impact on link adaptation and link quality dependent scheduling is reflected in the sector throughput results obtained under the PF scheduler. It is recalled that generally link adaptation and packet scheduling are performed on the basis of the link quality metric error model introduced in Subsection 4.5.2. As the encountered SINR variability is in magnitude comparable to the introduced link quality metric errors, the network performance has additionally been tested disabling the error model. The obtained sector throughput results are presented in Figure 5.5.

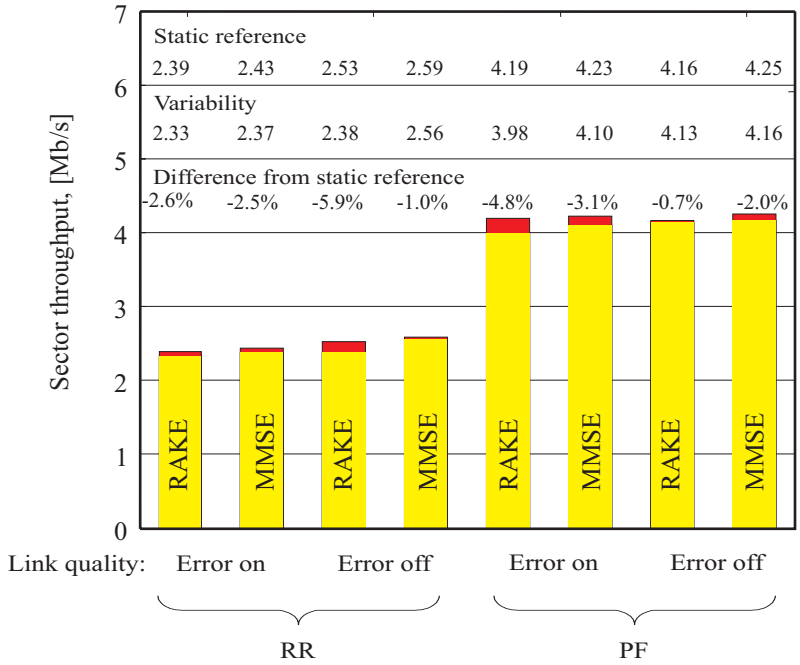

Figure 5.5: Effect of other-sector interference variability in the 1×1 SISO case, under the OWNP2 model, in PeA and in combination with an activity factor α of 0.5.

When inspecting the sector throughput results in Figure 5.5 the loss due to partial HS-DSCH activity is visible independent of receiver type, scheduler type and whether the link quality metric error model is enabled or disabled. The maximum loss is in the order of 6%. These results lead to the conclusion that the HS-DSCH system is robust enough to cope with the encountered degree of untrackable other-sector interference variability. Further, the link adaptation and packet scheduling algorithms are only marginally affected by the introduced errors on the link quality information. Moreover, although partial HS-DSCH transmission leads to small losses compared to a static reference system, it should be noted that the absolute sector throughput performance is enhanced due to a general reduction of the overall interference level. This reduction is given by (5.3), which under the selected parameter settings relates to an overall SINR mean gain of around 54%. Besides, results for the VhA environment and for interference variability effects caused by tx weight updates of a CLM1 system have been published in [Berg04a]. It was found that weight switching, similarly to HS-DSCH on/off switching, has marginal effect on sector throughput performance. The same was found for a set-up that combined on/off switching and tx weight updates. From now onwards, all sector throughput results are produced for full HS-DSCH activity, *i.e.* $\alpha = 1$. Further, the link quality metric error model is always activated from now on.

5.4 1×2 SIMO

The dual antenna MMSE receiver can exploit spatial interference colouring. How much can be gained, for example, with respect to dual antenna RAKE reception, and how much benefit does the second antenna bring to RAKE reception in the first place? To answer these questions this section is split into two subsections. Subsection 5.4.1 looks at selected effects of spatial interference colouring in the individual low and high DIR and G positions. In Subsection 5.4.2 the link level benefits encountered over the whole sector are related to network level performance.

5.4.1 Effects of Spatial Interference Colouring

To see the isolated MMSE receiver spatial interference suppression capabilities, the relatively frequency flat PeA environment is considered at the hDIR and the lDIR position. These correspond to a medium G of 5 dB, so that IPI has little influence on the overall interference situation. To support this claim the SINR statistics under the AWGN model are plotted in Figure 5.6. They are identical for the hDIR and the lDIR position. It can be seen that under the AWGN model RAKE and MMSE performance are hardly distinguishable. In terms of trace mean SINR their difference amounts to 0.15 dB. This is due to the fact that the AWGN model uses spatially white other-sector interference. It is concluded that in this special

situation the RAKE receiver performance can serve as reference performance to point out the isolated benefit of MMSE spatial interference suppression.

Comparing in Figure 5.6 the RAKE and MMSE performance under the OWNP2 model a spatial interference suppression benefit of the MMSE receiver becomes visible. This benefit is much more pronounced in the hDIR position of Figure 5.6 (a) than in the lDIR position of Figure 5.6 (b). In terms of trace mean SINR, it is found that the spatial interference suppression benefit amounts to 3.47 dB and 0.79 dB in the hDIR and lDIR position respectively. The significant spatial interference suppression benefit in the hDIR position can be attributed to the fact that a single dominant other-sector interferer exists that can partly be suppressed by the dual antenna MMSE receiver. In the lDIR position the interference is more evenly split between all interfering sectors, in which case the dual rx antenna MMSE receiver has not enough degrees of freedom to successfully suppress a significant part of the interference.

To support this claim an analytical expression for the benefit of OPC over MRC in the presence of one dominant interferer is derived in Appendix A.2.3, (A.63). Replacing, as previously, $\overline{INR} = DIR$, the spatial interference suppression benefit of MMSE over RAKE reception can be approximated by

$$\beta_{\substack{1\times 2SIMO-MMSE,\\ 1\times 2SIMO-RAKE}} = \frac{2\cdot(DIR+1)^4}{6\cdot(DIR)^3+11\cdot(DIR)^2+8\cdot(DIR)+2} \quad . \tag{5.4}$$

This analytical bound is plotted in Figure 5.7. The two individual points in Figure 5.7 indicate the simulated spatial interference suppression benefit of the MMSE receiver at the lDIR and the hDIR position. It can be seen that the analytical approximation can be used to predict the obtained simulation results.

The second effect for closer investigation is the one of rx correlation on the obtainable rx antenna array gain. From the MIMO multipath fading validation in Appendix C.1.2, Table C.1 it is known that the rx antenna correlation magnitude amounts to around 0.3. To avoid overlap with spatial interference suppression effects the RAKE receiver performance is analysed. As introduced in Subsection 1.4.1, and calculated for a flat uncorrelated Rayleigh fading channel in Appendix A.1.2, the expected array gain of dual antenna MRC over SISO amounts to around 3.01 dB. The actually obtained array gains in the lG and the hG position are displayed in Table 5.6. It can be seen that under the AWGN model the obtained array gains in the lG position come with 2.96 dB and 3.07 dB very close to the expected gain. However, at the hG position and generally under the OWNP2 model, the obtained array gains remain below the initial expectation. The lower than expected array gain can be attributed to spatial interference colouring. This is visualised in Figure 5.8, which presents plots of the elements insight the interference covariance matrices. To generate the plots, 100 approximately wavelength spaced interference covariance matrix snap shots are taken, and the ensemble average over

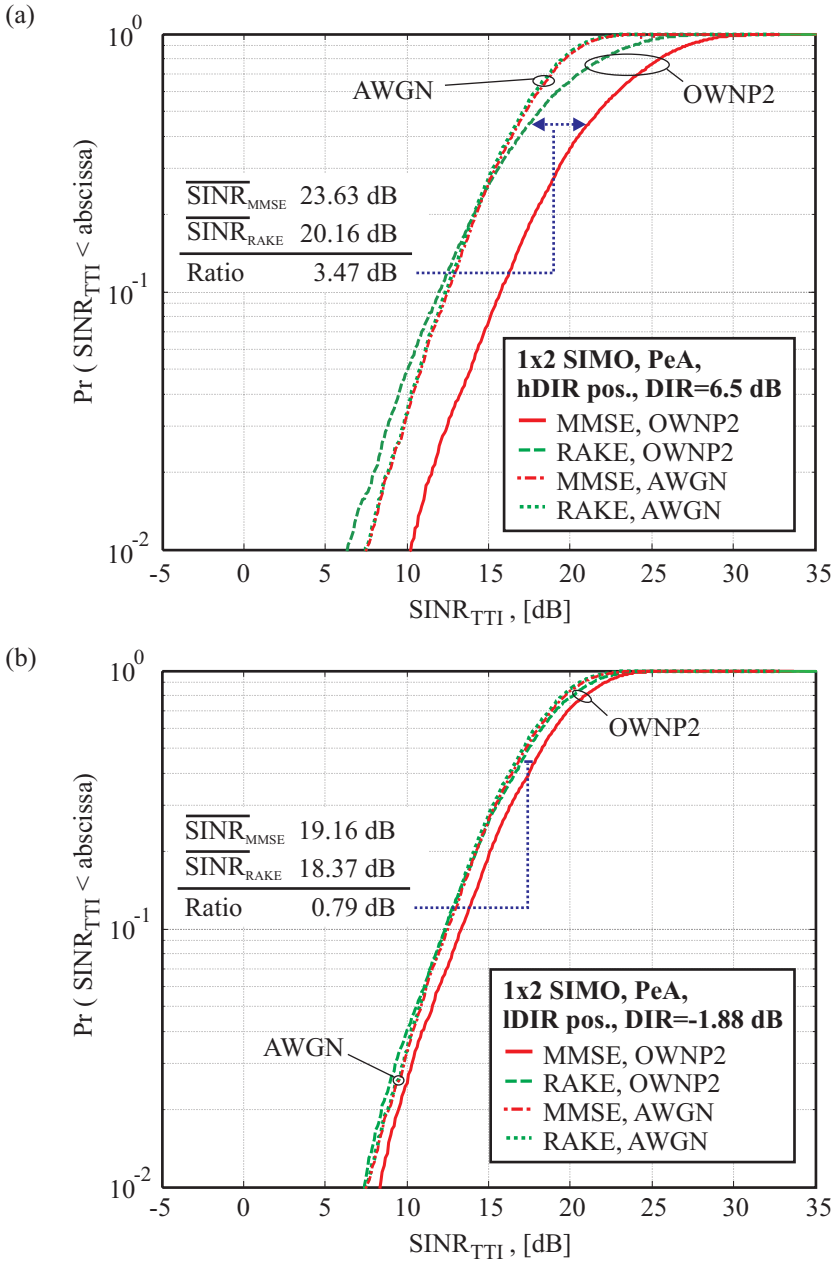

Figure 5.6: SINR cdfs of 1 × 2 SIMO RAKE and MMSE receiver to reveal the spatial interference suppression benefit of the MMSE. (a) hDIR position. (b) lDIR position.

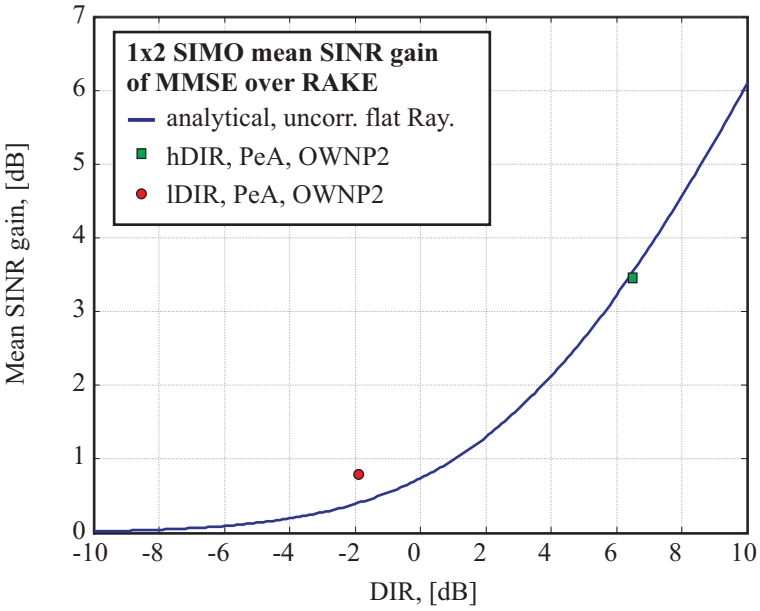

Figure 5.7: Simulated and analytically approximated spatial interference suppression benefit of the MMSE receiver.

PDP	Pos.	Array Gain, [dB] AWGN	OWNP2
PeA	**lG**	2.96	2.86
	hG	2.84	2.78
VhA	**lG**	3.07	2.56
	hG	2.53	2.61

Table 5.6: Obtained mean SINR and array gain of the RAKE receiver in a high and low G-factor position.

the absolutes of the elements inside the matrices, indexed x, y, is calculated as

$$\mathrm{E}\left\langle \left| \left(\mathbf{\Omega}_M^{HSDSCH,I} \right)_{[x,y]} \right| \right\rangle_{\text{100 wavelength spaced samples}}, \tag{5.5}$$

where $x \wedge y \in [1, \ldots (N_{FIR} \cdot N_{rx})]$. For comparability the dimensions of the covariance matrix plots corresponding to PeA and to VhA are kept equal, which means N_{FIR} is selected on the basis of the longer impulse response of the VhA environment. The colour scheme in Figure 5.8 relates to the absolute of the elements inside the matrixes on dB scale. While exact values are difficult to read and interpret, it is possible to distinguish between lighter colours associated with less interference power and darker colours associated with more interference power. This distinction between more and less dark will suffice to point out some of the main effects.

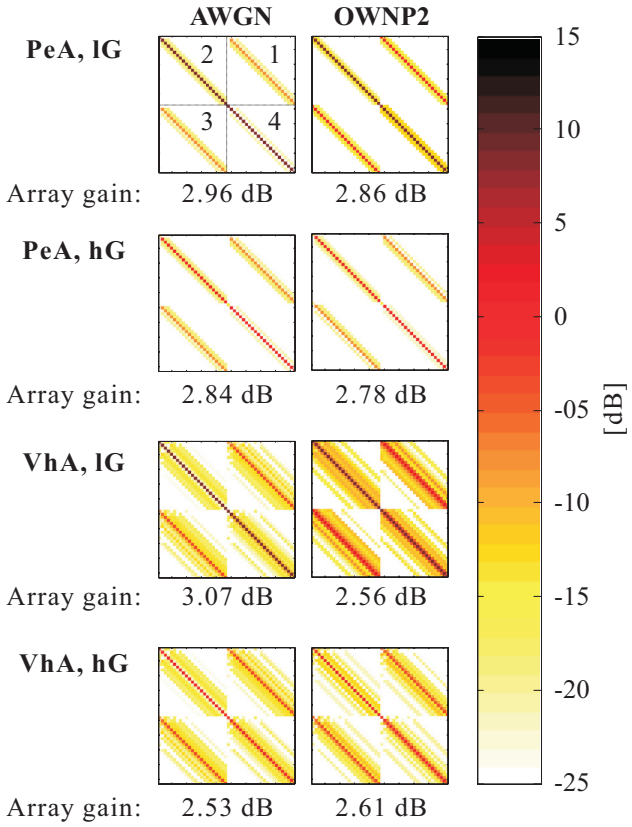

Figure 5.8: Ensemble average snap shots of the interference covariance matrix in the lG and the hG position. The off-diagonal submatrices, *i.e.* 1 and 3, display correlated interference contributions.

The rx antenna correlation is reflected through interference contributions in the odd numbered submatrices. If there was no rx correlation, these odd numbered submatrices would not contain interference signal components. Under the AWGN model the encountered contribution to the odd numbered submatrices comes purely from the own-sector IPI components. Those IPI components are in the lG position relatively small when compared to the strong diagonal loading from the other-sector AWGN contribution. This is reflected through the dark main diagonal and comparatively light coloured off-diagonals in Figure 5.8, AWGN, PeA lG and VhA lG. The assumption of uncorrelated rx interference is in these lG positions approximately fulfilled, leading to approximately 3 dB array gain independent of the degree of frequency selectivity. Turning to the hG positions, the own-sector rx correlation encountered under the AWGN as well as under the OWNP2 model, lets the benefit from the additional rx antenna shrink down to 2.53 dB. Under the OWNP2 model not even in the lG positions a full 3 dB array gain can be achieved as the odd numbered interference covariance submatrices reveal relatively strong rx correlated other-sector interference. As a rule of thumb it can be concluded that the higher the loading on the main diagonal of the interference covariance matrix, the

closer the actually obtained array gain comes to the desired array gain of around 3 dB.

To analytically assess the penalty due to interference correlation the expected array gain of an N_{rx} antenna element MRC is derived in Appendix A.3.2 on the basis of [Vaug03, (8.4.33)]. It writes

$$\beta_{1\times 2SIMO\_RAKE,correlatedint} = \frac{(N_{branch})^2}{(N_{branch})^2 \cdot |\rho_{rx}|^2 + N_{branch} \cdot \left(1 - |\rho_{rx}|^2\right)} \quad . \tag{5.6}$$

For the specific situation of $N_{rx} = 2$, and $|\rho_{rx}| = 0.3$, (5.6) delivers approximately 2.63 dB array gain instead of the 3.01 in the uncorrelated case. This analytical array gain matches well the encountered values under the AWGN and the OWNP2 model in those cases where the interference covariance contribution is not mainly confined to the main diagonal, *i.e.* those values ranging from 2.53 dB to 2.86 dB in Table 5.6 and Figure 5.8.

This subsection was especially devoted to interference colouring effects that influence the dual antenna MMSE and the dual antenna RAKE receiver performance. With respect to representing the benefit of MMSE spatial interference suppression, it is found that the AWGN model is unsuitable, as it models the other-sector interference as AWGN. On the contrary the OWNP2 model is suitable as it accounts for dominant other-sector interference. The amount of spatial interference suppression benefit depends on the DIR. An analytical expression was presented that predicts this benefit in situations that are close to uncorrelated flat Rayleigh fading.

With respect to RAKE reception it was confirmed that MRC/RAKE array gain is not a function of the desired signal's rx correlation [Ande00], nor is it directly a function of frequency selectivity. This is due to the fact that for each RAKE finger an individual MRC weight is used. Still it is found that in many situations less than the desired array gain is obtained. Under the OWNP2 model one reason is determined to be rx correlated other-sector interference. Under the AWGN model the other-sector interference is modelled as AWGN contribution. Thus a different explanation has to be sought to account for less than the expected array gain. Frequency selectivity in the own sector causes IPI. The IPI components experience, like the desired signal components, rx correlation. If the IPI components reach similar power levels as the elements on the main diagonal of the interference covariance matrix, then the IPI interference rx correlation decreases the array gain. Therefore there is less array gain, for example, in high G positions and in connection with frequency selectivity. This means that frequency selectivity indirectly influences the amount of obtainable array gain. No matter whether rx correlated interference contributions are due to other-sector or own-sector effects, an analytical expression for the array gain has been presented as a function of interference cor-

relation. The obtained analytical result can predict the simulation results in those cases where the rx antenna correlation $|\rho_{rx}|$ approximates the overall rx interference correlation.

5.4.2 Network Benefit of Second Rx Antenna and/or MMSE Receiver

This subsection shows how link level SINR gains over the baseline 1×1 SISO RAKE case, caused by enhancements such as a second rx antenna, an MMSE receiver or both, translate into actual sector throughput gains. For this purpose the first part of this subsection presents the link level SINR statistics as encountered over the sector area. The second part presents the encountered sector throughput performance and discusses the encountered sector throughput gains.

The SINR cdfs of the 1×1 SISO and 1×2 SIMO scheme are displayed in Figure 5.9. To increase the readability only the statistics under the OWNP2 model are plotted, while OWNP2 and AWGN mean SINR results are collected in Table 5.7.

Considering the RAKE receiver array gain in Table 5.7 it can be seen that only in the relatively frequency flat fading PeA environment and under the AWGN model the full 3 dB array gain is approximately obtained. Looking at RAKE AWGN performance in connection with the much more frequency selective VhA environment, the array gain is reduced to 2.81 dB. As discussed in the previous subsection, this is due to own sector IPI rx correlation. Similarly the RAKE OWNP2 performance suffers from correlated interference, this time also in the weekly frequency selective PeA environment, as the other-sector interference permanently exhibits rx correlation.

Further, it can be seen that the dual antenna MMSE receiver can efficiently

	1×1 **SISO**				1×2 **SIMO**			
	RAKE		**MMSE**		**RAKE**		**MMSE**	
	AWGN	**OWNP2**	**AWGN**	**OWNP2**	**AWGN**	**OWNP2**	**AWGN**	**OWNP2**
	Sector mean SINR, [dB]							
PeA	17.06	17.88	17.65	18.63	20.11	20.77	20.91	22.94
VhA	10.87	11.10	12.84	13.29	13.68	13.80	17.63	18.67
	Gain of 1×2 SIMO over 1×1 SISO, [dB]							
PeA	–	–	–	–	3.05	2.89	3.26	4.32
VhA	–	–	–	–	2.81	2.70	4.79	5.38
	Gain of MMSE over RAKE, [dB]							
PeA	–	–	0.59	0.75	–	–	0.80	2.17
VhA	–	–	1.97	2.19	–	–	3.95	4.87
	Gain of OWNP2 over AWGN, [dB]							
PeA	–	0.82	–	0.98	–	0.66	–	2.03
VhA	–	0.23	–	0.45	–	0.12	–	1.04

Table 5.7: 1×2 SIMO sector mean SINR and 1×1 SISO reference.

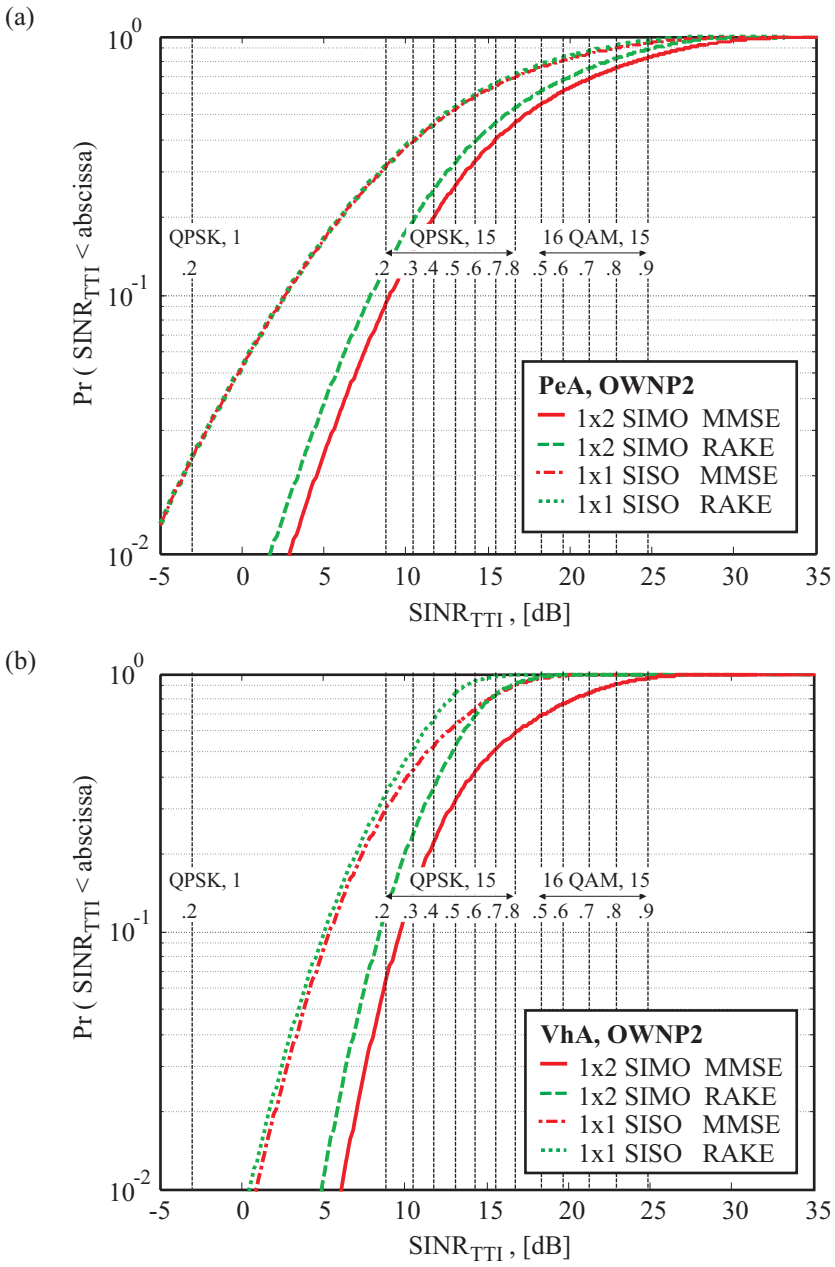

Figure 5.9: SINR statistics of 1×1 SISO and 1×2 SIMO scheme under the OWNP2 interference model as seen over the whole sector area.

exploit interference colouring through spatial interference suppression. This is reflected through the fact that all its array gains in Table 5.7 are larger than 3 dB. The MMSE receiver encounters the highest array and spatial interference suppression gain in the VhA OWNP2 situation, where the RAKE receiver suffers the highest rx correlation penalty. This shows that the interference colouring effects analysed for individual positions in the previous subsection can also be seen when looking at the sector level SINR statistics.

Comparing the 1×1 SISO RAKE and 1×1 SISO MMSE performance cdfs obtained in the PeA environment, *i.e.* Figure 5.9, (a), it can hardly be seen that the MMSE receiver has IPI suppression capabilities. As indicated in Table 5.7, the total sector mean SINR benefit over the SISO RAKE receiver is 0.59 and 0.75 dB for the AWGN and OWNP2 model respectively. The reason for this relatively small difference between RAKE and MMSE is that only very little IPI is present in the weakly frequency selective PeA environment. On the other hand, comparing SISO RAKE and SISO MMSE receiver SINR cdfs in the more frequency selective VhA environment of Figure 5.9 (b), it can be seen that IPI suppression gain leads to a clearly visible MMSE reception advantage over RAKE reception, especially pronounced at the top end of the SINR distribution. Expressed in terms of mean SINR, this benefit amounts to around 2 dB.

Similar IPI gain results can also be observed for the 1×2 SIMO case. However, in this dual rx antenna case the IPI suppression gain is encountered jointly with array gain and spatial interference suppression gain, leading to a mean SINR advantage of the dual antenna MMSE over the dual antenna RAKE receiver ranging from 0.8 dB up to 4.87 dB in the weekly frequency selective PeA AWGN and the highly frequency selective VhA OWNP2 environment respectively.

Further, recalling the effects of other-sector interference multipath fading, as discussed in Subsection 5.3.1, the gain of the mean SINR under the OWNP2 model over the mean SINR under the AWGN model shows that the AWGN model underestimates the mean SINR.

Before looking at the obtainable sector throughput, approximations of the post PF scheduling SINR cdfs are presented in Figure 5.10 for the PeA environment. The post PF scheduling cdf approximations are obtained through combination of the individual trace SINR cdfs taken to the power of the multi-user selection diversity order. This corresponds to approximating the PF scheduling as selection diversity mechanism as introduced in Subsection 2.2.5. It can be seen that PF scheduling causes a considerable shift of the mean SINR operation point. For example, it can be seen that after PF scheduling and in connection with RAKE reception 30% of the users are able to support the highest MCS with all 15 multicodes. Upgrading all UEs with MMSE receivers would not make any significant difference to those upper 30% as they are pushed out of the system's dynamic range.

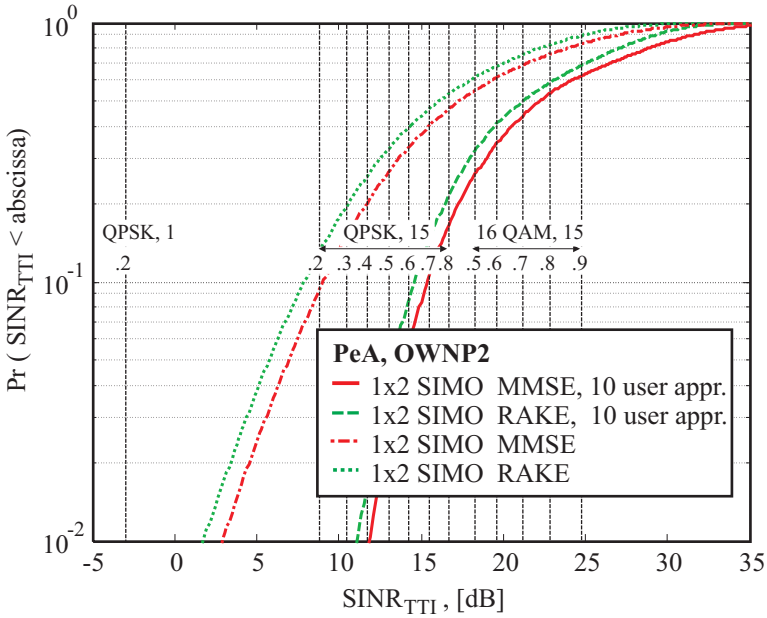

Figure 5.10: Approximation of post PF scheduling 1×2 SIMO SINR statistics for a user diversity order of 10 and pre-scheduling reference statistics.

After this example on how PF scheduling can affect the post scheduling SINR distribution, the sector throughput performance results are presented in Table 5.8. Unless explicitly mentioned the following discussion relates to the results under the OWNP2 model only. Further, sector throughput gains are frequently given in form of ratios. A gain of one, for example, indicates that two different set-ups relate to the same amount of sector throughput. A gain of two means that one set-up has 100% gain over the other.

It can be seen that a network deploying a RR scheduling strategy can, in connection with RAKE UE, obtain roughly 70% gain from an extra receive antenna, while a network with MMSE UE would obtain around 100% gain. These gains through an additional rx antenna are independent of the frequency selectivity of the environment. However, the link level results from Figure 5.9 suggest that the reasons behind the sector throughput gains in PeA and VhA are different. The PeA environment offers little inherent frequency diversity protection. Adding another receive antenna benefits in this case especially users in a poor situation, while an extra receive antenna for users already in a good situation pushes their SINR out of the systems dynamic range so that they hardly benefit in terms of throughput. In the VhA environment, on the other hand, the diversity order of the system is due to frequency diversity already much higher than in the PeA environment, while the mean SINR operation point of the system, as given in Table 5.7, is roughly 5 dB lower due to IPI . In such a situation not the antenna diversity advantage, but the mean array gain is the driving force behind the sector throughput gain.

Scheduler	PDP	1×1 SISO				1×2 SIMO			
		RAKE		MMSE		RAKE		MMSE	
		AWGN	OWNP2	AWGN	OWNP2	AWGN	OWNP2	AWGN	OWNP2
		Sector throughput, [Mb/s]							
RR	PeA	1.54	1.73	1.54	1.76	2.84	3.07	2.93	3.62
	VhA	1.07	1.25	1.32	1.43	2.14	2.14	2.60	3.10
PF	PeA	2.84	3.38	2.89	3.38	4.07	4.55	4.11	5.13
	VhA	1.63	1.76	1.83	2.13	2.63	2.77	3.18	3.77
		Gain of 1×2 SIMO over 1×1 SISO, [-]							
RR	PeA	–	–	–	–	1.84	1.77	1.90	2.06
	VhA	–	–	–	–	1.99	1.71	1.97	2.17
PF	PeA	–	–	–	–	1.43	1.35	1.42	1.52
	VhA	–	–	–	–	1.61	1.57	1.74	1.77
		Gain of MMSE over RAKE, [-]							
RR	PeA	–	–	1.00	1.02	–	–	1.03	1.18
	VhA	–	–	1.23	1.14	–	–	1.21	1.45
PF	PeA	–	–	1.02	1.00	–	–	1.01	1.13
	VhA	–	–	1.12	1.21	–	–	1.21	1.36
		Gain of OWNP2 over AWGN, [-]							
RR	PeA	–	1.12	–	1.14	–	1.08	–	1.24
	VhA	–	1.17	–	1.08	–	1.00	–	1.19
PF	PeA	–	1.19	–	1.17	–	1.12	–	1.25
	VhA	–	1.08	–	1.16	–	1.05	–	1.19
		Gain of PF over RR, [-]							
RR	PeA	–	–	–	–	–	–	–	–
	VhA	–	–	–	–	–	–	–	–
PF	PeA	1.84	1.95	1.88	1.92	1.43	1.48	1.40	1.42
	VhA	1.52	1.41	1.39	1.49	1.23	1.29	1.22	1.22

Table 5.8: 1×1 SISO and 1×2 SIMO sector throughput.

Looking in Table 5.8 at the sector throughput gain of a second receive antenna when the network is deploying a PF scheduling strategy, it can be seen that the gain, ranging from 35% to 77%, is generally reduced. Further, while under the RR scheduler the rx antenna gains were approximately the same in the PeA and the VhA environment, under the PF scheduling strategy rx antenna gains are considerably lower in the PeA environment. This is explained by the fact that the PF scheduler, as indicated by Figure 5.10, brings a considerable amount of diversity to the system, which on the other hand leads to diminishing rx antenna diversity returns. Moreover, multi-user selection diversity shifts the system's SINR operation point upwards. This shift combined with antenna array gain causes a large number of users to receive their data packets with very high, if not the highest MCS-multicode option, which, as seen from Figure 2.5, implies a very inefficient SINR to throughput mapping. This is confirmed by network simulation statistics showing that 37% of the data packets in the RAKE scenario and 44% of data packets in the MMSE scenario are sent using 16 QAM modulation.

Deploying an extra rx antenna in connection with PF scheduling, but in the VhA environment is from a sector throughput point of view more interesting than in the PeA environment, as the lower SINR operation point in the VhA environment leads to a more efficient rx antenna array gain to sector throughput map. Network simulation statistics revealing that for the RAKE and the MMSE scenario only 10% and 27% of data packets are sent with a higher order 16 QAM modulation confirm this assessment.

Looking at the sector throughput gain of the MMSE receiver scenario over the RAKE receiver scenario with numbers ranging from 0% to 45%, it becomes ap-

parent that the in parts impressive mean SINR gain numbers in Table 5.7, ranging from 0.59 dB (15%) to 4.87 dB (207%), cannot efficiently be mapped into sector throughput gain. The low gain number for the SISO case in the PeA environment can be related to the relatively low SINR gains in this weakly frequency flat fading environment. To explain why MMSE reception in the 1×2 SIMO case in the PeA environment, and in all SISO and SIMO cases in the VhA environment cannot even come close to the link level gains, a low and high G-factor SINR performance analysis was performed. It revealed that the most impressive SINR gains of the MMSE receiver are obtained for high G-factors. Users with high G are, however, likely to operate already far up in the dynamic range of the system, with the consequence that additional MMSE gains are not very effectively mapped to sector throughput. In the low G-factor positions, where an SINR increase relates nearly linearly to sector throughput, MMSE receiver performance tends to be similar to RAKE receiver performance. If one would have to trade-off dual antenna rx receiver complexity against single antenna MMSE receiver complexity, the absolute sector throughput gain numbers from Table 5.8 suggest to go for the dual rx antenna RAKE receiver solution. A similarly clear conclusion could not have been drawn from the absolute sector mean SINR numbers in Table 5.7 alone, where the results for dual rx RAKE and single rx MMSE are very close, especially for the VhA environment.

Comparing finally the sector throughput numbers obtained under the OWNP2 and the AWGN other-sector interference model it can be seen that the differences become relatively small, with a worst case underestimation of 25% through the much simpler AWGN model. These findings lead to the conclusion that at least in the SISO and also in the 1×2 SIMO RAKE case the simpler AWGN model suffices for approximate sector throughput estimation, whereas in the SIMO MMSE receiver case the OWNP2 model is preferable.

Besides presenting link and network performance numbers of the 1×2 SIMO scheme, this subsection outlined how link level gains map to sector throughput. In short, link level gains at the lower tail of the SINR distribution map approximately linearly into sector throughput. Link level gains enhancing specifically the SINR fading peaks, *i.e.* the upper tail of the SINR distribution, relate to higher order modulation and coding schemes and translate therefore less efficiently to sector throughput. In conclusion it is from a sector throughput point of view in the first place desirable to use diversity measures such as PF scheduling or rx diversity before additionally considering MMSE equalisation. Figure 5.11 condenses the findings of this subsection into expected sector throughput gains when upgrading the 1×1 SISO RAKE baseline scenario with RR scheduling by an additional rx antenna, MMSE reception and PF scheduling.

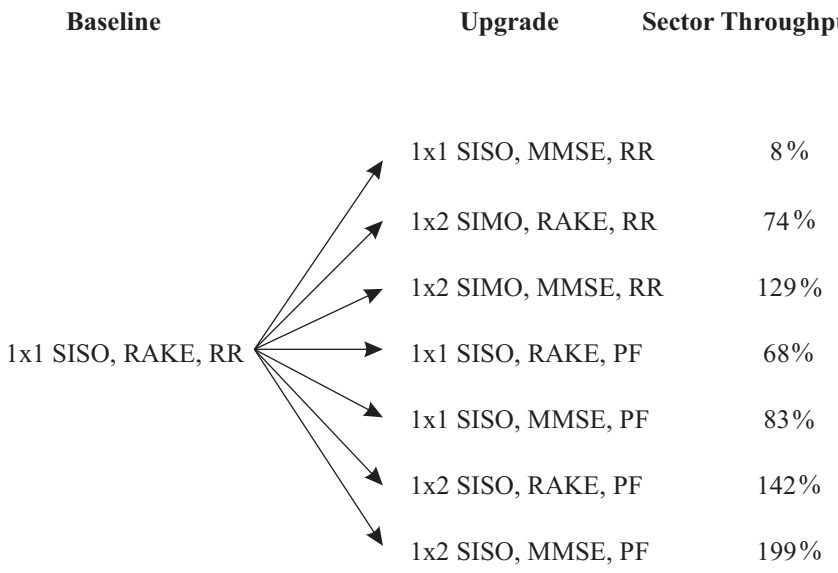

Figure 5.11: Sector throughput gain through upgrading the 1×1 SISO RAKE RR scenario. [1]The sector throughput gain is calculated as the average of the gains in the PeA and the VhA environment and for the OWNP2 model.

5.5 2×1 CLM1

The key question when deploying 2×1 CLM1 is which benefits can be obtained from the additional antenna with respect to a simpler 1×1 SISO configuration? To answer this question the following is split into two Subsections. Subsection 5.5.1 looks at link level effects in connection with the additional tx antenna. Subsection 5.5.2 looks at the impact of CLM1 SINR gains on sector throughput.

5.5.1 Tx Correlation - Trading Off Array Gain and Tx-Diversity

While a lot of research has been done in connection with CLM1, for example with respect to mobile speed and feedback errors, *e.g.* [Hama01b], [Gerl02], [Rami03a], the majority of contributions assumes uncorrelated tx antennas. The aspect of correlated tx antennas is less widely explored, which is the reason why this subsection particularly focuses on the difference incurred when the tx antenna spacing is varied from 10 wavelengths to 0.5 wavelength. Under the particular angular characteristics of the selected scenario this corresponds to tx correlation magnitudes in the order of 0.1 and 0.98 respectively. As the link level effects encountered in the lightly frequency selective PeA environment differ significantly from the effects in the much more frequency selective VhA environment, the following firstly looks at the link level performance in the weakly and the highly correlated PeA environment before turning the view to the weakly and the highly correlated VhA

environment.

The SINR cdfs collected for the lG position, the hG position, and over the whole sector area are plotted in Figure 5.12. The corresponding cdfs of the SISO cases serves as reference. Further, the SINR mean gains over SISO are given in Table 5.9. Comparing the slopes of the SISO cases and the slopes of the 2×1 CLM1 cases under hc, it can be seen that they appear to be rather similar. This indicates that due to the high tx correlation the 2×1 CLM1 configuration is not able to experience tx diversity. However, it can also be seen that the highly correlated 2×1 CLM1 case experiences a clear sector mean SINR gain, which through a look at Table 5.9 is found to range from 2.08 dB to 2.23 dB. On the other hand, the weakly correlated 2×1 CLM1 configuration can benefit from tx diversity. This is reflected through the steeper slopes of the corresponding SINR cdfs in Figure 5.12. Further, the mean SINR gain on sector level is from Table 5.9 found to range from 2.26 dB up to 2.43 dB. It is thus marginally higher than for the highly correlated antennas.

To obtain analytical bounds for the simulation results, the 2×1 CLM1 performance in uncorrelated flat Rayleigh fading and with AWGN other-sector interference, as presented in Appendix A.1.3, is recalled [Gerl02]

$$\begin{aligned} \beta_{2\times 1 CLM1} &= \left(1 + \frac{1}{\sqrt{2}}\right) \\ &\approx 2.32 \text{ dB} \end{aligned} \quad . \tag{5.7}$$

CLM1 is effectively an EGC scheme with additional phase restrictions. The EGC gain is [Jake94, (5.2-20)]

$$\begin{aligned} \beta_{2\times 1 EGC} &= \left(1 + \frac{\pi}{4}\right) \\ &\approx 2.52 \text{ dB} \end{aligned} \quad , \tag{5.8}$$

so that the pure phase penalty turns out to be

$$\beta_{\substack{2\times 1 CLM1, \\ 2\times 1 EGC}} \approx -0.2 \text{ dB} \quad . \tag{5.9}$$

With low tx correlation it is likely that the physical channel power from one antenna is higher than from the other. This makes an equal power split sub-optimum in uncorrelated channels. Increasing the tx correlation, the equal tx power split between the tx antennas becomes more and more optimum, approaching the expected gain of the tx MRC plus a phase granularity degradation. Using this argumentation the expected gain of CLM1 with high tx correlation is approximated as

$$\begin{aligned} \beta_{2\times 1 CLM1\_hc} &= \beta_{1\times 2 SIMO} \cdot \beta_{\substack{2\times 1 CLM1, \\ 2\times 1 EGC}} \\ &\approx 2.82 \text{ dB} \end{aligned} \quad . \tag{5.10}$$

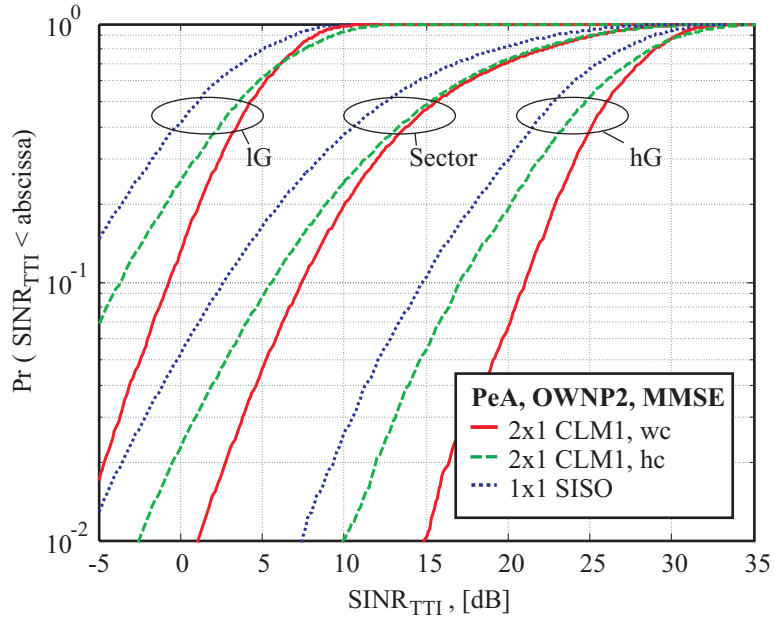

Figure 5.12: 2×1 CLM1 SINR cdfs for *weakly correlated* (wc) and *highly correlated* (hc) tx antennas and the PeA environment. The SISO cdfs serve as reference.

Pos.	**Tx corr.**	**RAKE**		**MMSE**	
		AWGN	**OWNP2**	**AWGN**	**OWNP2**
		Gain of 2×1 CLM1 over 1×1 SISO, [dB]			
lG	**wc**	2.24	2.21	2.24	2.21
	hc	2.47	2.51	2.48	2.51
hG	**wc**	2.11	2.10	2.11	2.01
	hc	1.75	1.65	1.95	1.81
Sector	**wc**	2.43	2.33	2.38	2.26
	hc	x	2.08	x	2.23

Table 5.9: 2×1 CLM1 mean SINR link performance numbers compared to SISO in the PeA environment. 'x' indicates that the simulation result has not been obtained.

Comparing specifically the mean SINR gain results in Table 5.9 for lG wc with the expected result from (5.7), a good match between simulation and analytical expectation is obtained. Comparing further the results for lG hc with the approximation for high correlation in (5.10), it can be observed that the analytical expression delivers the right trend, *i.e.* tx correlation increases the mean SINR gain. However, looking at the gains in the hG position and on sector level, it is found that instead of increasing mean gain, higher tx correlation actually has a slightly negative effect on the mean SINR performance. This can be explained revisiting the SINR cdfs in Figure 5.12. It is found that due to high tx correlation in hG and over whole sector area, tx diversity is lost. On the other hand, even in this weakly frequency selective PeA environment, IPI effects do not allow the exploitation the full fading peak benefit initially envisaged by high tx correlation, which explains the slight loss from increased tx correlation. This is also supported by the fact that the mean SINR for the RAKE receiver suffers more than the mean SINR of the MMSE.

Turning to the more frequency selective VhA environment, the obtained simulation results are given in Figure 5.13 and Table 5.10. Looking at the SINR cdfs it can again be seen that the CLM1 hc cases have similar slopes as the corresponding SISO cases. This shows that they have approximately the same diversity order. No additional tx diversity is obtained from CLM1 hc. However, CLM1 hc obtains a mean gain over SISO. Looking at the cdfs for CLM1 wc it can be seen that their diversity order is higher than the one of their CLM1 hc counterparts. However, the probability of encountering high fading peaks is at the same time reduced. This leads, for example, to a situation where CLM1 wc hG, over large parts of the cdf, appears to perform worse than the corresponding SISO scheme. Looking at the mean SINR performance relative to SISO as given in Table 5.10, it can be seen that in this specific situation CLM1 actually causes a mean SINR performance loss. Generally, the mean SINR gains of CLM1 are significantly reduced when compared with the gains in the PeA environment of Table 5.9. To explain this behaviour, it is recalled that the initial aim of CLM1 is to adjust the phase of the transmitted signals as to co-phase the signal components at the receiver, thus maximising the received power. In the flat fading situation such a task is relatively simple. Only the phase of a single flat fading component needs to be adjusted to match the other. In a frequency selective fading situation the signal from each tx antenna will reach the receiver through multiple delayed components, each with a random phase. To co-phase all delayed components would ideally require the option to individually phase weight every one of them. As only one common phase weight can be applied, the weight selection is not ideal for co-phasing the individual components. This leads to generally decreased performance in frequency selective environments. The expected SINR gain in a frequency selective environment for uncorrelated tx antennas and in connection with a RAKE receiver is on the basis of [Hama02], [Hott03, (11.40)] given as

$$\beta_{2\times 1 CLM1\_VhA\_wc} \approx 1.67 \text{ dB} \quad , \tag{5.11}$$

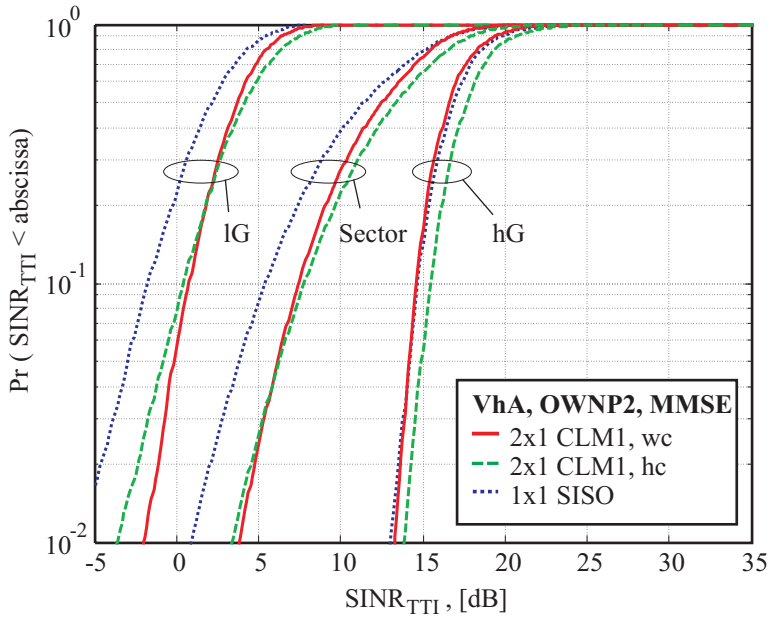

Figure 5.13: 2×1 CLM1 SINR cdfs for *weakly correlated* (wc) and *highly correlated* (hc) tx antennas and the VhA environment. The SISO cdfs serve as reference.

Pos.	Tx corr.	RAKE		MMSE	
		AWGN	OWNP2	AWGN	OWNP2
		Gain of 2 × 1 CLM1 over 1 × 1 SISO, [dB]			
lG	wc	1.60	1.44	1.60	1.40
	hc	2.19	2.03	2.22	2.06
hG	wc	0.74	0.71	-0.11	-0.36
	hc	0.76	0.74	0.98	0.82
Sector	wc	1.08	1.03	0.62	0.46
	hc	x	1.33	x	1.54

Table 5.10: 2 × 1 CLM1 mean SINR link performance numbers compared to SISO in the VhA environment. 'x' indicates that the simulation result has not been obtained.

which is outlined in more detail in Appendix A.3.3.

Looking in Table 5.10 at the mean SINR gain obtained in the lG wc case it can be seen that the results match well the analytical prediction of (5.11). However, when looking at the hG wc case or at the wc sector performance, it can be seen that the gains stay below the prediction. This can be explained by the weight selection criterion given in (4.10). It maximises the received signal power. Hence, it also maximises the received IPI from the desired HS-DSCH. If this IPI contributes with a significant part to the overall interference level, there is only very little to be gained from CLM1. The effect is significant in HSDPA, as a large part of the own sector power might be allocated to the HS-DSCH channel with the consequence that a large part of the own sector IPI is maximised at the UE.

Turning to the hc cases, it can be seen that high tx correlation generally increases the mean SINR gain. This is due to the fact that the even power split is more optimal in connection with tx correlation. Further, the VhA environment brings significant amounts of inherent frequency diversity, which is the reason why tx diversity loss due to higher tx correlation can be compensated.

It remains to look at the negative mean gains obtained in hG wc in connection with MMSE. For hG the MMSE receiver in a SISO situation approaches the performance of a zero forcer [Fran02]. It is thus able to remove nearly all IPI through channel inversion. If CLM1 is used, six virtual channels are active in the sector, and equalisation becomes more difficult. In connection with a generally small expected mean gain for the wc case, CLM1 can therefore cause a loss at high G-factors. On the one hand, for the hc situation the expected mean gain is higher, and on the other hand, the equalisation problem becomes easier to manage, which will be looked at in more detail in connection with the 2×2 CLM1 case.

It was shown that tx correlation has the potential to increase the array gain at the expense of tx diversity protection. Whereas the question whether tx correlation is beneficial is undecided for the nearly flat fading PeA environment, the results from Figure 5.13 and Table 5.10 indicate that tx correlation is desirable in connection with frequency selective fading, where loss of antenna diversity is compensated by frequency diversity. The following subsection shows how tx correlation affects network level performance.

5.5.2 Effects of Tx Correlation on Sector Throughput

Table 5.11 gives the sector throughput gains of 2×1 CLM1 wc and hc over the corresponding 1×1 SISO cases. It shows around 55% gain in connection with the RR scheduler and the PeA environment. This gain appears independent of receiver type and tx correlation. It is reduced to around 27% in the more frequency selective

			RAKE		MMSE	
			AWGN	**OWNP2**	**AWGN**	**OWNP2**
			Gain over 1×1 SISO, [-]			
RR	**PeA**	**wc**	1.66	1.58	1.66	1.56
		hc	x	1.54	x	1.55
	VhA	**wc**	1.42	1.25	1.30	1.30
		hc	x	1.40	x	1.49
PF	**PeA**	**wc**	1.35	1.20	1.30	1.21
		hc	x	1.32	x	1.35
	VhA	**wc**	1.19	1.16	1.19	1.11
		hc	x	1.32	x	1.34

Table 5.11: Sector throughput gain of 2×1 CLM1 over 1×1 SISO.

VhA environment and wc, but can be raised again to around 45% in the hc case. Although 2×1 CLM1 sector throughput gain is generally lower in connection with the PF scheduler, the gain trends for PF and RR scheduler are similar. At the lower end a sector throughput gain of only 11% is obtained in VhA wc and with MMSE receiver. This gain can be raised to 34% by going to hc.

Recalling the SINR results from the previous subsection, only in the PeA environment, it was not entirely clear if increased tx correlation would have a positive or negative effect on network level performance. Comparing the sector throughput for wc and hc in connection with the RR scheduler, it can be seen, that the wc cases perform marginally better. However, in connection with the PF scheduler, the hc cases have a clear advantage. To explain this behaviour the obtained SINR cdfs are plotted in Figure 5.14 jointly with their post PF scheduling approximation. It can be seen that for a multi user selection diversity of 10 the SINR statistics for hc turn out to be generally superior to those obtained for wc. The reason is that multi-user selection diversity emphasises the fading peaks and gives diversity protection against deep fades, with the result that tx diversity protections is not required.

Trading off the marginal losses caused by higher tx correlation in the PeA environment and under RR scheduling against the potential gains achieved through higher tx correlation in all other cases, a conclusion is that increased tx correlation has a positive effect on CLM1 network performance.

5.6 2×2 CLM1

Many effects encountered in connection with 2×2 CLM1 are already known from the 2×1 CLM1 and the 1×2 SIMO cases. However, 2×2 CLM1 is a MIMO situation, where the tx weights need to be matched to two rx antennas. This is

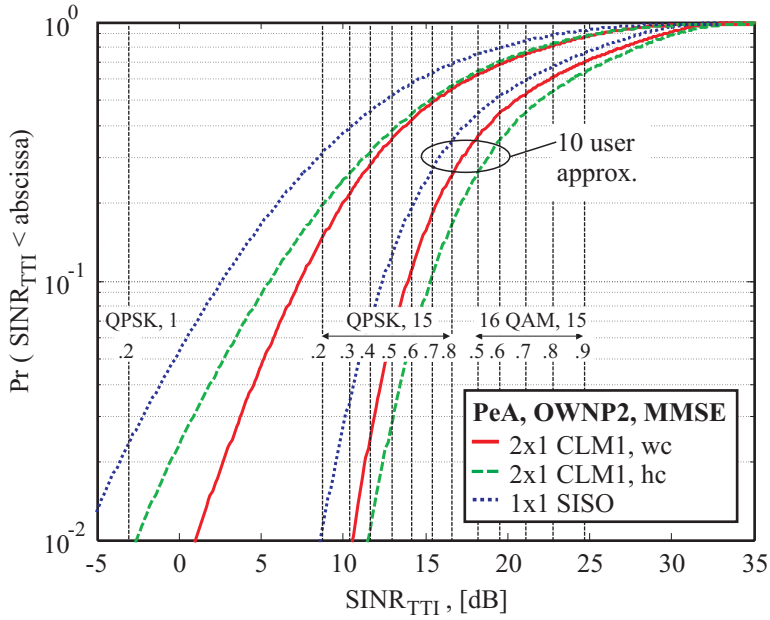

Figure 5.14: 2×1 CLM1 SINR cdfs in PeA for wc and hc and their 10 user selection diversity approximation. The SISO cdfs serve as reference.

in connection with a general CLM1 gain overview discussed in Subsection 5.6.1. Issues of MMSE equalisation and interference suppression are discussed in Subsection 5.6.2.

5.6.1 Tx Weight Matching to Two Rx Antennas

The tx weights are selected as to maximise the received power over both rx antennas. For weakly correlated tx antennas this leads to a situation where the selected weight set is not always optimum with respect to any individual rx antenna. A similar situation was already discussed in Subsection 5.5.1, where in connection with VhA the tx weights needed to be matched to several delayed multipath components. The following looks at the PeA environment to avoid overlap with multipath weight matching effects. The obtained mean SINR gains in the lG and hG position as well as seen over the whole sector area are collected in Table 5.12.

Additionally, to obtain analytical bounds an uncorrelated flat Rayleigh fading situation, with AWGN other-sector interference, is considered. In this situation the mean gain of 2×2 CLM1 can be calculated on the basis of [Hama01a], [Hott03,

		RAKE		MMSE	
		AWGN	**OWNP2**	**AWGN**	**OWNP2**
		Gain of 2x2 CLM1 over 1x1 SISO, [dB]			
lG	**wc**	4.82	4.55	4.82	5.07
	hc	5.35	5.28	5.35	6.05
hG	**wc**	4.58	4.23	4.88	5.17
	hc	4.49	4.30	5.25	6.01
Sector	**wc**	4.98	4.62	5.11	5.52
	hc	x	4.92	x	6.56

Table 5.12: Mean SINR gain of the 2×2 CLM1 over 1×2 SIMO in PeA.

(11.41)] as

$$\begin{aligned} \beta_{2\times 2CLM1} &= 2 + \frac{3}{32} \cdot \pi^2 \\ &\approx 4.66 \text{ dB} \end{aligned} \quad , \tag{5.12}$$

with more details provided in Appendix A.1.5. For correlated tx antennas the mean gain is expected to lie between

$$\begin{aligned} \beta_{2\times 2CLM1\_hc\_lower} &= \beta_{2\times 1CLM1} \cdot \beta_{1\times 2SIMO} \\ &\approx 5.33 \text{ dB} \end{aligned} \quad , \tag{5.13}$$

and

$$\begin{aligned} \beta_{2\times 2CLM1\_hc\_upper} &= \beta_{2\times 1CLM1\_hc} \cdot \beta_{1\times 2SIMO} \\ &\approx 5.83 \text{ dB} \end{aligned} \quad , \tag{5.14}$$

where $\beta_{2\times 1CLM1}$ and $\beta_{2\times 1CLM1\_hc}$ were introduced in Subsection 5.5.1. The lower and upper approximations of (5.13) and (5.14) are based on the fact that with correlated tx antennas it is possible to match the tx weights to two rx antennas [Ande00].

The gains for the MMSE receiver under the OWNP2 model cannot be compared with the analytical predictions as the predictions do not account for the MMSE receiver's other-sector interference suppression capabilities. For the RAKE receiver the wc cases are found to be well approximated by (5.12). Apart from the AWGN hG position increasing the tx correlation increases the mean SINR gain, which follows the predictions in (5.13) and (5.14).

Table 5.13 summarises the mean SINR and sector throughput results. While the benefit of tx correlation was partially undecided in PeA and for 2×1 CLM1, the results for 2×2 CLM1 show a clear benefit through tx correlation. This is not only due to the higher mean SINR gain for correlated tx antennas, but also due to the fact that a loss of tx diversity can be compensated through rx diversity.

	2×1 **CLM1**			2×2 **CLM1**		
	wc		**hc**	**wc**		**hc**
	Mean SINR gain over SISO, [dB]					
RAKE	2.33	$>$	2.08	4.62	$<$	4.92
MMSE	2.26	$\approx$	2.23	5.52	$<$	6.56
	Sector throughput gain over SISO, [–]					
RAKE, RR	1.58	$\approx$	1.53	2.32	$<$	2.53
RAKE, PF	1.20	$<$	1.32	1.51	$<$	1.71
MMSE, RR	1.56	$\approx$	1.54	2.62	$<$	2.95
MMSE, PF	1.21	$<$	1.34	1.66	$<$	1.96

Table 5.13: CLM1 gain overview in the PeA environment and under the OWNP2 model.

5.6.2 Tx Correlation, Equalisation and Interference Suppression

To assess the benefit of 2×2 CLM1 the simpler 1×2 SIMO case is throughout this subsection used as reference. The mean SINR gains of the MMSE in VhA are given in Table 5.14. While for 2×2 CLM1 hc performs better than 1×2 SIMO, Table 5.14 also shows that for 2×2 CLM1 wc actually inflicts an SINR loss in the hG position and seen over the whole sector area. This can be explained by the fact that, on one hand, as separately seen in Subsection 5.5.1 and Subsection 5.6.1, frequency selectivity and weak tx correlation do not allow to take a lot of benefit from the additional tx antenna. On the other hand, as already seen in Table 5.10, multiple virtual channels are experienced as multiple sources of interference, forming a more difficult equalisation problem for the MMSE receiver.

If the tx correlation is high, the virtual channels in the own sector, appear more distinct. Seen from an interference covariance matrix point of view, the eigenvalue spread increases with tx correlation. Simulations at a G-factor of 16 dB, for example, deliver in the hc case an average condition number that is found to be around 3.5 times higher than in the wc case. The higher eigenvalue spread can be

		AWGN	**OWNP2**
		Mean SINR Gain of 2×2 CLM1 over 1×2 SIMO, [dB]	
lG	wc	1.25	1.02
	hc	2.19	2.11
hG	wc	-1.27	-2.01
	hc	1.29	0.93
Sector	wc	-0.02	-0.64
	hc	x	1.78

Table 5.14: Mean SINR gains of the 2×2 CLM1 schemes in VhA and with MMSE reception over their 1×2 SIMO counterparts. 'x' indicates that the simulation result has not been obtained.

positively exploited by the MMSE receiver, which can be seen when revisiting the SINR expression from (3.41)

$$SINR_M^{K,I} \left| \begin{array}{l} idealest \\ MMSE \end{array} \right. \propto \sum_{e=1}^{N_{FIR} \cdot N_{rx}} \frac{|u_e|^2}{\lambda_e} \quad . \tag{5.15}$$

A higher eigenvalue spread relates to an increased probability of encountering low eigenvalues, and as seen in (5.15) low eigenvalues, λ_e, boost the overall SINR.

It remains to be seen whether the inferior 2×2 CLM1 wc performance with respect to the simpler 1×2 SIMO case also leads to a loss on network level. For this purpose the absolute mean SINRs of both schemes as well as their 10 user mean SINR approximation and their sector throughputs are collected in Table 5.15. As can be seen, the inferior mean SINR performance does not lead to an inferior sector throughput performance. To understand this initially counter intuitive behaviour, the SINR cdfs of both cases are shown in Figure 5.15 including their 10 multi-user selection diversity approximation.

It can be seen that due to simpler equalisation, the 1×2 SIMO case can obtain higher fading peaks. These peaks cause the higher mean SINR. On the other hand the 2×2 CLM1 scheme can especially at the lower tail of the distribution benefit from tx diversity. Relating these observations to the modulation and coding schemes indicated through the vertical grid, it can be seen that the high fading peaks of the 1×2 SISO scheme actually relate to the part of the system's dynamic range, where SINR gain does not efficiently translate into sector throughput. The tx diversity gains of the 2×2 CLM1 scheme, however, relate to the part of the system's dynamic range where SINR gains map approximately linearly into sector throughput. This explains the superior performance of 2×2 CLM1 on network level.

The example shows that sector mean SINR can give an indication of a network performance, *i.e.* most of the time schemes with a higher mean SINR will also perform superior in terms of sector throughput, but especially when a scheme creates high fading peaks that exceed the system's dynamic range this rule of thumb has to be treated very carefully.

	1×2 **SIMO**		2×2 **CLM1 wc**
Sector mean SINR, [dB]	18.67	>	17.93
Sector mean SINR, 10 user appr., [dB]	21.47	>	20.38
Sector throughput, RR, [Mb/s]	3.10	<	3.42
Sectro throughput, PF, [Mb/s]	3.77	<	3.89

Table 5.15: Comparison of link and network performance of 1×2 SIMO and 2×2 CLM1 wc for the OWNP2 model.

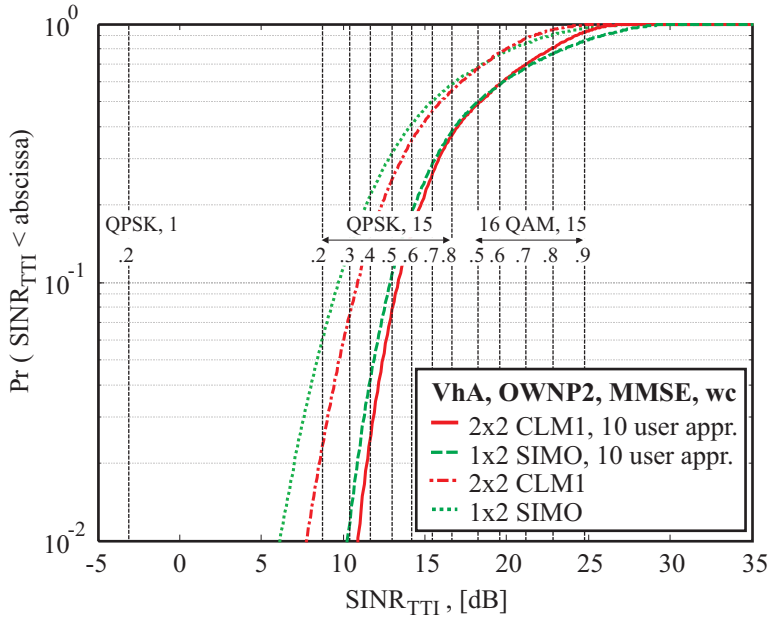

Figure 5.15: 2×2 CLM1 and 1×2 SIMO whole sector SINR cdfs to explain why a higher mean SINR does not necessarily correspond to a higher sector throughput.

5.7 2×2 SMP$_x$

The original SMP$_x$ scheme with full scheduling freedom is split into the subcases SMP$_{sel}$ and SMP$_{dual}$, with the aim of assessing spatial multiplexing performance, using the existing *single stream* HSDPA network simulator. Subsection 5.7.1 and Subsection 5.7.2 present SMP$_{sel}$ and SMP$_{dual}$ performance, respectively.

5.7.1 SMP$_{sel}$ - Setting SMP$_x$ Baseline

Intuitively one might think that SMP$_{sel}$ mean SINR performance is lower bounded by 1×2 SIMO as it should additionally benefit from selection transmit diversity. As derived in Appendix A.1.6, the analytical mean gain of 2×2 SMP$_{sel}$ over 1×1 SISO amounts in an uncorrelated flat Rayleigh fading situation with AWGN other-sector interference to 2.75, *i.e.* around 4.39 dB. Hence in theory the 2×2 SMP$_{sel}$ mean SINR is around 1.38 dB higher than the mean for 1×2 SIMO.

Table 5.16 gives the obtained mean SINR gain of 2×2 SMP$_{sel}$ over 1×2 SIMO. It can be seen that the analytical prediction describes well the RAKE PeA cases. Generally, the SMP$_{sel}$ SINR mean is superior to the SIMO mean, with exception of MMSE reception in VhA, hG or on sector level. To investigate this SMP$_{sel}$ mean SINR loss, the sector SINR cdfs as obtained for VhA MMSE

OWNP2 are displayed in Figure 5.16. Additionally the 10 multi-user selection diversity approximations are plotted. It can be seen that the 1×2 SIMO cdfs have less diversity protection, reflected through their less steep slopes. However, they exhibit considerably higher fading peaks, which cause their average SINR gains. Recalling the 2×2 SMP$_x$ virtual channel mapping matrix introduced in Subsection 4.3.4, it can be seen that although SMP$_{sel}$ receives an HS-DSCH transmission from only the selected virtual channel, a second virtual channel, transmitting parts of the PCPICH, the HS-SCCH, and the DCH channel power, is permanently received with 15% of the total sector power allocation. While in the high SINR regime the MMSE receiver in connection with 1×2 SIMO approaches the zero forcer, thus suppressing approximately all own sector IPI, the power received over

PDP	Pos.	RAKE		MMSE	
		AWGN	OWNP2	AWGN	OWNP2
		Mean SINR gain of 2×2 SMP$_{sel}$ over 1×2 SIMO, [dB]			
PeA	**lG**	1.36	1.22	1.36	1.01
	hG	1.44	1.30	1.22	0.70
	Sector	1.62	1.30	1.50	0.71
VhA	**lG**	0.88	0.90	0.87	0.65
	hG	0.80	0.68	-1.51	-2.17
	Sector	0.87	0.75	-0.30	-0.90

Table 5.16: Mean SINR gain of 2×2 SMP$_{sel}$ over 1×2 SIMO.

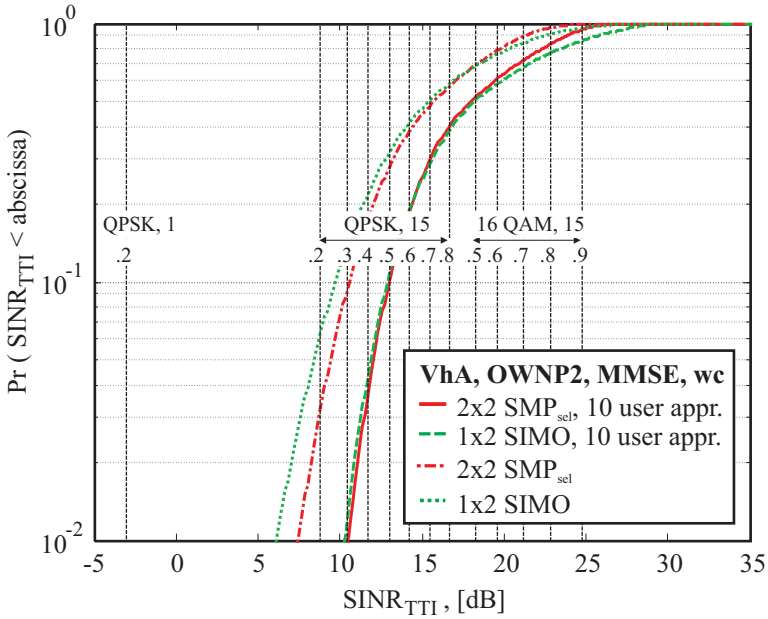

Figure 5.16: 2×2 SMP$_{sel}$ and 1×2 SIMO whole sector SINR cdfs.

the second SMP$_{sel}$ virtual channel forces the MMSE receiver to trade off channel inversion and virtual channel suppression. As already observed for the closed loop transmit diversity schemes, the presence of additional virtual channels renders the equalisation task more difficult, preventing 2×2 SMP$_{sel}$ MMSE from achieving the same high fading peaks as can be achieved in the 1×2 SIMO situation.

To see whether the link level losses of SMP$_{sel}$ relate to losses on network level, the SINR means and the sector throughputs of 1×2 SIMO and 2×2 SMP$_{sel}$ are given in Table 5.17. As can be seen, the superior mean SINR of the 1×2 SIMO scheme in connection with RR does not result in superior sector throughput. In connection with PF scheduling both schemes perform approximately the same.

These results can be explained revisiting the SINR cdf in Figure 5.16. Under the RR scheduler with no multi-user selection diversity, the transmit antenna selection diversity benefit of 2×2 SMP$_{sel}$ leads to SINR gains in the lower part of the system's dynamic range, which means that these gains are very efficiently mapped into sector throughput. On the contrary the high fading peaks of the 1×2 SIMO scheme relate to the upper part of the system's dynamic range, where the benefit of higher SINR decreases. The PF scheduler, however, introduces multi-user selection diversity to the system bringing the lower tails of the 1×2 SIMO and the 2×2 SMP$_{sel}$ scheme very close together so that the sector throughput difference between 1×2 SIMO and the 2×2 SMP$_{sel}$ becomes marginal.

An overview of 1×2 SIMO and 2×2 SMP$_{sel}$ sector throughput is provided in Figure 5.17. It can be seen that in most cases SMP$_{sel}$ brings a small benefit (up to 28%). This shows that SMP$_{sel}$, which was introduced as a subcase of SMP$_x$, sets a baseline for spatial multiplexing performance. Most currently considered spatial multiplexing schemes include the option of adaptively disabling one stream [3GPP04d]. This avoids that in non beneficial spatial multiplexing situations a dual stream transmission creates a loss with respect to SIMO.

	1×2 **SIMO**		2×2 **SMP**$_{sel}$
Sector mean SINR, [dB]	18.67	$>$	17.77
Sector mean SINR, 10 user appr., [dB]	21.47	$>$	20.03
Sector throughput, RR, [Mb/s]	3.10	$<$	3.20
Sectro throughput, PF, [Mb/s]	3.77	$\approx$	3.76

Table 5.17: Comparison of 2×2 SMP$_{sel}$ and 1×2 SIMO link and network performance in the VhA environment in connection with MMSE reception and for the OWNP2 model.

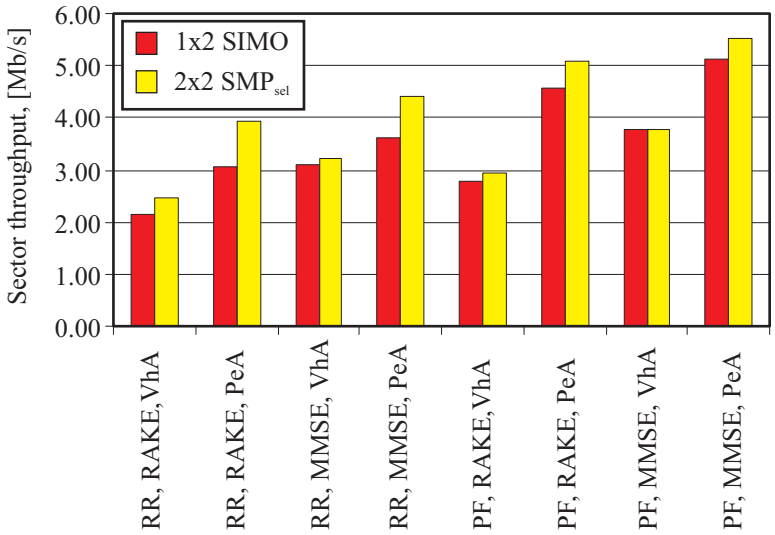

Figure 5.17: Sector throughput comparison between 1×2 SIMO and 2×2 SMP$_{sel}$ for the OWNP2 model.

5.7.2 SMP$_{dual}$ - Impact of Co-stream Transmission

SMP$_{dual}$ is based on the assumption that all available HS-DSCH codes are used on the interfering co-stream. On this simplifying assumption the single stream link adaptation and packet scheduling unit of the current network simulator implementation can operate on the SINR trace of the second stream. This trace is negatively impacted by co-stream interference. The obtained sector throughput numbers are then doubled, this way accounting for the data sent on the first stream.

The interesting question is, what is the price to pay for the ability to use an extra data stream, within the same sector? To answer this question the sector mean SINR gains of SMP$_{dual}$ over SISO and SIMO references are collected in Table 5.18. The negative values show that the mean SINR of SMP$_{dual}$ is in all cases smaller than the reference. The corresponding SINR cdfs under the OWNP2 model and for MMSE reception are displayed in Figure 5.18. Inspecting the slopes of the SINR cdfs in Figure 5.18 it can be seen that SMP$_{dual}$ has a lower tail slope similar to 1×2 SIMO, indicating a similar diversity order. Further, it can be seen that the dual stream cdfs have a significantly lower mean than their SIMO counterparts. The dual stream 'cost' can for the situations in Figure 5.18 be read from Table 5.18. Independent of the degree of frequency selectivity the cost amounts to approximately 6.5 dB. This can be explained through the arguments that a 3 dB power reduction is due to splitting the power between the streams. Additionally, the co-stream causes an interference increase in the order of 3 dB. Moreover, co-stream interference suppression takes up some of the MMSE receivers other-sector interference suppression capability.

PDP	Pos.	RAKE		MMSE	
		AWGN	OWNP2	AWGN	OWNP2
		Gain of 2×2 SMP$_{dual}$ over 1×1 SISO, [dB]			
PeA	**Sector**	-4.15	-4.72	-2.23	-2.34
VhA	**Sector**	-1.08	-1.33	-0.81	-0.93
		Gain of 2×2 SMP$_{dual}$ over 1×2 SIMO, [dB]			
PeA	**Sector**	-7.20	-7.61	-5.49	-6.65
VhA	**Sector**	-3.89	-4.03	-5.60	-6.30

Table 5.18: Mean SINR gain of SMP$_{dual}$ over SISO and SIMO references.

To underline this explanation analytically, the dual stream cost has been derived in Appendix A.2.4 for the uncorrelated flat Rayleigh fading case with AWGN other-sector interference and for MMSE/OPC reception. The obtained analytical bounds were first presented in Figure 2.10 as a function of $\overline{SINR}_{branch}$. In flat fading $\overline{SINR}_{branch}$ can be expressed as a function of the G-factor, *i.e.*

$$\overline{SINR}_{branch} = N_{sf} \cdot \eta^{HSDSCH,i} \cdot G \quad . \tag{5.16}$$

Using (5.16) the analytical bounds are re-plotted in Figure 5.19. Additionally, the obtained simulation results at the individual lG, lDIR, and hG positions are included. Their values are collected in Table 5.19.

It can be seen that the analytical predictions match well the obtained simulation results. Only in the OWNP2 hG case the SIMO and the SMP$_{sel}$ comparisons are a bit further off. This is due to the fact that the analytical predictions are based on the AWGN other-sector interference assumption. Thus they do not account for the other-sector interference suppression benefit obtained in OWNP2 based simulations.

After this look at the cost of dual stream transmission, what is its sector throughput benefit? For OWNP2 MMSE the answer is given in Figure 5.20, where the obtained sector throughputs for SIMO and SMP$_{dual}$ are displayed. Only in the PeA

Pos.	G,	OWNP2			AWGN		
	[dB]	1×1	1×2	2×2	1×1	1×2	2×2
		SISO	**SIMO**	**SMP**$_{sel}$	**SISO**	**SIMO**	**SMP**$_{sel}$
		Mean SINR gain of 2×2 SMP$_{dual}$ over above, [dB]					
lG	-8	-0.16	-3.70	-4.71	-0.27	-3.23	-4.59
lDIR	5	-1.72	-5.16	-6.25	x	x	x
hG	16	-2.99	-7.19	-7.89	-3	-6.23	-7.45

Table 5.19: Cost of dual stream transmission in PeA wc at the individual positions lG, lDIR and hG. 'x' indicates that the simulation result has not been obtained.

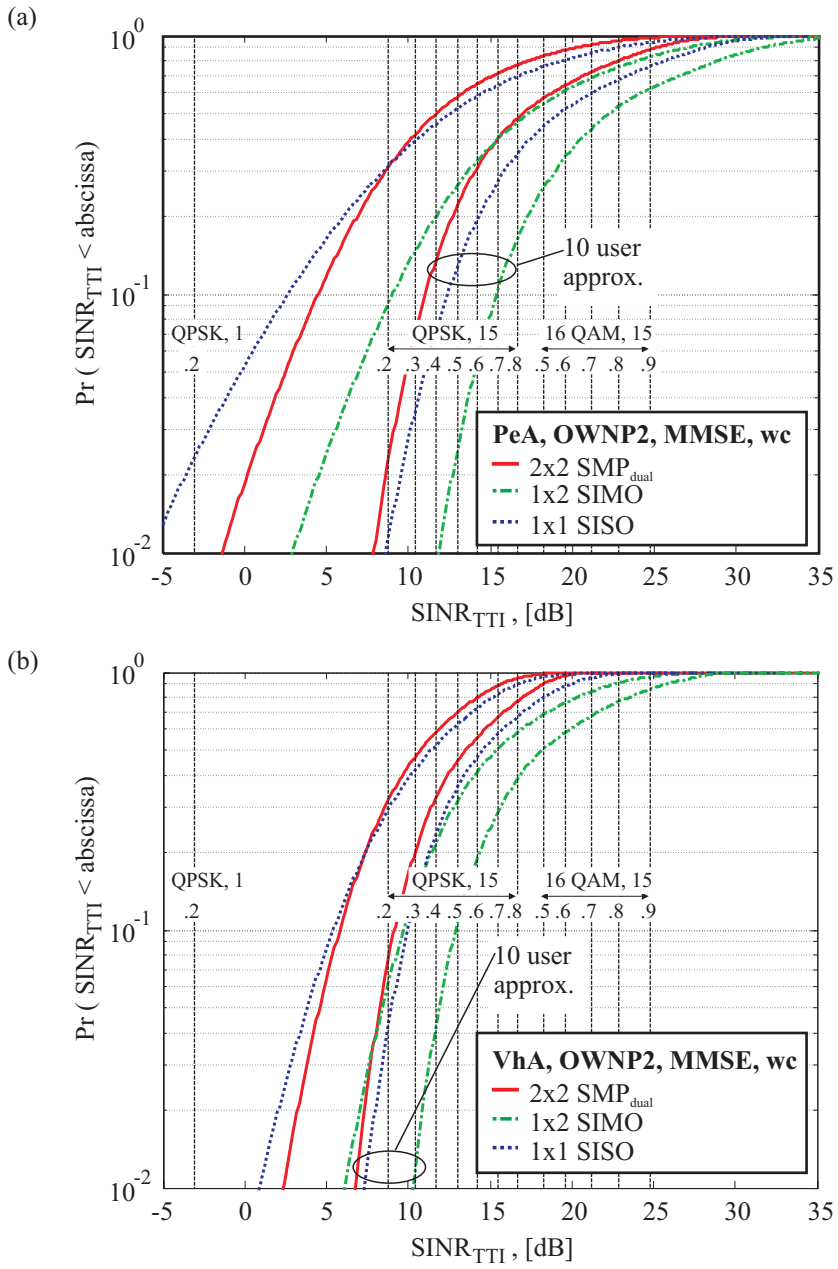

Figure 5.18: 2×2 SMP_{dual} SINR statistics as encountered over the whole sector area in (a) PeA and (b) VhA. 1×1 SISO and 1×2 SIMO serve as reverences.

case and in connection with PF scheduling SMP_{dual} can obtain a sector throughput benefit.

This can be explained as follows: Dual stream transmission is expensive in terms of mean SINR. As long as single stream SINR can be mapped efficiently

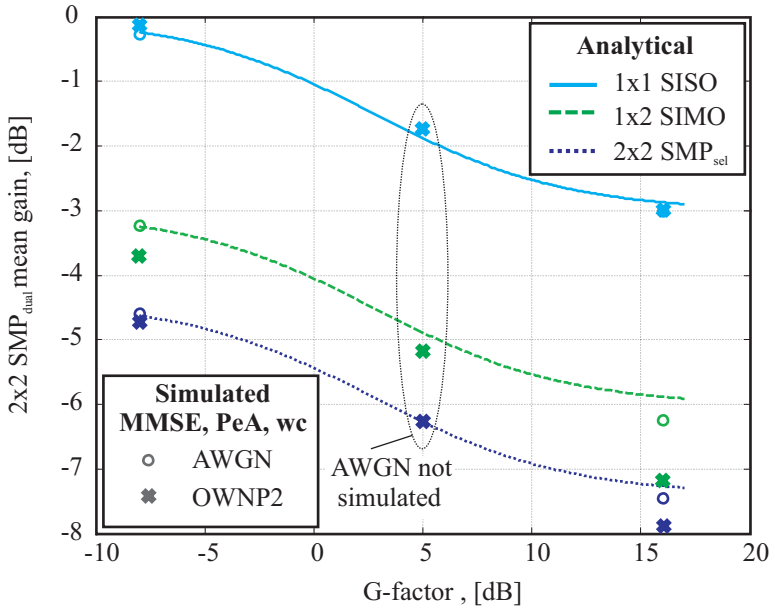

Figure 5.19: Cost of dual stream transmission. Comparison between analytical results in uncorrelated flat Rayleigh fading and simulation results in PeA wc.

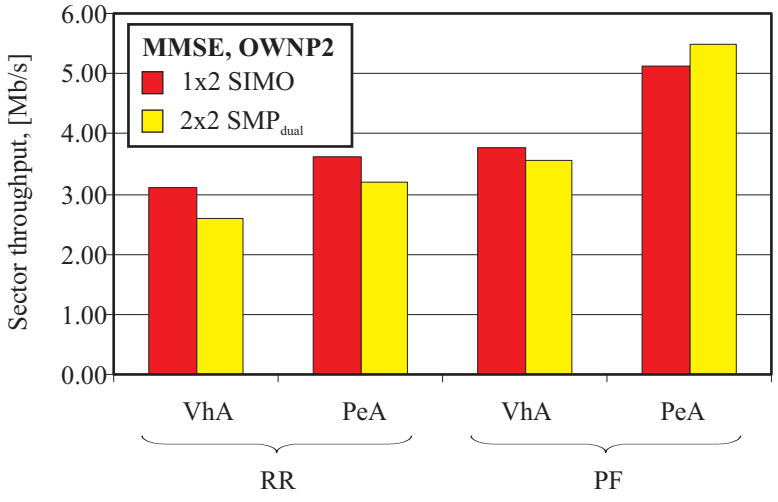

Figure 5.20: Sector throughput comparison of 2×2 SMP$_{dual}$ and 1×2 SIMO.

into throughput spatial multiplexing causes a sector throughput loss. Only if the SINR on the first stream can no longer efficiently be mapped into throughput, the 'excess' SINR can be used for dual stream transmission and bring a benefit to the system. In general the SINR operation point of the SIMO configuration in the PeA environment and with MMSE reception is high. PF scheduling lifts this SINR operation point further. In this particular scenario there is a sector throughput benefit from SMP$_{dual}$. Revisiting the corresponding 10 user approximation cdf in Figure 5.18 (a) it can be seen that around 40% of the SIMO users have excess SINR that does not increase their throughput. Switching on a co-stream reduces their SINR by around 6.5 dB, without significantly decreasing their throughput. However, now a second stream can be used, which leads to the overall sector throughput increase. This excess SINR occurs more frequently for high G-factor users.

To underpin this argumentation the average throughputs achieved at individual G-factors are collected. Throughput results for 1×2 SIMO MMSE as well as 2×2 SMP$_{dual}$ MMSE are in Figure 5.21 (a) and (b) plotted in combination with RR and PF scheduling respectively. It can be seen that in the VhA environment 1×2 SIMO performs very similar or better than SMP$_{dual}$. However, in the PeA environment 2×2 SMP$_{dual}$ performs at higher G-factors better than 1×2 SIMO. The point from which on 2×2 SMP$_{dual}$ performs better is reached earlier in connection with the PF scheduler.

In a 'fair' comparison the 2×2 SMP$_{dual}$ scheme has to compete with other 2×2 MIMO configurations. Through comparison with the 2×2 CLM1 hc scheme it is found that 2×2 SMP$_{dual}$ in the PeA environment performs better from 8 dB and 13 dB G-factors onwards under the PF and the RR scheduler respectively. However, when seen over the whole sector, the throughput of 2×2 CLM1 hc is found to be superior.

To conclude, spatial multiplexing is able to exploit excess SINR that cannot be efficiently utilised by a single stream. Thereby it provides an option to extend the dynamic range of the system. Using a smart SMP$_x$ packet scheduler that only switches on the co-stream in excess SINR situations and otherwise performs SMP$_{sel}$ has the potential to bring a sector throughput benefit to a 1×2 SIMO system.

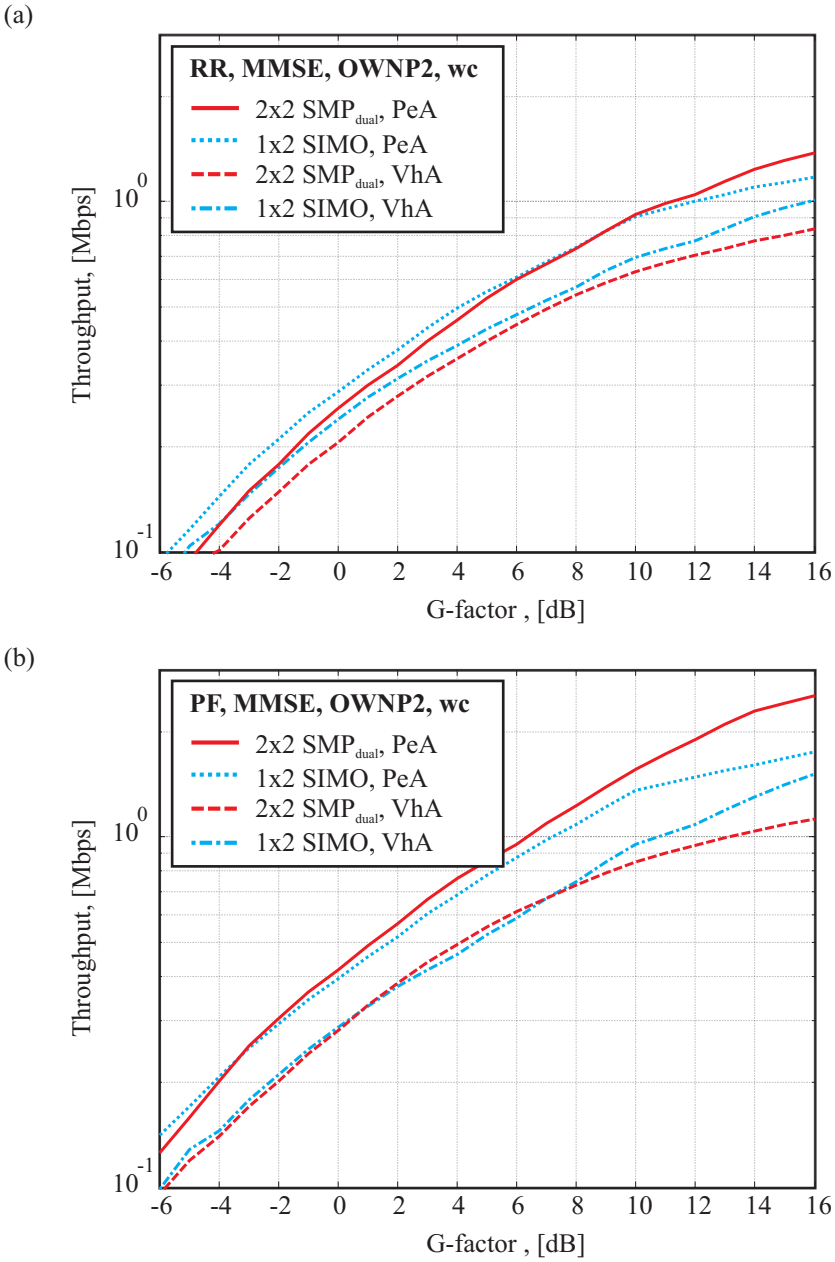

Figure 5.21: Average achieved throughput at specific G-factor positions for 2×2 SMP$_{dual}$ and 1×2 SIMO, both with MMSE reception. (a) and (b) use RR and PF scheduling respectively.

5.8 Network Performance Comparison

The following subsections compare the sector throughput performance of the different schemes. A table providing all sector throughput performance numbers can additionally be found in Annex I.VII.

5.8.1 Sector Throughput Overview

Figure 5.22 gives an overview of the sector throughput performance in connection with RR scheduling. It can be seen that MISO and SIMO schemes perform around 25% to 100% better than their SISO counter parts. On the whole, MIMO schemes perform best, with around 100% to 200% sector throughput benefit over SISO.

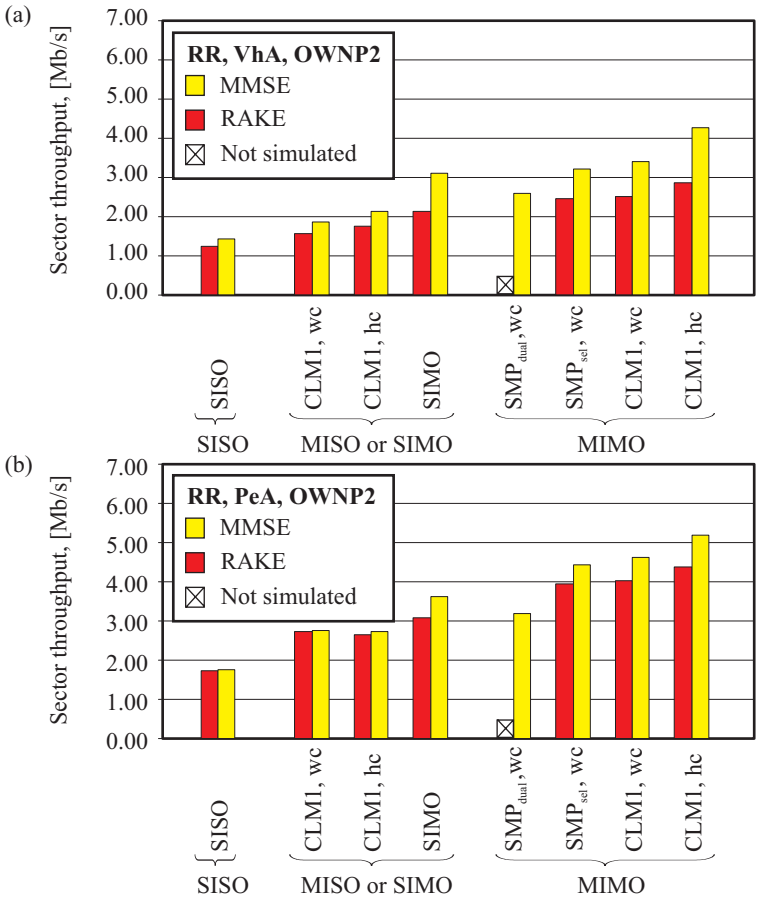

Figure 5.22: Sector throughput with RR scheduler, (a) in the PeA and (b) in VhA.

5.8.2 Benefit of MMSE Receiver

An overview of the MMSE receiver sector throughput gain over the RAKE receiver is presented in Table 5.20. Three general trends can be observed:

- There is an increased MMSE gain in the VhA environment. This is explained by increased opportunities to suppress IPI.
- There is an increased MMSE gain in connection with a second rx antenna. This is explained through the MMSE receiver's spatial interference suppression capabilities.
- There is an increased MMSE gain in connection with RR scheduling. This is explained by a generally lower SINR operation point in connection with RR scheduling. Thus the MMSE receiver's fading peaks can be utilised more efficiently. The SISO VhA case does not follow this trend, as its SINR operation point is generally lower. Fading peaks created by the MMSE get emphasised in connection with PF scheduling, and can due to the lower operation point still be efficiently exploited.

	VhA			**PeA**		
	RR		**PF**	**RR**		**PF**
	Sector throughput gain, MMSE over RAKE, [%]					
1×1 SISO	14	$<$	21	2	$>$	0
2×1 CLM1, wc	20	$>$	16	1	$\approx$	0
2×1 CLM1, hc	22	$\approx$	23	2	$\approx$	1
1×2 SIMO	45	$>$	36	18	$>$	13
2×2 SMP$_{dual}$, wc	x		x	x		x
2×2 SMP$_{sel}$, wc	30	$>$	28	12	$>$	9
2×2 CLM1, wc	37	$>$	30	15	$>$	10
2×2 CLM1, hc	49	$>$	42	19	$>$	14

Table 5.20: Sector throughput benefit of MMSE over RAKE.

5.8.3 Gain of PF over RR Scheduling

The sector throughput benefit of PF over RR scheduling is displayed in Figure 5.23. It can be seen that the gain of PF scheduling generally decreases with increasing frequency and antenna diversity order. While the gain of PF over RR scheduling in the SISO situation amounts to approximately 45% to 95% for the VhA and the PeA environment respectively, it decreases to around 15% to 30% in connection

with 2×2 CLM1. This shows the general effect of diminishing returns with increasing diversity order. Specifically with respect to channel dependent scheduling this effect became known under the synonym 'channel-hardening' [Hoch02]. Further, most investigated single stream multiple antenna deployments shift the mean SINR operation point of the system upwards. Thus PF mean SINR gain is less efficiently mapped to throughput. Only SMP_{dual} can, due to its dynamic range extension capability, very efficiently use the positive SINR operation point shift that comes along with PF scheduling.

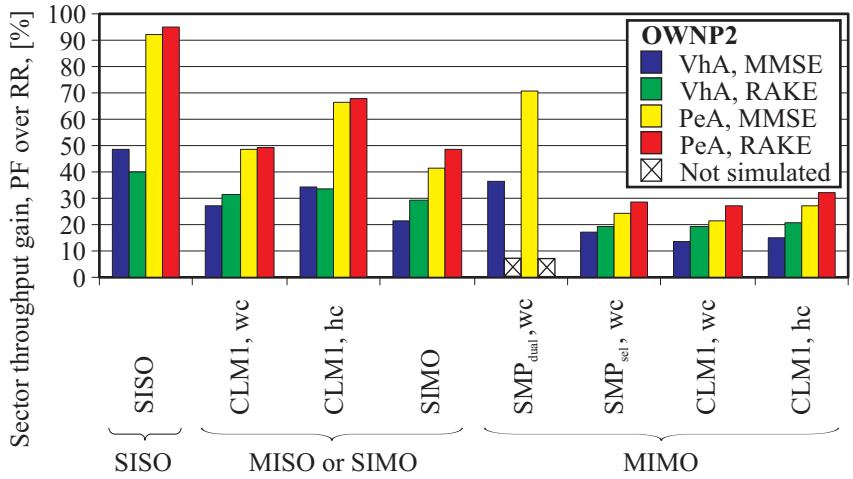

Figure 5.23: Sector throughput benefit of PF over RR scheduler.

5.8.4 Discrepancies between AWGN and OWNP2 Model

The sector throughput performance discrepancies between the AWGN and the OWNP2 model are displayed in Table 5.21. It can be seen that the AWGN model tends to underestimate sector throughput performance by up to 20%. As investigated in Subsection 5.3.1 this is partly due to replacing the other-sector interference term in the SINR formulation by its mean. The particularly pronounced underestimation in case of dual antenna MMSE receivers is, however, due to the fact that additionally spatial other-sector interference colouring is neglected.

5.9 Summary

Selected link and network level performance results were presented and discussed. The utilised trace based simulation approach does not only allow assessment of SINR statistics at sector level, but also provides the means to look at individual high and low G and DIR situations. This allows insight into effects, like for example

Scheme	RR				PF			
	RAKE		MMSE		RAKE		MMSE	
	VhA	PeA	VhA	PeA	VhA	VeA	VhA	PeA
	Sector throughput ratio, AWGN over OWNP2, [–]							
1×1 SISO	0.86	0.89	0.92	0.87	0.93	0.84	0.86	0.85
2×1 CLM1, wc	0.97	0.93	0.92	0.93	0.95	0.94	0.92	0.92
2×1 CLM1, hc	x	x	x	x	x	x	x	x
1×2 SIMO	1.00	0.92	0.84	0.81	0.95	0.89	0.84	0.80
2×2 SMP$_{sel}$, wc	1.01	0.97	0.92	0.86	0.99	0.92	0.90	0.87
2×2 SMP$_{dual}$, wc	x	x	0.90	0.84	x	x	0.91	0.81
2×2 CLM1, wc	1.02	1.01	0.91	0.89	1.01	0.98	0.92	0.91
2×2 CLM1, hc	x	x	x	x	x	x	x	x

Table 5.21: Comparison of AWGN and OWNP2 sector throughput.

other-sector interference variation and other-sector interference spatial colouring, that cannot be seen as clearly at sector level. Moreover, the trace based simulation approach allows benchmarking of individual simulation results against analytical bounds. For this purpose several, partly novel, analytical bounds are collected and derived in Appendix A. Especially the SINR performance in the relatively frequency flat fading PeA environment can often be predicted analytically. As the individual sections within this chapter present only selected performance results to emphasise specific observations, a complete list of the main simulation results can be found in Annex I.

Chapter 6

Conclusion

The main contributions of this dissertation are (i) the development of a general MIMO DS-CDMA SINR formulation, (ii) the development of an other-sector interference model for decoupled link and network simulations, (iii) the derivation of analytical bounds to benchmark and assess SINR simulation results, and (iv) the performance assessment of single and multiple antenna schemes within the HSDPA framework. The main findings are outlined throughout the following.

6.1 MIMO DS-CDMA SINR Formulation

A mathematical formulation has been derived to describe orthogonal as well as pseudo random spread MIMO DS-CDMA SINR, obtainable through RAKE or MMSE reception. Using a virtual channel concept the formulation allows to describe different multi-antenna schemes that might co-exist within the same sector to satisfy various signalling and data communication requirements. Simultaneous other channel transmission can especially influence the MMSE receiver's ability to perform channel equalisation and interference suppression. Thus the formulation, for example, allows to show that in frequency selective fading environments closed loop tx antenna schemes can cause a mean SINR loss with respect to single antenna transmission.

6.2 Other-Sector Interference Model

To assess, for example, the benefit of the MMSE receiver's spatial interference suppression capability, it is essential to describe other-sector interference powers individually. Similarly, to assess the impact of other-sector interference power

variation due to partial on/off switching or tx weight updates, an individual model of the other-sector interference powers as well as their transmit correlations is required.

Targeting a decoupled link and network simulation approach, an other-sector interference model has been developed that relates a user's average interference situation to two user-parameters, the *line of sight angle of connection* (AoC) and the *cell geometry factor* (G). The model, termed OWNP2, is based on the idea that the mean received powers from the interfering sectors at the same base station site can be calculated relative to the power of the serving sector using sector antenna pattern relations. The approach relies on the simplifying assumption that path loss and shadow fading from all sectors at the same site are identical. Thereby the model delivers a description of the mean received powers from the own site interfering sectors that is identical to the description in a full cellular scenario set-up. In the investigated macrocellular scenario the own site sectors are identified as the source of very dominant other-sector interference. Thus the developed model represents high *dominant interference ratio*s (DIRs) , *i.e.* $DIR > 2$ dB, accurately. To additionally account for situations where the own site interference is not the most dominant, the strongest two other site sectors are included in the individual interference description. A larger group of candidate sectors exist from which the two strongest other site sectors are recruited. Similarly to macro diversity effects, this leads to a situation where the mean powers of the two strongest other site sectors appear relatively stable and can be approximated as fractions of the overall other site power. The strongest other site sectors' AoCs can, with a certain probability, be related to the serving sector's AoC. Own and other site sector AoC modelling is used to indirectly describe the sectors' transmit correlation.

With only two user-parameters the developed model is able to approximate other-sector interference variability and spatial colouring encountered in a full hexagonal grid cellular set-up. Measured in terms of ΔSINR the OWNP2 model differs in the worst case by up to 0.3 dB from the full set-up, while on the other hand a simpler AWGN model does not allow to account for other-sector interference variations at all. The OWNP2 model is thus suitable for decoupled link and network simulations, where all other-sector interference effects are pre-computed and included in the link level simulation results. If other-sector interference is modelled as AWGN instead, a sector throughput underestimation of up to 20% can occur.

6.3 MIMO HSDPA Performance Assessment

The use of the MIMO DS-CDMA SINR formulation and the OWNP2 interference model has been demonstrated through different multiple antenna HSDPA

performance studies. Ten different antenna deployment scenarios have been investigated. At the base station single antenna transmission, *closed loop transmit diversity mode 1* (CLM1), and *spatial multiplexing* (SMP) were used. The mobile station used single or dual antenna RAKE/MRC or MMSE/OPC receivers. The selection of schemes was made partly with respect to ongoing 3GPP standardisation activities and with the aim of demonstrating the effects of all three multiple antenna gain mechanisms, *i.e.* array gain, diversity order increase, and interference suppression.

Among others it was investigated which effects other-sector interference variations, caused by partial HS-DSCH inactivity, have on link and network level performance. In the investigated macrocellular scenario very high DIR situations are rare, so that even when a large share of an interfering sector's transmit power is switched on or off, the impact of the induced untrackable interference power variations is small. Further, the HSDPA system has due to its fast HARQ functionality the means to compensate for erroneous link adaptation and packet scheduling decisions that might result from the interference variability. Thus sector throughput losses remain below 6% in all investigated situations.

Specifically with respect to dual antenna receiver performance it was shown that the RAKE receiver's array gain decreases due to correlated interference. Even for a low rx antenna correlation magnitude of 0.3, correlated interference from other sectors and/or from own sector IPI leads in VhA to an array gain of 2.7 dB instead of the desired 3 dB. On the contrary the dual antenna MMSE receiver exploits coloured interference and obtains in the same situation an array and interference suppression gain of 5.4 dB over the single antenna MMSE. Further, for a flat Rayleigh fading situation a novel analytical bound was developed that can be used to predict the MMSE receiver's spatial interference suppression benefit over the RAKE receiver.

With respect to the question how link gains relate to network performance, it was found that gains positively affecting the lower tail of the SINR distribution map very efficiently to sector throughput. However, link gains that benefit mainly the upper tail of the SINR distribution are less effectively mapped into sector throughput. This is the reason why especially MMSE configurations cannot translate their impressive SINR advantage to the full extent into sector throughput gain.

With respect to CLM1 it was found that whenever another source of diversity, *e.g.* frequency diversity or multi user selection diversity can be exploited, it is beneficial to use highly correlated tx antennas. The reasons are threefold:

(i) Transmit correlation renders the forced equal transmit power split of CLM1 more optimum.

(ii) Transmit correlation in a 2×1 and in a 2×2 MMSE situation gives more

structure to the interference, which in turn enhances the MMSE equalisation.

(iii) Transmit correlation allows to match transmit weights more efficiently to multiple receive antennas.

In the best case, *i.e.* 2×2 CLM1 MMSE in VhA, transmit correlation was found to increase the sector mean SINR by 2.4 dB.

Assessment of *spatial multiplexing with full weight selection freedom* (SMP$_x$) requires a dual stream capable link adaptation and packet scheduling unit, which was not implemented in the used network level simulator. Thus two sub cases, SMP$_{sel}$ and SMP$_{dual}$, have been assessed. 2×2 SMP$_{sel}$ implements selection transmit diversity, which in terms of sector throughput performs either comparably or better than the 1×2 SIMO reference. This implies that an adaptive spatial multiplexing scheme, with the option to disable one stream, does not cause a sector throughput loss. SMP$_{dual}$ implements a forced dual stream transmission. Simulations are based on the assumption that the interfering co-stream uses all available HS-DSCH multicodes. For high G-factors and generally in the PeA environment in connection with PF scheduling it is found that SMP$_{dual}$ MMSE performs better than the 1×2 SIMO MMSE reference. SMP$_{dual}$ is the only one of the investigated schemes that indirectly extends the system's dynamic range. In the very high SINR regime, it allows to trade off SINR for an additional stream. Both streams then operate in the lower part of the system's dynamic range, where SINR maps more beneficially to sector throughput. It is concluded that adaptive spatial multiplexing, including the SMP$_{sel}$ baseline, has the potential to outperform a SIMO system. Analytical bounds were derived that predict the mean SINR 'cost' of a co-stream transmission. Bounds and simulations indicate that an excess SINR of around 6.5 dB is required to make a co-stream transmission worthwhile.

Finally, comparing the sector throughput of the simplest 1×1 SISO RAKE RR case with the best performing 2×2 CLM1 hc MMSE PF case, around 280% to 300% sector throughput gain can be achieved in the PeA and the VhA environment respectively. This shows that the combination of different HSDPA physical layer enhancement techniques, such as multiple antennas, advanced receivers and channel dependent scheduling, can be used to gradually adjust network sector throughput capacity to accommodate growing data traffic volumes.

6.4 Future Work

The SINR operation point is the key to answer the question which benefit can be obtained from multi-antenna processing. This operation point does not only depend on the G-factor distribution, the degree of frequency selectivity and the scheduling mechanism, but also on implementation specific imperfections that have not been

considered throughout this dissertation. One point for future work is therefore to consider how base station power amplifier non linearities, limited receive filter size, channel and received signal covariance estimation, and receive filter adaptation influence the SINR operation point as well as the general shape of the obtainable SINR distribution. Should these imperfections not shift the SINR operation point by several dB downwards, then the obtained results indicate that investigating the deployment of more advanced receivers or bigger tx and rx antenna array constellations alone will not be able to enhance network capacity significantly. This can be explained through Figure 6.1.

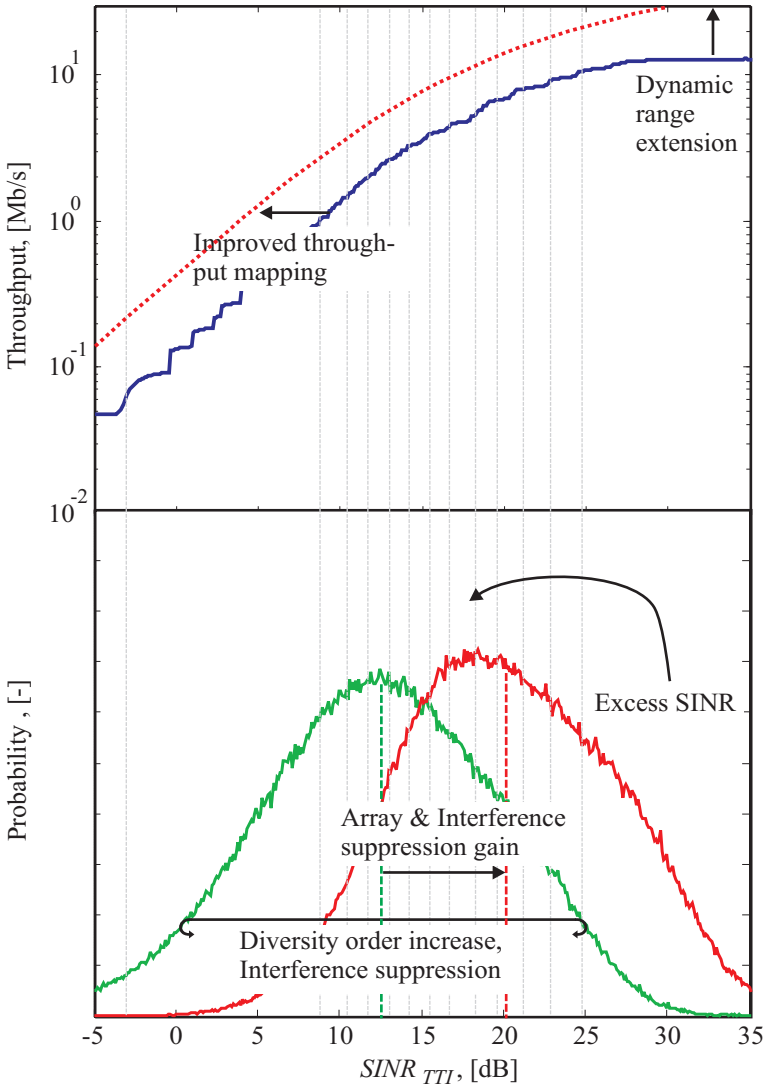

Figure 6.1: Ways to influence sector throughput.

In the investigated scenarios, the three antenna gain mechanisms are able to decrease the variance and increase the mean of the SINR distribution. In the considered single stream set-up this causes a considerable amount of excess SINR that is not efficiently mapped into throughput. Little can be expected from improved throughput mapping and dynamic range extensions as the existing system is already operating very close to the Shannon limit. One of the main tasks for future work is thus to use the excess SINR efficiently. Adaptive spatial multiplexing is a promising way forward allowing plenty of further research:

- Adaptive spatial multiplexing can be performed over different transmit weight sets, *i.e.* over virtual channels that differ from the physical radio propagation channels. For full adaptivity the UE needs to predict the obtainable SINR on every possible virtual channel, conditioned on potential co-stream decisions. This requires to trade off tx array gain and tx interference suppression gain against added SINR prediction and receiver adaptation complexity.
- While in the presented work spatial multiplexing was performed reusing the same code space, it is possible to deploy a secondary scrambling code instead. Under a secondary scrambling code the UE sees all interfering multicodes, but with a processing gain, whereas with orthogonal spreading the UE sees only one interfering multicode, but without the advantage of processing gain. Thus the overall interference situation is similar. However, there might be other advantages of a secondary scrambling code deployment. Especially co-stream interference predictability and therefore SINR predictability and receiver adaptation might become easier since secondary scrambling code transmission decouples the experienced co-stream interference power from multicode link adaptation decisions on the co-stream.
- Research is also needed on how to limit the required link quality feedback and how to exploit it most beneficially for multistream link adaptation and packet scheduling decisions.

Only when successful measures are in place to deal with the excess SINR, more advanced receivers or larger antenna array constellations might be considered.

Appendix A

MIMO HSDPA - SINR Bounds

This appendix provides the background material to the analytical bounds presented in Chapter 2. These results are used to validate and interpret the SINR statistics obtained via simulations. The Appendix is split into three sections. Table A.1 provides an overview of Section A.1 and Section A.2. In Section A.1 SINR statistics in flat Rayleigh fading, with decorrelated antenna elements and pure AWGN interference, are presented. With exception of the statistics for SMP$_{sel}$ these results are standard text book material. Section A.2 looks at the SINR statistics if interference consists of AWGN plus one single dominant flat Rayleigh fading interferer. This dominant interference situation is in Table A.1 marked as 1DOM. It can either arise when a strong signal is received from another sector or in case of spatial multiplexing within the same sector where the co-stream causes strong dominant interference. Only in these situations, there is a difference between MRC and OPC

Tx-rx scheme			Interference	Subsection
1×1	SISO	MRC, OPC	AWGN	A.1.1
1×2	SIMO	MRC, OPC	AWGN	A.1.2
2×1	CLM1	MRC, OPC	AWGN	A.1.3
4	Branch	MRC, OPC	AWGN	A.1.4
2×2	CLM1	MRC, OPC	AWGN	A.1.5
2×2	SMP$_{sel}$	MRC, OPC	AWGN	A.1.6
1×1	SISO	MRC, OPC	1DOM	A.2.1
1×2	SIMO	MRC	1DOM	A.2.2
1×2	SIMO	OPC	1DOM	A.2.3
2×2	SMP$_{dual}$	OPC	1DOM	A.2.4

Table A.1: Overview of the antenna schemes in connection with a specific interference situation as treated in Section A.1 and A.2.

antenna combining as indicated in the third column of Table A.1. Although being based on the public literature the results in Section A.2 contain a certain degree of novelty. Finally, a collection of further bounds taken from the public literature for different correlated or frequency selective environments in connection with pure AWGN interference is provided in Section A.3.

A.1 SINR Statistics in AWGN Interference

The flat Rayleigh fading envelop of a mean normalised complex channel transfer function is denoted $|h|$. Its power is central chi-square distributed with two degrees of freedom. Its cdf is given by [Jake94, pp.17], [Proa87, p. 30]

$$\Pr\left(|h|^2 \leqslant |h_{ref}|^2\right) = 1 - e^{-|h_{ref}|^2} \quad , \tag{A.1}$$

and its *probability density function* (pdf) by

$$\mathrm{pr}\left(|h|^2\right) = e^{-|h|^2} \quad . \tag{A.2}$$

Its first and second moment are [Proa87, (1.1.109)].

$$\mathrm{E}\left\{|h|^2\right\} = 1 \quad , \tag{A.3}$$

and

$$\mathrm{E}\left\{\left(|h|^2\right)^2\right\} = 2 \quad . \tag{A.4}$$

Should different i.i.d flat Rayleigh fading envelopes be required so are they denoted with a subscript index, *e.g.* $|h_1|$, $|h_2|$. In case of AWGN interference and noise the instantaneous signal power of an antenna branch is given by

$$P_{sig} = |h|^2 \cdot \overline{P}_{sig} \quad , \tag{A.5}$$

and the overall interference plus noise power of that branch is

$$P_{int} = \overline{P}_{int} \quad . \tag{A.6}$$

The instantaneous signal to interference plus noise ratio is

$$\begin{aligned} SINR_{branch} &= \frac{P_{sig}}{P_{int}} \\ &= |h|^2 \cdot \frac{\overline{P}_{sig}}{\overline{P}_{int}} \\ &= |h|^2 \cdot \overline{SINR}_{branch} \quad , \end{aligned} \tag{A.7}$$

where the mean signal to noise ratio $\overline{SINR}_{branch}$ is inherently defined. Using MRC or OPC to combine N_{branch} branches the probability that the post branch combining $SINR_{N_{bramch}}$ drops below a reference value $SINR_{ref}$ is given by [Jake94, p. 319]

$$\begin{aligned}&\Pr\left(SINR_{N_{branch}} < SINR_{ref}\right)\\&= 1 - e^{-\left(\frac{SINR_{ref}}{\overline{SINR}_{branch}}\right)} \cdot \sum_{n=1}^{N_{branch}} \frac{\left(\frac{SINR_{ref}}{\overline{SINR}_{branch}}\right)^{n-1}}{(n-1)!}\end{aligned} \quad . \tag{A.8}$$

A.1.1 1×1 SISO Reference

The SINR in a 1×1 SISO case is given by

$$\begin{aligned}SINR_{1\times 1SISO} &= SINR_{branch}\\&= |h|^2 \cdot \overline{SINR}_{branch}\end{aligned} \quad . \tag{A.9}$$

Its cdf defaults back to the cdf of the initially introduced Rayleigh fading variable, *i.e.*

$$\begin{aligned}&\Pr\left(SINR_{1\times 1SISO} < SINR_{ref}\right)\\&= \Pr\left(|h|^2 \cdot \overline{SINR}_{branch} \leqslant |h_{ref}|^2 \cdot \overline{SINR}_{branch}\right)\\&= 1 - e^{-\left(\frac{SINR_{ref}}{\overline{SINR}_{branch}}\right)}\end{aligned} \quad . \tag{A.10}$$

Its pdf writes

$$\mathrm{pr}\left(SINR_{1\times 1SISO}\right) = \frac{1}{\overline{SINR}_{branch}} \cdot e^{-\left(\frac{SINR_{1\times 1SISO}}{\overline{SINR}_{branch}}\right)} \quad , \tag{A.11}$$

and the first moment is

$$\begin{aligned}
&\mathrm{E}\left\{SINR_{1\times 1SISO}\right\} \\
&= \int_0^{+\infty} SINR_{1\times 1SISO} \cdot \mathrm{pr}\left(SINR_{1\times 1SISO}\right) \cdot dSINR_{1\times 1SISO} \\
&= \int_0^{+\infty} \frac{SINR_{1\times 1SISO}}{\overline{SINR}_{branch}} \cdot e^{-\left(\frac{SINR_{1\times 1SISO}}{\overline{SINR}_{branch}}\right)} \cdot dSINR_{1\times 1SISO} \\
&= \int_0^{+\infty} \frac{SINR_{1\times 1SISO}}{\overline{SINR}_{branch}} \cdot e^{-\left(\frac{SINR_{1\times 1SISO}}{\overline{SINR}_{branch}}\right)} \cdot d\frac{SINR_{1\times 1SISO}}{\overline{SINR}_{branch}} \cdot \overline{SINR}_{branch} \\
&= \mathrm{Gamma}\left(2\right) \cdot \overline{SINR}_{branch} \\
&= \overline{SINR}_{branch}
\end{aligned} \quad , \tag{A.12}$$

where $\mathrm{Gamma}\left(\cdot\right)$ represents the Gamma-function [Moon00, p. 478]. The above is mainly included to introduce some basic notation and steps.

A.1.2 1×2 SIMO, 2 Branch Combining

In the 1×2 SIMO case (A.8) simplifies to

$$\begin{aligned}
&\Pr\left(SINR_{1\times 2SIMO} < SINR_{ref}\right) \\
&= 1 - e^{-\left(\frac{SINR_{ref}}{\overline{SINR}_{branch}}\right)} \cdot \left(1 + \frac{SINR_{ref}}{\overline{SINR}_{branch}}\right) \\
&= 1 - e^{-\left(\frac{SINR_{ref}}{\overline{SINR}_{branch}}\right)} - \frac{SINR_{ref}}{\overline{SINR}_{branch}} \cdot e^{-\left(\frac{SINR_{ref}}{\overline{SINR}_{branch}}\right)}
\end{aligned} \quad , \tag{A.13}$$

with pdf

$$\begin{aligned}
\mathrm{pr}\left(SINR_{1\times 2SIMO}\right) &= \frac{1}{\overline{SINR}_{branch}} \cdot e^{-\left(\frac{SINR_{1\times 2SIMO}}{\overline{SINR}_{branch}}\right)} \\
&\quad - \frac{1}{\overline{SINR}_{branch}} \cdot e^{-\left(\frac{SINR_{1\times 2SIMO}}{\overline{SINR}_{branch}}\right)} \\
&\quad + \frac{SINR_{1\times 2SIMO}}{\left(\overline{SINR}_{branch}\right)^2} \cdot e^{-\left(\frac{SINR_{1\times 2SIMO}}{\overline{SINR}_{branch}}\right)} \\
&= \frac{SINR_{1\times 2SIMO}}{\left(\overline{SINR}_{branch}\right)^2} \cdot e^{-\left(\frac{SINR_{1\times 2SIMO}}{\overline{SINR}_{branch}}\right)}
\end{aligned} \quad , \tag{A.14}$$

and first moment

$$\begin{aligned}
&\mathrm{E}\left\{SINR_{1\times 2SIMO}\right\} \\
&= \int_0^{+\infty} SINR_{1\times 2SIMO} \cdot \mathrm{pr}\left(SINR_{1\times 2SIMO}\right) \cdot dSINR_{1\times 2SIMO} \\
&= \int_0^{+\infty} \left(\frac{SINR_{1\times 2SIMO}}{\overline{SINR}_{branch}}\right)^2 \cdot e^{-\left(\frac{SINR_{1\times 2SIMO}}{\overline{SINR}_{branch}}\right)} \cdot dSINR_{1\times 2SIMO} \\
&= \int_0^{+\infty} \left(\frac{SINR_{1\times 2SIMO}}{\overline{SINR}_{branch}}\right)^2 \cdot e^{-\left(\frac{SINR_{1\times 2SIMO}}{\overline{SINR}_{branch}}\right)} \cdot d\frac{SINR_{1\times 2SIMO}}{\overline{SINR}_{branch}} \cdot \overline{SINR}_{branch} \\
&= \mathrm{Gamma}\left(3\right) \cdot \overline{SINR}_{branch} \\
&= 2 \cdot \overline{SINR}_{branch}
\end{aligned} \quad . \tag{A.15}$$

Its array gain over 1×1 SISO is therefore

$$\begin{aligned}
\beta_{1\times 2SIMO} &= \frac{\overline{SINR}_{1\times 2SIMO}}{\overline{SINR}_{1\times 1SISO}} \\
&= 2 \\
&\approx 3.01 \text{ dB}
\end{aligned} \quad . \tag{A.16}$$

A.1.3 2×1 CLM1

CLM1 splits the transmit power evenly between the two tx antennas. Its performance is therefore upper bounded by the performance of 2 branch EGC. The 2 branch EGC array gain is [Jake94, p. 321],

$$\begin{aligned}
\beta_{2EGC} &= \left(1 + \frac{\pi}{4}\right) \\
&\approx 2.52 \text{ dB}
\end{aligned} \quad . \tag{A.17}$$

Neglecting weight feedback delays the exact 2×1 CLM1 array gain, taking into account the phase granularity of the transmit weights, is derived in [Gerl02] as

$$\begin{aligned}
\beta_{2\times 1CLM1} &= \left(1 + \frac{1}{\sqrt{2}}\right) \\
&\approx 2.32 \text{ dB}
\end{aligned} \quad . \tag{A.18}$$

And the 2×1 CLM1 antenna diversity order remains 2 [Love03]. Therefore the post combining SINR cdf can be obtained through the mean adjusted 1×2 SIMO

SINR cdf, *i.e.*

$$\begin{aligned}
&\Pr\left(SINR_{2\times1CLM1} < SINR_{ref}\right) \\
&= 1 - e^{-\left(\frac{SINR_{ref}}{\overline{SINR}_{branch}\cdot\beta_{\substack{2\times1CLM1,\\1\times2SIMO}}}\right)} \\
&- \frac{SINR_{ref}}{\overline{SINR}_{branch}\cdot\beta_{\substack{2\times1CLM1,\\1\times2SIMO}}}\cdot e^{-\left(\frac{SINR_{ref}}{\overline{SINR}_{branch}\cdot\beta_{\substack{2\times1CLM1,\\1\times2SIMO}}}\right)} \quad ,
\end{aligned} \tag{A.19}$$

where the mean adjustment is given by

$$\begin{aligned}
\beta_{\substack{2\times1CLM1,\\1\times2SIMO}} &= \frac{\beta_{2\times1CLM1}}{\beta_{1\times2SIMO}} \\
&= \frac{1}{2} + \frac{1}{2\sqrt{2}} \\
&\approx -0.69 \text{ dB} \quad .
\end{aligned} \tag{A.20}$$

A.1.4 4 Branch Combining

Although 4 branch MRC or OPC is not directly used in any multiple antenna deployment, the 4 branch results are presented in the following as they deliver a starting point to come to the SINR distribution of selected 2×2 systems using mean adjustments. The cdf based on (A.8) is

$$\begin{aligned}
&\Pr\left(SINR_{4branch} < SINR_{ref}\right) \\
&= 1 + \left(\begin{array}{l}
-1 - \left(\frac{SINR_{ref}}{\overline{SINR}_{branch}}\right) \\
-\frac{1}{2}\cdot\left(\frac{SINR_{ref}}{\overline{SINR}_{branch}}\right)^2 \\
-\frac{1}{6}\cdot\left(\frac{SINR_{ref}}{\overline{SINR}_{branch}}\right)^3
\end{array}\right)\cdot e^{-\left(\frac{SINR_{ref}}{\overline{SINR}_{branch}}\right)} \quad ,
\end{aligned} \tag{A.21}$$

and the pdf turns after some simplification into

$$\text{pr}\left(SINR_{4branch}\right) = \frac{1}{6}\cdot\frac{\left(SINR_{4branch}\right)^3}{\left(\overline{SINR}_{branch}\right)^4}\cdot e^{-\left(\frac{SINR_{4branch}}{\overline{SINR}_{branch}}\right)} \quad . \tag{A.22}$$

Its first moment is

$$\begin{aligned}
&\mathrm{E}\left\{SINR_{4branch}\right\} \\
&= \int_0^{+\infty} SINR_{4branch} \cdot \mathrm{pr}\left(SINR_{4branch}\right) \cdot dSINR_{4branch} \\
&= \int_0^{+\infty} SINR_{4branch} \cdot \frac{1}{6} \cdot \frac{\left(SINR_{4branch}\right)^3}{\left(\overline{SINR}_{branch}\right)^4} \cdot e^{-\left(\frac{SINR_{4branch}}{\overline{SINR}_{branch}}\right)} \cdot dSINR_{4branch} \\
&= \frac{1}{6} \cdot \int_0^{+\infty} \left(\frac{SINR_{4branch}}{\overline{SINR}_{branch}}\right)^4 \cdot e^{-\left(\frac{SINR_{4branch}}{\overline{SINR}_{branch}}\right)} \cdot d\frac{SINR_{4branch}}{\overline{SINR}_{branch}} \cdot \overline{SINR}_{branch} \\
&= \frac{1}{6} \cdot \mathrm{Gamma}\left(5\right) \cdot \overline{SINR}_{branch} \\
&= 4 \cdot \overline{SINR}_{branch}
\end{aligned} \tag{A.23}$$

And the array gain over 1×1 SISO is therefore

$$\begin{aligned}
\beta_{4branch} &= \frac{\overline{SINR}_{4branch}}{\overline{SINR}_{1\times 1 SISO}} \\
&= 4 \\
&\approx 6.02 \text{ dB}
\end{aligned} \quad . \tag{A.24}$$

A.1.5 2×2 CLM1

From [Ande98] it is known that in a 2×2 branch system with tx and rx MRC the expected array gain is

$$\begin{aligned}
\beta_{2\times 2branch} &= 3.5 \\
&\approx 5.44 \text{ dB}
\end{aligned} \quad . \tag{A.25}$$

It is thus approximately 0.58 dB lower than the array gain of the 4 branch combiner. The reason is that the transmit weights have to phase align the received signal at two rx antenna elements, leading for uncorrelated antenna elements to an inherent suboptimum match to either rx antenna. Still $\beta_{2\times 2branch}$ serves as upper bound as with 2×2 CLM1 the transmit weight selection is limited to an even power split and $\frac{\pi}{2}$ phase granularity. The exact 2×2 CLM1 array gain can on the basis of

[Hama01a, Corollary 1.], [Hott03, (11.41)] be derived as

$$\begin{aligned}\beta_{2\times 2CLM1} &= 2\cdot\left(1+\frac{\pi}{16}\cdot\mathrm{Gamma}\left(\frac{1}{2}\right)\cdot\mathrm{Gamma}\left(\frac{5}{2}\right)\right)\\ &= 2+\frac{3}{32}\cdot\pi^2\\ &\approx 4.66\text{ dB}\end{aligned}\quad , \tag{A.26}$$

where a factor 2 was inserted to account for dual antenna combining at the receiver side. The antenna diversity order remains 4 [Love03], so that the cdf can be obtained from (A.21) through mean adjustment, *i.e.*

$$\begin{aligned}&\Pr\left(SINR_{2\times 2CLM1} < SINR_{ref}\right)\\ &= 1+\left(\begin{array}{l}-1\\ -\left(\dfrac{SINR_{ref}}{\overline{SINR}_{branch}\cdot\beta_{\substack{2\times 2CLM1,\\ 4branch}}}\right)\\ -\dfrac{1}{2}\cdot\left(\dfrac{SINR_{ref}}{\overline{SINR}_{branch}\cdot\beta_{\substack{2\times 2CLM1,\\ 4branch}}}\right)^2\\ -\dfrac{1}{6}\cdot\left(\dfrac{SINR_{ref}}{\overline{SINR}_{branch}\cdot\beta_{\substack{2\times 2CLM1,\\ 4branch}}}\right)^3\end{array}\right)\cdot e^{-\left(\frac{SINR_{ref}}{\overline{SINR}_{branch}\cdot\beta_{\substack{2\times 2CLM1,\\ 4branch}}}\right)}\end{aligned}\quad , \tag{A.27}$$

where the mean adjustment is given by

$$\begin{aligned}\beta_{\substack{2\times 2CLM1,\\ 4branch}} &= \frac{\beta_{2\times 2CLM1}}{\beta_{4branch}}\\ &= \frac{2+\frac{3}{32}\cdot\pi^2}{4}\\ &\approx -1.36\text{ dB}\end{aligned}\quad . \tag{A.28}$$

A.1.6 2×2 SMP$_{sel}$

One subcase of SMP$_x$ is to select the better transmit antenna and transmit only a single data stream from the selected antenna. The experienced interference remains AWGN, and 2×2 SMP$_{sel}$ can be described as the combination of tx antenna selection combining and rx antenna MRC or OPC. The probability that the SINR of a signal that could be obtained from a pool of N_u sources is simultaneously

lower than a reference is given by

$$\Pr\left(\bigcup_{u=1}^{N_u} SINR_{source,u} < SINR_{ref}\right) = \prod_{u=1}^{N_u} \Pr\left(SINR_{source,u} < SINR_{ref}\right) \quad , \tag{A.29}$$

which in the case of identical SINR statistics simplifies to [Jake94, p. 315],

$$\Pr\left(\bigcup_{u=1}^{N_u} SINR_{\text{source,u}} < SINR_{ref}\right) = \Pr\left(SINR_{\text{source,u}} < SINR_{ref}\right)^{N_u} \quad . \tag{A.30}$$

This means that the cdf of 2×2 SMP$_{sel}$ can be obtained from the cdf of the 1×2 SIMO case as

$$\begin{aligned}
&\Pr\left(SINR_{2\times 2SMP_{sel}} < SINR_{ref}\right) \\
&= \Pr\left(SINR_{1\times 2SIMO} < SINR_{ref}\right)^2 \\
&= \left(1 - e^{-\left(\frac{SINR_{ref}}{\overline{SINR}_{branch}}\right)} - \frac{SINR_{ref}}{\overline{SINR}_{branch}} \cdot e^{-\left(\frac{SINR_{ref}}{\overline{SINR}_{branch}}\right)}\right)^2 \quad ,
\end{aligned} \tag{A.31}$$

and its pdf turns into

$$\begin{aligned}
&\mathrm{pr}\left(SINR_{2\times 2SMP_{sel}}\right) \\
&= 2 \cdot \frac{SINR_{2\times 2SMP_{sel}}}{\left(\overline{SINR}_{branch}\right)^2} \cdot e^{-\left(\frac{SINR_{2\times 2SMP_{sel}}}{\overline{SINR}_{branch}}\right)} \\
&\cdot \left(1 - e^{-\left(\frac{SINR_{2\times 2SMP_{sel}}}{\overline{SINR}_{branch}}\right)} - \frac{SINR_{2\times 2SMP_{sel}}}{\overline{SINR}_{branch}} \cdot e^{-\left(\frac{SINR_{2\times 2SMP_{sel}}}{\overline{SINR}_{branch}}\right)}\right) \quad . \\
&= \left(\begin{array}{l}
2 \cdot \frac{SINR_{2\times 2SMP_{sel}}}{\left(\overline{SINR}_{branch}\right)^2} \cdot e^{-\left(\frac{SINR_{2\times 2SMP_{sel}}}{\overline{SINR}_{branch}}\right)} \\
- 2 \cdot \frac{SINR_{2\times 2SMP_{sel}}}{\left(\overline{SINR}_{branch}\right)^2} \cdot e^{-2\cdot\left(\frac{SINR_{2\times 2SMP_{sel}}}{\overline{SINR}_{branch}}\right)} \\
- 2 \cdot \frac{\left(SINR_{2\times 2SMP_{sel}}\right)^2}{\left(\overline{SINR}_{branch}\right)^3} \cdot e^{-2\cdot\left(\frac{SINR_{2\times 2SMP_{sel}}}{\overline{SINR}_{branch}}\right)}
\end{array}\right)
\end{aligned} \tag{A.32}$$

The first moment is given by

$$
\begin{aligned}
&\mathrm{E}\left\{SINR_{2\times 2SMP_{sel}}\right\} \\
&= \int_0^{+\infty} SINR_{2\times 2SMP_{sel}} \cdot \mathrm{pr}\left(SINR_{2\times 2SMP_{sel}}\right) \cdot dSINR_{2\times 2SMP_{sel}} \\
&= 2 \cdot \overline{SINR}_{branch} \\
&\left(\int_0^{+\infty} \left(\frac{SINR_{2\times 2SMP_{sel}}}{\overline{SINR}_{branch}} \right)^2 \cdot e^{-\cdot \left(\frac{SINR_{2\times 2SMP_{sel}}}{\overline{SINR}_{branch}} \right)} \cdot d\frac{SINR_{2\times 2SMP_{sel}}}{\overline{SINR}_{branch}} \right. \\
&- \int_0^{+\infty} \left(\frac{SINR_{2\times 2SMP_{sel}}}{\overline{SINR}_{branch}} \right)^2 \cdot e^{-2\cdot \left(\frac{SINR_{2\times 2SMP_{sel}}}{\overline{SINR}_{branch}} \right)} \cdot d\frac{SINR_{2\times 2SMP_{sel}}}{\overline{SINR}_{branch}} \\
&\left. - \int_0^{+\infty} \left(\frac{SINR_{2\times 2SMP_{sel}}}{\overline{SINR}_{branch}} \right)^3 \cdot e^{-2\cdot \left(\frac{SINR_{2\times 2SMP_{sel}}}{\overline{SINR}_{branch}} \right)} \cdot d\frac{SINR_{2\times 2SMP_{sel}}}{\overline{SINR}_{branch}} \right) .
\end{aligned}
\tag{A.33}
$$

Besides using the Gamma function, it is used that [Papu94, p. 312]

$$
\int x^2 \cdot e^{ax} \cdot dx = \left(\frac{a^2x^2 - 2ax + 2}{a^3} \right) \cdot e^{ax} \quad , \tag{A.34}
$$

and

$$
\int x^n \cdot e^{ax} dx = \frac{x^n \cdot e^{ax}}{a} - \frac{n}{a} \cdot \int x^{n-1} \cdot e^{ax} dx \quad , \tag{A.35}
$$

so that the first moment simplifies to

$$
\begin{aligned}
&\mathrm{E}\left\{SINR_{2\times 2SMP_{sel}}\right\} \\
&= 2\cdot\overline{SINR}_{branch}\cdot(\mathrm{Gamma}\,(3) \\
&- \left[\left(\begin{array}{l} -\left(\dfrac{SINR_{2\times 2SMP_{sel}}}{2\cdot\overline{SINR}_{branch}}\right)^2 \\ -\left(\dfrac{SINR_{2\times 2SMP_{sel}}}{2\cdot\overline{SINR}_{branch}}\right)-\dfrac{1}{4}\end{array}\right)\cdot e^{-2\left(\frac{SINR_{2\times 2SMP_{sel}}}{\overline{SINR}_{branch}}\right)}\right]_0^{\infty} \\
&- \left[-\left(\frac{SINR_{2\times 2SMP_{sel}}}{2\cdot\overline{SINR}_{branch}}\right)^3\cdot e^{-2\left(\frac{SINR_{2\times 2SMP_{sel}}}{\overline{SINR}_{branch}}\right)}\right]_0^{\infty} \\
&- \left[\frac{3}{2}\cdot\int_0^{+\infty}\left(\begin{array}{l}\left(\dfrac{SINR_{2\times 2SMP_{sel}}}{\overline{SINR}_{branch}}\right)^2 \\ \cdot\, e^{-2\cdot\left(\frac{SINR_{2\times 2SMP_{sel}}}{\overline{SINR}_{branch}}\right)}\end{array}\right)\cdot d\frac{SINR_{2\times 2SMP_{sel}}}{\overline{SINR}_{branch}}\right]_0^{\infty}\Bigg) \\
&= \left(4-\frac{1}{2}-\frac{3}{4}\right)\cdot\overline{SINR}_{branch} \\
&= \left(2+\frac{3}{4}\right)\cdot\overline{SINR}_{branch}
\end{aligned}
\tag{A.36}
$$

Thus the array gain of 2×2 SMP$_{sel}$ is given by

$$
\begin{aligned}
\beta_{2\times 2SMP_{sel}} &= \frac{\overline{SINR}_{2\times 2SMP_{sel}}}{\overline{SINR}_{1\times 1SISO}} \\
&= 2+\frac{3}{4} \\
&\approx 4.39 \text{ dB}
\end{aligned}
\quad , \tag{A.37}
$$

and the cdf can be obtained from (A.21) through mean adjustment, *i.e.*

$$\begin{aligned}
&\Pr\left(SINR_{2\times 2SMP_{sel}} < SINR_{ref}\right) \\
&= 1 + \left(\begin{array}{l} -1 \\ -\left(\dfrac{SINR_{ref}}{\overline{SINR}_{branch} \cdot \beta_{\substack{2\times 2SMP_{sel},\\ 4branch}}} \right) \\ -\left(\dfrac{SINR_{ref}}{2 \cdot \overline{SINR}_{branch} \cdot \beta_{\substack{2\times 2SMP_{sel},\\ 4branch}}} \right)^2 \\ -\left(\dfrac{SINR_{ref}}{6 \cdot \overline{SINR}_{branch} \cdot \beta_{\substack{2\times 2SMP_{sel},\\ 4branch}}} \right)^3 \end{array} \right) \cdot e^{-\left(\frac{SINR_{ref}}{\overline{SINR}_{branch} \cdot \beta_{\substack{2\times 2SMP_{sel},\\ 4branch}}} \right)} ,
\end{aligned} \tag{A.38}$$

where the mean adjustment is

$$\begin{aligned}
\beta_{\substack{2\times 2SMP_{sel},\\ 4branch}} &= \frac{\beta_{2\times 2SMP_{sel}}}{\beta_{4branch}} \\
&= \frac{2 + \frac{3}{4}}{4} \\
&\approx -1.63 \text{ dB} \quad .
\end{aligned} \tag{A.39}$$

A.2 SINR Statistics with Single Dominant Interferer

The following focuses on a situation where only one flat Rayleigh fading interferer is present. All other interferers are experienced as AWGN. Such a situation can either arise when a user receives strong interference from just one other sector or when SMP_{dual} is used, in which case strong interference is received from the co-stream. Related and more general analytical work can be found in [Boga80], [Vill99], [Pham99], [Rao01], [Akyi01], [Akyi02], [Cui04], [Tokg04].

The mean power of the dominant interferer is denoted $\overline{P}_{dom}$, and the mean dominant interference power to AWGN ratio is denoted $\overline{INR}$. As previously the signal power is given by

$$P_{sig} = |h_1|^2 \cdot \overline{P}_{sig} \quad , \tag{A.40}$$

with mean $\overline{P}_{sig}$ and Rayleigh fading variable $|h_1|$. The mean signal to AWGN ratio is given as

$$\overline{SNR} = \overline{P}_{sig} \cdot \frac{\overline{INR}}{\overline{P}_{dom}} \quad . \tag{A.41}$$

The overall instantaneous interference plus noise power is

$$P_{int} = |h_3|^2 \cdot \overline{P}_{dom} + \frac{\overline{P}_{dom}}{\overline{INR}} \quad , \tag{A.42}$$

where $|h_3|$ is another Rayleigh fading variable independent of $|h_1|$. The mean interference power is therefore

$$\overline{P}_{int} = \overline{P}_{dom} + \frac{\overline{P}_{dom}}{\overline{INR}} \quad . \tag{A.43}$$

Using (A.41) and (A.43) the ratio of mean signal to mean interference power can be written as

$$\frac{\overline{P}_{sig}}{\overline{P}_{int}} = \frac{\overline{SNR}}{\overline{INR}+1} \quad . \tag{A.44}$$

While for AWGN interference MRC and OPC perform identical, with non spatially white interference OPC has interference suppression opportunities and performs superior to MRC. The flat fading SISO case without combining is used as a reference.

A.2.1 1×1 SISO Reference Case

The instantaneous interference plus noise ratio is

$$SINR_{1\times 1SISO} = \frac{P_{sig}}{P_{int}} \quad , \tag{A.45}$$

and its pdf corresponds to a 'modified F_c distribution' [Akyi01], [Rao01]. Instead of obtaining the mean SINR from the modified F_c distribution, Taylor Series Expansion [Papu94, p. 155] is used to approximate the mean. Thereby the expectation over the ratio of two uncorrelated variables X and Y can under the condition $\mathrm{E}\{X\} \neq 0$ be approximated as [Rice88, p.147]

$$\begin{aligned} \mathrm{E}\left\{\frac{Y}{X}\right\} &\approx \left(\frac{\mathrm{E}\{Y\}}{\mathrm{E}\{X\}} + \mathrm{Var}\{X\} \cdot \frac{\mathrm{E}\{Y\}}{(\mathrm{E}\{X\})^3}\right) \\ &\approx \frac{\mathrm{E}\{Y\}}{\mathrm{E}\{X\}} \cdot \left(\frac{(\mathrm{E}\{X\})^2 + \mathrm{Var}\{X\}}{(\mathrm{E}\{X\})^2}\right) \\ &\approx \frac{\mathrm{E}\{Y\}}{\mathrm{E}\{X\}} \cdot \left(\frac{\mathrm{E}\left\{(X)^2\right\}}{(\mathrm{E}\{X\})^2}\right) \end{aligned} \quad . \tag{A.46}$$

Using (A.46) the approximation of the mean SINR writes

$$
\begin{aligned}
&\overline{SINR}_{1\times 1 SISO} \\
&= \frac{\mathrm{E}\left\{P_{sig}\right\}}{\mathrm{E}\left\{P_{int}\right\}} \cdot \left(\frac{\mathrm{E}\left\{\left(P_{int}\right)^2\right\}}{\left(\mathrm{E}\left\{P_{int}\right\}\right)^2} \right) \\
&= \frac{\overline{P}_{sig}}{\overline{P}_{int}} \cdot \left(\frac{\mathrm{E}\left\{\left(|h_3|^2 \cdot \overline{P}_{dom} + \frac{\overline{P}_{dom}}{\overline{INR}}\right)^2\right\}}{\left(\mathrm{E}\left\{|h_3|^2 \cdot \overline{P}_{dom} + \frac{\overline{P}_{dom}}{\overline{INR}}\right\}\right)^2} \right) \\
&= \frac{\overline{P}_{sig}}{\overline{P}_{int}} \cdot \left(\frac{\mathrm{E}\left\{\left(|h_3|^2 \cdot \overline{INR} + 1\right)^2\right\}}{\left(\mathrm{E}\left\{|h_3|^2 \cdot \overline{INR} + 1\right\}\right)^2} \right) \\
&= \frac{\overline{P}_{sig}}{\overline{P}_{int}} \cdot \left(\frac{\mathrm{E}\left\{\left(|h_3|^2\right)^2\right\} \cdot \left(\overline{INR}\right)^2 + 2 \cdot \mathrm{E}\left\{|h_3|^2\right\} \cdot \overline{INR} + 1}{\left(\mathrm{E}\left\{|h_3|^2\right\} \cdot \overline{INR} + 1\right)^2} \right) \\
&= \frac{\overline{P}_{sig}}{\overline{P}_{int}} \cdot \left(\left(\frac{\overline{INR}}{\overline{INR}+1} \right)^2 + 1 \right)
\end{aligned}
\quad . \tag{A.47}
$$

A.2.2 1×2 SIMO-MRC

With MRC the signal voltages are combined coherently. The mean signal power after 2 branch MRC is thus four times the mean single branch power [Vaug03, p. 572], *i.e.*

$$\mathrm{E}\left\{P_{sig}\,|_{2MRC}\right\} = 4 \cdot \overline{P}_{sig} \quad . \tag{A.48}$$

The interference term after MRC is the sum of the interference terms on each branch, *i.e.*

$$P_{int}\,|_{2MRC} = \left(|h_3|^2 + |h_4|^2\right) \cdot \overline{P}_{dom} + 2 \cdot \frac{\overline{P}_{dom}}{\overline{INR}} \quad , \tag{A.49}$$

where $|h_4|$ is a Rayleigh fading variable independent of $|h_1|$ and $|h_3|$. The expec-

tation over the interference power is

$$\begin{aligned}\mathrm{E}\left\{P_{int}\,|_{2MRC}\right\} &= \mathrm{E}\left\{\left(|h_3|^2+|h_4|^2\right)\cdot\overline{P}_{dom}+2\cdot\frac{\overline{P}_{dom}}{\overline{INR}}\right\}\\ &= \left(\mathrm{E}\left\{|h_3|^2\right\}+\mathrm{E}\left\{|h_4|^2\right\}\right)\cdot\overline{P}_{dom}+2\cdot\frac{\overline{P}_{dom}}{\overline{INR}}\\ &= 2\cdot\left(\overline{P}_{dom}+\frac{\overline{P}_{dom}}{\overline{INR}}\right)\end{aligned} \quad . \tag{A.50}$$

Hence the ratio of mean signal power to mean interference power is double the ratio of the single branch case in (A.44), *i.e.*

$$\begin{aligned}\frac{\mathrm{E}\left\{P_{sig}\,|_{2MRC}\right\}}{\mathrm{E}\left\{P_{int}\,|_{2MRC}\right\}} &= \frac{4\cdot\overline{P}_{sig}}{2\cdot\left(\overline{P}_{dom}+\frac{\overline{P}_{dom}}{\overline{INR}}\right)}\\ &= 2\cdot\frac{\mathrm{E}\left\{P_{sig}\right\}}{\mathrm{E}\left\{P_{int}\right\}}\\ &= 2\cdot\frac{\overline{P}_{sig}}{\overline{P}_{int}}\end{aligned} \quad . \tag{A.51}$$

Similarly as in the 1×1 SISO reference case the mean SINR can be approximated

using Taylor Series expansion, *i.e.*

$$
\begin{aligned}
&\overline{SINR}_{1\times 2SIMO-MRC} \\
&= \frac{\mathrm{E}\left\{P_{sig}\,|_{2MRC}\right\}}{\mathrm{E}\left\{P_{int}\,|_{2MRC}\right\}} \cdot \left(\frac{\mathrm{E}\left\{\left(P_{int}\,|_{2MRC}\right)^2\right\}}{\left(\mathrm{E}\left\{P_{int}\,|_{2MRC}\right\}\right)^2} \right) \\
&= \frac{2\cdot\overline{P}_{sig}}{\overline{P}_{int}} \cdot \frac{E\left\{\left(\left(|h_3|^2+|h_4|^2\right)\cdot\overline{P}_{dom}+2\cdot\frac{\overline{P}_{dom}}{\overline{INR}}\right)^2\right\}}{\left(E\left\{\left(|h_3|^2+|h_4|^2\right)\cdot\overline{P}_{dom}+2\cdot\frac{\overline{P}_{dom}}{\overline{INR}}\right\}\right)^2} \\
&= \frac{2\cdot\overline{P}_{sig}}{\overline{P}_{int}} \cdot \frac{E\left\{\left(\left(|h_3|^2+|h_4|^2\right)\cdot\overline{INR}+2\right)^2\right\}}{\left(E\left\{\left(|h_3|^2+|h_4|^2\right)\cdot\overline{INR}+2\right\}\right)^2} \\
&= \frac{2\cdot\overline{P}_{sig}}{\overline{P}_{int}} \cdot \frac{E\left\{\left(\begin{array}{l}\left(\begin{array}{l}\left(|h_3|^2\right)^2 \\ +2\cdot|h_3|^2|h_4|^2 \\ +\left(|h_4|^2\right)^2\end{array}\right)\cdot\left(\overline{INR}\right)^2 \\ +4\cdot\left(|h_3|^2+|h_4|^2\right)\cdot\overline{INR}+4\end{array}\right)\right\}}{\left(E\left\{\left(|h_3|^2+|h_4|^2\right)\cdot\overline{INR}+2\right\}\right)^2} \\
&= \frac{2\cdot\overline{P}_{sig}}{\overline{P}_{int}} \cdot \frac{\left(\begin{array}{l}\left(\begin{array}{l}E\left\{\left(|h_3|^2\right)^2\right\} \\ +2\cdot E\left\{|h_4|^2\right\}\cdot E\left\{|h_3|^2\right\} \\ +E\left\{\left(|h_4|^2\right)^2\right\}\end{array}\right)\cdot\left(\overline{INR}\right)^2 \\ +4\cdot\left(E\left\{|h_3|^2\right\}+E\left\{|h_4|^2\right\}\right)\cdot\overline{INR}+4\end{array}\right)}{\left(\left(E\left\{|h_3|^2\right\}+E\left\{|h_4|^2\right\}\right)\cdot\overline{INR}+2\right)^2} \\
&= \frac{2\cdot\overline{P}_{sig}}{\overline{P}_{int}} \cdot \frac{\left((2+2+2)\cdot\left(\overline{INR}\right)^2+4\cdot(1+1)\cdot\overline{INR}+4\right)}{\left((1+1)\cdot\overline{INR}+2\right)^2} \\
&= \frac{2\cdot\overline{P}_{sig}}{\overline{P}_{int}} \cdot \frac{\left(\frac{3}{2}\cdot\left(\overline{INR}\right)^2+2\cdot\overline{INR}+1\right)}{\left(\overline{INR}+1\right)^2} \\
&= \frac{2\cdot\overline{P}_{sig}}{\overline{P}_{int}} \cdot \left(\frac{\left(\overline{INR}\right)^2}{2\cdot\left(\overline{INR}+1\right)^2}+1 \right)
\end{aligned}
\tag{A.52}
$$

which, using (A.44), can also as be written as

$$\begin{aligned}\overline{SINR}_{1\times 2SIMO-MRC} &= 2\cdot\frac{\overline{SNR}}{\left(\overline{INR}+1\right)}\cdot\left(\frac{\left(\overline{INR}\right)^2}{2\cdot\left(\overline{INR}+1\right)^2}+1\right)\\ &= \overline{SNR}\cdot\left(\frac{\left(\overline{INR}\right)^2+2\cdot\left(\overline{INR}+1\right)^2}{\left(\overline{INR}+1\right)^3}\right)\end{aligned} \quad . \tag{A.53}$$

Looking at the asymptotic behaviour

$$\lim_{\overline{INR}\downarrow 0}\overline{SINR}_{1\times 2SIMO-MRC} = 2\cdot\overline{SNR} \quad , \tag{A.54}$$

$$\lim_{\overline{INR}\uparrow\infty}\overline{SINR}_{1\times 2SIMO-MRC} = 0 \quad , \tag{A.55}$$

which shows that if the dominant interferer's power goes to 0, the mean SINR approaches the mean *signal to noise ratio* (SNR) times the dual branch array gain. If the dominant interferer's power, however, approaches ∞, the mean SINR approaches 0.

A.2.3 1×2 SIMO-OPC

Based on [Vill99, (18)] the SINR cdf in a 1×2 SIMO-OPC case is derived as

$$\begin{aligned}&\Pr\left(SINR_{1\times 2SIMO-OPC} < SINR_{ref}\right)\\ &= \frac{1}{2\cdot\overline{INR}}\cdot e^{\frac{-SINR_{ref}\cdot\left(1+2\cdot\overline{INR}\right)}{\overline{SNR}}} - \left(\frac{1}{2\cdot\overline{INR}}+1\right)\cdot e^{\frac{-SINR_{ref}}{\overline{SNR}}}+1\end{aligned} \quad . \tag{A.56}$$

The pdf writes

$$\begin{aligned}&\mathrm{pr}\left(SINR_{1\times 2SIMO-OPC}\right) =\\ &-\frac{\left(1+2\cdot\overline{INR}\right)}{2\cdot\overline{INR}\cdot\overline{SNR}}\cdot e^{\frac{-SINR_{1\times 2SIMO-OPC}\cdot\left(1+2\cdot\overline{INR}\right)}{\overline{SNR}}}\\ &+\left(\frac{1}{2\cdot\overline{INR}\cdot\overline{SNR}}+\frac{1}{\overline{SNR}}\right)\cdot e^{\frac{-SINR_{1\times 2SIMO-OPC}}{\overline{SNR}}}\end{aligned} \quad . \tag{A.57}$$

Thus the first moment can be expressed as

$$\begin{aligned}
&\mathrm{E}\left\{SINR_{1\times 2SIMO-OPC}\right\} \\
&= \int_0^{+\infty} \left(\begin{array}{l} SINR_{1\times 2SIMO-OPC} \\ \cdot \,\mathrm{pr}\left(SINR_{1\times 2SIMO-OPC}\right) \end{array} \right) \cdot dSINR_{1\times 2SIMO-OPC} \\
&= -\frac{\left(1+2\cdot\overline{INR}\right)}{2\cdot\overline{INR}\cdot\overline{SNR}} \\
&\cdot \int_0^{+\infty} \left(\begin{array}{l} SINR_{1\times 2SIMO-OPC} \\ \cdot\, e^{\frac{-SINR_{1\times 2SIMO-OPC}\cdot\left(1+2\cdot\overline{INR}\right)}{\overline{SNR}}} \end{array} \right) \cdot dSINR_{1\times 2SIMO-OPC} \\
&+ \left(\frac{1}{2\cdot\overline{INR}\cdot\overline{SNR}} + \frac{1}{\overline{SNR}} \right) \\
&\cdot \int_0^{+\infty} \left(\begin{array}{l} SINR_{1\times 2SIMO-OPC} \\ \cdot\, e^{\frac{-SINR_{1\times 2SIMO-OPC}}{\overline{SNR}}} \end{array} \right) \cdot dSINR_{1\times 2SIMO-OPC}
\end{aligned} \qquad \text{(A.58)}$$

Using [Papu94, p.312]

$$\begin{aligned}
\int_0^{+\infty} x\cdot e^{-ax}\cdot dx &= \left[\frac{-ax-1}{a^2}\cdot e^{-ax}\right]_0^{+\infty} \\
&= \frac{1}{a^2}
\end{aligned} \quad , \qquad \text{(A.59)}$$

the first moment simplifies to

$$\begin{aligned}
&\mathrm{E}\left\{SINR_{1\times 2SIMO-OPC}\right\} \\
&= -\frac{\left(1+2\cdot\overline{INR}\right)}{2\cdot\overline{INR}\cdot\overline{SNR}} \frac{\left(\overline{SNR}\right)^2}{\left(1+2\cdot\overline{INR}\right)^2} \\
&+ \left(\frac{1}{2\cdot\overline{INR}\cdot\overline{SNR}} + \frac{1}{\overline{SNR}} \right) \cdot \left(\overline{SNR}\right)^2 \\
&= -\frac{\overline{SNR}}{2\cdot\overline{INR}\cdot\left(1+2\cdot\overline{INR}\right)} + \left(\frac{\overline{SNR}}{2\cdot\overline{INR}} + \overline{SNR} \right) \\
&= \overline{SNR}\cdot\left(\frac{1}{2\cdot\overline{INR}} + 1 - \frac{1}{2\cdot\overline{INR}\cdot\left(1+2\cdot\overline{INR}\right)} \right) \\
&= \overline{SNR}\cdot\left(\frac{\left(1+2\cdot\overline{INR}\right)^2 - 1}{2\cdot\overline{INR}\cdot\left(1+2\cdot\overline{INR}\right)} \right) \\
&= \overline{SNR}\cdot\left(\frac{2+2\cdot\overline{INR}}{1+2\cdot\overline{INR}} \right)
\end{aligned} \quad . \qquad \text{(A.60)}$$

Looking at the asymptotic behaviour,

$$\lim_{\overline{INR}\downarrow 0} \overline{SINR}_{1\times 2SIMO-OPC} = 2\cdot\overline{SNR} \quad , \tag{A.61}$$

$$\lim_{\overline{INR}\uparrow \infty} \overline{SINR}_{1\times 2SIMO-OPC} = \overline{SNR} \quad , \tag{A.62}$$

which shows that if the dominant interferer's power goes to 0, the mean SINR approaches the mean SNR times dual branch array gain as obtained in (A.54) for the MRC. However, if the dominant interferer's power approaches ∞, the mean SINR approaches the mean SNR at one branch. This means that one degree of freedom is used for interference suppression. Further, comparison with (A.55) shows that the benefit of OPC over MRC approaches ∞ with increasing dominant interferer's power.

More specifically, using the results from (A.53) and (A.60) the array (processing) gain of OPC over the MRC is in the presence of one dominant interferer therewith

$$\begin{aligned}
&\beta_{\substack{1\times 2SIMO-OPC,\\ 1\times 2SIMO-MRC}} \\
&= \frac{\overline{SNR}\cdot\left(\frac{2+2\cdot\overline{INR}}{1+2\cdot\overline{INR}}\right)}{\overline{SNR}\cdot\left(\frac{\left(\overline{INR}\right)^2+2\cdot\left(\overline{INR}+1\right)^2}{\left(\overline{INR}+1\right)^3}\right)} \\
&= \frac{\left(2+2\cdot\overline{INR}\right)\left(\overline{INR}+1\right)^3}{\left(\left(\overline{INR}\right)^2+2\cdot\left(\overline{INR}+1\right)^2\right)\left(1+2\cdot\overline{INR}\right)} \\
&= \frac{2\cdot\left(\overline{INR}+1\right)^4}{\left(3\cdot\left(\overline{INR}\right)^2+4\cdot\left(\overline{INR}\right)+2\right)\left(1+2\cdot\overline{INR}\right)} \\
&= \frac{2\cdot\left(\overline{INR}+1\right)^4}{6\cdot\left(\overline{INR}\right)^3+11\cdot\left(\overline{INR}\right)^2+8\cdot\left(\overline{INR}\right)+2} \quad .
\end{aligned} \tag{A.63}$$

A.2.4 2×2 SMP$_{dual}$-OPC

The SMP$_{dual}$ situation can be seen as 1×2 SIMO-OPC situation, where dominant interference is coming from the spatial multiplexed co-stream. It is assumed that the transmit power is evenly split between the two tx antennas. This leads to

$$\overline{SNR} = \frac{\overline{SINR}_{branch}}{2} \quad , \tag{A.64}$$

where $\overline{SINR}_{branch}$ is the mean SINR per branch as introduced in the pure AWGN interference situation related to (A.7). The SINR cdf per stream is now given by

(A.56) and the first moment by (A.60). One might wonder what it costs to switch on a second stream. Pricing it in terms of mean SINR this question can be answered by comparing the first moment of 2×2 SMP$_{dual}$-OPC, *i.e.*

$$\overline{SINR}_{2\times 2SMP_{dual}-OPC} = \overline{SNR} \cdot \left(\frac{2 + 2 \cdot \overline{INR}}{1 + 2 \cdot \overline{INR}} \right) \quad , \tag{A.65}$$

with the first moment of 2×2 SMP$_{sel}$ as given in (A.36), *i.e.*

$$\begin{aligned} \overline{SINR}_{2\times 2SMP_{sel}} &= \left(2 + \frac{3}{4} \right) \cdot \overline{SINR}_{branch} \\ &= 2 \cdot \left(2 + \frac{3}{4} \right) \cdot \overline{SNR} \end{aligned} \quad , \tag{A.66}$$

where the second step made use of (A.64). Hence the cost of a second stream in terms of mean SINR degradation on each stream is

$$\begin{aligned} \beta_{\substack{2\times 2SMP_{dual}-OPC, \\ 2\times 2SMP_{sel}}} &= \frac{\overline{SNR} \cdot \left(\frac{2+2\cdot\overline{INR}}{1+2\cdot\overline{INR}} \right)}{2 \cdot \left(2 + \frac{3}{4} \right) \cdot \overline{SNR}} \\ &= \frac{\left(4 + 4 \cdot \overline{INR} \right)}{\left(11 + 22 \cdot \overline{INR} \right)} \end{aligned} \quad , \tag{A.67}$$

with asymptotic behaviour as

$$\begin{aligned} \lim_{\overline{INR}\downarrow 0} \beta_{\substack{2\times 2SMP_{dual}-OPC, \\ 2\times 2SMP_{sel}}} &= \frac{4}{11} \\ &\approx -4.39 \text{ dB} \end{aligned} \quad , \tag{A.68}$$

$$\begin{aligned} \lim_{\overline{INR}\uparrow \infty} \beta_{\substack{2\times 2SMP_{dual}-OPC, \\ 2\times 2SMP_{sel}}} &= \frac{2}{11} \\ &\approx -7.40 \text{ dB} \end{aligned} \quad . \tag{A.69}$$

Similarly the cost of co-stream transmission can be obtained with respect to 1×1 SISO, 1×2 SIMO, 2×1 CLM1 and 2×2 CLM1, *i.e.*

$$\begin{aligned} \beta_{\substack{2\times 2SMP_{dual}-OPC, \\ 1\times 1SISO}} &= \frac{\overline{SNR} \cdot \left(\frac{2+2\cdot\overline{INR}}{1+2\cdot\overline{INR}} \right)}{2 \cdot \overline{SNR}} \\ &= \left(\frac{1 + \overline{INR}}{1 + 2 \cdot \overline{INR}} \right) \end{aligned} \quad , \tag{A.70}$$

$$\begin{aligned} \beta_{\substack{2\times 2SMP_{dual}-OPC, \\ 1\times 2SIMO}} &= \frac{\overline{SNR} \cdot \left(\frac{2+2\cdot\overline{INR}}{1+2\cdot\overline{INR}} \right)}{4 \cdot \overline{SNR}} \\ &= \left(\frac{1 + \overline{INR}}{2 + 4 \cdot \overline{INR}} \right) \end{aligned} \quad , \tag{A.71}$$

$$\beta_{\substack{2\times 2SMP_{dual}-OPC,\\ 2\times 1CLM1}} = \frac{\overline{SNR}\cdot\left(\frac{2+2\cdot\overline{INR}}{1+2\cdot\overline{INR}}\right)}{\left(1+\frac{1}{\sqrt{2}}\right)\cdot 2\cdot\overline{SNR}} = \frac{\left(1+\overline{INR}\right)}{\left(1+\frac{1}{\sqrt{2}}\right)\cdot\left(1+2\cdot\overline{INR}\right)} \quad , \tag{A.72}$$

$$\beta_{\substack{2\times 2SMP_{dual}-OPC,\\ 2\times 2CLM1}} = \frac{\overline{SNR}\cdot\left(\frac{2+2\cdot\overline{INR}}{1+2\cdot\overline{INR}}\right)}{2\cdot\left(2+\frac{3}{32}\cdot\pi^2\right)\cdot\overline{SNR}} = \frac{1+\overline{INR}}{\left(1+2\cdot\overline{INR}\right)\cdot\left(2+\frac{3}{32}\cdot\pi^2\right)} \quad . \tag{A.73}$$

As can be seen from the derivations in Chapter 3, the value of $\overline{INR}$ depends on the amount of orthogonal code resources reused on the co-stream. In a flat fading channel only the co-stream code resource that is identical to the code resource used on the desired stream causes interference. Denoting the number of co-stream code resources as $\tilde{N}_{codeco}$ the mean dominant to AWGN interference ratio is

$$\overline{INR} = \frac{1}{\tilde{N}_{codeco}}\cdot\overline{SNR} = \frac{1}{\tilde{N}_{codeco}}\cdot\frac{\overline{SINR}_{branch}}{2} \quad . \tag{A.74}$$

A.3 Further Useful Bounds

Till now all the derivations were based on the assumption of a flat Rayleigh fading propagation environment with decorrelated antenna elements at either end of the link. Interference was pure AWGN or AWGN plus one dominant interfering component, also decorrelated over the rx antenna elements. The following gives additional useful bounds lifting some of the assumptions used in Section A.1 and Section A.2.

A.3.1 2×2 Branch Combining in Correlated Environments

A flat fading environment is assumed with correlation at one or both ends of the link. Interference is AWGN, uncorrelated over the rx antenna elements.

In (A.25) it was observed that the 2×2 branch combining configuration experienced a reduced array gain with respect to 4 branch combining. The reason being that tx phase alignment of the signal seen at 2 rx antennas is inherently in an

uncorrelated environment suboptimum with respect to each individual rx antenna. However, correlation at either end of the link leads to a situation where the jointly optimum weights are also individually optimum, so that the 2×2 configuration achieves the same array gain as the 4 branch combiner, *i.e.*

$$\begin{aligned} \beta_{2\times 2branch,corr} &= 4 \\ &\approx 6.01 \text{ dB} \end{aligned} \quad . \tag{A.75}$$

This comes, however, at the expense of the achievable diversity order. Further details can be found in [Ande98].

A.3.2 1×2 SIMO-MRC with Interference Correlation between the Antenna Elements

The SINR after N_{branch} MRC combining with correlated interference over the branches is in [Vaug03, p. 572] given as

$$\begin{aligned} &\overline{SINR}_{N_{branch}}\Big|_{\substack{correlated \\ noise}} \\ &= \frac{(N_{branch})^2 \cdot \overline{P}_{sig}}{(N_{branch})^2 \cdot \overline{P}_{intcor} + N_{branch} \cdot \overline{P}_{intuncor}} \end{aligned} \quad , \tag{A.76}$$

where $\overline{P}_{intcor}$ represents the mean correlated interference branch power and $\overline{P}_{intuncor}$ represents the remaining uncorrelated mean interference power. Let the overall per branch mean interference power be given as $\overline{P}_{int}$. Further let the amount of correlation be specified by the envelope correlation coefficient $|\rho_{rx}|$. Correlated and uncorrelated interference power are then given by [Tran04]

$$\overline{P}_{intcor} = |\rho_{rx}|^2 \cdot \overline{P}_{int} \quad , \tag{A.77}$$

and

$$\overline{P}_{intuncor} = \left(1 - |\rho_{rx}|^2\right) \cdot \overline{P}_{int} \quad . \tag{A.78}$$

Hence (A.76) can be rewritten as

$$\begin{aligned} &\overline{SINR}_{N_{branch}}\Big|_{\substack{correlated \\ noise}} \\ &= \frac{(N_{branch})^2}{(N_{branch})^2 \cdot |\rho_{rx}|^2 + N_{branch} \cdot \left(1 - |\rho_{rx}|^2\right)} \cdot \frac{\overline{P}_{sig}}{\overline{P}_{int}} \end{aligned} \quad . \tag{A.79}$$

Looking at a specific 1×2 SIMO-MRC case with $|\rho_{rx}| = 0.3$, the mean gain over 1×1 SISO can for relatively stable interference be approximated as

$$\begin{aligned} &\beta_{1\times 2 SIMO-MRC, correlated\, noise} \\ &\approx \frac{(2)^2}{(2)^2 \cdot |0.3|^2 + 2 \cdot \left(1 - |0.3|^2\right)} \\ &\approx 2.63 \text{ dB} \end{aligned} \quad , \tag{A.80}$$

where the approximation is due to $\frac{\overline{P}_{sig}}{\overline{P}_{int}} \approx \overline{SINR}_{branch}$.

A.3.3 2×1 CLM1 Array Gain in Frequency Selective Fading

The array gain of 2×1 CLM1 in a frequency selective Rayleigh fading environment for uncorrelated tx antennas and in connection with a RAKE receiver can on the basis of [Hama02], [Hott03, (11.40)] be written as

$$\begin{aligned} &\beta_{2\times 1 CLM1, frequency\_selective} \\ &= 1 + \frac{1}{\sqrt{2}} \cdot \sum_{l_1=1}^{N_L} E\left\{|h_{l_1}|^2\right\} \\ &\cdot \prod_{l_2=1, l_2\neq l_1}^{N_L} \frac{\left(E\left\{|h_{l_1}|^2\right\}\right)^2}{\left(E\left\{|h_{l_1}|^2\right\}\right)^2 - \left(E\left\{|h_{l_2}|^2\right\}\right)^2} \end{aligned} \quad , \tag{A.81}$$

where, different from the previous sections, the $E\left\{|h_l|^2\right\}$ represent the mean tap powers of the corresponding PDP, and N_l represents the total number of resolvable Rayleigh fading taps. The tap powers are normalised so that

$$\sum_{l_1=1}^{N_L} E\left\{|h_{l_1}|^2\right\} = 1 \quad . \tag{A.82}$$

Evaluating (A.81) using the standard ITU-Pedestrian A and ITU-Vehicular A PDPs [ITU97] the 2×1 CLM1 gain is given by

$$\beta_{2\times 1 CLM1, PeA} \approx 2.31 \text{ dB} \quad , \tag{A.83}$$

$$\beta_{2\times 1 CLM1, VhA} \approx 1.67 \text{ dB} \quad , \tag{A.84}$$

where a comparison with (A.18) reveals that the 2×1 CLM1 array gain in flat Rayleigh fading and in a ITU-Pedestrian A fading environment are nearly identical.

Appendix B

SINR Formulation - Intermediate Steps

Section B.1 and Section B.2 provide the intermediate steps used to derive the SINR expressions presented in Chapter 3. Section B.3 shows how the SINR formulation can be extended to additionally describe scenarios with multiple scrambling codes used per sector. Besides, in Section B.4 the derived RAKE receiver SINR expression is compared with the expressions in [Rami03a], [Rami03b].

B.1 Space-Time Rx Filters

The mean vector and the received signal covariance matrix are the two elements needed to formulate the post despreading RAKE and the post despreading MMSE receive filters. The following derives the elements inside the mean vector and inside the received signal covariance matrix, as well as the elements inside their chip averaged representations. The statistical properties of data sequences and spreading codes play a vital role in the derivations and are therefore outlined first.

B.1.1 Spreading Code and Data Sequence Properties

The expectations over the spreading code chips are

$$\mathrm{E}_c\left\{c^{k,i}\left[q\right]\right\} = 0 \;\forall\; k, i \quad . \tag{B.1}$$

Using sub indexes to denote potentially different realisations of an index, *e.g.* i_1 and i_2 with no further restrictions indicate two scrambling code indexes that are

either identical or different. The expectation over the product of two code chips is given by

$$\mathrm{E}_c\left\{c^{k_1,i_1}\left[q_1\right]\cdot c^{k_2,i_2}\left[q_2\right]\right\}=0\,\forall\,q,k,i \quad , \tag{B.2}$$

which is, on one hand, based on the i.i.d assumption from Section 3.2 and on the other hand on the fact that the code chips are limited to the complex values $\pm\frac{1}{\sqrt{2}}\pm\frac{1}{\sqrt{2}}j$.

Taking the expectation of a code chip and a complex conjugate code chip delivers

$$\begin{aligned}&\forall\,q,k,i\\&\mathrm{E}_c\left\{c^{k_1,i_1}\left[q_1\right]\cdot\left(c^{k_2,i_2}\left[q_2\right]\right)^*\right\}=\delta\left(q_1-q_2\right)\cdot\delta\left(k_1-k_2\right)\cdot\delta\left(i_1-i_2\right)\end{aligned} \quad , \tag{B.3}$$

which basically means that everything but the expectation over a complex conjugate chip pair has an expectation of zero, the expectation over a complex conjugate chip pair and thereby the code chip power, however, is one.

Further, the expectation over the product of four code chips will be required when looking at the post despreading received signal covariance matrix, *i.e.*

$$\mathrm{E}_c\left\{c^{k_1,i_1}\left[q_1\right]\cdot\left(c^{k_2,i_2}\left[q_2\right]\right)^*\cdot c^{k_3,i_3}\left[q_3\right]\cdot\left(c^{k_4,i_4}\left[q_4\right]\right)^*\right\} \quad . \tag{B.4}$$

On the condition $(q_1\neq q_4\vee q_2\neq q_3\vee i_1\neq i_4\vee i_2\neq i_3)$ it is possible to split the single expectation into a product of expectations due to independence of the spreading codes across chips and sectors, *i.e.*

$$\begin{aligned}&\forall\,k\ \wedge\ (q_1\neq q_4\vee q_2\neq q_3\vee i_1\neq i_4\vee i_2\neq i_3)\\&\mathrm{E}_c\left\{c^{k_1,i_1}\left[q_1\right]\cdot\left(c^{k_2,i_2}\left[q_2\right]\right)^*\cdot c^{k_3,i_3}\left[q_3\right]\cdot\left(c^{k_4,i_4}\left[q_4\right]\right)^*\right\}\\&=\mathrm{E}_c\left\{c^{k_1,i_1}\left[q_1\right]\cdot\left(c^{k_2,i_2}\left[q_2\right]\right)^*\right\}\cdot\mathrm{E}_c\left\{c^{k_3,i_3}\left[q_3\right]\cdot\left(c^{k_4,i_4}\left[q_4\right]\right)^*\right\}\\&=\delta\left(q_1-q_2\right)\cdot\delta\left(k_1-k_2\right)\cdot\delta\left(i_1-i_2\right)\cdot\delta\left(q_3-q_4\right)\cdot\delta\left(k_3-k_4\right)\cdot\delta\left(i_3-i_4\right)\end{aligned} \quad . \tag{B.5}$$

This basically expresses that for a product of two different complex conjugate chip pairs the expectation turns to one, but is zero if two complex conjugate chip pairs do not exist. Taking the complementary case, which can be seen as dealing with two chip aligned code pairs from the same sector, the expectation delivers

$$\begin{aligned}&\forall\,k\ \wedge\ (q_1=q_4\wedge q_2=q_3\wedge i_1=i_4\wedge i_2=i_3)\\&\mathrm{E}_c\left\{c^{k_1,i_1}\left[q_1\right]\cdot\left(c^{k_2,i_2}\left[q_2\right]\right)^*\cdot c^{k_3,i_3}\left[q_3\right]\cdot\left(c^{k_4,i_4}\left[q_4\right]\right)^*\right\}\\&=\mathrm{E}_c\left\{c^{k_1,i_1}\left[q_1\right]\cdot\left(c^{k_2,i_1}\left[q_2\right]\right)^*\cdot c^{k_3,i_1}\left[q_2\right]\cdot\left(c^{k_4,i_1}\left[q_1\right]\right)^*\right\}\\&=\delta\left(k_1-k_2\right)\cdot\delta\left(k_1-k_3\right)\cdot\delta\left(k_1-k_4\right)\end{aligned} \quad , \tag{B.6}$$

where the second line exploits the equality conditions. Moreover, the expectation cannot be split into a product of expectations without imposing an additional restriction on the relationship between q_1 and q_2.

The data sequence corresponding to spreading code resource k, i and virtual channel m is denoted $\left\{d_m^{k,i}\right\}$. In Section 3.2 it is assumed that its symbols are i.i.d between the points of a complex constellation diagram, between different channelisation code resources k, between different scrambling code resources i, and between different virtual broadcast channels m. Further, they are normalised to a mean power of one. Thus the expectations over the data symbol sequence can be summarised as

$$\mathrm{E}_d\left\{d_m^{k,i}\left[p\right]\right\} = 0 \quad , \tag{B.7}$$

and

$$\begin{aligned} &\forall\, p, k, i, m \\ &\mathrm{E}_d\left\{d_{m_1}^{k_1,i_1}\left[p_1\right]\left(d_{m_2}^{k_2,i_2}\left[p_2\right]\right)^*\right\} \\ &= \delta\left(p_1 - p_2\right) \cdot \delta\left(k_1 - k_2\right) \cdot \delta\left(i_1 - i_2\right) \cdot \delta\left(m_1 - m_2\right) \quad . \end{aligned} \tag{B.8}$$

B.1.2 The Post Despreading Receiver Filter Input Vector

Stacking N_{sf} consecutive observations of the received signal vector $\mathbf{r}\left[q\right]$ next to each other and right multiplying with the complex conjugate of the spreading code vector $\mathbf{c}^{K,I}\left[p\right]$ delivers the post despreading receive filter input vector $\mathbf{z}_M^{K,I}\left[p\right]$ for

the desired symbol in the centre of a decoding block, *i.e.*

$$\mathbf{z}_M^{K,I}[p] =$$
$$\begin{bmatrix} \begin{bmatrix} r_1\left[q-\frac{N_{FIR}-1}{2}\right] & r_1\left[q-\frac{N_{FIR}-1}{2}+1\right] & \cdots & r_1\left[q-\frac{N_{FIR}-1}{2}+N_{sf}-1\right] \\ r_1\left[q-\frac{N_{FIR}-1}{2}+1\right] & r_1\left[q-\frac{N_{FIR}-1}{2}+2\right] & \cdots & \vdots \\ \vdots & \vdots & \ddots & \vdots \\ r_1\left[q+\frac{N_{FIR}-1}{2}\right] & \cdots & \cdots & r_1\left[q+\frac{N_{FIR}-1}{2}+N_{sf}-1\right] \end{bmatrix} \\ \begin{bmatrix} r_2\left[q-\frac{N_{FIR}-1}{2}\right] & r_2\left[q-\frac{N_{FIR}-1}{2}+1\right] & \cdots & r_2\left[q-\frac{N_{FIR}-1}{2}+N_{sf}-1\right] \\ r_2\left[q-\frac{N_{FIR}-1}{2}+1\right] & r_2\left[q-\frac{N_{FIR}-1}{2}+2\right] & \cdots & \vdots \\ \vdots & \vdots & \ddots & \vdots \\ r_2\left[q+\frac{N_{FIR}-1}{2}\right] & \cdots & \cdots & r_2\left[q+\frac{N_{FIR}-1}{2}+N_{sf}-1\right] \end{bmatrix} \\ \begin{bmatrix} r_{N_{rx}}\left[q-\frac{N_{FIR}-1}{2}\right] & r_{N_{rx}}\left[q-\frac{N_{FIR}-1}{2}+1\right] & \cdots & r_{N_{rx}}\left[q-\frac{N_{FIR}-1}{2}+N_{sf}-1\right] \\ r_{N_{rx}}\left[q-\frac{N_{FIR}-1}{2}+1\right] & r_{N_{rx}}\left[q-\frac{N_{FIR}-1}{2}+2\right] & \cdots & \vdots \\ \vdots & \vdots & \ddots & \vdots \\ r_{N_{rx}}\left[q+\frac{N_{FIR}-1}{2}\right] & \cdots & \cdots & r_{N_{rx}}\left[q+\frac{N_{FIR}-1}{2}+N_{sf}-1\right] \end{bmatrix} \end{bmatrix} \cdot \begin{bmatrix} \left(c^{K,I}[q]\right)^* \\ \left(c^{K,I}[q+1]\right)^* \\ \vdots \\ \left(c^{K,I}[q+N_{sf}-1]\right)^* \end{bmatrix}$$

(B.9)

where the term $\pm\left[\frac{N_{FIR}-1}{2}\right]$ indicates that $\frac{N_{FIR}-1}{2} = N_L - 1$ despread samples before and after the desired chip are considered in the estimation process. When comparing (B.9) with the equivalent representation in Figure 3.2 it should be noted that in (B.9) the 'oldest' received signal contribution is in the top left corner with time running to the bottom right, whereas the time representation in Figure 3.2 is in reversed order.

Using the assumption that the channel from all transmit antennas to all receive antennas is stationary during one decoding block, $\mathbf{z}_M^{K,I}[p]$ can be rewritten as

$$\mathbf{z}_M^{K,I}[p] = \sum_{i=1}^{N_{\text{sec}}} \sum_{m=1}^{N_{vir}} \mathbf{H}_m^i \cdot \mathbf{S}_m^i[p] \cdot \left(\mathbf{c}^{K,I}[p]\right)^* + \mathbf{\Psi}[p] \cdot \left(\mathbf{c}^{K,I}[p]\right)^*,$$

(B.10)

where $\mathbf{\Psi}[p]$ with the dimensions $N_{FIR} \cdot N_{rx} \times N_{sf}$ contains N_{sf} i.i.d realisations of the thermal noise vector first defined in connection with (3.24). Further, $\mathbf{S}_m^i[p]$, with the dimensions $N_{FIR} \cdot N_{rx} \times N_{sf}$, contains N_{sf} consecutive realisations of the combined chip sequence from sector i over virtual channel m. It was first defined

in (3.9), and its elements are given by

$$\mathbf{S}_m^i[p] = \begin{bmatrix} s_m^i\left[q-\frac{N_{FIR}-1}{2}\right] & s_m^i\left[q-\frac{N_{FIR}-1}{2}+1\right] & \cdots & s_m^i\left[q-\frac{N_{FIR}-1}{2}+N_{sf}-1\right] \\ s_m^i\left[q-\frac{N_{FIR}-1}{2}+1\right] & s_m^i\left[q-\frac{N_{FIR}-1}{2}+2\right] & \cdots & \vdots \\ \vdots & \vdots & \ddots & \vdots \\ s_m^i[q] & s_m^i[q+1] & \cdots & s_m^i[q+N_{sf}-1] \\ \vdots & \vdots & \ddots & \vdots \\ s_m^i\left[q+\frac{N_{FIR}-1}{2}+N_L-1\right] & \cdots & \cdots & s_m^i\left[q-\frac{N_{FIR}-1}{2}+N_L-1+N_{sf}-1\right] \end{bmatrix}. \tag{B.11}$$

B.1.3 The Mean Vector

The mean vector $\boldsymbol{\nu}_M^{K,I}[p]$ is given as

$$\begin{aligned} &\boldsymbol{\nu}_M^{K,I}[p] \\ &= \mathrm{E}_{d,\psi}\left\{\mathbf{z}_M^{K,I}[p]\cdot\left(d[p]_M^{K,I}\right)^*\right\} \\ &= \mathrm{E}_{d,\psi}\left\{\left(\sum_{i=1}^{N_{\mathrm{sec}}}\sum_{m=1}^{N_{vir}}\mathbf{H}_m^i\cdot\mathbf{S}_m^i[p]\cdot\left(\mathbf{c}^{K,I}[p]\right)^* + \boldsymbol{\Psi}[p]\cdot\left(\mathbf{c}^{K,I}[p]\right)^*\right)\cdot\left(d[p]_M^{K,I}\right)^*\right\} \\ &= \sum_{i=1}^{N_{\mathrm{sec}}}\sum_{m=1}^{N_{vir}}\mathrm{E}_d\left\{\mathbf{H}_m^i\cdot\mathbf{S}_m^i[p]\cdot\left(\mathbf{c}^{K,I}[p]\right)^*\cdot\left(d[p]_M^{K,I}\right)^*\right\} \\ &+ \mathrm{E}_{d,\psi}\left\{\boldsymbol{\Psi}[p]\cdot\left(\mathbf{c}^{K,I}[p]\right)^*\cdot\left(d[p]_M^{K,I}\right)^*\right\} \\ &= \mathrm{E}_d\left\{\mathbf{H}_M^I\cdot\mathbf{S}_M^I[p]\cdot\left(\mathbf{c}^{K,I}[p]\right)^*\cdot\left(d[p]_M^{K,I}\right)^*\right\}, \end{aligned} \tag{B.12}$$

where the expectation $\mathrm{E}_{d,\psi}\{\cdot\}$ is taken over the users' symbols and thermal noise. The simplifications make use of (B.7) and (B.8). The last expectation is

easier tackled by an element wise analysis, *i.e.*

$$
\begin{aligned}
&\left(\boldsymbol{\nu}_M^{K,I}[p]\right)_{[a,1]} \\
&= \left(\mathrm{E}_d\left\{\mathbf{H}_M^I \cdot \mathbf{S}_M^I[p] \cdot \left(\mathbf{c}^{K,I}[p]\right)^* \cdot \left(d[p]_M^{K,I}\right)^*\right\}\right)_{[a,1]} \\
&= \sum_{w=1}^{N_L+N_{FIR}-1} \sum_{x=1}^{N_{sf}} \left(\left(\mathbf{H}_M^I\right)_{[a,w]}\right. \\
&\left. \cdot\, \mathrm{E}_d\left\{s_M^I\left[q-\frac{N_{FIR}-1}{2}+x-1+w-1\right] \cdot \left(c^{K,I}[q+x-1]\right)^* \cdot \left(d_M^{K,I}\left[\left\lceil\frac{q-x-1}{N_{sf}}\right\rceil\right]\right)^*\right\}\right) \\
&= \sum_{w=1}^{N_L+N_{FIR}-1} \sum_{x=1}^{N_{sf}} \left(\left(\mathbf{H}_M^I\right)_{[a,w]} \cdot \sum_{k=1}^{N_{code}} \sqrt{P_M^{k,I}} \cdot c^{k,I}\left[q-\frac{N_{FIR}-1}{2}+x-1+w-1\right] \cdot \left(c^{K,I}[q+x-1]\right)^*\right. \\
&\left. \cdot\, \mathrm{E}_d\left\{d_M^{k,I}\left[\left\lceil\frac{q-\frac{N_{FIR}-1}{2}+x-1+w-1}{N_{sf}}\right\rceil\right] \cdot \left(d_M^{K,I}\left[\left\lceil\frac{q-x-1}{N_{sf}}\right\rceil\right]\right)^*\right\}\right) \\
&= \sqrt{P_M^{K,I}} \cdot \sum_{w=1}^{N_L+N_{FIR}-1} \sum_{x=1}^{N_{sf}} \left(\left(\mathbf{H}_M^I\right)_{[a,w]} \cdot c^{K,I}\left[q-\frac{N_{FIR}-1}{2}+x-1+w-1\right] \cdot \left(c^{K,I}[q+x-1]\right)^*\right. \\
&\left. \cdot\, \delta\left(\left\lceil\left\lceil\frac{q-\frac{N_{FIR}-1}{2}+x-1+w-1}{N_{sf}}\right\rceil\right\rceil - \left\lceil\left\lceil\frac{q-x-1}{N_{sf}}\right\rceil\right\rceil\right)\right) \\
&= \sqrt{P_M^{K,I}} \cdot \sum_{w=N_L}^{N_L+N_{sf}-1} \sum_{x=1}^{N_{sf}} \left(\mathbf{H}_M^I\right)_{[a,w]} \cdot c^{K,I}\left[q-\frac{N_{FIR}-1}{2}+x-1+w-1\right] \cdot \left(c^{K,I}[q+x-1]\right)^*
\end{aligned}
\quad , \tag{B.13}
$$

where $a \in [1, 2 \ldots (N_{rx} \cdot N_{FIR})]$. The derivation in (B.13) makes use of (B.8), and is also based on

$$
\begin{aligned}
&\delta\left(\left\lceil\left\lceil\frac{q-\frac{N_{FIR}-1}{2}+x-1+w-1}{N_{sf}}\right\rceil\right\rceil - \left\lceil\left\lceil\frac{q+x-1}{N_{sf}}\right\rceil\right\rceil\right) = 1 \\
&\Leftrightarrow \left\lceil\left\lceil\frac{q-\frac{N_{FIR}-1}{2}+x-1+w-1}{N_{sf}}\right\rceil\right\rceil - \left\lceil\left\lceil\frac{q+x-1}{N_{sf}}\right\rceil\right\rceil = 0 \\
&\Leftrightarrow \left|\left(q-\frac{N_{FIR}-1}{2}+x-1+w-1\right) - (q+x-1)\right| < N_{sf} \\
&\Leftrightarrow \left|\left(w-\frac{N_{FIR}-1}{2}-1\right)\right| < N_{sf} \\
&\Leftrightarrow |(w-N_L)| < N_{sf}
\end{aligned}
\quad , \tag{B.14}
$$

with $N_{FIR} = 2 \cdot N_L - 1$. For $w \in [N_L, \ldots N_L + N_{sf} - 1]$ the introduced inequality holds. For all other w the Dirac-function in (B.13) equates to zero.

B.1.4 The Received Signal Covariance Matrix

The post despreading received signal covariance matrix is given by

$$
\begin{aligned}
&\mathbf{\Gamma}_M^{K,I}[p] \\
&= \mathrm{E}_{d,\psi}\left\{\mathbf{z}_M^{K,I}[p]\cdot\left(\mathbf{z}_M^{K,I}[p]\right)^H\right\} \\
&= \mathrm{E}_d\left\{\sum_{i_1=1}^{N_{\mathrm{sec}}}\sum_{i_2=1}^{N_{\mathrm{sec}}}\sum_{m_1=1}^{N_{vir}}\sum_{m_2=1}^{N_{vir}}\mathbf{H}_{m_1}^{i_1}\cdot\mathbf{S}_{m_1}^{i_1}[p]\cdot\left(\mathbf{c}^{K,I}[p]\right)^*\cdot\left(\mathbf{c}^{K,I}[p]\right)^T\cdot\left(\mathbf{S}_{m_2}^{i_2}[p]\right)^H\cdot\left(\mathbf{H}_{m_2}^{i_2}\right)^H\right\} \\
&+ \mathrm{E}_\psi\left\{\mathbf{\Psi}[p]\cdot\left(\mathbf{c}^{K,I}[p]\right)^*\cdot\left(\mathbf{c}^{K,I}[p]\right)^T\cdot(\mathbf{\Psi}[p])^H\right\} \\
&= \sum_{i=1}^{N_{\mathrm{sec}}}\sum_{m=1}^{N_{vir}}\mathbf{H}_m^i\cdot E_d\left\{\mathbf{S}_m^i\cdot\left(\mathbf{c}^{K,I}[p]\right)^*\cdot\left(\mathbf{c}^{K,I}[p]\right)^T\cdot\left(\mathbf{S}_m^i[p]\right)^H\right\}\cdot\left(\mathbf{H}_m^i\right)^H \\
&+ \mathrm{E}_\psi\left\{\mathbf{\Psi}[p]\cdot\left(\mathbf{c}^{K,I}[p]\right)^*\cdot\left(\mathbf{c}^{K,I}[p]\right)^T\cdot(\mathbf{\Psi}[p])^H\right\}
\end{aligned}
\quad , \tag{B.15}
$$

where the last step is due to the i.i.d property of data over different virtual channels m and different sectors i, which, using (B.8), leads to the elimination of all cross terms with $m_1 \neq m_2$ and $i_1 \neq i_2$. The elements $\left(\left(\mathbf{c}^{K,I}[p]\right)^*\cdot\left(\mathbf{c}^{K,I}[p]\right)^T\right)_{[x,y]}$ are given by $\left(c^{K,I}[q+x-1]\right)^*\cdot\left(c^{K,I}[q+y-1]\right)^T$, where $x,y\in[1,2\ldots N_{sf}]$. Furthermore,

$$
\begin{aligned}
&\mathbf{S}_m^i[p]\cdot\left(\mathbf{c}^{K,I}[p]\right)^*\cdot\left(\mathbf{c}^{K,I}[p]\right)^T\cdot\left(\mathbf{S}_m^i[p]\right)^H = \\
&\begin{bmatrix}
s_m^i\left[q-\frac{N_{FIR}-1}{2}\right] & s_m^i\left[q-\frac{N_{FIR}-1}{2}+1\right] & \cdots & s_m^i\left[q-\frac{N_{FIR}-1}{2}+N_{sf}-1\right] \\
s_m^i\left[q-\frac{N_{FIR}-1}{2}+1\right] & s_m^i\left[q-\frac{N_{FIR}-1}{2}+2\right] & \cdots & \vdots \\
\vdots & \vdots & \ddots & \vdots \\
s_m^i\left[q+\frac{N_{FIR}-1}{2}+N_L-1\right] & \cdots & \cdots & s_m^i\left[q+\frac{N_{FIR}-1}{2}+N_L-1+N_{sf}-1\right]
\end{bmatrix} \\
&\cdot\begin{bmatrix}
\left(c^{K,I}[q]\right)^*\left(c^{K,I}[q]\right) & \left(c^{K,I}[q]\right)^*\left(c^{K,I}[q+1]\right) & \cdots & \left(c^{K,I}[q]\right)^*\left(c^{K,I}\left[q+N_{sf}-1\right]\right) \\
\left(c^{K,I}[q+1]\right)^*\left(c^{K,I}[q]\right) & \left(c^{K,I}[q+1]\right)^*\left(c^{K,I}[q+1]\right) & \cdots & \vdots \\
\vdots & \vdots & \ddots & \vdots \\
\left(c^{K,I}\left[q+N_{sf}-1\right]\right)^*\left(c^{K,I}[q]\right) & \cdots & \cdots & \left(c^{K,I}\left[q+N_{sf}-1\right]\right)^*\left(c^{K,I}\left[q+N_{sf}-1\right]\right)
\end{bmatrix} \\
&\cdot\begin{bmatrix}
\left(s_m^i\left[q-\frac{N_{FIR}-1}{2}\right]\right)^* & \left(s_m^i\left[q-\frac{N_{FIR}-1}{2}+1\right]\right)^* & \cdots & \left(s_m^i\left[q+\frac{N_{FIR}-1}{2}+N_L-1\right]\right)^* \\
\left(s_m^i\left[q-\frac{N_{FIR}-1}{2}+1\right]\right)^* & \left(s_m^i\left[q-\frac{N_{FIR}-1}{2}+2\right]\right)^* & \cdots & \vdots \\
\vdots & \vdots & \ddots & \vdots \\
\left(s_m^i\left[q-\frac{N_{FIR}-1}{2}+N_{sf}-1\right]\right)^* & \cdots & \cdots & \left(s_m^i\left[q+\frac{N_{FIR}-1}{2}+N_L-1+N_{sf}-1\right]\right)^*
\end{bmatrix}
\end{aligned}
\quad , \tag{B.16}
$$

The individual elements are given by

$$\begin{aligned}
&\left(\mathbf{S}_m^i[p]\cdot\left(\mathbf{c}^{K,I}[p]\right)^*\cdot\left(\mathbf{c}^{K,I}[p]\right)^T\cdot\left(\mathbf{S}_m^i[p]\right)^H\right)_{[w,z]}\\
&=\sum_{x=1}^{N_{sf}}\sum_{y=1}^{N_{sf}}\left(\begin{array}{l}
s_m^i\left[q-\dfrac{N_{FIR}-1}{2}+x-1+w-1\right]\\
\cdot\left(c^{K,I}[q+x-1]\right)^*\cdot c^{K,I}[q+y-1]\\
\cdot\left(s_m^i\left[q-\dfrac{N_{FIR}-1}{2}+y-1+z-1\right]\right)^*
\end{array}\right)\\
&=\sum_{x=1}^{N_{sf}}\sum_{y=1}^{N_{sf}}\sum_{k_1=1}^{N_{sf}}\sum_{k_2=1}^{N_{sf}}\left(\begin{array}{l}
\sqrt{P_m^{k_1,i}}\cdot\sqrt{P_m^{k_2,i}}\\
\cdot c^{k_1,i}\left[q-\dfrac{N_{FIR}-1}{2}+x-1+w-1\right]\\
\cdot\left(c^{k_2,i}\left[q-\dfrac{N_{FIR}-1}{2}+y-1+z-1\right]\right)^*\\
\cdot\left(c^{K,I}[q+x-1]\right)^*\cdot c^{K,I}[q+y-1]\\
\cdot d_m^{k_1,i}\left[\left\lceil\dfrac{q-\frac{N_{FIR}-1}{2}+x-1+w-1}{N_{sf}}\right\rceil\right]\\
\cdot\left(d_m^{k_2,i}\left[\left\lceil\dfrac{q-\frac{N_{FIR}-1}{2}+y-1+z-1}{N_{sf}}\right\rceil\right]\right)^*
\end{array}\right),
\end{aligned}\tag{B.17}$$

where w and z are $\in[1,2,\ldots,(N_L+N_{FIR}-1)]$. Taking the expectation over the i.i.d data symbols leads to

$$\begin{aligned}
&\left(\mathrm{E}_d\left\{\mathbf{S}_m^i[p]\cdot\left(\mathbf{c}^{K,I}[p]\right)^*\cdot\left(\mathbf{c}^{K,I}[p]\right)^T\cdot\left(\mathbf{S}_m^i[p]\right)^H\right\}\right)_{[w,z]}\\
&=\sum_{x=1}^{N_{sf}}\sum_{y=1}^{N_{sf}}\sum_{k=1}^{N_{sf}}\left(\begin{array}{l}
P_m^{k,i}\\
\cdot c^{k,i}\left[q-\dfrac{N_{FIR}-1}{2}+x-1+w-1\right]\\
\cdot\left(c^{k,i}\left[q-\dfrac{N_{FIR}-1}{2}+y-1+z-1\right]\right)^*\\
\cdot\left(c^{K,I}[q+x-1]\right)^*\\
\cdot c^{K,I}[q+y-1]\\
\cdot\delta\left(\begin{array}{l}\left\lceil\dfrac{q-\frac{N_{FIR}-1}{2}+x-1+w-1}{N_{sf}}\right\rceil\\
-\left\lceil\dfrac{q-\frac{N_{FIR}-1}{2}+y-1+z-1}{N_{sf}}\right\rceil\end{array}\right)
\end{array}\right),
\end{aligned}\tag{B.18}$$

where as previously the cross terms for $k_1\neq k_2$ are dropped based on the independence assumption of data symbols associated with different code resources,

i.e. (B.8), and similar to (B.14) the remaining Dirac-term only equates to one if

$$\begin{aligned}&\delta\left(\left\lceil\frac{q-\frac{N_{FIR}-1}{2}+x-1+w-1}{N_{sf}}\right\rceil-\left\lceil\frac{q-\frac{N_{FIR}-1}{2}+y-1+z-1}{N_{sf}}\right\rceil\right)=1\\&\Leftrightarrow|x+w-y-z|<N_{sf}\end{aligned}\quad.\tag{B.19}$$

Shifting the focus on the noise term in (B.15) it can be seen that its elements are given by

$$\begin{aligned}&\left(\mathbf{\Psi}\left[p\right]\cdot\left(\mathbf{c}^{K,I}\left[p\right]\right)^{*}\cdot\left(\mathbf{c}^{K,I}\left[p\right]\right)^{T}\cdot\left(\mathbf{\Psi}\left[p\right]\right)^{H}\right)_{[a,b]}\\&=\sum_{x=1}^{N_{sf}}\sum_{y=1}^{N_{sf}}\psi\left(q+a-1\right)\cdot\left(\psi\left(q+b-1\right)\right)^{*}\cdot\left(c^{K,I}\left(q+x-1\right)\right)^{*}\cdot c^{K,I}\left(q+y-1\right)\end{aligned},\tag{B.20}$$

where $a,b\in[1,2\ldots(N_{rx}\cdot N_{FIR})]$. Taking the expectation over the i.i.d noise samples delivers

$$\begin{aligned}&\mathrm{E}_{\Psi}\left\{\mathbf{\Psi}\cdot\left(\mathbf{c}^{K,I}\left[p\right]\right)^{*}\cdot\left(\mathbf{c}^{K,I}\left[p\right]\right)^{T}\cdot\left(\mathbf{\Psi}\left[p\right]\right)^{H}\right\}\\&=P^{th}\cdot\mathbf{I}_{(N_{FIR}\cdot N_{rx})}\cdot\sum_{x=1}^{N_{sf}}\sum_{y=1}^{N_{sf}}\left(c^{K,I}\left(q+x-1\right)\right)^{*}\cdot c^{K,I}\left(q+y-1\right)\end{aligned}\quad.\tag{B.21}$$

B.1.5 The Chip Averaged Mean Vector

The chip average mean vector $\overline{\boldsymbol{\nu}}_M^{K,I}$ is derived from $\boldsymbol{\nu}_M^{K,I}$ through expectation over the code chips, *i.e.*

$$\begin{aligned}\overline{\boldsymbol{\nu}}_M^{K,I}&=\mathrm{E}_c\left\{\boldsymbol{\nu}_M^{K,I}[p]\right\}\\&=\mathrm{E}_c\left\{\mathrm{E}_d\left\{\mathbf{H}_M^I\cdot\mathbf{S}_M^I\left[p\right]\cdot\left(\mathbf{c}^{K,I}\left[p\right]\right)^{*}\cdot\left(d\left[p\right]_M^{K,I}\right)^{*}\right\}\right\}.\end{aligned}\tag{B.22}$$

Based on the result from (B.13) the elements of the chip averaged mean vector are

$$\begin{aligned}&\left(\overline{\boldsymbol{\nu}}_M^K\right)_{[a,1]}\\&=\sqrt{P_M^{K,I}}\cdot\sum_{w=N_L}^{N_L+N_{sf}-1}\sum_{x=1}^{N_{sf}}\left(\mathbf{H}_M^I\right)_{[a,w]}\cdot\underbrace{\mathrm{E}_c\left\{c^{K,I}\left[q-\frac{N_{FIR}-1}{2}+x-1+w-1\right]\cdot\left(c^{K,I}\left[q+x-1\right]\right)^{*}\right\}}_{\begin{array}{l}1,\text{ if }w=\frac{N_{FIR}-1}{2}+1\\0,\text{ if }w\neq\frac{N_{FIR}-1}{2}+1\end{array}}\\&=N_{sf}\cdot\sqrt{P_M^{K,I}}\cdot\left(\mathbf{H}_M^I\right)_{\left[a,\frac{N_{FIR}-1}{2}+1\right]}\end{aligned},\tag{B.23}$$

where $a \in [1, 2 \ldots (N_{rx} \cdot N_{FIR})]$ so that, recalling (3.23), the average mean vector turns out to be

$$\begin{aligned}\overline{\boldsymbol{\nu}}_M^{K,I} &= N_{sf} \cdot \sqrt{P_M^{K,I}} \cdot \left(\mathbf{H}_M^I\right)_{\left[:, \frac{N_{FIR}-1}{2}+1\right]} \\ &= N_{sf} \cdot \sqrt{P_M^{K,I}} \cdot \left(\mathbf{H}_M^I\right)_{[:, N_L]} \\ &= N_{sf} \cdot \sqrt{P_M^{K,I}} \cdot \mathbf{h}_M^I \end{aligned} \quad . \tag{B.24}$$

B.1.6 The Chip Averaged Received Signal Covariance Matrix

Considering (B.15), (B.18) and (B.20) the chip averaged received signal covariance matrix is given by

$$\begin{aligned}&\overline{\boldsymbol{\Gamma}}_M^{K,I} \\ &= \mathrm{E}_c\left\{\boldsymbol{\Gamma}_M^{K,I}[p]\right\} \\ &= \sum_{i=1}^{N_{\mathrm{sec}}} \sum_{m=1}^{N_{vir}} \mathbf{H}_m^i \cdot \underbrace{\mathrm{E}_c\left\{\mathrm{E}_d\left\{\mathbf{S}_m^i \cdot \left(\mathbf{c}^{K,I}[p]\right)^* \cdot \left(\mathbf{c}^{K,I}[p]\right)^T \cdot \left(\mathbf{S}_m^i[p]\right)^H\right\}\right\}}_{\mathbf{R}_m^i} \cdot \left(\mathbf{H}_m^i\right)^H \\ &+ P^{th} \cdot \mathbf{I}_{(N_{rx} \cdot N_{FIR})} \cdot \mathrm{E}_c\left\{\sum_{x=1}^{N_{sf}} \sum_{y=1}^{N_{sf}} \left(c^{K,I}(q+x-1)\right)^* \cdot c^{K,I}(q+y-1)\right\} \\ &= \sum_{i=1}^{N_{\mathrm{sec}}} \sum_{m=1}^{N_{vir}} \mathbf{H}_m^i \cdot \mathbf{R}_m^i \cdot \left(\mathbf{H}_m^i\right)^H + N_{sf} \cdot P^{th} \cdot \mathbf{I}_{(N_{rx} \cdot N_{FIR})} \end{aligned} \quad , \tag{B.25}$$

where the elements of $\mathbf{R}_m^i$ are defined as

$$\left(\mathbf{R}_m^i\right)_{[w,z]} = \sum_{x=1}^{N_{sf}} \sum_{y=1}^{N_{sf}} \sum_{k=1}^{N_{sf}} \left(\begin{array}{l} P_m^{k,i} \\ \cdot \mathrm{E}_c\left\{ \begin{array}{l} c^{k,i}\left[q - \frac{N_{FIR}-1}{2} + x - 1 + w - 1\right] \\ \cdot \left(c^{k,i}\left[q - \frac{N_{FIR}-1}{2} + y - 1 + z - 1\right]\right)^* \\ \cdot \left(c^{K,I}[q+x-1]\right)^* \cdot c^{K,I}[q+y-1] \end{array} \right\} \\ \cdot \delta\left(\left\lceil \frac{q - \frac{N_{FIR}-1}{2} + x - 1 + w - 1}{N_{sf}} \right\rceil - \left\lceil \frac{q - \frac{N_{FIR}-1}{2} + y - 1 + z - 1}{N_{sf}} \right\rceil \right) \end{array} \right) \quad . \tag{B.26}$$

From (B.1), (B.2), (B.3), (B.5), and (B.6) it can be seen that two complex conjugate chip pairs are required to lead to an expectation equating to one. Looking first at the

contribution from a different sector, *i.e.* $i \neq I$, two complex conjugate chip pairs can only exist if $w = z \wedge x = y$, which occurs exactly N_{sf}-times for the diagonal elements of $\mathbf{R}_m^i$, and independent of the channelisation code allocation. Noting further that for $w = z$, (B.19) simplifies to $|x - y| < N_{sf}$, and the Dirac-term in (B.26) equates to one over the entire range of x and y. The correlation matrix $\mathbf{R}_m^i$ can then be written as

$$\mathbf{R}_m^i = N_{sf} \cdot \sum_{k=1}^{N_{sf}} P_m^{k,i} \cdot \mathbf{I}_{N_{FIR}} \; \forall \; i \neq I \quad . \tag{B.27}$$

Considering now the contribution from the wanted sector, *i.e.* $i = I$, complex conjugate chip pairs can be formed for $w = z \wedge x = y$, but also for $w = z \wedge w = \frac{N_{FIR}-1}{2} + 1$. Letting first $w \neq \frac{N_{FIR}-1}{2} + 1$ the expectation is fully specified through (B.5), so that the diagonal elements of $\mathbf{R}_m^I$, with exception of $\left(\mathbf{R}_m^I\right)_{\left[\frac{N_{FIR}-1}{2}+1, \frac{N_{FIR}-1}{2}+1\right]}$, are given by

$$\left(\mathbf{R}_m^I\right)_{[w,z]} = N_{sf} \cdot \sum_{k=1}^{N_{code}} P_m^{k,I} \quad . \tag{B.28}$$

For $w = \frac{N_{FIR}-1}{2} + 1$ the expectation is specified by (B.6) where, independent of the relationship between x and y, the expectation equates to one for $K = k$ and to zero for $K \neq k$ so that

$$\left(\mathbf{R}_m^I\right)_{\left[\frac{N_{FIR}-1}{2}+1, \frac{N_{FIR}-1}{2}+1\right]} = (N_{sf})^2 \cdot P_m^{K,I} \quad . \tag{B.29}$$

$\mathbf{R}_m^I$ is hence given by

$$\mathbf{R}_m^I = N_{sf} \cdot \begin{bmatrix} \sum_{k=1}^{N_{sf}} P_m^{k,I} & & & & & & \\ & \ddots & & & & & \\ & & \sum_{k=1}^{N_{sf}} P_m^{k,I} & & & & \\ & & & N_{sf} \cdot P_m^{K,I} & & & \\ & & & & \sum_{k=1}^{N_{sf}} P_m^{k,I} & & \\ & & & & & \ddots & \\ & & & & & & \sum_{k=1}^{N_{sf}} P_m^{k,I} \end{bmatrix} , \tag{B.30}$$

It has the dimensions $(N_L + N_{FIR} - 1) \times (N_L + N_{FIR} - 1)$ and all off diagonal elements are filled with zeros. $\mathbf{R}_m^I$ can be rewritten as

$$\begin{aligned}\mathbf{R}_m^I = {} & N_{sf} \cdot \sum_{k=1}^{N_{sf}} P_m^{k,I} \cdot \mathbf{I}_{N_{FIR}} \\ & + \left((N_{sf})^2 \cdot P_m^{K,I} - N_{sf} \cdot \sum_{k=1}^{N_{sf}} P_m^{k,I} \right) \\ & \cdot \mathbf{e}_{\frac{N_{FIR}-1}{2}+1} \cdot \left(\mathbf{e}_{\frac{N_{FIR}-1}{2}+1} \right)^H \end{aligned} , \tag{B.31}$$

where all but the $\left(\frac{N_{FIR}-1}{2}+1\right)$-th element of the column vector $\mathbf{e}$ are zero, the $\left(\frac{N_{FIR}-1}{2}+1\right)$-th element, however, is one.

Using (B.25), (B.27), and (B.31), and bearing (3.23) in mind, the chip average

received signal covariance matrix is expressed as

$$
\begin{aligned}
\overline{\mathbf{\Gamma}}_M^{K,I} &= \sum_{i=1}^{N_{\text{sec}}} \sum_{m=1}^{N_{vir}} \mathbf{H}_m^i \cdot \mathbf{R}_m^i \cdot \left(\mathbf{H}_m^i\right)^H \\
&\quad + N_{sf} \cdot P^{th} \cdot \mathbf{I}_{(N_{rx} \cdot N_{FIR})} \\
&= N_{sf} \cdot \sum_{i=1}^{N_{\text{sec}}} \sum_{m=1}^{N_{vir}} \sum_{k=1}^{N_{sf}} P_m^{k,i} \cdot \mathbf{H}_m^i \left(\mathbf{H}_m^i\right)^H \\
&\quad - N_{sf} \cdot \sum_{m=1}^{N_{vir}} \sum_{k=1}^{N_{sf}} P_m^{k,I} \cdot \mathbf{h}_m^I \left(\mathbf{h}_m^I\right)^H \\
&\quad + \left(N_{sf}\right)^2 \cdot \sum_{m=1}^{N_{vir}} P_m^{K,I} \cdot \mathbf{h}_m^I \left(\mathbf{h}_m^I\right)^H \\
&\quad + N_{sf} \cdot P^{th} \cdot \mathbf{I}_{(N_{rx} \cdot N_{FIR})} \\
&= N_{sf} \cdot \sum_{i=1}^{N_{\text{sec}}} \sum_{m=1}^{N_{vir}} P_m^i \cdot \mathbf{H}_m^i \left(\mathbf{H}_m^i\right)^H \\
&\quad - N_{sf} \cdot \sum_{m=1}^{N_{vir}} P_m^I \cdot \mathbf{h}_m^I \left(\mathbf{h}_m^I\right)^H \\
&\quad + \left(N_{sf}\right)^2 \cdot \sum_{m=1}^{N_{vir}} P_m^{K,I} \cdot \mathbf{h}_m^I \left(\mathbf{h}_m^I\right)^H \\
&\quad + N_{sf} \cdot P^{th} \cdot \mathbf{I}_{(N_{rx} \cdot N_{FIR})} \\
&= N_{sf} \cdot P_M^I \underbrace{\left(\begin{array}{r} \displaystyle\sum_{i=1}^{N_{\text{sec}}} \sum_{m=1}^{N_{vir}} \frac{P_m^i}{P_M^I} \cdot \mathbf{H}_m^i \left(\mathbf{H}_m^i\right)^H \\ \displaystyle - \sum_{m=1}^{N_{vir}} \frac{P_m^I}{P_M^I} \cdot \mathbf{h}_m^I \left(\mathbf{h}_m^I\right)^H \\ \displaystyle + N_{sf} \cdot \sum_{\substack{m=1 \\ m \neq M}}^{N_{vir}} \frac{P_m^{K,I}}{P_M^I} \cdot \mathbf{h}_m^I \left(\mathbf{h}_m^I\right)^H \\ \displaystyle + \frac{P^{th}}{P_M^I} \cdot \mathbf{I}_{(N_{rx} \cdot N_{FIR})} \end{array} \right)}_{\mathbf{\Omega}_M^{K,I}} \\
&\quad + \left(N_{sf}\right)^2 \cdot P_M^{K,I} \cdot \mathbf{h}_M^I \left(\mathbf{h}_M^I\right)^H
\end{aligned}
\tag{B.32}
$$

where the second last step made use of (3.10).

B.2 SINR Expressions

After recalling the general symbol level SINR expression introduced in (3.33), the following derives the specific SINR expressions for the chip averaged MMSE and the chip averaged RAKE receiver.

B.2.1 General Symbol Level SINR

Following the formulation in [Fran02] the desired signal power, independent of the receiver type, is captured by $\left|\left(\overline{\mathbf{g}}_M^{K,I}\right)^H \cdot \overline{\boldsymbol{\nu}}_M^{K,I}\right|^2$, and the total received power including desired power, interference power, and noise power is given by $\left(\overline{\mathbf{g}}_M^{K,I}\right)^H \overline{\mathbf{\Gamma}}_M^{K,I} \overline{\mathbf{g}}_M^{K,I}$ so that the symbol level SINR is

$$SINR_M^{K,I} = \frac{\left|\left(\widehat{\overline{\mathbf{g}}}_M^{K,I}\right)^H \cdot \overline{\boldsymbol{\nu}}_M^{K,I}\right|^2}{\left(\widehat{\overline{\mathbf{g}}}_M^{K,I}\right)^H \overline{\mathbf{\Gamma}}_M^{K,I} \widehat{\overline{\mathbf{g}}}_M^{K,I} - \left|\left(\widehat{\overline{\mathbf{g}}}_M^{K,I}\right)^H \cdot \overline{\boldsymbol{\nu}}_M^{K,I}\right|^2} \quad , \tag{B.33}$$

where $[\widehat{\cdot}]$ indicates the estimate of the true value.

B.2.2 Symbol level MMSE SINR

Specifically for the MMSE receiver case the SINR expression rewrites

$$SINR_M^{K,I}\Big|_{MMSE} = \frac{\left|\left(\widehat{\overline{\boldsymbol{\nu}}}_M^{K,I}\right)^H \left(\widehat{\overline{\mathbf{\Gamma}}}_M^{K,I}\right)^{-1} \overline{\boldsymbol{\nu}}_M^{K,I}\right|^2}{\left(\widehat{\overline{\boldsymbol{\nu}}}_M^{K,I}\right)^H \left(\widehat{\overline{\mathbf{\Gamma}}}_M^{K,I}\right)^{-1} \overline{\mathbf{\Gamma}}_M^{K,I} \left(\widehat{\overline{\mathbf{\Gamma}}}_M^{K,I}\right)^{-1} \widehat{\overline{\boldsymbol{\nu}}}_M^{K,I} - \left|\left(\widehat{\overline{\boldsymbol{\nu}}}_M^{K,I}\right)^H \left(\widehat{\overline{\mathbf{\Gamma}}}_M^{K,I}\right)^{-1} \overline{\boldsymbol{\nu}}_M^{K,I}\right|^2} \quad , \tag{B.34}$$

where $\overline{\boldsymbol{\nu}}_M^{K,I}$ and $\overline{\mathbf{\Gamma}}_M^{K,I}$ are given in (B.24) and (B.32) respectively. Using the Sherman-Morrison Formula [Moon00, p. 258], *i.e.*

$$\left(\mathbf{A^{-1}} + \mathbf{u}\mathbf{v}^H\right)^{-1} = \mathbf{A} - \frac{\mathbf{A}\mathbf{u}\mathbf{v}^H\mathbf{A}}{1 + \mathbf{v}^H\mathbf{A}\mathbf{u}} \quad , \tag{B.35}$$

the inverse of the despread, chip averaged, received signal covariance matrix can be rewritten as

$$
\begin{aligned}
\left(\overline{\mathbf{\Gamma}}_M^{K,I}\right)^{-1} &= \left(\underbrace{N_{sf}P_M^I\mathbf{\Omega}_M^{K,I}}_{\mathbf{A^{-1}}} + \underbrace{\left(N_{sf}\right)^2 P_M^{K,I}\mathbf{h}_M^I}_{\mathbf{u}}\underbrace{\left(\mathbf{h}_M^I\right)^H}_{\mathbf{v}}\right)^{-1} \\
&= \mathbf{A} - \frac{\mathbf{A}\mathbf{u}\mathbf{v}^H\mathbf{A}}{1+\mathbf{v}^H\mathbf{A}\mathbf{u}} \\
&= \frac{1}{N_{sf}P_M^I}\left(\mathbf{\Omega}_M^{K,I}\right)^{-1} \\
&\quad - \frac{\frac{1}{N_{sf}P_M^I}\left(\mathbf{\Omega}_M^{K,I}\right)^{-1}\left(N_{sf}\right)^2 P_M^{K,I}\mathbf{h}_M^I\left(\mathbf{h}_M^I\right)^H\frac{1}{N_{sf}P_M^I}\left(\mathbf{\Omega}_M^{K,I}\right)^{-1}}{1+\left(\mathbf{h}_M^I\right)^H\frac{1}{N_{sf}P_M^I}\left(\mathbf{\Omega}_M^{K,I}\right)^{-1}\left(N_{sf}\right)^2 P_M^{K,I}\mathbf{h}_M^I} \\
&= \frac{1}{N_{sf}P_M^I}\left(\mathbf{\Omega}_M^{K,I}\right)^{-1} \\
&\quad - \frac{\frac{P_M^{K,I}}{\left(P_M^I\right)^2}\left(\mathbf{\Omega}_M^{K,I}\right)^{-1}\mathbf{h}_M^I\left(\mathbf{h}_M^I\right)^H\left(\mathbf{\Omega}_M^{K,I}\right)^{-1}}{1+\frac{N_{sf}P_M^{K,I}}{P_M^I}\left(\mathbf{h}_M^I\right)^H\left(\mathbf{\Omega}_M^{K,I}\right)^{-1}\mathbf{h}_M^I}
\end{aligned}
, \tag{B.36}
$$

and its estimate is given by

$$
\begin{aligned}
\left(\widehat{\overline{\mathbf{\Gamma}}}_M^{K,I}\right)^{-1} &= \frac{1}{N_{sf}P_M^I}\left(\widehat{\mathbf{\Omega}}_M^{K,I}\right)^{-1} \\
&\quad - \frac{\frac{P_M^{K,I}}{\left(P_M^I\right)^2}\left(\widehat{\mathbf{\Omega}}_M^{K,I}\right)^{-1}\widehat{\mathbf{h}}_M^I\left(\widehat{\mathbf{h}}_M^I\right)^H\left(\widehat{\mathbf{\Omega}}_M^{K,I}\right)^{-1}}{1+\frac{N_{sf}P_M^{K,I}}{P_M^I}\left(\widehat{\mathbf{h}}_M^I\right)^H\left(\widehat{\mathbf{\Omega}}_M^{K,I}\right)^{-1}\widehat{\mathbf{h}}_M^I}
\end{aligned}
. \tag{B.37}
$$

Using this rewritten versions of the inverse of the despread chip averaged received signal covariance matrix and its estimate, and substituting also the mean vector and

its estimate, the term $\left(\widehat{\overline{\boldsymbol{\nu}}}_M^{K,I}\right)^H \left(\widehat{\overline{\boldsymbol{\Gamma}}}_M^{K,I}\right)^{-1} \overline{\boldsymbol{\nu}}_M^{K,I}$ can be rewritten as

$$
\begin{aligned}
&\left(\widehat{\overline{\boldsymbol{\nu}}}_M^{K,I}\right)^H \left(\widehat{\overline{\boldsymbol{\Gamma}}}_M^{K,I}\right)^{-1} \overline{\boldsymbol{\nu}}_M^{K,I} \\
&= \left(N_{sf}\right)^2 P_M^{K,I} \left(\widehat{\mathbf{h}}_M^I\right)^H \\
&\cdot \begin{pmatrix} \frac{1}{N_{sf} P_M^I} \left(\widehat{\boldsymbol{\Omega}}_M^{K,I}\right)^{-1} \\ - \frac{\frac{P_M^{K,I}}{\left(P_M\right)^2} \left(\widehat{\boldsymbol{\Omega}}_M^{K,I}\right)^{-1} \widehat{\mathbf{h}}_M^I \left(\widehat{\mathbf{h}}_M^I\right)^H \left(\widehat{\boldsymbol{\Omega}}_M^{K,I}\right)^{-1}}{1 + \frac{N_{sf} P_M^{K,I}}{P_M^I} \left(\widehat{\mathbf{h}}_M^I\right)^H \left(\widehat{\boldsymbol{\Omega}}_M^{K,I}\right)^{-1} \widehat{\mathbf{h}}_M^I} \end{pmatrix} \mathbf{h}_M^I \\
&= \left(N_{sf}\right)^2 P_M^{K,I} \\
&\cdot \frac{\begin{pmatrix} \frac{1}{N_{sf} P_M^I} \left(\widehat{\mathbf{h}}_M^I\right)^H \left(\widehat{\boldsymbol{\Omega}}_M^{K,I}\right)^{-1} \mathbf{h}_M^I \\ + \frac{P_M^{K,I}}{\left(P_M^I\right)^2} \left(\widehat{\mathbf{h}}_M^I\right)^H \left(\widehat{\boldsymbol{\Omega}}_M^{K,I}\right)^{-1} \widehat{\mathbf{h}}_M^I \left(\widehat{\mathbf{h}}_M^I\right)^H \left(\widehat{\boldsymbol{\Omega}}_M^{K,I}\right)^{-1} \mathbf{h}_M^I \\ - \frac{P_M^{K,I}}{\left(P_M^I\right)^2} \left(\widehat{\mathbf{h}}_M^I\right)^H \left(\widehat{\boldsymbol{\Omega}}_M^{K,I}\right)^{-1} \widehat{\mathbf{h}}_M^I \left(\widehat{\mathbf{h}}_M^I\right)^H \left(\widehat{\boldsymbol{\Omega}}_M^{K,I}\right)^{-1} \mathbf{h}_M^I \end{pmatrix}}{1 + \frac{N_{sf} P_M^{K,I}}{P_M^I} \left(\widehat{\mathbf{h}}_M^I\right)^H \left(\widehat{\boldsymbol{\Omega}}_M^{K,I}\right)^{-1} \widehat{\mathbf{h}}_M^I} \\
&= \begin{pmatrix} \frac{N_{sf} P_M^{K,I}}{P_M^I} \left(\widehat{\mathbf{h}}_M^I\right)^H \left(\widehat{\boldsymbol{\Omega}}_M^{K,I}\right)^{-1} \mathbf{h}_M^I \\ \hline 1 + \frac{N_{sf} P_M^{K,I}}{P_M^I} \left(\widehat{\mathbf{h}}_M^I\right)^H \left(\widehat{\boldsymbol{\Omega}}_M^{K,I}\right)^{-1} \widehat{\mathbf{h}}_M^I \end{pmatrix}
\end{aligned}
\tag{B.38}
$$

and the term $\left(\widehat{\overline{\boldsymbol{\nu}}}_M^{K,I}\right)^H \left(\widehat{\overline{\mathbf{\Gamma}}}_M^{K,I}\right)^{-1} \overline{\mathbf{\Gamma}}_M^{K,I} \left(\widehat{\overline{\mathbf{\Gamma}}}_M^{K,I}\right)^{-1} \widehat{\overline{\boldsymbol{\nu}}}_M^{K,I}$ can be rewritten as

$$
\begin{aligned}
&\left(\widehat{\overline{\boldsymbol{\nu}}}_M^{K,I}\right)^H \left(\widehat{\overline{\mathbf{\Gamma}}}_M^{K,I}\right)^{-1} \overline{\mathbf{\Gamma}}_M^{K,I} \left(\widehat{\overline{\mathbf{\Gamma}}}_M^{K,I}\right)^{-1} \widehat{\overline{\boldsymbol{\nu}}}_M^{K,I} \\
&= \left(N_{sf}\right)^2 P_M^{K,I} \left(\widehat{\mathbf{h}}_M^I\right)^H \\
&\cdot \left(\frac{1}{N_{sf} P_M^I} \left(\widehat{\mathbf{\Omega}}_M^{K,I}\right)^{-1} - \frac{\frac{P_M^{K,I}}{\left(P_M^I\right)^2} \left(\widehat{\mathbf{\Omega}}_M^{K,I}\right)^{-1} \widehat{\mathbf{h}}_M^I \left(\widehat{\mathbf{h}}_M^I\right)^H \left(\widehat{\mathbf{\Omega}}_M^{K,I}\right)^{-1}}{1 + \frac{N_{sf} P_M^{K,I}}{P_M^I} \left(\widehat{\mathbf{h}}_M^I\right)^H \left(\widehat{\mathbf{\Omega}}_M^{K,I}\right)^{-1} \widehat{\mathbf{h}}_M^I} \right) \\
&\cdot \left(N_{sf} P_M^I \mathbf{\Omega}_M^{K,I} + \left(N_{sf}\right)^2 P_M^{K,I} \mathbf{h}_M^I \left(\mathbf{h}_M^I\right)^H \right) \\
&\cdot \left(\frac{1}{N_{sf} P_M^I} \left(\widehat{\mathbf{\Omega}}_M^{K,I}\right)^{-1} - \frac{\frac{P_M^{K,I}}{\left(P_M^I\right)^2} \left(\widehat{\mathbf{\Omega}}_M^{K,I}\right)^{-1} \widehat{\mathbf{h}}_M^I \left(\widehat{\mathbf{h}}_M^I\right)^H \left(\widehat{\mathbf{\Omega}}_M^{K,I}\right)^{-1}}{1 + \frac{N_{sf} P_M^{K,I}}{P_M^I} \left(\widehat{\mathbf{h}}_M^I\right)^H \left(\widehat{\mathbf{\Omega}}_M^{K,I}\right)^{-1} \widehat{\mathbf{h}}_M^I} \right) \left(\widehat{\mathbf{h}}_M^I\right) \\
&= \left(\begin{array}{l}
\left(N_{sf}\right)^2 P_M^{K,I} \left(\widehat{\mathbf{h}}_M^I\right)^H \\
\cdot \left(\frac{1}{N_{sf} P_M^I} \left(\widehat{\mathbf{\Omega}}_M^{K,I}\right)^{-1} - \frac{\frac{P_M^{K,I}}{\left(P_M^I\right)^2} \left(\widehat{\mathbf{\Omega}}_M^{K,I}\right)^{-1} \widehat{\mathbf{h}}_M^I \left(\widehat{\mathbf{h}}_M^I\right)^H \left(\widehat{\mathbf{\Omega}}_M^{K,I}\right)^{-1}}{1 + \frac{N_{sf} P_M^{K,I}}{P_M^I} \left(\widehat{\mathbf{h}}_M^I\right)^H \left(\widehat{\mathbf{\Omega}}_M^{K,I}\right)^{-1} \widehat{\mathbf{h}}_M^I} \right) \\
\cdot N_{sf} P_M^I \mathbf{\Omega}_M^{K,I} \\
\cdot \left(\frac{1}{N_{sf} P_M^I} \left(\widehat{\mathbf{\Omega}}_M^{K,I}\right)^{-1} - \frac{\frac{P_M^{K,I}}{\left(P_M^I\right)^2} \left(\widehat{\mathbf{\Omega}}_M^{K,I}\right)^{-1} \widehat{\mathbf{h}}_M^I \left(\widehat{\mathbf{h}}_M^I\right)^H \left(\widehat{\mathbf{\Omega}}_M^{K,I}\right)^{-1}}{1 + \frac{N_{sf} P_M^{K,I}}{P_M^I} \left(\widehat{\mathbf{h}}_M^I\right)^H \left(\widehat{\mathbf{\Omega}}_M^{K,I}\right)^{-1} \widehat{\mathbf{h}}_M^I} \right) \\
\cdot \left(\widehat{\mathbf{h}}_M^I\right) \\
+ \left(N_{sf}\right)^2 P_M^{K,I} \left(\widehat{\mathbf{h}}_M^I\right)^H \\
\cdot \left(\frac{1}{N_{sf} P_M^I} \left(\widehat{\mathbf{\Omega}}_M^{K,I}\right)^{-1} - \frac{\frac{P_M^{K,I}}{\left(P_M^I\right)^2} \left(\widehat{\mathbf{\Omega}}_M^{K,I}\right)^{-1} \widehat{\mathbf{h}}_M^I \left(\widehat{\mathbf{h}}_M^I\right)^H \left(\widehat{\mathbf{\Omega}}_M^{K,I}\right)^{-1}}{1 + \frac{N_{sf} P_M^{K,I}}{P_M^I} \left(\widehat{\mathbf{h}}_M^I\right)^H \left(\widehat{\mathbf{\Omega}}_M^{K,I}\right)^{-1} \widehat{\mathbf{h}}_M^I} \right) \\
\cdot \left(N_{sf}\right)^2 P_M^{K,I} \mathbf{h}_M^I \left(\mathbf{h}_M^I\right)^H \\
\cdot \left(\frac{1}{N_{sf} P_M} \left(\widehat{\mathbf{\Omega}}_M^{K,I}\right)^{-1} - \frac{\frac{P_M^{K,I}}{\left(P_M^I\right)^2} \left(\widehat{\mathbf{\Omega}}_M^{K,I}\right)^{-1} \widehat{\mathbf{h}}_M^I \left(\widehat{\mathbf{h}}_M^I\right)^H \left(\widehat{\mathbf{\Omega}}_M^{K,I}\right)^{-1}}{1 + \frac{N_{sf} P_M^{K,I}}{P_M^I} \left(\widehat{\mathbf{h}}_M^I\right)^H \left(\widehat{\mathbf{\Omega}}_M^{K,I}\right)^{-1} \widehat{\mathbf{h}}_M^I} \right) \\
\cdot \left(\widehat{\mathbf{h}}_M^I\right)
\end{array} \right)
\end{aligned}
$$

which turns into

$$\left(\widehat{\overline{\boldsymbol{\nu}}}_M^{K,I}\right)^H \left(\widehat{\overline{\boldsymbol{\Gamma}}}_M^{K,I}\right)^{-1} \overline{\boldsymbol{\Gamma}}_M^{K,I} \left(\widehat{\overline{\boldsymbol{\Gamma}}}_M^{K,I}\right)^{-1} \widehat{\overline{\boldsymbol{\nu}}}_M^{K,I}$$

$$= \left(\begin{array}{l} (N_{sf})^2 P_M^{K,I} \dfrac{\left(\begin{array}{l} \frac{1}{N_{sf} P_M^I} \left(\widehat{\mathbf{h}}_M^I\right)^H \left(\widehat{\boldsymbol{\Omega}}_M^{K,I}\right)^{-1} \\ + \frac{P_M^{K,I}}{\left(P_M^I\right)^2} \left(\widehat{\mathbf{h}}_M^I\right)^H \left(\widehat{\boldsymbol{\Omega}}_M^{K,I}\right)^{-1} \widehat{\mathbf{h}}_M^I \left(\widehat{\mathbf{h}}_M^I\right)^H \left(\widehat{\boldsymbol{\Omega}}_M^{K,I}\right)^{-1} \\ - \frac{P_M^{K,I}}{\left(P_M^I\right)^2} \left(\widehat{\mathbf{h}}_M^I\right)^H \left(\widehat{\boldsymbol{\Omega}}_M^{K,I}\right)^{-1} \widehat{\mathbf{h}}_M^I \left(\widehat{\mathbf{h}}_M^I\right)^H \left(\widehat{\boldsymbol{\Omega}}_M^{K,I}\right)^{-1} \end{array} \right)}{1 + \frac{N_{sf} P_M^{K,I}}{P_M^I} \left(\widehat{\mathbf{h}}_M^I\right)^H \left(\widehat{\boldsymbol{\Omega}}_M^{K,I}\right)^{-1} \widehat{\mathbf{h}}_M^I} \\ \\ N_{sf} P_M^I \boldsymbol{\Omega}_M^{K,I} \dfrac{\left(\begin{array}{l} \frac{1}{N_{sf} P_M^I} \left(\widehat{\boldsymbol{\Omega}}_M^{K,I}\right)^{-1} \left(\widehat{\mathbf{h}}_M^I\right) \\ + \frac{P_M^{K,I}}{\left(P_M^I\right)^2} \left(\widehat{\boldsymbol{\Omega}}_M^{K,I}\right)^{-1} \left(\widehat{\mathbf{h}}_M^I\right) \left(\widehat{\mathbf{h}}_M^I\right)^H \left(\widehat{\boldsymbol{\Omega}}_M^{K,I}\right)^{-1} \widehat{\mathbf{h}}_M^I \\ - \frac{P_M^{K,I}}{\left(P_M^I\right)^2} \left(\widehat{\boldsymbol{\Omega}}_M^{K,I}\right)^{-1} \widehat{\mathbf{h}}_M^I \left(\widehat{\mathbf{h}}_M^I\right)^H \left(\widehat{\boldsymbol{\Omega}}_M^{K,I}\right)^{-1} \left(\widehat{\mathbf{h}}_M^I\right) \end{array} \right)}{1 + \frac{N_{sf} P_M^{K,I}}{P_M^I} \left(\widehat{\mathbf{h}}_M^I\right)^H \left(\widehat{\boldsymbol{\Omega}}_M^{K,I}\right)^{-1} \widehat{\mathbf{h}}_M^I} \\ \\ + (N_{sf})^2 P_M^{K,I} \dfrac{\left(\begin{array}{l} \frac{1}{N_{sf} P_M^I} \left(\widehat{\mathbf{h}}_M^I\right)^H \left(\widehat{\boldsymbol{\Omega}}_M^{K,I}\right)^{-1} \mathbf{h}_M^I \\ + \frac{P_M^{K,I}}{\left(P_M^I\right)^2} \left(\widehat{\mathbf{h}}_M^I\right)^H \left(\widehat{\boldsymbol{\Omega}}_M^{K,I}\right)^{-1} \widehat{\mathbf{h}}_M^I \left(\widehat{\mathbf{h}}_M^I\right)^H \left(\widehat{\boldsymbol{\Omega}}_M^{K,I}\right)^{-1} \mathbf{h}_M^I \\ - \frac{P_M^{K,I}}{\left(P_M^I\right)^2} \left(\widehat{\mathbf{h}}_M^I\right)^H \left(\widehat{\boldsymbol{\Omega}}_M^{K,I}\right)^{-1} \widehat{\mathbf{h}}_M^I \left(\widehat{\mathbf{h}}_M^I\right)^H \left(\widehat{\boldsymbol{\Omega}}_M^{K,I}\right)^{-1} \mathbf{h}_M^I \end{array} \right)}{1 + \frac{N_{sf} P_M^{K,I}}{P_M^I} \left(\widehat{\mathbf{h}}_M^I\right)^H \left(\widehat{\boldsymbol{\Omega}}_M^{K,I}\right)^{-1} \widehat{\mathbf{h}}_M^I} \\ \\ (N_{sf})^2 P_M^{K,I} \dfrac{\left(\begin{array}{l} \frac{1}{N_{sf} P_M^I} \left(\mathbf{h}_M^I\right)^H \left(\widehat{\boldsymbol{\Omega}}_M^{K,I}\right)^{-1} \left(\widehat{\mathbf{h}}_M^I\right) \\ + \frac{N_{sf} P_M^{K,I}}{P_M^I} \frac{1}{N_{sf} P_M^I} \left(\mathbf{h}_M^I\right)^H \left(\widehat{\boldsymbol{\Omega}}_M^{K,I}\right)^{-1} \left(\widehat{\mathbf{h}}_M^I\right) \left(\widehat{\mathbf{h}}_M^I\right)^H \left(\widehat{\boldsymbol{\Omega}}_M^{K,I}\right)^{-1} \widehat{\mathbf{h}}_M^I \\ - \frac{P_M^{K,I}}{\left(P_M^I\right)^2} \left(\mathbf{h}_M^I\right)^H \left(\widehat{\boldsymbol{\Omega}}_M^{K,I}\right)^{-1} \widehat{\mathbf{h}}_M^I \left(\widehat{\mathbf{h}}_M^I\right)^H \left(\widehat{\boldsymbol{\Omega}}_M^{K,I}\right)^{-1} \left(\widehat{\mathbf{h}}_M^I\right) \end{array} \right)}{1 + \frac{N_{sf} P_M^{K,I}}{P_M^I} \left(\widehat{\mathbf{h}}_M^I\right)^H \left(\widehat{\boldsymbol{\Omega}}_M^{K,I}\right)^{-1} \widehat{\mathbf{h}}_M^I} \end{array} \right) ,$$

and finally into

$$\left(\widehat{\overline{\boldsymbol{\nu}}}_M^{K,I}\right)^H \left(\widehat{\overline{\boldsymbol{\Gamma}}}_M^{K,I}\right)^{-1} \overline{\boldsymbol{\Gamma}}_M^{K,I} \left(\widehat{\overline{\boldsymbol{\Gamma}}}_M^{K,I}\right)^{-1} \widehat{\overline{\boldsymbol{\nu}}}_M^{K,I}$$

$$= \left(\begin{array}{l} (N_{sf})^2 P_M^{K,I} \left(\dfrac{\frac{1}{N_{sf} P_M^I} \left(\widehat{\mathbf{h}}_M^I\right)^H \left(\widehat{\boldsymbol{\Omega}}_M^{K,I}\right)^{-1}}{1 + \frac{N_{sf} P_M^{K,I}}{P_M^I} \left(\widehat{\mathbf{h}}_M^I\right)^H \left(\widehat{\boldsymbol{\Omega}}_M^{K,I}\right)^{-1} \widehat{\mathbf{h}}_M^I} \right) \\ N_{sf} P_M^I \boldsymbol{\Omega}_M^{K,I} \left(\dfrac{\frac{1}{N_{sf} P_M^I} \left(\widehat{\boldsymbol{\Omega}}_M^{K,I}\right)^{-1} \left(\widehat{\mathbf{h}}_M^I\right)}{1 + \frac{N_{sf} P_M^{K,I}}{P_M^I} \left(\widehat{\mathbf{h}}_M^I\right)^H \left(\widehat{\boldsymbol{\Omega}}_M^{K,I}\right)^{-1} \widehat{\mathbf{h}}_M^I} \right) \\ + (N_{sf})^2 P_M^{K,I} \left(\dfrac{\frac{1}{N_{sf} P_M^I} \left(\widehat{\mathbf{h}}_M^I\right)^H \left(\widehat{\boldsymbol{\Omega}}_M^{K,I}\right)^{-1} \mathbf{h}_M^I}{1 + \frac{N_{sf} P_M^{K,I}}{P_M^I} \left(\widehat{\mathbf{h}}_M^I\right)^H \left(\widehat{\boldsymbol{\Omega}}_M^{K,I}\right)^{-1} \widehat{\mathbf{h}}_M^I} \right) \\ (N_{sf})^2 P_M^K \left(\dfrac{\frac{1}{N_{sf} P_M^I} \left(\mathbf{h}_M^I\right)^H \left(\widehat{\boldsymbol{\Omega}}_M^{K,I}\right)^{-1} \left(\widehat{\mathbf{h}}_M^I\right)}{1 + \frac{N_{sf} P_M^{K,I}}{P_M^I} \left(\widehat{\mathbf{h}}_M^I\right)^H \left(\widehat{\boldsymbol{\Omega}}_M^{K,I}\right)^{-1} \widehat{\mathbf{h}}_M^I} \right) \end{array} \right) ,$$

$$= \left(\begin{array}{l} \left(\dfrac{\frac{N_{sf} P_M^{K,I}}{P_M^I} \left(\widehat{\mathbf{h}}_M^I\right)^H \left(\widehat{\boldsymbol{\Omega}}_M^{K,I}\right)^{-1} \boldsymbol{\Omega}_M^{K,I} \left(\widehat{\boldsymbol{\Omega}}_M^{K,I}\right)^{-1} \left(\widehat{\mathbf{h}}_M^I\right)}{\left(1 + \frac{N_{sf} P_M^{K,I}}{P_M^I} \left(\widehat{\mathbf{h}}_M^I\right)^H \left(\widehat{\boldsymbol{\Omega}}_M^{K,I}\right)^{-1} \widehat{\mathbf{h}}_M^I\right)^2} \right) \\ + \left(\dfrac{\frac{\left(N_{sf}\right)^2 \left(P_M^{K,I}\right)^2}{\left(P_M^I\right)^2} \left(\widehat{\mathbf{h}}_M^I\right)^H \left(\widehat{\boldsymbol{\Omega}}_M^{K,I}\right)^{-1} \mathbf{h}_M^I \left(\mathbf{h}_M^I\right)^H \left(\widehat{\boldsymbol{\Omega}}_M^{K,I}\right)^{-1} \left(\widehat{\mathbf{h}}_M^I\right)}{\left(1 + \frac{N_{sf} P_M^{K,I}}{P_M^I} \left(\widehat{\mathbf{h}}_M^I\right)^H \left(\widehat{\boldsymbol{\Omega}}_M^{K,I}\right)^{-1} \widehat{\mathbf{h}}_M^I\right)^2} \right) \end{array} \right)$$

(B.39)

so that the SINR expression becomes

$$
\begin{aligned}
SINR_M^{K,I}\Big|_{\;MMSE} \;=\; & \\
& \frac{\left|\left(\frac{\frac{N_{sf}P_M^{K,I}}{P_M^I}\left(\widehat{\mathbf{h}}_M^I\right)^H\left(\widehat{\mathbf{\Omega}}_M^{K,I}\right)^{-1}\mathbf{h}_M^I}{1+\frac{N_{sf}P_M^{K,I}}{P_M^I}\left(\widehat{\mathbf{h}}_M^I\right)^H\left(\widehat{\mathbf{\Omega}}_M^{K,I}\right)^{-1}\widehat{\mathbf{h}}_M^I}\right)\right|^2}{\left(\begin{array}{l}\left(\frac{\frac{N_{sf}P_M^{K,I}}{P_M^I}\left(\widehat{\mathbf{h}}_M^I\right)^H\left(\widehat{\mathbf{\Omega}}_M^{K,I}\right)^{-1}\mathbf{\Omega}_M^{K,I}\left(\widehat{\mathbf{\Omega}}_M^{K,I}\right)^{-1}\left(\widehat{\mathbf{h}}_M^I\right)}{\left(1+\frac{N_{sf}P_M^{K,I}}{P_M^I}\left(\widehat{\mathbf{h}}_M^I\right)^H\left(\widehat{\mathbf{\Omega}}_M^{K,I}\right)^{-1}\widehat{\mathbf{h}}_M^I\right)^2}\right) \\ +\left(\frac{\frac{\left(N_{sf}\right)^2\left(P_M^{K,I}\right)^2}{\left(P_M^I\right)^2}\left(\widehat{\mathbf{h}}_M^I\right)^H\left(\widehat{\mathbf{\Omega}}_M^{K,I}\right)^{-1}\mathbf{h}_M^I\left(\mathbf{h}_M^I\right)^H\left(\widehat{\mathbf{\Omega}}_M^{K,I}\right)^{-1}\left(\widehat{\mathbf{h}}_M^I\right)}{\left(1+\frac{N_{sf}P_M^{K,I}}{P_M^I}\left(\widehat{\mathbf{h}}_M^I\right)^H\left(\widehat{\mathbf{\Omega}}_M^{K,I}\right)^{-1}\widehat{\mathbf{h}}_M^I\right)^2}\right) \\ -\left|\left(\frac{\frac{N_{sf}P_M^{K,I}}{P_M^I}\left(\widehat{\mathbf{h}}_M^I\right)^H\left(\widehat{\mathbf{\Omega}}_M^{K,I}\right)^{-1}\mathbf{h}_M^I}{1+\frac{N_{sf}P_M^{K,I}}{P_M^I}\left(\widehat{\mathbf{h}}_M^I\right)^H\left(\widehat{\mathbf{\Omega}}_M^{K,I}\right)^{-1}\widehat{\mathbf{h}}_M^I}\right)\right|^2\end{array}\right)} \\
& = \frac{\left|\left(\frac{N_{sf}P_M^{K,I}}{P_M^I}\left(\widehat{\mathbf{h}}_M^I\right)^H\left(\widehat{\mathbf{\Omega}}_M^{K,I}\right)^{-1}\mathbf{h}_M^I\right)\right|^2}{\left(\begin{array}{l}\left(\frac{N_{sf}P_M^{K,I}}{P_M^I}\left(\widehat{\mathbf{h}}_M^I\right)^H\left(\widehat{\mathbf{\Omega}}_M^{K,I}\right)^{-1}\mathbf{\Omega}_M^{K,I}\left(\widehat{\mathbf{\Omega}}_M^{K,I}\right)^{-1}\left(\widehat{\mathbf{h}}_M^I\right)\right) \\ +\frac{\left(N_{sf}\right)^2\left(P_M^{K,I}\right)^2}{\left(P_M^I\right)^2}\left(\widehat{\mathbf{h}}_M^I\right)^H\left(\widehat{\mathbf{\Omega}}_M^{K,I}\right)^{-1}\mathbf{h}_M^I\left(\mathbf{h}_M^I\right)^H\left(\widehat{\mathbf{\Omega}}_M^{K,I}\right)^{-1}\left(\widehat{\mathbf{h}}_M^I\right) \\ -\left|\frac{N_{sf}P_M^{K,I}}{P_M^I}\left(\widehat{\mathbf{h}}_M^I\right)^H\left(\widehat{\mathbf{\Omega}}_M^{K,I}\right)^{-1}\mathbf{h}_M^I\right|^2\end{array}\right)} \\
& = \frac{\left|\left(\frac{N_{sf}P_M^{K,I}}{P_M^I}\left(\widehat{\mathbf{h}}_M^I\right)^H\left(\widehat{\mathbf{\Omega}}_M^{K,I}\right)^{-1}\mathbf{h}_M^I\right)\right|^2}{\left(\frac{N_{sf}P_M^{K,I}}{P_M^I}\left(\widehat{\mathbf{h}}_M^I\right)^H\left(\widehat{\mathbf{\Omega}}_M^{K,I}\right)^{-1}\mathbf{\Omega}_M^{K,I}\left(\widehat{\mathbf{\Omega}}_M^{K,I}\right)^{-1}\left(\widehat{\mathbf{h}}_M^I\right)\right)} \\
& = N_{sf}\frac{P_M^{K,I}}{P_M^I}\cdot\frac{\left|\left(\left(\widehat{\mathbf{h}}_M^I\right)^H\left(\widehat{\mathbf{\Omega}}_M^{K,I}\right)^{-1}\mathbf{h}_M^I\right)\right|^2}{\left(\widehat{\mathbf{h}}_M^I\right)^H\left(\widehat{\mathbf{\Omega}}_M^{K,I}\right)^{-1}\mathbf{\Omega}_M^{K,I}\left(\widehat{\mathbf{\Omega}}_M^{K,I}\right)^{-1}\left(\widehat{\mathbf{h}}_M^I\right)}
\end{aligned}
\tag{B.40}
$$

B.2.3 Symbol level RAKE SINR

Using (B.24) the symbol level SINR expression from (B.33) rewrites specifically for the RAKE receiver

$$
SINR_M^{K,I}\Big|_{\;RAKE} \;=\; \frac{\left|\left(\widehat{\boldsymbol{\nu}}_M^{K,I}\right)^H\overline{\boldsymbol{\nu}}_M^{K,I}\right|^2}{\left(\widehat{\boldsymbol{\nu}}_M^{K,I}\right)^H\overline{\mathbf{\Gamma}}_M^{K,I}\widehat{\boldsymbol{\nu}}_M^{K,I}-\left|\left(\widehat{\boldsymbol{\nu}}_M^{K,I}\right)^H\overline{\boldsymbol{\nu}}_M^{K,I}\right|^2}\,. \tag{B.41}
$$

Considering further (3.32) and that $|\cdot|^2 = (\cdot)^H(\cdot)$ the SINR expression turns into

$$
\begin{aligned}
&SINR_M^{K,I}\Big|_{RAKE} = \\
&\frac{\left|\left(N_{sf}\sqrt{P_M^{K,I}}\widehat{\mathbf{h}}_M^I\right)^H\left(N_{sf}\sqrt{P_M^{K,I}}\mathbf{h}_M^I\right)\right|^2}{\left(\begin{array}{l}\left(N_{sf}\sqrt{P_M^{K,I}}\widehat{\mathbf{h}}_M^I\right)^H\left(\begin{array}{l}N_{sf}P_M^I\boldsymbol{\Omega}_M^{K,I}\\ +(N_{sf})^2P_M^{K,I}\mathbf{h}_M^I\left(\mathbf{h}_M^I\right)^H\end{array}\right)\left(N_{sf}\sqrt{P_M^{K,I}}\widehat{\mathbf{h}}_M^I\right)\\ -\left|\left(N_{sf}\sqrt{P_M^{K,I}}\widehat{\mathbf{h}}_M^I\right)^H\left(N_{sf}\sqrt{P_M^{K,I}}\mathbf{h}_M^I\right)\right|^2\end{array}\right)}\\
&=\frac{N_{sf}P_M^{K,I}\left|\left(\widehat{\mathbf{h}}_M^I\right)^H\left(\mathbf{h}_M^I\right)\right|^2}{\left(\begin{array}{l}P_M^I\left(\widehat{\mathbf{h}}_M^I\right)^H\boldsymbol{\Omega}_M^{K,I}\widehat{\mathbf{h}}_M^I\\ +N_{sf}P_M^{K,I}\left(\widehat{\mathbf{h}}_M^I\right)^H\mathbf{h}_M^I\left(\mathbf{h}_M^I\right)^H\widehat{\mathbf{h}}_M^I\\ -N_{sf}P_M^{K,I}\left(\mathbf{h}_M^I\right)^H\widehat{\mathbf{h}}_M^I\left(\widehat{\mathbf{h}}_M^I\right)^H\mathbf{h}_M^I\end{array}\right)}\\
&=N_{sf}\frac{P_M^{K,I}}{P_M^I}\frac{\left|\left(\widehat{\mathbf{h}}_M^I\right)^H\left(\mathbf{h}_M^I\right)\right|^2}{\left(\widehat{\mathbf{h}}_M^I\right)^H\boldsymbol{\Omega}_M^{K,I}\widehat{\mathbf{h}}_M^I}
\end{aligned}
\tag{B.42}
$$

B.3 Secondary Scrambling Code Deployment

The usage of *secondary scrambling code* (SSC) extends the available downlink code space, *i.e.* all Walsh-Hadamard channelisation codes could in combination with SSCs be reused for additional downlink transmissions. The spread data sequences transmitted over an SSC are, however, not orthogonal to the spread data sequences transmitted under the *primary scrambling code* (PSC) and *vice versa*. The deployment of additional scrambling codes therefore leads to an increase in own-sector interference.

For notational simplicity only a single index i was used in Chapter 3 to relate to sector i and a single unique scrambling code i. The introduction of one or more secondary scrambling codes, however, calls for means to distinguish the parts of sector power allocated to each scrambling code. Confined to this Appendix a fourth index s is therefore introduced that indexes the N_s different scrambling codes in

sector i. Using this new scrambling code index (3.32) rewrites

$$\overline{\mathbf{\Gamma}}_M^{K,I,S} = N_{sf}\overline{P}_M^I \underbrace{\left(\begin{array}{l} \sum\limits_{i=1}^{N_{\mathrm{sec}}} \sum\limits_{s=1}^{N_s} \sum\limits_{m=1}^{N_{vir}} \dfrac{\overline{P}_m^{i,s}}{\overline{P}_M^I} \cdot \mathbf{H}_m^i \left(\mathbf{H}_m^i\right)^H \\ - \sum\limits_{m=1}^{N_{vir}} \dfrac{\overline{P}_m^{I,S}}{\overline{P}_M^I} \cdot \mathbf{h}_m^I \left(\mathbf{h}_m^I\right)^H \\ + N_{sf} \sum\limits_{\substack{m=1 \\ m \neq M}}^{N_{vir}} \dfrac{\overline{P}_m^{K,I,S}}{\overline{P}_M^I} \cdot \mathbf{h}_m^I \left(\mathbf{h}_m^I\right)^H \\ + \dfrac{\sigma_v^2}{\overline{P}_M^I} \cdot \mathbf{I}_{(N_{rx} \cdot N_{FIR})} \end{array} \right)}_{\mathbf{\Omega}_M^{K,I,S}} + (N_{sf})^2 \cdot \overline{P}_M^{K,I,S} \cdot \mathbf{h}_M^I \left(\mathbf{h}_M^I\right)^H \quad , \tag{B.43}$$

where the small area mean received signal power sum previously defined in (3.10) is redefined as

$$P_m^i = \sum_{s=1}^{N_s} \sum_{k=1}^{N_{sf}} P_m^{k,i,s} \quad , \tag{B.44}$$

and $P_m^{k,i,s}$ relates to the power sector i gives to scrambling code resource s, channelisation code resource k, and virtual broadcast channel m.

Replacement of $\mathbf{\Omega}_M^{K,I}$ in (3.34) and (3.35) with the new $\mathbf{\Omega}_M^{K,I,S}$ delivers the symbol level SINR after MMSE or RAKE reception in case of secondary scrambling code deployment.

B.4 Comparison with [Rami03a] and [Rami03b]

The following relates the RAKE receiver SINR formulation in (3.35) to the '1Tx-1Rx', and the 'CLTD' SINR expressions in [Rami03a], [Rami03b]. On the same assumptions two independent SINR expressions are then summed to represent the '2Rake' and the 'CLTD+2Rake' cases. To follow the comparison specifically for the closed loop transmit diversity cases, it is beneficial to be familiar with the CLM1 implementation of the virtual channel concept as presented in Subsection 4.3.3.

The simplifications are based on the assumptions:

- Ideal channel estimation.
- Uncorrelated radio propagation channel impulse responses.
- Uncorrelated interfering signals at the RAKE fingers.
- No co-stream transmission, *i.e.* no code reuse.
- In case of CLM1 the interfering sectors are assumed to transmit their power equally distributed between the four tx weight options.

Recall the RAKE receiver SINR formulation in case of ideal channel estimation as given in (3.37), *i.e.*

$$SINR_M^{K,I}\left|\begin{array}{c} idealest \\ RAKE \end{array}\right. = N_{sf}\frac{P_M^{K,I}}{P_M^I}\frac{\left|\left(\mathbf{h}_M^I\right)^H\left(\mathbf{h}_M^I\right)\right|^2}{\left(\mathbf{h}_M^I\right)^H\mathbf{\Omega}_M^{K,I}\mathbf{h}_M^I} \quad . \tag{B.45}$$

If only a single receive antenna is used, $\mathbf{H}_m^i = \mathbf{H}_{n,m}^i$ and $\mathbf{h}_m^i = \mathbf{h}_{n,m}^i$. Further, the assumptions of uncorrelated interfering signals over the RAKE fingers is used to justify the approximation

$$\sum_{i=1}^{N_{\text{sec}}}\sum_{m=1}^{N_{vir}}\frac{P_m^i}{P_M^I}\cdot\mathbf{H}_{n,m}^i\left(\mathbf{H}_{n,m}^i\right)^H \approx \sum_{i=1}^{N_{\text{sec}}}\sum_{m=1}^{N_{vir}}\frac{P_m^i}{P_M^I}\cdot\left(\mathbf{h}_{n,m}^i\right)^H\mathbf{h}_{n,m}^i\cdot\mathbf{I}_{N_{FIR}} \quad , \tag{B.46}$$

so that $\mathbf{\Omega}_M^{K,I}$ from (3.32) reduces to

$$\begin{aligned}\mathbf{\Omega}_M^{K,I} &= \sum_{i=1}^{N_{\text{sec}}}\sum_{m=1}^{N_{vir}}\frac{P_m^i}{P_M^I}\cdot\mathbf{H}_{n,m}^i\left(\mathbf{H}_{n,m}^i\right)^H + \frac{P^{th}}{P_M^I}\cdot\mathbf{I}_{N_{FIR}} \\ &\quad + N_{sf}\underbrace{\sum_{\substack{m=1\\ m\neq M}}^{N_{vir}}\frac{P_m^{K,I}}{P_M^I}\cdot\mathbf{h}_{n,m}^I\left(\mathbf{h}_{n,m}^I\right)^H}_{0} \\ &\quad \underbrace{-\sum_{m=1}^{N_{vir}}\frac{P_m^I}{P_M^I}\cdot\mathbf{h}_{n,m}^I\left(\mathbf{h}_{n,m}^I\right)^H}_{\mathbf{h}_{n,M}^I\left(\mathbf{h}_{n,M}^I\right)^H} \\ &\approx \left(\sum_{i=1}^{N_{\text{sec}}}\sum_{m=1}^{N_{vir}}\frac{P_m^i}{P_M^I}\left(\mathbf{h}_{n,m}^i\right)^H\mathbf{h}_{n,m}^i + \frac{P^{th}}{P_M^I}\right)\cdot\mathbf{I}_{N_{FIR}} - \mathbf{h}_{n,M}^I\left(\mathbf{h}_{n,M}^I\right)^H \quad .\end{aligned} \tag{B.47}$$

Thus the SINR at the single receive antenna n can be written as

$$
\begin{aligned}
&SINR_{n,M}^{K,I}\Big|_{\substack{idealest,\,uncorr\\ RAKE}} \\
&= N_{sf}\frac{P_M^{K,I}}{P_M^I}\frac{\left|\left(\mathbf{h}_{n,M}^I\right)^H\left(\mathbf{h}_{n,M}^I\right)\right|^2}{\left(\mathbf{h}_{n,M}^I\right)^H\left(\left(\sum_{i=1}^{N_{\sec}}\sum_{m=1}^{N_{vir}}\frac{P_m^i}{P_M^I}\left(\mathbf{h}_{n,m}^i\right)^H\mathbf{h}_{n,m}^i+\frac{P^{th}}{P_M^I}\right)\cdot\mathbf{I}_{N_{FIR}}-\mathbf{h}_{n,M}^I\left(\mathbf{h}_{n,M}^I\right)^H\right)\mathbf{h}_{n,M}^I} \\
&= N_{sf}\frac{P_M^{K,I}}{P_M^I}\frac{\left(\mathbf{h}_{n,M}^I\right)^H\left(\mathbf{h}_{n,M}^I\right)}{\left(\sum_{i=1}^{N_{\sec}}\sum_{m=1}^{N_{vir}}\frac{P_m^i}{P_M^I}\left(\mathbf{h}_{n,m}^i\right)^H\mathbf{h}_{n,m}^i+\frac{P^{th}}{P_M^I}\right)-\left(\mathbf{h}_{n,M}^I\right)^H\mathbf{h}_{n,M}^I}
\end{aligned}
\tag{B.48}
$$

Rearranging and rewriting the SINR expression in terms of its multipath components delivers

$$
\begin{aligned}
&SINR_{n,M}^{K,I}\Big|_{\substack{idealest,\,uncorr\\ RAKE}} = \\
&\sum_{l_1=1}^{N_L}\frac{N_{sf}P_M^{K,I}\left(\left(\mathbf{h}_{n,M}^I\right)^H\right)_{[l_1]}\left(\mathbf{h}_{n,M}^I\right)_{[l_1]}}{P^{th}+\sum_{i=1}^{N_{\sec}}\sum_{m=1}^{N_{vir}}\sum_{l_2=1}^{N_L}\left(P_m^i\left(\left(\mathbf{h}_{n,m}^i\right)^H\right)_{[l_2]}\left(\mathbf{h}_{n,m}^i\right)_{[l_2]}-P_M^I\left(\left(\mathbf{h}_{n,M}^I\right)^H\right)_{[l_2]}\left(\mathbf{h}_{n,M}^I\right)_{[l_2]}\right)},
\end{aligned}
\tag{B.49}
$$

where it was used that the last N_L-1 elements of the N_{FIR} long column vector $\mathbf{h}_{n,m}^i$ are zero.

For a 1×1 SISO situation, $N_{vir}=1$. This makes (B.49) equivalent to the '1Tx-1Rx' SINR expression in [Rami03b, (1)], [Rami03a, (6.6)]. If, however, a simple CLM1 configuration is considered, where the interfering sectors are transmitting the pilots over virtual channel one and two and all other interference power is evenly distributed over virtual channel three to six[1], *i.e.* $\boldsymbol{\omega}^i = \begin{bmatrix} \frac{1}{2} & \frac{1}{2} & \frac{1}{4} & \frac{1}{4} & \frac{1}{4} & \frac{1}{4} \end{bmatrix}^T$, $\boldsymbol{\eta} = \begin{bmatrix} \eta^{PCPICH} & \eta^{OTHER} \end{bmatrix}^T$, (B.49) can be equivalently related to the 'CLTD' SINR expression in [Rami03b, (3)], [Rami03a, (6.8)]. This becomes apparent recalling the virtual channel definition from (3.18) so that

$$
\begin{aligned}
\left(\left(\mathbf{h}_{n,M}^I\right)^H\right)_{[l_1]}\left(\mathbf{h}_{n,M}^I\right)_{[l_1]} &= \left|\left(\mathbf{h}_{n,M}^I\right)_{[l_1]}\right|^2 \\
&= \left|\left(\left(\underline{\mathbf{h}}_{n,1}^I\right)\cdot w_{1,M}^I+\underline{\mathbf{h}}_{n,2}^I\cdot w_{2,M}^I\right)_{[l_1]}\right|^2,
\end{aligned}
\tag{B.50}
$$

and using the virtual cannel definitions for the summands in the denominator of (B.49) delivers

[1] When the HS-DSCH transmission is used with a large fraction of the total sector transmit power, such an even distribution is unlikely.

$$
\begin{aligned}
&\sum_{m=1}^{N_{vir}} \overline{P}_m^i \left(\mathbf{h}_{n,m}^i\right)^H \mathbf{h}_{n,m}^i \\
&= P^i \cdot \sum_{m=1}^{N_{vir}} \boldsymbol{\omega}_m^i \cdot \boldsymbol{\eta}^i \cdot \left(\mathbf{h}_{n,m}^i\right)^H \mathbf{h}_{n,m}^i \\
&\overset{\mathrm{P}^i}{=} \cdot \left(\begin{array}{l} \frac{1}{2} \cdot \eta^{PCPICH} \cdot \left(\left(\underline{\mathbf{h}}_{n,1}^i\right)^H \underline{\mathbf{h}}_{n,1}^i + \left(\underline{\mathbf{h}}_{n,2}^i\right)^H \underline{\mathbf{h}}_{n,2}^i \right) \\ + \frac{1}{4} \cdot \eta^{OTHER} \cdot \sum_{u=1}^{4} \left(\frac{1}{\sqrt{2}} \underline{\mathbf{h}}_{n,1}^i + \frac{1}{\sqrt{2}} \cdot e^{j\frac{\pi}{4}(2u+1)} \underline{\mathbf{h}}_{n,2}^i \right)^H \left(\frac{1}{\sqrt{2}} \underline{\mathbf{h}}_{n,1}^i + \frac{1}{\sqrt{2}} \cdot e^{j\frac{\pi}{4}(2u+1)} \underline{\mathbf{h}}_{n,2}^i \right) \end{array} \right) \\
&\overset{\mathrm{P}^i}{=} \cdot \left(\begin{array}{l} \frac{1}{2} \cdot \eta^{PCPICH} \cdot \left(\left(\underline{\mathbf{h}}_{n,1}^i\right)^H \underline{\mathbf{h}}_{n,1}^i + \left(\underline{\mathbf{h}}_{n,2}^i\right)^H \underline{\mathbf{h}}_{n,2}^i \right) \\ + \frac{1}{4} \cdot \eta^{OTHER} \cdot \sum_{u=1}^{4} \left(\frac{1}{2} \left(\underline{\mathbf{h}}_{n,1}^i\right)^H \underline{\mathbf{h}}_{n,1}^i + \frac{1}{2} \left(\underline{\mathbf{h}}_{n,2}^i\right)^H \underline{\mathbf{h}}_{n,2}^i + \mathrm{Re}\left\{ \left(\underline{\mathbf{h}}_{n,1}^i\right)^H \underline{\mathbf{h}}_{n,2}^i \cdot e^{j\frac{\pi}{4}(2u+1)} \right\} \right) \end{array} \right), \\
&\overset{\mathrm{P}^i}{=} \cdot \left(\begin{array}{l} \frac{1}{2} \cdot \eta^{PCPICH} \cdot \left(\left(\underline{\mathbf{h}}_{n,1}^i\right)^H \underline{\mathbf{h}}_{n,1}^i + \left(\underline{\mathbf{h}}_{n,2}^i\right)^H \underline{\mathbf{h}}_{n,2}^i \right) \\ + \frac{1}{2} \cdot \eta^{OTHER} \cdot \left(\left(\underline{\mathbf{h}}_{n,1}^i\right)^H \underline{\mathbf{h}}_{n,1}^i + \left(\underline{\mathbf{h}}_{n,2}^i\right)^H \underline{\mathbf{h}}_{n,2}^i \right) \\ + \underbrace{\frac{1}{4} \cdot \eta^{OTHER} \cdot \sum_{u=1}^{4} \mathrm{Re}\left\{ \left(\underline{\mathbf{h}}_{n,1}^i\right)^H \underline{\mathbf{h}}_{n,2}^i \cdot e^{j\frac{\pi}{4}(2u+1)} \right\}}_{0} \end{array} \right) \\
&\overset{\mathrm{P}^i}{=} \cdot \left(\frac{1}{2} \cdot \underbrace{\left(\eta^{PCPICH} + \eta^{OTHER}\right)}_{1} \cdot \left(\left(\underline{\mathbf{h}}_{n,1}^i\right)^H \underline{\mathbf{h}}_{n,1}^i + \left(\underline{\mathbf{h}}_{n,2}^i\right)^H \underline{\mathbf{h}}_{n,2}^i \right) \right) \\
&= \frac{1}{2} \cdot P^i \cdot \left(\left(\underline{\mathbf{h}}_{n,1}^i\right)^H \underline{\mathbf{h}}_{n,1}^i + \left(\underline{\mathbf{h}}_{n,2}^i\right)^H \underline{\mathbf{h}}_{n,2}^i \right)
\end{aligned}
\tag{B.51}
$$

which in terms of multipath components can be written as

$$
\begin{aligned}
&\sum_{m=1}^{N_{vir}} P_m^i \left(\mathbf{h}_{n,m}^i\right)^H \mathbf{h}_{n,m}^i \\
&= \frac{1}{2} \cdot P^i \cdot \sum_{l=1}^{N_L} \left(\left(\left(\underline{\mathbf{h}}_{n,1}^i\right)^H \right)_{[l]} \left(\underline{\mathbf{h}}_{n,1}^i\right)_{[l]} + \left(\left(\underline{\mathbf{h}}_{n,2}^i\right)^H \right)_{[l]} \left(\underline{\mathbf{h}}_{n,2}^i\right)_{[l]} \right) .
\end{aligned}
\tag{B.52}
$$

Thus (B.49) turns into

$$SINR_{n,M}^{K,I}\left|\begin{array}{c} idealest, uncorr \\ RAKE \end{array}\right. = \sum_{l_1=1}^{N_L} \frac{N_{sf} P_M^{K,I} \left| \left(\left(\underline{\mathbf{h}}_{n,1}^{I} \right) \cdot w_{1,M}^{I} + \underline{\mathbf{h}}_{n,2}^{I} \cdot w_{2,M}^{I} \right)_{[l_1]} \right|^2}{P^{th} + \sum_{i=1}^{N_{sec}} \sum_{l_2=1}^{N_L} \left(\begin{array}{l} \frac{1}{2} \cdot P^{i} \cdot \left(\begin{array}{l} \left(\left(\underline{\mathbf{h}}_{n,1}^{i} \right)^H \right)_{[l_2]} \left(\underline{\mathbf{h}}_{n,1}^{i} \right)_{[l_2]} \\ + \left(\left(\underline{\mathbf{h}}_{n,2}^{i} \right)^H \right)_{[l_2]} \left(\underline{\mathbf{h}}_{n,2}^{i} \right)_{[l_2]} \end{array} \right) \\ - \frac{1}{2} \cdot P^{I} \cdot \left(\begin{array}{l} \left(\left(\underline{\mathbf{h}}_{n,1}^{I} \right)^H \right)_{[l_2]} \left(\underline{\mathbf{h}}_{n,1}^{I} \right)_{[l_2]} \\ + \left(\left(\underline{\mathbf{h}}_{n,2}^{I} \right)^H \right)_{[l_2]} \left(\underline{\mathbf{h}}_{n,2}^{I} \right)_{[l_2]} \end{array} \right) \end{array} \right)} \quad , \tag{B.53}$$

through which the equivalent relation to [Rami03b, (3)], [Rami03a, (6.8)] becomes apparent.

In case of more than one receive antenna, the single antenna SINRs are simply added, which models MRC over the antenna elements if the same amount of interference and noise power is experienced on both rx branches, *i.e.*

$$SINR_{M}^{K,I}\left|\begin{array}{c} idealest, uncorr \\ RAKE \end{array}\right. = \sum_{n=1}^{N_{rx}} SINR_{n,M}^{K,I}\left|\begin{array}{c} idealest, uncorr \\ RAKE \end{array}\right. \quad , \tag{B.54}$$

In the case of $N_{rx} = 2$, (B.54) is equivalent to the expressions for '2Rake' and 'CLTD + 2Rake' in [Rami03b, (4), (5)], [Rami03a, (6.9), (6.10)]. One should, however, bear in mind that the simple summation over the receive antennas can overestimate the performance, especially in an CLM1 situation, when tx weights are not chosen optimally with respect to two rx antennas.

Appendix C

Modelling Framework - Simulator Validation

To gain confidence in the produced simulation results it is necessary to validate the different simulator implementations. For this purpose the performance of the simulators is compared against references as depicted in Figure C.1. The Figure also gives an outline of the main sections within this Appendix.

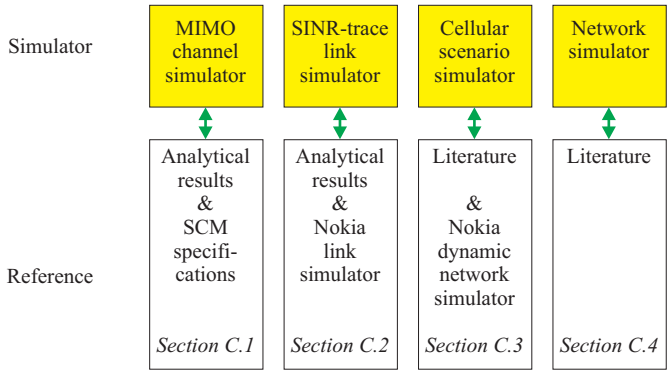

Figure C.1: Simulator validation outline.

C.1 MIMO Channel Simulator Validation

To validate the MIMO channel simulator performance the obtained fading statistics, the spatial correlations, and Doppler spectra are compared against SCM reference values and analytical bounds. The section closes with a look at two different chip alignment procedures used as a simple substitute for real receive filtering.

C.1.1 Channel Fading Statistics

Figure C.2 compares the fading statistics of the generated MIMO channels from Table 4.2 (solid lines) with analytical bounds obtained from (A.1) through mean adjustment (dotted lines). Additionally, the fading statistics of a single path mean normalised flat Rayleigh fading channel are plotted as reference (dashed line).

The statistics have been obtained from 30000 simulated slots at a terminal speed of 3 km/h. At 2 GHz this corresponds to a travelled distance of approximately 111 wavelengths. Knowing that a Rayleigh fade of 20 dB below the mean occurs statistically once in 100 uncorrelated fading samples, which under the 360° uniform AoA distribution can roughly be obtained over a travelled distance of 50 wavelengths, it appears that the selected simulation length can only roughly capture the Rayleigh fading behaviour. To significantly improve the statistical representation a multiple of the selected simulation length, *e.g.* 500 wavelengths, would be desirable. However, assessing the additional processing burden the simulation length is kept at 111 wavelengths. Additional results on the statistical significance of the multipath fading channel simulations can be found in Appendix D.1.

C.1.2 Tx and Rx Correlation

For validation purposes [SCM 03] explicitly states the tx and rx correlation properties for various antenna spacings, rms angle spreads, and angles of arrival at a fixed angle of connection of 20°. Using the bootstrap method from [Zoub98, Table 11] the per-path tx and rx correlation magnitudes have been estimated from the MIMO channel fading statistics produced by the MIMO channel simulator. Per-path correlation magnitude estimates and their 90% confidence intervals are given in Table C.1. The SCM reference values are marked bold. It can be seen that the SCM reference values lie inside the 90% confidence intervals obtained from MIMO multipath fading simulations. This indicates that tx and rx correlation are modelled as desired.

C.1.3 Doppler Spectrum

For each time series of channel paths, $\{h\}$, the Doppler spectrum is estimated and compared with the analytical Doppler spectrum derived in [Clar68]. Normalised by the maximum Doppler shift f_m the analytical expression writes

$$S\left(\frac{f_d}{f_m}\right) = \frac{1}{\pi \cdot \sqrt{1 - \left(\frac{f_d}{f_m}\right)^2}} \quad , \tag{C.1}$$

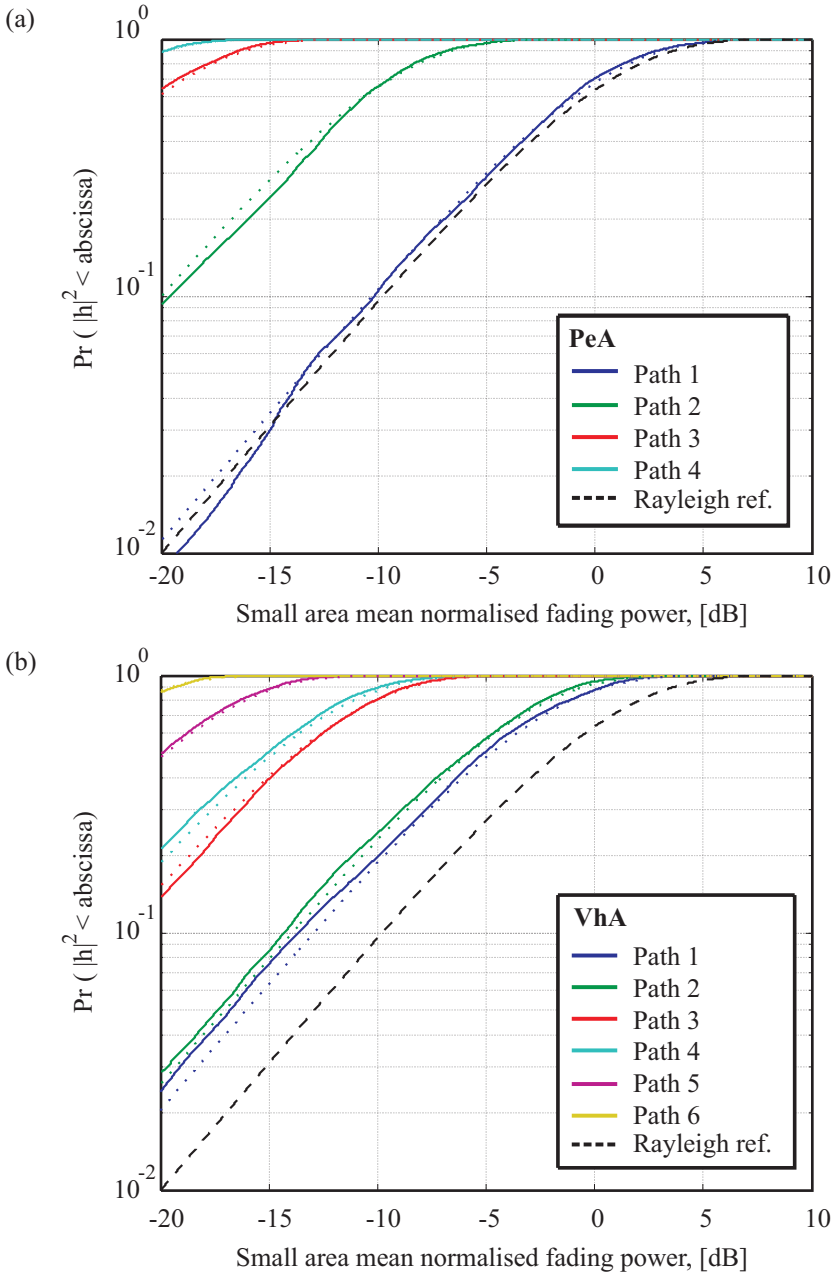

Figure C.2: Fading statistics: (a) corresponding to PeA and (b) corresponding to VhA.

	PeA wc	PeA hc	VhA wc	VhA hc
Tx conf. lower	0.0040	0.9652	0.0357	0.9660
Tx corr. mag.	0.0440	0.9676	0.0822	0.9677
Tx conf. upper	0.0736	0.9698	0.1192	0.9694
Tx SCM ref.	**0.0704**	**0.9688**	**0.0704**	**0.9688**
Rx conf. lower	0.2556	0.2727	0.2785	0.2891
Rx corr. mag.	0.2965	0.3138	0.3256	0.3256
Rx conf. upper	0.3346	0.3440	0.3600	0.3657
Rx SCM ref.	**0.3042**	**0.3042**	**0.3042**	**0.3042**

Table C.1: Correlation magnitude comparison. Bold marks the SCM reference values [SCM 03, p. 13].

where f_d is the Doppler frequency. Both spectra are plotted in Figure C.3. A good match between estimate and analytical result is obtained, validating the angular characteristics at the mobile terminal.

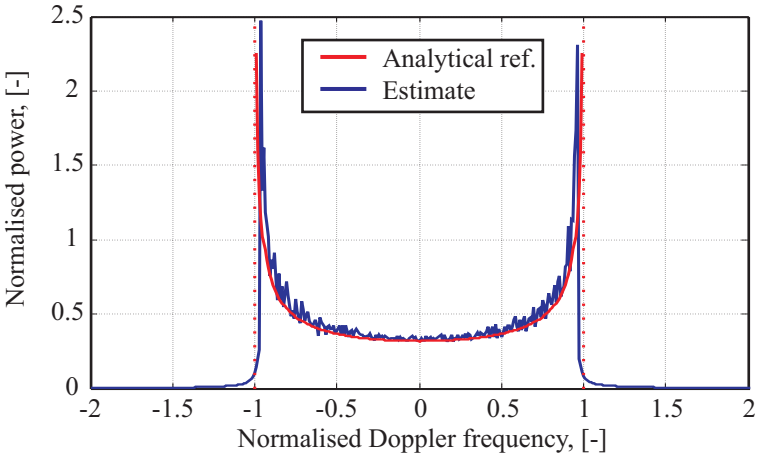

Figure C.3: Comparison between analytical and estimated normalised Doppler spectrum.

C.1.4 Chip Alignment Effects

Figure C.4 displays the impulse responses for the ITU-Pedestrian A channel and the ITU-Vehicular A channel [ITU97], [SCM 03], as well as their chip aligned modifications.

To get an idea of the impact the different chip alignment procedures can have on the SINR statistics, SINR cdfs for a simple SISO situation with AWGN other-sector interference are plotted in Figure C.5 using the G-factors of -9 dB, 0 dB and 17 dB and for the ITU-Pedestrian A (PeA) as well as for the ITU-Vehicular A

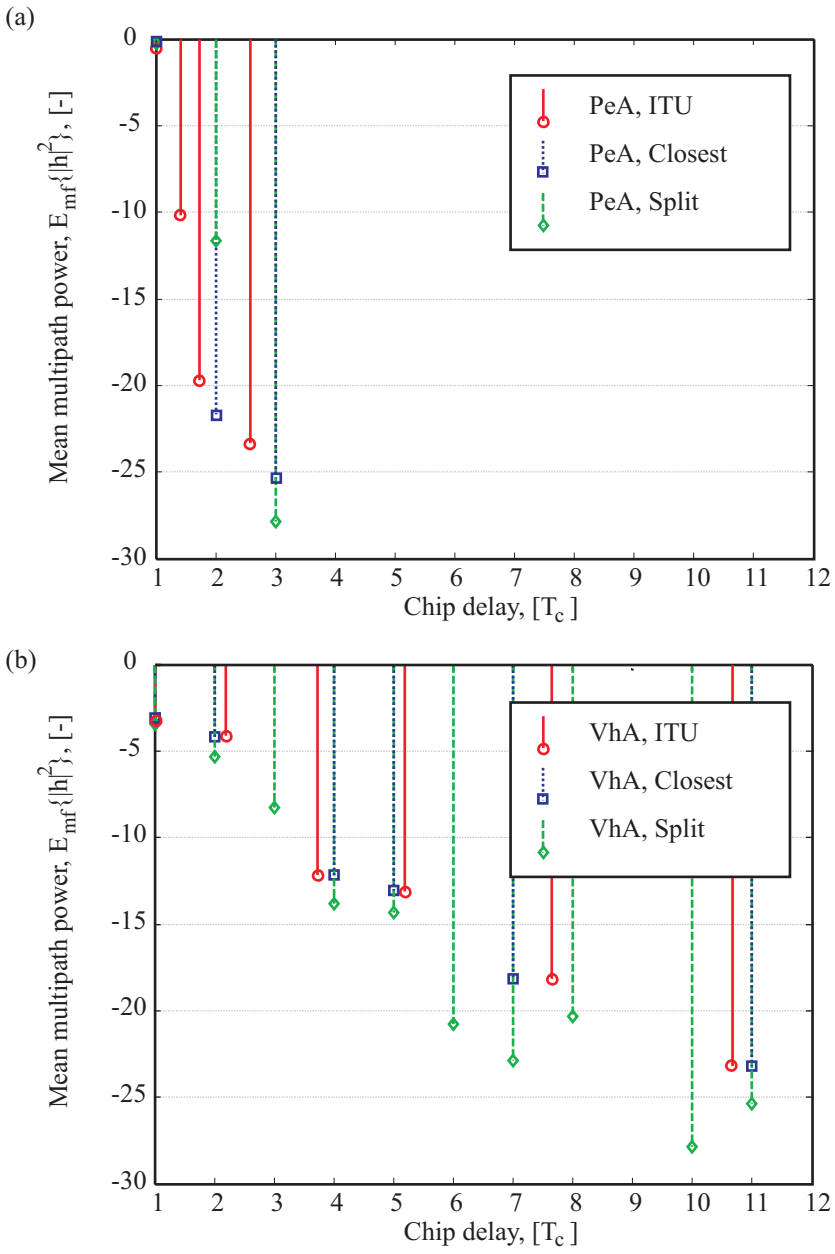

Figure C.4: Effects of different chip alignment procedures on the ITU-Pedestrian A and the ITU-Vehicular A PDP.

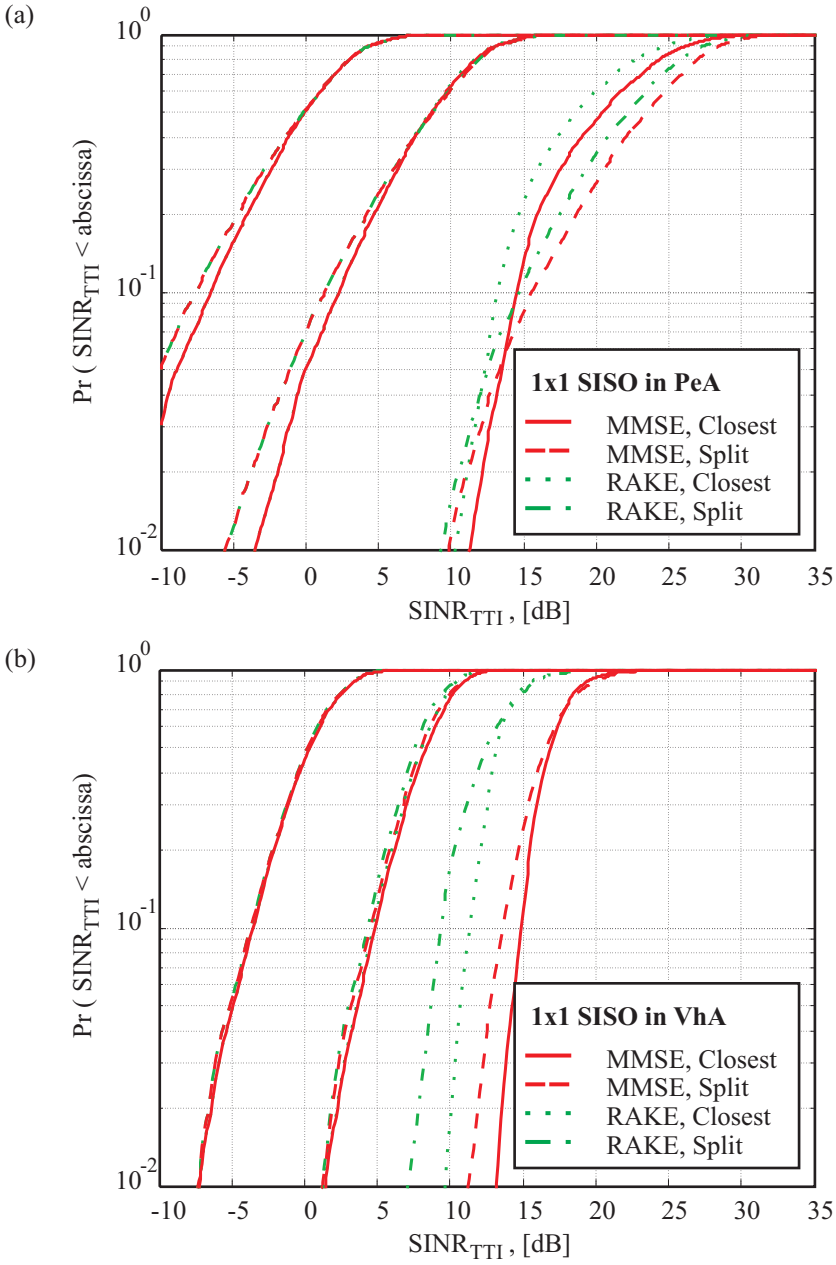

Figure C.5: Effect of chip alignment procedures on SINR statistics.

(VhA) PDP.

It can be seen that especially for a high G-factor like $G = 17$ dB the SINR statistics can vary dramatically depending on the selected chip alignment procedure. RAKE reception and MMSE reception are similarly affected. When comparing SINR statistics it is important to use identical chip alignment procedures. The Nokia internal link level simulator used as reference implements the closest chip alignment procedure. This 'Closest' procedure is thus selected for the link level SINR simulations presented throughout.

C.2 Link Simulator Validation

Operation of the SINR link level simulator is validated via comparison with the analytical SINR statistics presented in Chapter 2, and via comparison with results obtained from a Nokia internal link level simulator. The test case simulation parameters are summarised in Table C.2.

Parameter	**Setting**
MIMO channel case	Flat uncorr. Rayleigh (SCM Case VI), or VhA wc (SCM Case II.2)
AoC, θ^I	20°
Interference model	AWGN
N_{sf}	16
$\tilde{N}_{codeco}$	15 (only relevant for 2×2 SMP$_{dual}$)
$\eta^{HSDSCH,i}$	0.7
Speed	3 km/h
Number of simulated slots	30000

Table C.2: Parameter settings for AWGN other-sector interference link simulator validation

C.2.1 Comparison with Analytical Bounds

The analytical bounds in Chapter 2 use the mean SINR obtained in a flat fading 1×1 SISO link, *i.e.* $\overline{SINR}_{branch}$, as reference. For comparison this SINR needs to be related to the link simulator settings from Table C.2. For a flat uncorrelated Rayleigh fading channel and for the AWGN other-sector interference model $\overline{SINR}_{branch}$ can be expressed as

$$\overline{SINR}_{branch} = N_{sf} \cdot \eta^{HSDSCH,i} \cdot G \quad , \tag{C.2}$$

which accounts for the processing gain, the sector power allocation to the HS-DSCH channel and the own to other-sector small area mean received power ratio

respectively.

For a G-factor of 0 dB the $\overline{SINR}_{branch}$ is approximately 10.5 dB. For this G-factor Figure C.6 (a) plots the obtained link level simulation results jointly with the analytical bounds that have previously been presented in Figure 2.9. Analytical and simulation result in Figure C.6 (a) use the same line style. However, all simulation results are plotted in black. For all but the 2×2 SMP$_{dual}$ scheme, RAKE/MRC and MMSE/OPC receiver results are identical. The analytical results for 2×2 SMP$_{dual}$-OPC correspond to the MMSE receiver simulation results only. A more detailed plot of the analytical and simulated 2×2 SMP$_{dual}$ results is presented in Figure C.6 (b), where the solid lines mark the analytical and the dotted lines the simulated results.

For all antenna configurations a good match is obtained. Discrepancies are in the order of tenth of a dB. This validates the link simulator implementation for the case of a flat uncorrelated Rayleigh fading channel. Especially the results in Figure C.6 (b) are taken as validation for the MMSE receiver implementation in general.

C.2.2 Comparison with Nokia Link Simulation Results

To test the simulator operation also in correlated frequency selective fading, the simulation results are compared against results from a Nokia internal link simulator in the VhA wc channel case of Table 4.2 [1]. Only RAKE receiver performance results for the SISO, SIMO, and CLM1 case are available as reference. These are presented in Figure C.7 and Figure C.8 for the G-factors -9 dB, 0 dB and 17 dB.

Inspection of Figure C.7 and Figure C.8 reveals some discrepancy especially at the low G-factor of -9 dB. For a G of 0 dB and a G of 17 dB the discrepancies are in the order of tenth of a dB. In general such differences are to be expected when comparing two very different simulator implementations, and the presented comparison is interpreted as validation of link simulator performance also in frequency selective fading.

C.3 Cellular Scenario Simulator Validation

The aim of the following is twofold. Firstly, it is evaluated which x-y step size, and how many shadow fading realisations are needed to generate stable G-factor statistics within the cellular scenario simulator. Secondly, the obtained G-factor

[1] The reference link level results are generated by Wei Na, who is with the Cellular Systems Division at Aalborg University.

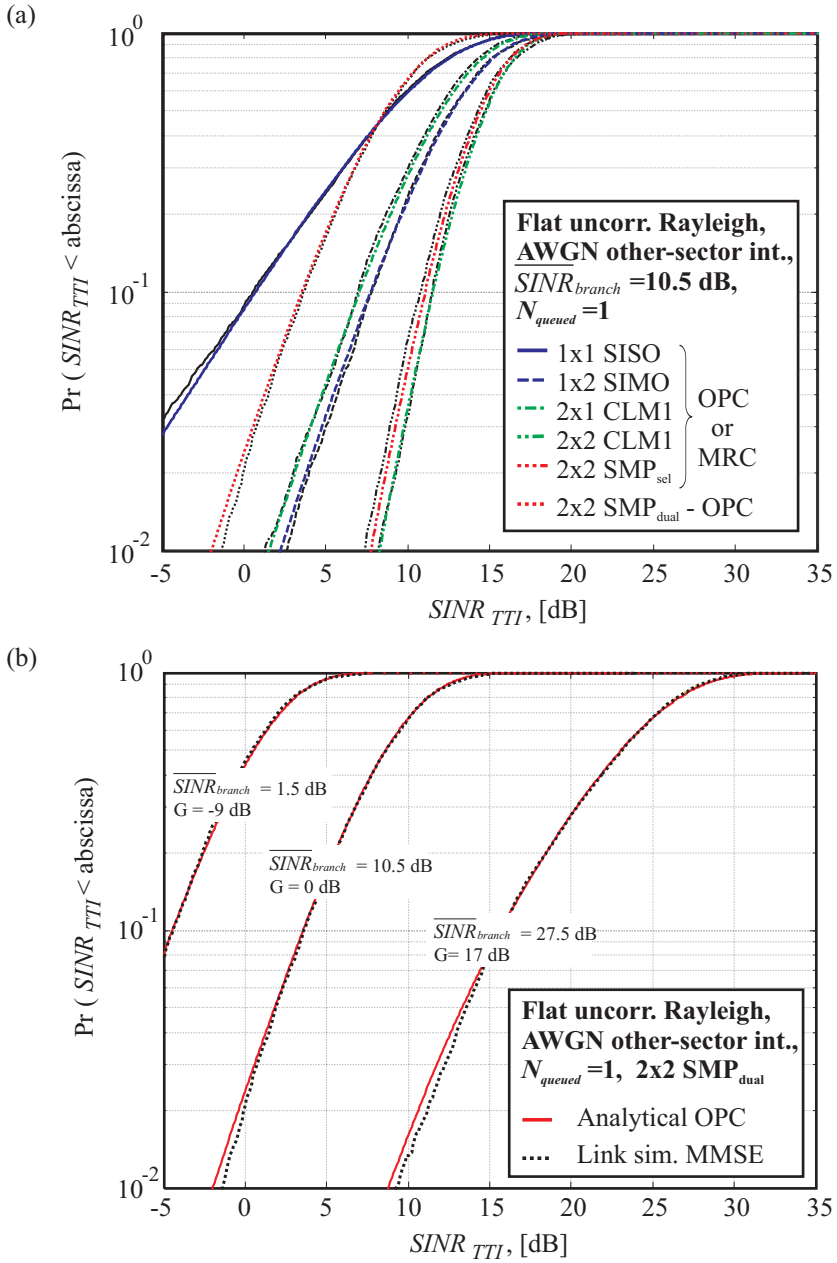

Figure C.6: Comparison of analytical bounds and link level simulation results in a flat uncorrelated Rayleigh fading test channel, with AWGN other sector interference.

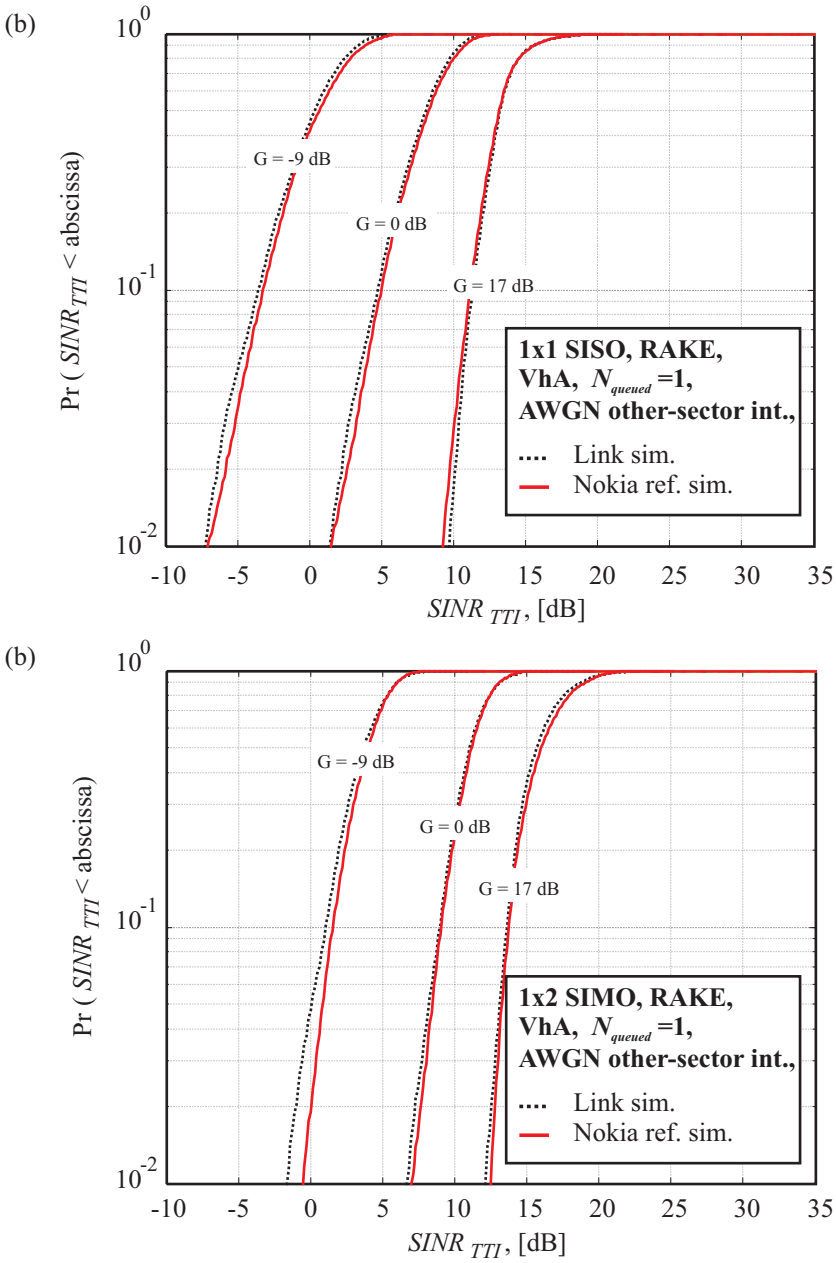

Figure C.7: 1×1 SISO and 1×2 SIMO comparison with Nokia reference results in VhA.

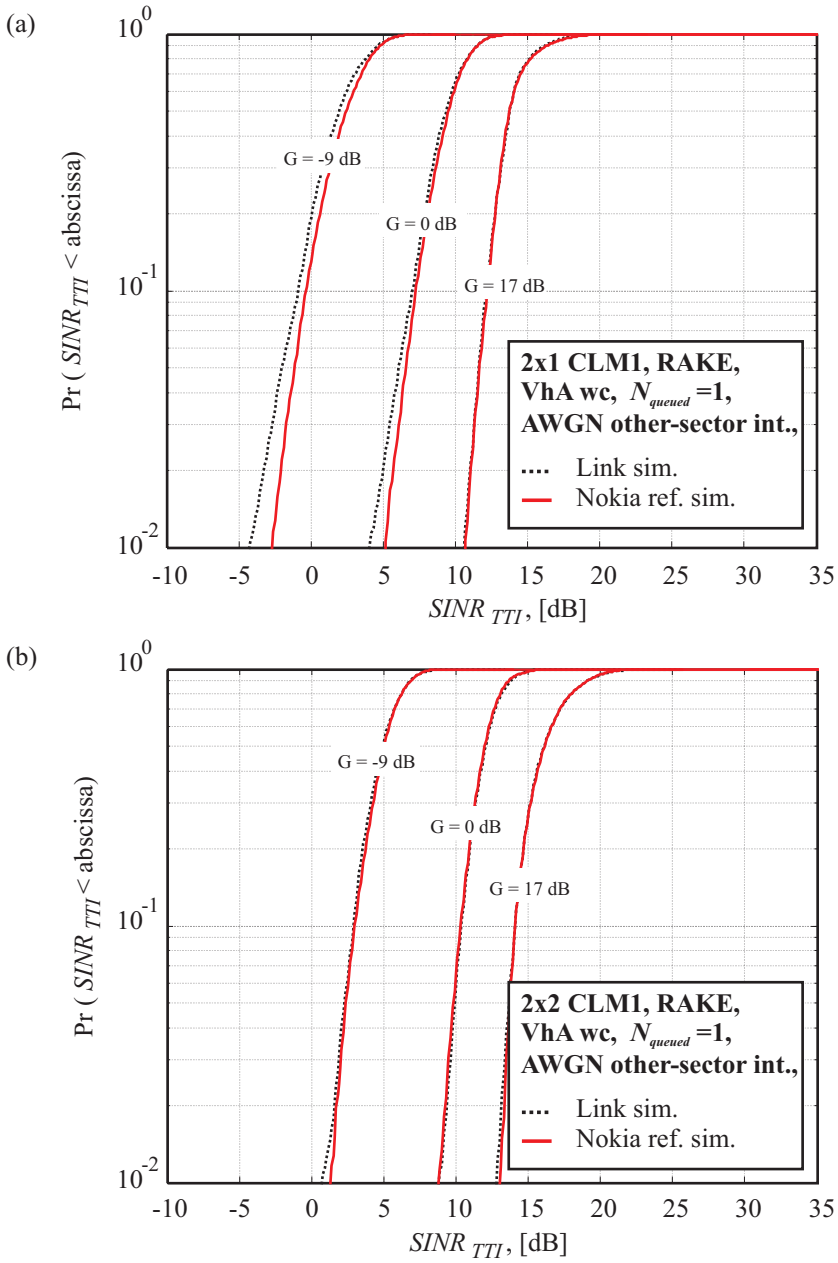

Figure C.8: 2×1 CLM1 and 2×2 CLM1 comparison with Nokia reference results in VhA wc.

and AoC distribution results are compared against open literature results and results collected with a Nokia internal dynamic network simulator.

Figure C.9 displays the G-factor distribution collecting G values at broadside. The reason for not collecting the G values over the whole sector area is that a stable G-factor distribution will in the AWGN and the OWNP2 other-sector interference models be required for every separate AoC value. It can be seen that decreasing the step size from 20 m to 10 m samples and increasing the number of shadow fading realisations per sampling point from 400 to 800 does no longer change the G-factor distribution. It is concluded that a 20 m step size and 400 shadow fading realisations per point are sufficient to obtain stable G-factor statistics. This resolution is used throughout to generate cellular scenario simulation results.

Figure C.10 (a) compares the G-factor distribution seen over the whole sector area with the distribution in [Huan03] and a distribution obtained from a Nokia internal dynamic network simulator[2]. Figure C.10 (b) compares the obtained AoC histograms. From Figure C.10 (a) it can be concluded that the G-factor distribution essentially covers the same range as the reference distributions. It can be seen, however, that the G-factor distribution obtained with the cellular scenario simulator

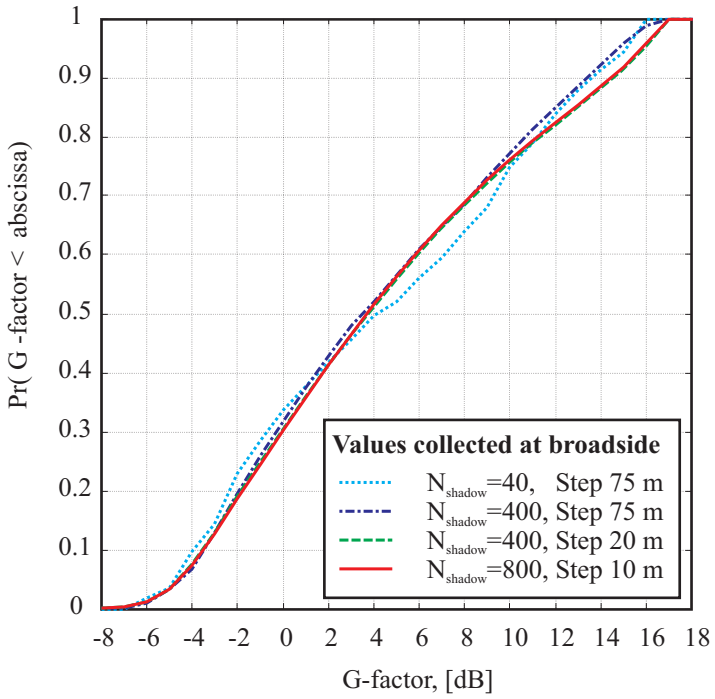

Figure C.9: Test of required x-y grid step size and number of shadow fading realisations to obtain a stable G-factor distribution.

[2]The Nokia reference results are provided by Per-Henrik Michaelsen. He is with Nokia Networks Aalborg R&D, Denmark.

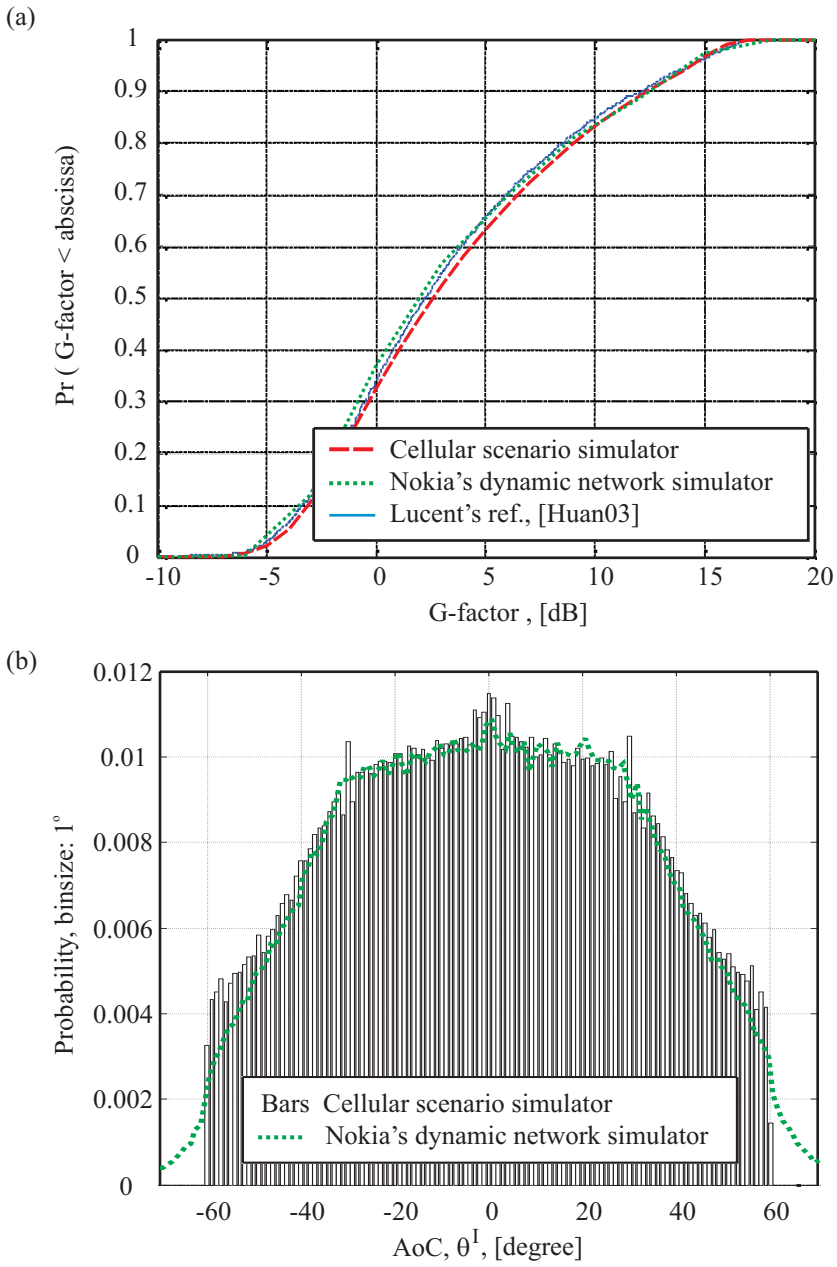

Figure C.10: Comparison of G and AoC statistics from different simulators.

differs in some parts from the reference distribution by up to 0.5 dB. Nevertheless, to produce comparative tx rx scheme results within the same simulator this difference can be regarded as minor.

From the comparison in Figure C.10 (b) it can be seen that the AoC histogram collected with the cellular scenario simulator matches approximately the histogram collected with Nokia's dynamic network simulator. Differences are especially encountered at the upper and lower tails. They can be explained by the fact that in the dynamic network simulator real UE mobility models are implemented. Further, the serving sector is selected based on pilot power measurements. Serving sector AoC values $> 60°$ can therefore be explained by the fact that a user moving within the beam overlap region from one sector beam into the coverage of the neighbouring sector beam needs some time to determine that the small area mean received power of the neighbouring sector is in fact higher than the small area mean received power of its current serving sector. Additional time is needed to perform a handover to the neighbouring sector. This explains why serving sector AoC values $> 60°$ may occur in dynamic network simulations. In general the match between the two AoC distributions is a validation of the AoC distribution simulation capability of the cellular scenario simulator.

C.4 Network Simulator Validation

The intention of this section is twofold. Firstly, the turbo decoder performance model is compared with two models in the open literature. Secondly, obtained network level sector throughput results are compared with results available in the open literature to validate not only the performance of the network level simulator, but also to some extent the performance of the entire simulation chain.

C.4.1 Turbo Decoder Performance Comparison with Literature

To validate the turbo decoder performance curves the $SINR_{eff}$ requirements to obtain a 10% PEP are compared with the results published in [Lao03] and [Chiu04]. Reference results are only available for MCS 4 and MCS 8 as well as ΔSINR $= 0$ dB. These are displayed in Table C.3. It is observed that only smaller differences are encountered with respect to the 10% PEP $SINR_{eff}$ requirement. To compare not only the 10% PEP requirement, but also the shape of the transition region the obtained results are in Figure C.11 plotted over those from [Lao03, Fig. 3]. The test shows that also the obtained transition behaviour fits approximately the behaviour in the open literature.

	Modulation scheme	ECR	$SINR_{eff}$ for 10% PEP, [dB] Obtained	[Chiu04]	[Lao03]
MCS 4	QPSK	0.5	1.2	1.8	1.25
MCS 8	16 QAM	0.5	6.5	7	6.5

Table C.3: Comparison of turbo decoder $SINR_{eff}$ requirements to achieve a PEP of 10%. All values consider a ΔSINR $= 0$ dB, equivalent to an AWGN channel.

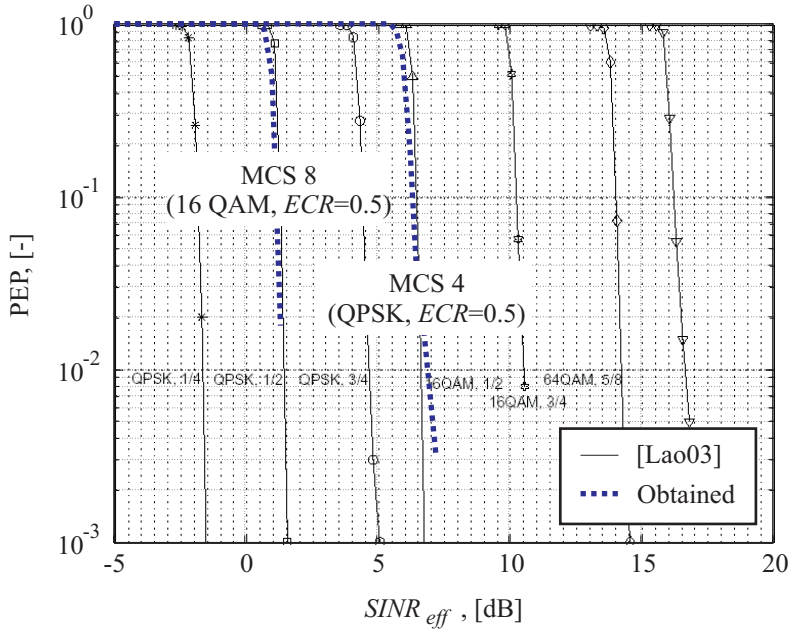

Figure C.11: Turbo decoder performance comparison with [Lao03, Fig. 3]

C.4.2 Comparison of Network Results with Literature

While related network performance figures are for example presented in [Love01], [Peis02], [McBe03] and [Love03], comparison of absolute numbers often becomes difficult due to discrepancies in the simulation set-up. A comparable system configuration is, however, used for the dynamic network simulation results in [Pede04], where 7 W out of 20 W maximum sector power are given to the HS-DSCH transmission, *i.e.* 0.35 of the maximum sector power. Assuming that link SINR gain maps linearly into sector throughput gain, when multicode link adaptation can be utilised, the HS-DSCH SISO PF RAKE sector throughput results in [Pede04] scaled as

$$\frac{0.7}{0.35} \cdot 0.9 \text{ Mb/s} = 1.8 \text{ Mb/s} \quad , \tag{C.3}$$

match well the 1×1 SISO PF RAKE results of 1.76 Mb/s in the VhA environment as given in Table I.7. Further using the reported gain of the PF scheduler over the

RR schedule, *i.e.* 36%, a guess of the RR sector throughput delivers

$$\frac{1.8}{1.36}\ \text{Mb/s} \ = 1.32\ \text{Mb/s} \quad , \tag{C.4}$$

which relates well to the obtained RR result of 1.25 Mb/s as presented in Table I.7.

In [Rami03a] 9 W out of 20 W sector power are given to HS-DSCH transmissions. Using a similar scaling as above, *i.e.* $0.7 \cdot \frac{9\,\text{W}}{20\,\text{W}} = \frac{0.7}{0.45}$, the ratios of absolute results from Table I.7 to the absolute results in [Rami03a, p. 127] are given in Table C.4. The discrepancy ranges from 5% to 33%, which for different simulators and in parts different parameter settings is to be expected. It is concluded that the comparison with [Pede04] and the comparison with [Rami03a] indicate that the produced network results are within the expected range.

Scheme	**RR, RAKE**		**PF, RAKE**	
	VhA	**PeA**	**VhA**	**PeA**
	Sector throughput ratio, [–]			
1×1 SISO	1.13	1.18	1.05	1.21
2×1 CLM1, wc	1.12	1.27	1.12	1.31
1×2 SIMO	1.14	1.15	1.22	1.27
2×2 CLM1, wc	1.15	1.23	1.24	1.33

Table C.4: Sector throughput result comparison. Obtained sector throughput divided by sector throughput of [Rami03a, p. 127]. A scaling of 0.7/0.45 is used to account for different sector power allocation.

Appendix D

Performance Results - Statistical Significance Assessment

All the presented simulation results are random results that for a specified level of confidence can be reproduced with a certain accuracy. As depicted in Figure 1.7, the simulation accuracy and the processing load depend on the complexity of the simulation models and the number of executed Monte Carlo iterations. The simulation models are validated in Appendix C. The statistical significances of the MIMO channel simulation results, the SINR link simulation results, and the network level simulation results are assessed in Section D.1 to Section D.3 respectively. Different statistical significance performance measures are used as indicated in Figure D.1. It is found that with 99% confidence the mean multipath fading channel power, the sector mean SINR results, and the sector throughput results can be reproduced with

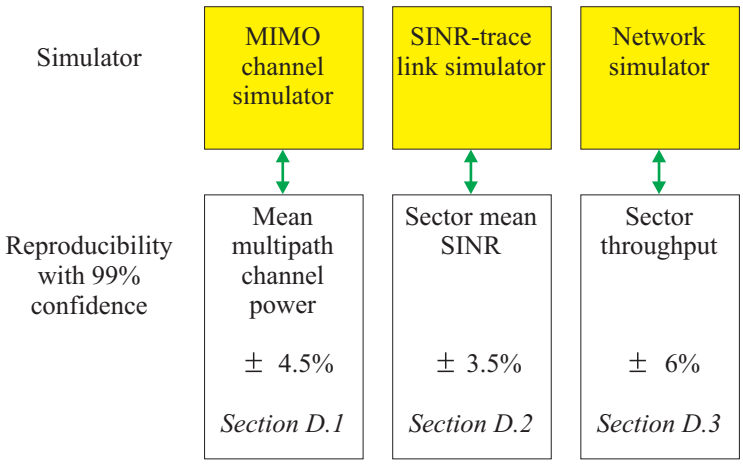

Figure D.1: Statistical significance evaluation overview.

an accuracy of 4.5%, 3.5% and 6% respectively.

D.1 MIMO Channel Simulation Accuracy

As seen in Figure C.2 the MIMO channel fading statistics approximately reassemble Rayleigh fading on a per path basis. To assess which effect channel simulation inaccuracies have on link and network level performance the statistics of the obtained multipath fading channel means are analysed. Taking one channel impulse response power sample, *i.e.* $\left(\underline{\mathbf{h}}^i_{n,z}\right)^H \cdot \underline{\mathbf{h}}^i_{n,z}$, from each of the 10000 simulated TTIs (30000 slots) delivers a set of 10000 multipath channel power samples. From this original set 1000 bootstrap re-sampled sets are drawn, following the procedure in [Zoub98, Table 2]. Each re-sampled set is denoted $boot\left\{\left(\underline{\mathbf{h}}^i_{n,z}\right)^H \cdot \underline{\mathbf{h}}^i_{n,z}\right\}$. The ensemble average over the 10000 elements in every set is written as

$$\mathrm{E}\left\langle boot\left\{\left(\underline{\mathbf{h}}^i_{n,z}\right)^H \cdot \underline{\mathbf{h}}^i_{n,z}\right\}\right\rangle_{10000} \quad . \tag{D.1}$$

For every set the relative deviation from the true mean is then calculated as

$$\frac{\mathrm{E}\left\langle boot\left\{\left(\underline{\mathbf{h}}^i_{n,z}\right)^H \cdot \underline{\mathbf{h}}^i_{n,z}\right\}\right\rangle_{10000} - \mathrm{E}_{mf}\left\{\left(\underline{\mathbf{h}}^i_{n,z}\right)^H \cdot \underline{\mathbf{h}}^i_{n,z}\right\}}{\mathrm{E}_{mf}\left\{\left(\underline{\mathbf{h}}^i_{n,z}\right)^H \cdot \underline{\mathbf{h}}^i_{n,z}\right\}} \quad , \tag{D.2}$$

where the true mean, $\mathrm{E}_{mf}\left\{\left(\underline{\mathbf{h}}^i_{n,z}\right)^H \cdot \underline{\mathbf{h}}^i_{n,z}\right\}$, is with (3.20) given as 1. The distribution of the encountered relative sample mean deviations is displayed in Figure D.2. It can be seen that the simulated mean channel power distribution corresponding to the VhA profile is, with a relative standard deviation of 1.11%, more stable than the mean distribution corresponding to the PeA profile, with a standard deviation of 1.72%. This can be explained by the lower degree of frequency diversity in the PeA channel. Besides, both mean distributions can well be approximated by Gaussian reference distributions with corresponding standard deviations. The 99% the 95% and the 90% confidence interval values are directly obtained from the 1000 bootstrapped mean estimates. They are indicated through the vertical lines in Figure D.2, and their values are given in Table D.1. It can be seen that with 99% confidence the mean multipath channel power results can be reproduced with an accuracy higher than ± 4.5 %. From (4.15) and (4.16) it appears that the means of the multipath fading channel powers directly influence the SINR statistics. However, as the SINR statistics depend on a combination of several random processes, their statistical significance cannot be directly deduced. The SINR statistical significance is therefore assessed in the following subsection.

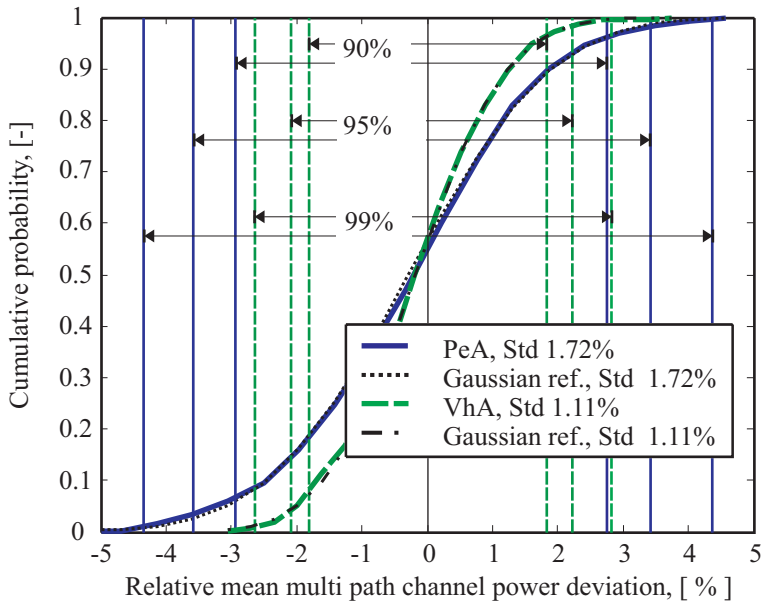

Figure D.2: Statistical significance of the simulated mean multipath fading MIMO channel power.

Confidence level, [%]	Confidence interval, [%] VhA	PeA
99	$[-2.63, 2.83]$	$[-4.34, 4.36]$
95	$[-2.07, 2.22]$	$[-3.59, 3.41]$
90	$[-1.81, 1.83]$	$[-2.95, 2.75]$

Table D.1: Confidence intervals of the relative mean multipath channel power.

D.2 Link Level Simulation Accuracy

The statistical significance of the obtained link level results is measured in terms of the reproducibility of the sector mean SINR. It is influenced by the random processes related to multipath fading, as well as HS-DSCH activity, and tx weight updates. Using a similar bootstrap re-sampling procedure as in Section D.1 1000 bootstrap re-sampled sets are produced from each SINR_{TTI} trace. The ensemble average over each re-sampled set is taken, and the relative deviation per trace is calculated as

$$\frac{\mathrm{E}\left\langle boot\left\{SINR_{TTI}\right\}\right\rangle_{10000} - \mathrm{E}\left\langle SINR_{TTI}\right\rangle_{10000}}{\mathrm{E}\left\langle SINR_{TTI}\right\rangle_{10000}} \quad . \tag{D.3}$$

Using the corresponding AoC-G probabilities the relative trace mean deviation distributions are combined to deliver the relative sector mean deviation distribution. The estimated relative standard deviations of these sector mean SINR distributions are given in Table D.2. The 2×1 CLM1 case in PeA hc and in connection with

Scheme	Tx corr.	Relative sector mean SINR Std, $\tilde{\sigma}_{SINR}$, [%]			
		RAKE		MMSE	
		VhA	PeA	VhA	PeA
1×1 SISO	–	0.52	1.13	0.58	1.14
2×1 CLM1	wc	0.43	0.83	0.47	0.84
2×1 CLM1	hc	0.51	1.13	0.59	**1.14**
1×2 SIMO	–	0.47	0.88	0.47	0.86
2×2 SMP$_{dual}$	wc	0.47	1.00	0.46	0.90
2×2 SMP$_{sel}$	wc	0.37	0.66	0.37	0.64
2×2 CLM1	wc	0.41	0.66	0.39	0.63
2×2 CLM1	hc	0.49	0.89	0.49	0.87

Table D.2: Relative Standard deviation of the sector mean SINRs. Worst case marked bold.

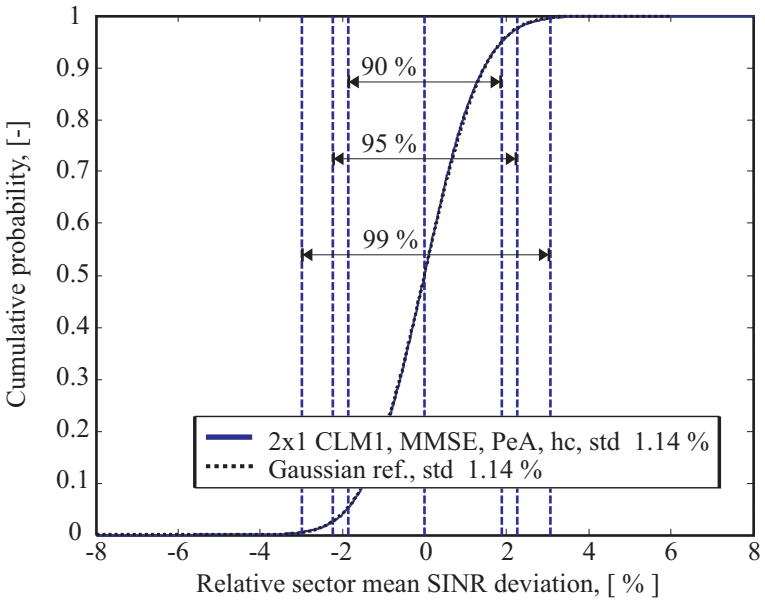

Figure D.3: Statistical significance of sector mean SINR.

MMSE reception reveals the worst case relative standard deviation. Its relative sector mean SINR distribution is plotted in Figure D.3 together with a Gaussian reference distribution. The 99%, the 95%, and the 90% confidence interval values are directly obtained from the 1000 bootstrapped mean estimates. They are indicated through the vertical lines in Figure D.3. Their values are given in Table D.3. It can be seen that with 99% confidence the sector mean SINR results can be reproduced with an accuracy higher than ± 3.5 %. The reason why this accuracy can be higher than the multipath mean accuracy of the previous section is that the sec-

Confidence level, [%]	Confidence interval, [%] 2×1 CLM1, MMSE, PeA hc
99	$[-3.00, 3.07]$
95	$[-2.25, 2.27]$
90	$[-1.87, 1.89]$

Table D.3: Relative sector mean SINR confidence interval values.

tor mean SINR is obtained using statistics from all 72 AoC-G SINR traces, while the results in the previous section only related to an individual multipath fading channel, *i.e.* one trace.

D.3 Network Level Simulation Accuracy

Network performance is reflected in the sector throughput. Its estimate depends on the random processes for user arrival, user-parameter assignment, channel quality metric model, ACK/NACK model, and the underlying SINR trace statistics. Using a single SINR user-performance database, and running 100 network level simulations for the RR and the PF scheduler, 100 different sector throughput results are obtained per scheduler. Their relative distributions are displayed in Figure D.4. They can be approximated by Gaussian distributions with relative sector throughput standard deviation, $\widetilde{\sigma}_{TP}|_{link}^{const}$, of 1.94 % and 1.15 % for the RR and PF scheduler respectively. As the underlying SINR-trace link results were reused in all 100 network level simulations, $\widetilde{\sigma}_{TP}|_{link}^{const}$ is a measure for the statistical significance of the network random processes related to user arrival, user-parameter assignment, channel quality metric model and ACK/NACK model only. The combined link-network overall standard deviation of the sector throughput is calculated as [Rice88, p.142], [Papu94, p. 257]

$$\widetilde{\sigma}_{TP} = \sqrt{\left(\widetilde{\sigma}_{TP}|_{link}^{const}\right)^2 + \left(\widetilde{\sigma}_{SINR}\right)^2} \tag{D.4}$$

Assuming that the overall sector throughput estimation error is Gaussian distributed with standard deviation $\widetilde{\sigma}_{TP}$, the worst case confidence intervals for the overall sector throughput are calculated on the basis of the worst case result from Table D.2 and the results for the RR and PF scheduler from Figure D.4. The obtained confidence intervals are provided in Table D.4. It is concluded that with 99% confidence the obtained sector throughput results can be reproduced with an accuracy higher than ± 6 %.

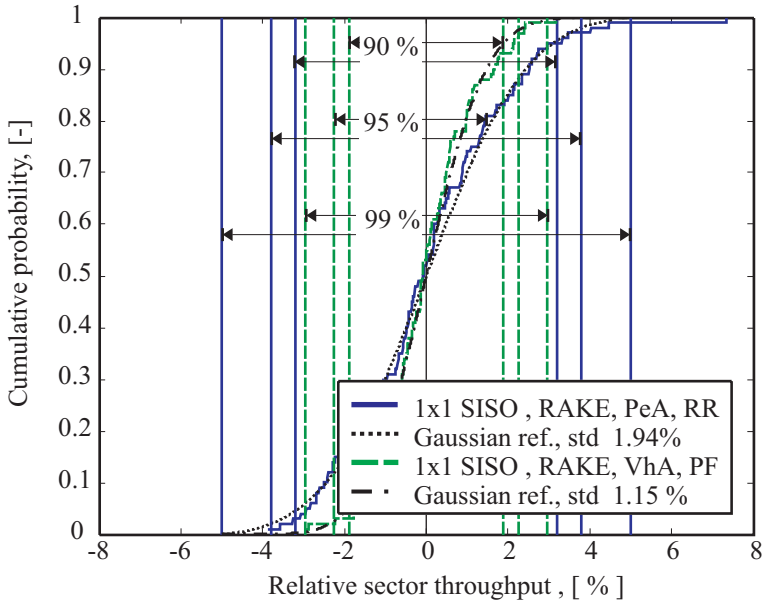

Figure D.4: Statistical significance of sector throughput results, using constant link level statistics.

Scheduler	$\widetilde{\sigma}_{SINR}$, [%]	$\widetilde{\sigma}_{TP}\|_{\substack{const,\\link}}$, [%]	$\widetilde{\sigma}_{TP}$, [%]	Confidence interval, Gaussian appr., [%]		
				99%	95%	90%
RR	1.14	1.94	2.25	± 5.70	± 4.41	± 3.70
PF	1.14	1.15	1.62	± 4.17	± 3.18	± 2.66

Table D.4: Relative sector throughput confidence interval values.

Annex I

Tabulated Performance Results

Section I.I to Section I.VI give the mean SINR performance results of the investigated antenna schemes, while Section I.VII gives the obtained sector throughput performance.

Gains are calculated as the ratio of one set-up over another. Mean SINR gain ratios are expressed in dB. Sector throughput gain ratios are expressed in linear.

I.I 1×1 SISO

PDP	Pos.	1×1 SISO			
		RAKE		MMSE	
		AWGN	OWNP2	AWGN	OWNP2
		Mean SINR, [dB]			
PeA	hDIR	15.15	17.62	15.27	17.97
	lDIR	15.15	15.55	15.27	15.72
	lG	2.23	3.04	2.23	3.05
	hG	23.61	24.05	24.54	25.20
	Sector	17.16	17.88	17.75	18.63
VhA	hDIR	11.23	11.58	12.34	13.04
	lDIR	11.23	11.58	12.34	12.88
	lG	2.05	2.61	2.08	2.82
	hG	13.94	13.94	17.34	17.71
	Sector	10.97	11.10	12.94	13.29
		Gain over 1×1 SISO, [dB]			
PeA	hDIR	–	–	–	–
	lDIR	–	–	–	–
	lG	–	–	–	–
	hG	–	–	–	–
	Sector	–	–	–	–
VhA	hDIR	–	–	–	–
	lDIR	–	–	–	–
	lG	–	–	–	–
	hG	–	–	–	–
	Sector	–	–	–	–
		Gain of MMSE over RAKE, [dB]			
PeA	hDIR	–	–	0.12	0.35
	lDIR	–	–	0.12	0.17
	lG	–	–	0.00	0.01
	hG	–	–	0.93	1.15
	Sector	–	–	0.59	0.75
VhA	hDIR	–	–	1.11	1.46
	lDIR	–	–	1.11	1.30
	lG	–	–	0.03	0.21
	hG	–	–	3.40	3.77
	Sector	–	–	1.97	2.19
		Gain of OWNP2 over AWGN, [dB]			
PeA	hDIR	–	2.47	–	2.70
	lDIR	–	0.40	–	0.45
	lG	–	0.81	–	0.82
	hG	–	0.44	–	0.66
	Sector	–	0.71	–	0.88
VhA	hDIR	–	0.35	–	0.70
	lDIR	–	0.35	–	0.54
	lG	–	0.56	–	0.74
	hG	–	0.00	–	0.37
	Sector	–	0.13	–	0.35

Table I.1: 1×1 SISO mean SINR performance.

I.II 1×2 SIMO

PDP	Pos.	1×2 SIMO			
		RAKE		MMSE	
		AWGN	OWNP2	AWGN	OWNP2
		Mean SINR, [dB]			
PeA	hDIR	17.89	20.16	18.04	23.63
	lDIR	17.89	18.37	18.04	19.16
	lG	5.19	5.90	5.19	6.59
	hG	26.45	26.83	27.77	29.40
	Sector	20.11	20.77	20.91	22.94
VhA	hDIR	14.16	14.40	16.07	18.40
	lDIR	14.16	14.16	16.07	16.76
	lG	5.12	5.17	5.19	6.02
	hG	16.47	16.55	23.71	24.77
	Sector	13.68	13.80	17.63	18.67
		Gain over 1×1 SISO, [dB]			
PeA	hDIR	2.74	2.54	2.77	5.66
	lDIR	2.74	2.82	2.77	3.44
	lG	2.96	2.86	2.96	3.54
	hG	2.84	2.78	3.23	4.20
	Sector	2.95	2.89	3.16	4.32
VhA	hDIR	2.93	2.82	3.73	5.36
	lDIR	2.93	2.58	3.73	3.88
	lG	3.07	2.56	3.11	3.20
	hG	2.53	2.61	6.37	7.06
	Sector	2.71	2.70	4.69	5.38
		Gain of MMSE over RAKE, [dB]			
PeA	hDIR	–	–	0.15	3.47
	lDIR	–	–	0.15	0.79
	lG	–	–	0.00	0.69
	hG	–	–	1.32	2.57
	Sector	–	–	0.80	2.17
VhA	hDIR	–	–	1.91	4.00
	lDIR	–	–	1.91	2.60
	lG	–	–	0.07	0.85
	hG	–	–	7.24	8.22
	Sector	–	–	3.95	4.87
		Gain of OWNP2 over AWGN, [dB]			
PeA	hDIR	–	2.27	–	5.59
	lDIR	–	0.48	–	1.12
	lG	–	0.71	–	1.40
	hG	–	0.38	–	1.63
	Sector	–	0.66	–	2.03
VhA	hDIR	–	0.24	–	2.33
	lDIR	–	0.00	–	0.69
	lG	–	0.05	–	0.83
	hG	–	0.08	–	1.06
	Sector	–	0.12	–	1.04

Table I.2: 1×2 SIMO mean SINR performance.

I.III 2×1 CLM1

PDP	Pos.	2×1 CLM1, wc				2×1 CLM1, hc			
		RAKE		MMSE		RAKE		MMSE	
		AWGN	OWNP2	AWGN	OWNP2	AWGN	OWNP2	AWGN	OWNP2
		Mean SINR, [dB]							
PeA	hDIR	17.37	18.98	17.50	19.25	17.87	20.35	18.08	20.94
	lDIR	17.13	17.76	17.26	17.93	17.22	17.83	17.42	18.08
	lG	4.47	5.25	4.47	5.26	4.70	5.55	4.71	5.56
	hG	25.72	26.15	26.65	27.21	25.36	25.70	26.49	27.01
	Sector	19.49	20.21	20.03	20.89	x	19.96	x	20.86
VhA	hDIR	12.41	12.55	13.47	13.86	12.80	13.06	14.38	14.99
	lDIR	12.59	12.67	13.62	13.83	12.72	12.80	14.16	14.40
	lG	3.65	4.05	3.68	4.22	4.24	4.64	4.30	4.88
	hG	14.68	14.65	17.23	17.35	14.70	14.68	18.32	18.53
	Sector	11.95	12.13	13.46	13.76	x	12.44	x	14.83
		Gain over 1×1 SISO, [dB]							
PeA	hDIR	2.22	1.36	2.23	1.28	2.72	2.73	2.81	2.97
	lDIR	1.98	2.21	1.99	2.21	2.07	2.28	2.15	2.36
	lG	2.24	2.21	2.24	2.21	2.47	2.51	2.48	2.51
	hG	2.11	2.10	2.11	2.01	1.75	1.65	1.95	1.81
	Sector	2.33	2.33	2.28	2.26	x	2.08	x	2.23
VhA	hDIR	1.18	0.97	1.13	0.82	1.57	1.48	2.04	1.95
	lDIR	1.36	1.09	1.28	0.95	1.49	1.22	1.82	1.52
	lG	1.60	1.44	1.60	1.40	2.19	2.03	2.22	2.06
	hG	0.74	0.71	-0.11	-0.36	0.76	0.74	0.98	0.82
	Sector	0.98	1.03	0.52	0.46	x	1.33	x	1.54
		Gain of MMSE over RAKE, [dB]							
PeA	hDIR	–	–	0.13	0.27	–	–	0.21	0.59
	lDIR	–	–	0.13	0.17	–	–	0.20	0.25
	lG	–	–	0.00	0.01	–	–	0.01	0.01
	hG	–	–	0.93	1.06	–	–	1.13	1.31
	Sector	–	–	0.54	0.68	–	–	x	0.89
VhA	hDIR	–	–	1.06	1.31	–	–	1.58	1.93
	lDIR	–	–	1.03	1.16	–	–	1.44	1.60
	lG	–	–	0.03	0.17	–	–	0.06	0.24
	hG	–	–	2.55	2.70	–	–	3.62	3.85
	Sector	–	–	1.51	1.62	–	–	x	2.40
		Gain of OWNP2 over AWGN, [dB]							
PeA	hDIR	–	1.61	–	1.75	–	2.48	–	2.86
	lDIR	–	0.63	–	0.67	–	0.61	–	0.66
	lG	–	0.78	–	0.79	–	0.85	–	0.85
	hG	–	0.43	–	0.56	–	0.34	–	0.52
	Sector	–	0.72	–	0.86	–	x	–	x
VhA	hDIR	–	0.14	–	0.39	–	0.26	–	0.61
	lDIR	–	0.08	–	0.21	–	0.08	–	0.24
	lG	–	0.40	–	0.54	–	0.40	–	0.58
	hG	–	-0.03	–	0.12	–	-0.02	–	0.21
	Sector	–	0.18	–	0.30	–	x	–	x
		Gain of hc over wc, [dB]							
PeA	hDIR	–	–	–	–	0.50	1.37	0.58	1.69
	lDIR	–	–	–	–	0.09	0.07	0.16	0.15
	lG	–	–	–	–	0.23	0.30	0.24	0.30
	hG	–	–	–	–	-0.36	-0.45	-0.16	-0.20
	Sector	–	–	–	–	x	-0.25	x	-0.03
VhA	hDIR	–	–	–	–	0.39	0.51	0.91	1.13
	lDIR	–	–	–	–	0.13	0.13	0.54	0.57
	lG	–	–	–	–	0.59	0.59	0.62	0.66
	hG	–	–	–	–	0.02	0.03	1.09	1.18
	Sector	–	–	–	–	x	0.30	x	1.08

Table I.3: 2×1 CLM1 mean SINR performance. 'x' indicates that the simulation result has not been obtained.

I.IV 2×2 CLM1

PDP	Pos.	2×2 CLM1, wc				2×2 CLM1, hc			
		RAKE		MMSE		RAKE		MMSE	
		AWGN	OWNP2	AWGN	OWNP2	AWGN	OWNP2	AWGN	OWNP2
		Mean SINR, [dB]							
PeA	hDIR	19.79	21.10	19.94	23.73	20.61	22.90	20.87	26.41
	lDIR	19.69	20.07	19.84	20.73	20.08	20.56	20.31	21.50
	lG	7.05	7.59	7.05	8.12	7.58	8.32	7.58	9.10
	hG	28.19	28.28	29.42	30.37	28.10	28.35	29.79	31.21
	Sector	22.04	22.50	22.76	24.15	x	22.79	x	25.19
VhA	hDIR	15.00	14.99	16.84	18.08	15.78	15.70	18.49	20.70
	lDIR	15.15	15.08	16.96	17.29	15.36	15.33	17.98	18.49
	lG	6.37	6.35	6.44	7.04	7.25	7.19	7.38	8.13
	hG	17.20	17.12	22.44	22.76	17.16	17.23	25.00	25.70
	Sector	14.50	14.58	17.61	18.03	x	15.11	x	20.45
		Gain over 1×1 SISO, [dB]							
PeA	hDIR	4.64	3.48	4.67	5.76	5.46	5.28	5.60	8.44
	lDIR	4.54	4.52	4.57	5.01	4.93	5.01	5.04	5.78
	lG	4.82	4.55	4.82	5.07	5.35	5.28	5.35	6.05
	hG	4.58	4.23	4.88	5.17	4.49	4.30	5.25	6.01
	Sector	4.88	4.62	5.01	5.52	x	4.92	x	6.56
VhA	hDIR	3.77	3.41	4.50	5.04	4.55	4.12	6.15	7.66
	lDIR	3.92	3.50	4.62	4.41	4.13	3.75	5.64	5.61
	lG	4.32	3.74	4.36	4.22	5.20	4.58	5.30	5.31
	hG	3.26	3.18	5.10	5.05	3.22	3.29	7.66	7.99
	Sector	3.53	3.48	4.67	4.74	x	4.01	x	7.16
		Gain of MMSE over RAKE, [dB]							
PeA	hDIR	–	–	0.15	2.63	–	–	0.26	3.51
	lDIR	–	–	0.15	0.66	–	–	0.23	0.94
	lG	–	–	0.00	0.53	–	–	0.00	0.78
	hG	–	–	1.23	2.09	–	–	1.69	2.86
	Sector	–	–	0.72	1.65	–	–	x	2.39
VhA	hDIR	–	–	1.84	3.09	–	–	2.71	5.00
	lDIR	–	–	1.81	2.21	–	–	2.62	3.16
	lG	–	–	0.07	0.69	–	–	0.13	0.94
	hG	–	–	5.24	5.64	–	–	7.84	8.47
	Sector	–	–	3.11	3.44	–	–	x	5.34
		Gain of OWNP2 over AWGN, [dB]							
PeA	hDIR	–	1.31	–	3.79	–	2.29	–	5.54
	lDIR	–	0.38	–	0.89	–	0.48	–	1.19
	lG	–	0.54	–	1.07	–	0.74	–	1.52
	hG	–	0.09	–	0.95	–	0.25	–	1.42
	Sector	–	0.46	–	1.39	–	x	–	x
VhA	hDIR	–	-0.01	–	1.24	–	-0.08	–	2.21
	lDIR	–	-0.07	–	0.33	–	-0.03	–	0.51
	lG	–	-0.02	–	0.60	–	-0.06	–	0.75
	hG	–	-0.08	–	0.32	–	0.07	–	0.70
	Sector	–	0.08	–	0.42	–	x	–	x
		Gain of hc over wc, [dB]							
PeA	hDIR	–	–	–	–	0.82	1.80	0.93	2.68
	lDIR	–	–	–	–	0.39	0.49	0.47	0.77
	lG	–	–	–	–	0.53	0.73	0.53	0.98
	hG	–	–	–	–	-0.09	0.07	0.37	0.84
	Sector	–	–	–	–	x	0.30	x	1.04
VhA	hDIR	–	–	–	–	0.78	0.71	1.65	2.62
	lDIR	–	–	–	–	0.21	0.25	1.02	1.20
	lG	–	–	–	–	0.88	0.84	0.94	1.09
	hG	–	–	–	–	-0.04	0.11	2.56	2.94
	Sector	–	–	–	–	x	0.53	x	2.42

Table I.4: 2×2 CLM1 mean SINR performance. 'x' indicates that the simulation result has not been obtained.

I.V 2×2 SMP$_{sel}$

PDP	Pos.	2×2 SMP$_{sel}$			
		RAKE		MMSE	
		AWGN	OWNP2	AWGN	OWNP2
		Mean SINR, [dB]			
PeA	hDIR	19.22	20.83	19.37	23.21
	lDIR	x	19.66	x	20.25
	lG	6.55	7.12	6.55	7.60
	hG	27.89	28.13	28.99	30.10
	Sector	21.73	22.07	22.41	23.65
VhA	hDIR	14.89	14.95	16.50	17.75
	lDIR	x	14.99	x	17.02
	lG	6.00	6.07	6.06	6.67
	hG	17.27	17.23	22.20	22.60
	Sector	14.55	14.55	17.33	17.77
		Gain over 1×1 SISO, [dB]			
PeA	hDIR	4.07	3.21	4.10	5.24
	lDIR	x	4.11	x	4.53
	lG	4.32	4.08	4.32	4.55
	hG	4.28	4.08	4.45	4.90
	Sector	4.57	4.19	4.66	5.02
VhA	hDIR	3.66	3.37	4.16	4.71
	lDIR	x	3.41	x	4.14
	lG	3.95	3.46	3.98	3.85
	hG	3.33	3.29	4.86	4.89
	Sector	3.58	3.45	4.39	4.48
		Gain of MMSE over RAKE, [dB]			
PeA	hDIR	–	–	0.14	2.37
	lDIR	–	–	x	0.59
	lG	–	–	0.00	0.48
	hG	–	–	1.10	1.97
	Sector	–	–	0.68	1.58
VhA	hDIR	–	–	1.60	2.80
	lDIR	–	–	x	2.03
	lG	–	–	0.06	0.60
	hG	–	–	4.93	5.37
	Sector	–	–	2.78	3.22
		Gain of OWNP2 over AWGN, [dB]			
PeA	hDIR	–	1.61	–	3.84
	lDIR	–	x	–	x
	lG	–	0.57	–	1.05
	hG	–	0.24	–	1.11
	Sector	–	0.34	–	1.24
VhA	hDIR	–	0.06	–	1.25
	lDIR	–	x	–	x
	lG	–	0.07	–	0.61
	hG	–	-0.04	–	0.40
	Sector	–	0.00	–	0.44

Table I.5: 2×2 SMP$_{sel}$ mean SINR performance. 'x' indicates that the simulation result has not been obtained.

I.VI 2×2 SMP$_{dual}$

PDP	Pos.	2×2 SMP$_{dual}$			
		RAKE		MMSE	
		AWGN	OWNP2	AWGN	OWNP2
		Mean SINR, [dB]			
PeA	hDIR	12.45	13.34	13.24	15.69
	lDIR	x	12.75	x	14.00
	lG	1.95	2.45	1.96	2.89
	hG	17.12	17.10	21.54	22.21
	Sector	12.91	13.16	15.42	16.29
VhA	hDIR	10.19	10.25	11.58	12.50
	lDIR	x	10.26	x	11.95
	lG	2.03	2.02	2.07	2.60
	hG	11.99	11.90	16.23	16.43
	Sector	9.79	9.77	12.03	12.36
		Gain over 1×1 SISO, [dB]			
PeA	hDIR	-2.70	-4.28	-2.03	-2.28
	lDIR	x	-2.80	x	-1.72
	lG	-0.28	-0.59	-0.27	-0.16
	hG	-6.49	-6.95	-3.00	-2.99
	Sector	-4.25	-4.72	-2.33	-2.34
VhA	hDIR	-1.04	-1.33	-0.76	-0.54
	lDIR	x	-1.32	x	-0.93
	lG	-0.02	-0.59	-0.01	-0.22
	hG	-1.95	-2.04	-1.11	-1.28
	Sector	-1.18	-1.33	-0.91	-0.93
		Gain of MMSE over RAKE, [dB]			
PeA	hDIR	–	–	0.79	2.35
	lDIR	–	–	x	1.25
	lG	–	–	0.01	0.44
	hG	–	–	4.42	5.11
	Sector	–	–	2.51	3.13
VhA	hDIR	–	–	1.39	2.25
	lDIR	–	–	x	1.69
	lG	–	–	0.04	0.58
	hG	–	–	4.24	4.53
	Sector	–	–	2.24	2.59
		Gain of OWNP2 over AWGN, [dB]			
PeA	hDIR	–	0.89	–	2.45
	lDIR	–	x	–	x
	lG	–	0.50	–	0.93
	hG	–	-0.02	–	0.67
	Sector	–	0.25	–	0.87
VhA	hDIR	–	0.06	–	0.92
	lDIR	–	x	–	x
	lG	–	-0.01	–	0.53
	hG	–	-0.09	–	0.20
	Sector	–	-0.02	–	0.33

Table I.6: 2×2 SMP$_{dual}$ mean SINR performance. 'x' indicates that the simulation result has not been obtained.

I.VII Network Performance Comparison

Scheme		RR				PF			
		RAKE		MMSE		RAKE		MMSE	
		VhA	PeA	VhA	PeA	VhA	PeA	VhA	PeA
		Sector throughput, [Mb/s]							
1×1 SISO		1.25	1.73	1.43	1.76	1.76	3.38	2.13	3.38
2×1 CLM1	wc	1.56	2.73	1.86	2.75	2.05	4.07	2.36	4.08
2×1 CLM1	hc	1.75	2.66	2.13	2.72	2.33	4.46	2.86	4.52
1×2 SIMO		2.14	3.07	3.10	3.62	2.77	4.55	3.77	5.13
2×2 SMP$_{dual}$	wc	x	x	2.60	3.20	x	x	3.55	5.48
2×2 SMP$_{sel}$	wc	2.46	3.94	3.20	4.42	2.93	5.07	3.76	5.51
2×2 CLM1	wc	2.50	4.02	3.42	4.62	2.98	5.10	3.89	5.62
2×2 CLM1	hc	2.87	4.38	4.28	5.20	3.46	5.79	4.93	6.63
		Gain over 1×1 SISO, [–]							
1×1 SISO		–	–	–	–	–	–	–	–
2×1 CLM1	wc	1.24	1.58	1.30	1.56	1.16	1.20	1.11	1.21
2×1 CLM1	hc	1.39	1.53	1.48	1.54	1.33	1.32	1.34	1.34
1×2 SIMO		1.70	1.77	2.16	2.05	1.57	1.35	1.77	1.52
2×2 SMP$_{dual}$	wc	x	x	1.81	1.82	x	x	1.67	1.62
2×2 SMP$_{sel}$	wc	1.96	2.28	2.23	2.51	1.67	1.50	1.76	1.63
2×2 CLM1	wc	1.99	2.32	2.38	2.62	1.70	1.51	1.82	1.66
2×2 CLM1	hc	2.29	2.53	2.98	2.95	1.97	1.71	2.31	1.96
		Gain over RR, [–]							
1×1 SISO		–	–	–	–	1.40	1.95	1.49	1.92
2×1 CLM1	wc	–	–	–	–	1.31	1.49	1.27	1.48
2×1 CLM1	hc	–	–	–	–	1.33	1.68	1.34	1.66
1×2 SIMO		–	–	–	–	1.30	1.48	1.22	1.42
2×2 SMP$_{dual}$	wc	–	–	–	–	x	x	1.37	1.71
2×2 SMP$_{sel}$	wc	–	–	–	–	1.19	1.28	1.17	1.25
2×2 CLM1	wc	–	–	–	–	1.19	1.27	1.14	1.22
2×2 CLM1	hc	–	–	–	–	1.21	1.32	1.15	1.27
		Gain over RAKE, [–]							
1×1 SISO		–	–	1.14	1.02	–	–	1.21	1.00
2×1 CLM1	wc	–	–	1.20	1.01	–	–	1.16	1.00
2×1 CLM1	hc	–	–	1.22	1.02	–	–	1.23	1.01
1×2 SIMO		–	–	1.45	1.18	–	–	1.36	1.13
2×2 SMP$_{dual}$	wc	–	–	x	x	–	–	x	x
2×2 SMP$_{sel}$	wc	–	–	1.30	1.12	–	–	1.28	1.09
2×2 CLM1	wc	–	–	1.37	1.15	–	–	1.30	1.10
2×2 CLM1	hc	–	–	1.49	1.19	–	–	1.42	1.14

Table I.7: Sector throughput performance under the OWNP2 interference model. 'x' indicates that the simulation result has not been obtained.

Scheme		**RR**				**PF**			
		RAKE		**MMSE**		**RAKE**		**MMSE**	
		VhA	**PeA**	**VhA**	**PeA**	**VhA**	**PeA**	**VhA**	**PeA**
		Sector throughput, [Mb/s]							
1×1 SISO		1.07	1.54	1.32	1.54	1.63	2.84	1.83	2.89
2×1 CLM1	wc	1.52	2.55	1.71	2.55	1.94	3.82	2.17	3.77
2×1 CLM1	hc	x	x	x	x	x	x	x	x
1×2 SIMO		2.14	2.84	2.60	2.93	2.63	4.07	3.18	4.11
2×2 SMP$_{dual}$	wc	2.50	3.83	2.95	3.82	2.91	4.65	3.38	4.81
2×2 SMP$_{sel}$	wc	x	x	2.33	2.70	x	x	3.25	4.44
2×2 CLM1	wc	2.55	4.08	3.12	4.10	3.01	5.02	3.57	5.14
2×2 CLM1	hc	x	x	x	x	x	x	x	x
		Gain over 1×1 SISO, [–]							
1×1 SISO		–	–	–	–	–	–	–	–
2×1 CLM1	wc	1.41	1.65	1.30	1.66	1.19	1.34	1.19	1.31
2×1 CLM1	hc	x	x	x	x	x	x	x	x
1×2 SIMO		1.99	1.84	1.97	1.91	1.61	1.44	1.74	1.42
2×2 SMP$_{dual}$	wc	x	x	2.25	2.49	x	x	1.85	1.67
2×2 SMP$_{sel}$	wc	x	x	1.77	1.76	x	x	1.77	1.54
2×2 CLM1	wc	2.38	2.64	2.37	2.66	1.85	1.77	1.95	1.78
2×2 CLM1	hc	x	x	x	x	x	x	x	x
		Gain over RR, [–]							
1×1 SISO		–	–	–	–	1.52	1.84	1.39	1.88
2×1 CLM1	wc	–	–	–	–	1.28	1.50	1.27	1.48
2×1 CLM1	hc	–	–	–	–	x	x	x	x
1×2 SIMO		–	–	–	–	1.23	1.44	1.23	1.40
2×2 SMP$_{dual}$	wc	–	–	–	–	x	x	1.14	1.26
2×2 SMP$_{sel}$	wc	–	–	–	–	x	x	1.39	1.65
2×2 CLM1	wc	–	–	–	–	1.18	1.23	1.14	1.25
2×2 CLM1	hc	–	–	–	–	x	x	x	x
		Gain over RAKE, [–]							
1×1 SISO		–	–	1.22	1.00	–	–	1.12	1.02
2×1 CLM1	wc	–	–	1.13	1.00	–	–	1.12	0.99
2×1 CLM1	hc	–	–	x	x	–	–	x	x
1×2 SIMO		–	–	1.21	1.03	–	–	1.21	1.01
2×2 SMP$_{dual}$	wc	–	–	x	x	–	–	x	x
2×2 SMP$_{sel}$	wc	–	–	x	x	–	–	x	x
2×2 CLM1	wc	–	–	1.22	1.00	–	–	1.18	1.02
2×2 CLM1	hc	–	–	x	x	–	–	x	x

Table I.8: Sector throughput performance under the AWGN interference model. 'x' indicates that the simulation result has not been obtained.

Bibliography

[3GPP01a] 3GPP. Physical layer aspects of UTRA high speed downlink packet access (release 4). Technical Report TR 25.848 (V4.0.0), Technical Specification Group Radio Access Network, March 2001.

[3GPP01b] 3GPP. Tx diversity solutions for multiple antennas (release 5). Technical Report TR 25.869 (V1.0.0), Technical Specification Group Radio Access Network, June 2001.

[3GPP02a] 3GPP. High speed downlink packet access: Physical layer aspects (release 5). Technical Specification TR 25.858 (V5.0.0), Technical Specification Group Radio Access Network, March 2002.

[3GPP02b] 3GPP. Physical channels and mapping of transport channels onto physical channels (FDD)(release 1999). Technical Specification TS 25.211 (V3.11.0), Technical Specification Group Radio Access Network, June 2002.

[3GPP03a] 3GPP. Feasibility study for OFDM for UTRAN enhancement. Technical Report TR 25.892 (V0.1.1), Technical Specification Group Radio Access Network, February 2003.

[3GPP03b] 3GPP. Physical channels and mapping of transport channels onto physical channels (FDD)(release 5). Technical Specification TS 25.211 (V5.5.0), Technical Specification Group Radio Access Network, September 2003.

[3GPP03c] 3GPP. Spreading and modulation (FDD). Technical Specification TS 25.213 (V6.0.0), Technical Specification Group Radio Access Network, December 2003.

[3GPP04a] 3GPP. Base station (BS) radio transmission and reception (FDD). Technical Specification TS 25.104 (V6.8.0), Technical Specification Group Radio Access Network, December 2004.

[3GPP04b] 3GPP. Beamforming enhancements. Technical Report TR 25.887 (V6.0.0), Technical Specification Group Radio Access Network, March 2004.

[3GPP04c] 3GPP. High speed download packet access (HSDPA) enhancements (release 6). Technical Report TR 25.899 (V6.1.0), Technical Specification Group Radio Access Network, September 2004.

[3GPP04d] 3GPP. Multiple-input multiple output in UTRA. Technical Report TR 25.876 (V1.7.0), Technical Specification Group Radio Access Network, August 2004.

[3GPP04e] 3GPP. Multiplexing and channel coding (FDD). Technical Specification TS 25.212 (V6.3.0), Technical Specification Group Radio Access Network, December 2004.

[3GPP04f] 3GPP. Physical channels and mapping of transport channels onto physical channels (FDD) (release 6). Technical Specification TS 25.211 (V6.1.0), Technical Specification Group Radio Access Network, July 2004.

[3GPP04g] 3GPP. Physical layer procedures (FDD). Technical Specification TS 25.214 (V6.2.0), Technical Specification Group Radio Access Network, July 2004.

[3GPP04h] 3GPP. Tx diversity solutions for multiple antennas. Technical Report TR 25.869 (V1.2.1), Technical Specification Group Radio Access Network, Febuary 2004.

[3GPP04i] 3GPP. User equipment (UE) radio transmission and reception (FDD). Technical Specification TS 25.101 (V6.4.0), Technical Specification Group Radio Access Network, March 2004.

[3GPP04j] 3GPP, 3rd Generation Partnership Project. A global initiative; shaping the future of mobile communication standards. web page, August 2004. http://www.3gpp.org/.

[Ahme01] M. Ahmed, J. Pautler, and K. Rohani. CDMA receiver performance for multiple-input multiple-output antenna systems. In *IEEE VTS 54th Vehicular Technology Conference*, vol. 3, pp. 1309–1313, October 2001.

[Akyi01] Y. Akyildiz and B. Rao. Statistical performance analysis of optimum combining with co-channel interferers and flat Rayleigh fading. In *IEEE Global Telecommunications Conference*, vol. 6, pp. 3663–3667, November 2001.

[Akyi02] Y. Akyildiz and B. Rao. Maximum ratio combining performance with imperfect channel estimates. In *IEEE International Conference on Acoustics, Speech, and Signal Processing*, vol. 3, pp. III–2485 – III–2488, May 2002.

[Alam98] S. M. Alamouti. A simple transmitter diversity scheme for wireless communications. *IEEE Journal on Selected Areas in Communications*, 16(8):1451–1458, October 1998.

[Amei03] P. J. Ameigeiras Gutiérrez. *Packet scheduling and quality of service in HSDPA*. Dissertation, Aalborg University, Aalborg, Denmark, December 2003.

[Ande98] J. B. Andersen. High gain antennas in a random environment. In *Ninth IEEE International Symposium on Personal, Indoor, and Mobile Radio Communications*, vol. 3, pp. 1275–1279. Boston, USA, September 1998.

[Ande99] S. Andersson, B. Carlqvist, B. Hagerman, and R. Lagerholm. Enhancing cellular network capacity with adaptive antennas. *Ericsson Review*, (3):138–141, 1999.

[Ande00] J. B. Andersen. Antenna arrays in mobile communications: Gain, diversity and channel capacity. *Antennas and Propagation Magazine*, 42(2):12–16, April 2000.

[Baum03] T. Baumgartner. *Smart Antenna Strategies for the UMTS FDD Downlink*. Dissertation, Vienna University of Technology, Vienna, Austria, August 2003.

[Bend00] P. Bender, P. Black, M. Grob, R. Padovani, N. Sindhushayana, and A. Viterbi. CDMA/HDR: a bandwidth-efficient high-speed wireless data service for normadic users. *IEEE Communications Magazine*, 38(7):70–77, July 2000.

[Bene96] S. Benedetto and G. Montorsi. Design of parallel concatenated convolutional codes. *IEEE Transactions on Communications*, 44(5):591–600, May 1996.

[Berg02] L. T. Berger and L. Schumacher. Modified space-time transmission in DS-CDMA downlink facilitating MISO channel equalization. In *IEEEth 56th Vehicular Technology Conference*, vol. 2, pp. 941–945. Vancouver, Canada, September 2002.

[Berg03] L. T. Berger, T. E. Kolding, J. Ramiro Moreno, P. Ameigeiras, L. Schumacher, and P. E. Mogensen. Interaction of transmit diversity and proportional fair scheduling. In *IEEE 57th Vehicular Technology Conference*, vol. 4, pp. 2423–2427. Jeju, Korea, April 2003.

[Berg04a] L. T. Berger, T. E. Kolding, P. E. Mogensen, F. Frederiksen, and K. I. Pedersen. Effects of other-sector interference variation on detection, link adaptation and scheduling in HSDPA. In *The Nordic Radio Symposium*, no. 5. Oulu, Finland, August 2004. Session 10 - WCDMA Enhancements.

[Berg04b] L. T. Berger, T. E. Kolding, P. E. Mogensen, and L. Schumacher. Geometry based other-sector interference modelling for downlink system simulations. In *The Seventh International Symposium on Wireless Personal Multimedia Communications (WPMC04)*, vol. 2, pp. 309–313. Abano Terme, Italy, September 2004.

[Bhag96] P. Bhagwat, B. P., A. Krishna, and S. K. Tripathi. Enhancing throughput over wireless lans using channel state dependent packet scheduling. In *IEEE Proceedings of the INFOCOM*, vol. 3, pp. 1133–1140, March 1996.

[Boga80] V. M. Bogatchev and I. G. Kiselev. Optimum combining of signals in space-diversity reception. *Telecommun. Radio Eng.*, 34/35(10):83–85, October 1980.

[Bonn03] L. Bonnot. Closed-loop transmit diversity and opportunistic beamforming for HSDPA. M.Sc. thesis, Aalborg University, Aalborg, Denmark, May 2003. supervised by Lars T. Berger.

[Bora92] G. K. Boray and M. D. Srinath. Conjugate gradient techniques for adaptive filtering. *IEEE Transactions on Circuits and Sytems I: Fundamental Theory and Applications*, 39 (1):1–10, January 1992.

[Brat99] P. I. Bratanov. *User mobility modeling in cellular communications networks*. Dissertation, Vienna University of Technology, Vienna, Austria, February 1999.

[Brat03] P. I. Bratanov and E. Bonek. Mobility model of vehicle-borne terminals in urban cellular systems. *IEEE Transactions on Vehicular Technology*, 52(4):947–952, July 2003.

[Bren55] D. G. Brennan. On the maximum signal to noise ratio realization from several noisy signals. In *IRE*, vol. 43, p. 1530, October 1955.

[Brun04] J. Bruna and A. Farrés. New modeling techniques for WCDMA-HSDPA. M.Sc. thesis, Aalborg University, Aalborg, Denmark, May 2004. supervised by Troels E. Kolding, Frank Frederiksen and Troels B. Sorensen.

[Bueh00] R. M. Buehrer, N. S. Correal-Mendoza, and B. D. Woerner. A simulation comparison of multiuser receivers for cellular CDMA. *IEEE Transactions on Vehicular Technology*, 49(4):1065–1085, July 2000.

[Chas85] D. Chase. Code combining–a maximum-likelihood decoding approach for combining an arbitrary number of noisy packets. *IEEE Transactions on Communications*, 33(5): 385–393, May 1985.

[Chiu04] C.-S. Chiu and C.-C. Lin. Comparative downlink shared channel evaluation of WCDMA release 99 and HSDPA. In *IEEE International Conference on Networking, Sensing and Control*, vol. 2, pp. 1165–1170, March 2004.

[Chua96] S.-G. Chua and A. Goldsmith. Variable-rate variable-power MQAM for fading channels. In *IEEE 46th Vehicular Technology Conference*, vol. 2, pp. 815–819, April 1996.

[Chua02] C.-N. Chuah, D. N. C. Tse, J. M. Kahn, and R. A. Valenzuela. Capacity scaling in MIMO wireless systems under correlated fading. *IEEE Transactions on Information Theory*, 48(3):637–650, March 2002.

[Clar68] R. H. Clarke. A statistical theory of mobile-radio reception. *Bell Systems Technical Journal*, 47:957–1000, 1968.

[COST91] COST231. Urban transmission loss models for mobile radio in the 900 and 1,800 MHz bands. Technical report, Commission of the European Communities, European Cooperation in the Field of Scientific and Technical Research, The Hague, Netherlands, September 1991.

[Cui04] X. W. Cui, Q. T. Zhang, and Z. M. Feng. Outage performance for maximal ratio combiner in the presence of unequal-power co-channel interferers. In *IEEE Communications Letters*, vol. 8, pp. 289–291, May 2004.

[Das01] A. Das, F. Khan, A. Sampath, and H. Su. Performance of hybrid ARQ for high speed downlink packet access in UMTS. In *IEEE VTS 54th Vehicular Technology Conference*, vol. 4, pp. 2133–2137, October 2001.

[Deng03] Y. Deng and Z. Xu. Performance of low-complexity downlink channel estimation for long-coded CDMA systems. In *IEEE International Conference on Acoustics, Speech, and Signal Processing*, vol. 4, pp. 117–120, April 2003.

[Derr02] R. T. Derryberry, S. D. Gray, D. M. Ionescu, G. Mandyam, and B. Raghothaman. Transmit diversity in 3G CDMA. *IEEE Communications Magazine*, 40(4):68–75, April 2002.

[Digg04] S. N. Diggavi, N. Al-Dhahir, S. A., and A. R. Calderbank. Great expectations: The value of spatial diversity in wireless networks. *Proceedings of the IEEE*, 92(2):219–270, February 2004.

[Duel95] A. Duel-Hallen, J. Holtzman, and Z. Zvonar. Multiuser detection for CDMA systems. *IEEE Personal Communications*, pp. 46–58, April 1995.

[Elle84] F. Ellersick. A conversation with Claude Shannon. *IEEE Communications Magazine*, 22(5):123–126, May 1984.

[Elli02] R. C. Elliot and W. A. Krzymień. Scheduling algorthms for the cdma2000 packet data evolution. In *IEEE 56th Vehicular Technology Conference*, vol. 1, pp. 304–310. Vancouver, Canada, September 2002.

[ETSI98] ETSI. Universal mobile telecommunications system (UMTS); Selection procedures for the choice of radio transmission technologies of the UMTS. Technical Report TR 101 112 V3.2.0,(UMTS 30.03 version 3.2.0), The Special Mobile Group (SMG) of the European Telecommunications Standards Institute (ETSI), April 1998.

[Fern04] P. Fernandes, P. Kyritsi, L. T. Berger, and J. Mártires. Effects of multi user MIMO scheduling freedom on cellular downlink system throughput. In *IEEE 60th Vehicular Technology Conference*, vol. 2, pp. 1148–1152. Los Angeles, USA, September 2004.

[Fono02] J. R. Fonollosa, M. Heikkilä, X. Mestre, A. Pagés, A. Pollard, L. Schumacher, L. T. Berger, A. Wiesel, and J. Ylitalo. Adaptive modulation schemes for MIMO HSDPA. In *IST Mobile & Wireless Telecommunications Summit 2002*, pp. 78–82. Thessaloniki, Greece, June 2002.

[Fosc96] G. J. Foschini. Layered space-time architecture for wireless communication in a fading environment when using multi-element antennas. *Bell Labs Technical Journal*, 2(2): 41–59, Autumn 1996.

[Fosc98] G. J. Foschini and M. J. Gans. On limits of wireless communications in a fading environment when using multiple antennas. *Wireless Personal Communications*, (6):311–335, 1998.

[Fran98] C. D. Frank and E. Vistotsky. Adaptive interference suppression for direct-sequence CDMA systems with long spreading codes. In *36th Allerton Conference on Cummunication, Control and Computing*, pp. 411–420. Monticello, Italy, September 1998.

[Fran02] C. D. Frank, E. Vistotsky, and U. Madhow. Adaptive interference suppression for direct-sequence CDMA systems with long spreading sequences. *VLSI Signal Processing, Special issue on Signal Processing for Wireless Communications: Algorithms, Performance, and Architecture*, 30(1):273–291, January 2002.

[Fred02] F. Frederiksen and T. E. Kolding. Performance and modeling of WCDMA/HSDPA transmission/H-ARQ schemes. In *IEEE 56th Vehicular Technology Conference*, vol. 1, pp. 472–476. Vancouver, Canada, September 2002.

[Fuhl97] J. Fuhl, J.-P. Rossi, and E. Bonek. High-resolution 3-D direction-of-arrival determination for urban mobile radio. *IEEE Transactions on Antennas and Propagation*, 45(4): 672–682, April 1997.

[Gerl02] H. Gerlach. SNR loss due to feedback quantization and errors in closed loop transmit diversity systems. In *The 13th IEEE International Symposium on Personal, Indoor and Mobile Radio Communications*, vol. 5, pp. 2117–2120, September 2002.

[Gesb03] D. Gesbert, M. Shafi, D.-s. Shiu, P. J. Smith, and A. Naguib. From theory to practice: an overview of MIMO space-time coded wireless systems. *IEEE Journal on Selected Areas in Communications*, 21(3):281–302, April 2003.

[Ghau98] I. Ghauri and D. T. M. Slock. Linear receivers for the DS-CDMA downlink exploiting orthogonality of spreading sequences. In *32nd Asilomar Conference on Signals, Systems and Computers*, vol. 1, pp. 650–654. Pacific Grove, Canada, November 1998.

[Gold97] A. J. Goldsmith and P. Varaiya. Capacity of fading channels with channel side information. *IEEE Transactions on Information Theory*, 43(6):1986–1992, November 1997.

[Guiz04] E. Guizzo. Closing in on the perfect code. *IEEE Spectrum*, 41(3):36–42, March 2004.

[Hadi02] H. Hadinejad-Mahram, H. Elders-Boll, and G. Alirezaei. Performance evaluation of advanced receivers for WCDMA downlink detection. In *The 5th International Symposium on Wireless Personal Multimedia Communications*, vol. 2, pp. 367–371, October 2002.

[Hama99] S. Hämäläinen, H. Holma, and K. Sipilä. Advanced WCDMA radio network simulator. In *IEEE International Symposium on Personal, Indoor and Mobile Radio Conference*, pp. 951–955. Osaka, Japan, September 1999.

[Hama01a] J. Hämäläinen and R. Wichman. Feedback schemes for FDD WCDMA systems in multipath environments. In *IEEE VTS 53rd Vehicular Technology Conference*, vol. 1, pp. 238–242, May 2001.

[Hama01b] J. Hämäläinen and R. Wichman. The effect of feedback delay to the closed-loop transmit diversity in FDD WCDMA. In *12th IEEE International Symposium on Personal, Indoor and Mobile Radio Communications*, vol. 1, pp. D–27 – D–31, September 2001.

[Hama02] J. Hämäläinen and R. Wichman. Combining multiuser diversity and WCDMA transmit diversity modes. In *5th Nordic Signal Processing Symposium*. On Board, Hurtigruten from Tromsø to Trondheim, Norway, October 2002.

[Hamm00] J. S. Hammerschmidt and C. Brunner. The implications of array and multipath geometries in spatial processing. In *IEE/IEEE ITC-2000*, pp. 11–16. Acapulco, Mexico, May 2000.

[Hanl98] S. V. Hanly and D. N. C. Tse. Multiaccess fading channels. II. Delay-limited capacities. *IEEE Transactions on Information Theory*, 44(7):2816–2831, 1998.

[Hara01] Y. Hara, D. K. Park, and Y. Kamio. Analysis of RAKE receiver in W-CDMA systems with downlink beamforming. In *IEEE VTS 54th Vehicular Technology Conference*, vol. 3, pp. 1457 – 1461, October 2001.

[Hayk94] S. Haykin. *Communication Systems*. Wiley, New York, USA, 3rd edition, 1994. ISBN 0-471-57178-8.

[Hayk96] S. Haykin. *Adaptive filter theory*. Information and system sciences. Prentice-Hall, Inc, Upper Saddle River, USA, 3rd edition, 1996. ISBN 0-13-322760.

[Heat01] R. W. Heath, M. Airy, and A. J. Paulraj. Multiuser diversity for MIMO wireless systems with linear receivers. In *Asilomar Conference, Signals, Systems, and Computers*, pp. 1194–1199. Pacific Grove, Canada, November 2001.

[Hedb00] T. Hedberg and S. Parkvall. Evolving WCDMA. *Ericsson Review*, (2):124–131, 2000.

[Heik99] M. J. Heikkila, P. Komulainen, and J. Lilleberg. Interference suppression in CDMA downlink through adaptive channel equalization. In *Vehicular Technology Conference*, vol. 2, pp. 978–982. Amsterdam, Netherlands, September 1999.

[Heik02] M. J. Heikkilä, K. Ruotsalainen, and J. Lilleberg. Space-time equalization using conjugate-gradient algorithm in WCDMA downlink. In *13th IEEE International Symposium on Personal Indoor Mobile and Radio Communications*. Lisbon, Portugal, September 2002.

[Heik03] M. J. Heikkilä, K. Majonen, J. Fonollosa, A. Pagés, J. Ylitalo, E. Tiirola, and A. Pollard. Performance evaluation. Deliverable D4, I-METRA, September 2003. Workpackage 4.

[Hoch02] B. M. Hochwald, T. L. Marzetta, and V. Tarokh. Multi-antenna channel-hardening and its implications for rate feedback and scheduling. *IEEE Transactions on Information Theory*, 2002. to appear.

[Holm04] H. Holma and A. Toskala, editors. *WCDMA for UMTS, Radio Access For Third Generation Mobile Communications*. Wiley, Chichester, UK, third edition, 2004. ISBN 0-470-87096-6.

[Holt00] J. M. Holtzman. CDMA forward link waterfilling power control. In *IEEE 51st Vehicular Technology Conference*, pp. 1636–1667. Tokyo, Japan, May 2000.

[Holt01] J. M. Holtzman. Asymptotic analysis of proportional fair algorithm. In *12th IEEE International Symposium on Personal, Indoor and Mobile Radio Communications*, vol. 2, pp. F33–F37, 2001.

[Hool99] K. Hooli, M. Latva-aho, and M. Juntti. Multiple access interference suppression with linear chip equalizers in WCDMA downlink receivers. In *Global Telecommunication Conference*, no. Part A, pp. 467–471. Rio de Janero, Brazil, December 1999.

[Hool01] K. Hooli, M. Latva-aho, and M. Juntti. Performance evaluation of adaptive chip-level channel equalizers in WCDMS downlink. In *IEEE International Conference on Communications*, vol. 6, pp. 1974–1979. Helsinki, Finland, June 2001.

[Hopp01] R. Hoppe, H. Buddendick, G. Wolfle, and F. M. Landstorfer. Dynamic simulator for studying WCDMA radio network performance. In *IEEE VTS 53rd Vehicular Technology Conference*, vol. 4, pp. 2771–2775, May 2001.

[Hott03] A. Hottinen, O. Trikkonen, and R. Wichman. *Multi-antenna Tranceiver Techniques for 3G and Beyond*. Wiley, Chichester, UK, 2003. ISBN 0470 84542 2.

[Huan03] H. Huang, S. Venkatesan, A. Kogiantis, and N. Sharma. Increasing the peak data rate of 3G downlink packet data systems using multiple antennas. In *IEEE 57th Vehicular Technology Conference*. Jeju, Korea, April 2003. Session 2D-1.

[I ME03] I-METRA Consortium. Welcome to the IST-2000-30148 I-METRA project. web page, August 2003. http://www.ist-imetra.org/.

[Ikeg84] F. Ikegami, S. Yoshida, T. Takeuchi, and M. Umehira. Propagation factors controlling mean field strength on urban streets. *IEEE Transactions on Antennas and Propagation*, 32(8):822–829, August 1984.

[Inga04] M. A. Ingale, K. Pajukoski, P.-H. Michaelsen, K. I. Pedersen, and P. E. Mogensen. Performance of space time transmit diversity in WCDMA. In *The Nordic Radio Symposium*, no. 4. Oulu, Finland, August 2004. Session 10 - WCDMA Enhancements.

[ITU97] ITU. Guidelines for evaluation of radio transmission technologies for IMT-2000. Recommendation ITU-R M.1225, International Telecommunication Union, Geneva, Switzerland, 1997.

[Jake94] W. C. Jakes. *Microwave Mobile Communication*. IEEE Press, New Jersey, USA, IEEE reprinted edition, 1994. ISBN 0-7803-1069-1.

[Jeru00] M. C. Jeruchim, P. Balaban, and K. S. Shanmugan. *Simulation of Communication Systems, Modeling, Methodology and Techniques*. Information Technology: Transmission, Processing, and Storage. Kluwer Academic/Plenum Publishers, 2nd edition, 2000. ISBN 0-306-46267-2.

[Kahn54] L. Kahn. Ratio squarer. In *IRE*, vol. 42, p. 1704, November 1954.

[Kerm02] J. P. Kermoal, L. Schumacher, K. I. Pedersen, P. E. Mogensen, and F. Frederiksen. A stochastic MIMO radio channel model with experimental validation. *IEEE Journal on Selected Areas in Communications*, 20(6):1211–1226, August 2002.

[Klei96] A. Klein, G. K. K. Kaleh, and P. W. Baier. Zero forcing and minimum mean-square-error equalization for multiuser detection in code-division multiple-access channels. *IEEE Transactions on Vehicular Technology*, 45(2):276–287, May 1996.

[Klei97] A. Klein. Data detection algorithms specially designed for the downlink of CDMA mobile radio systems. In *IEEE 47th Vehicular Technology Conference*, vol. 1, pp. 203–207, 1997.

[Klin99] T. Klingenbrunn and P. Mogensen. Modelling cross-correlated shadowing in network simulations. In *IEEE VTS 50th Vehicular Technology Conference*, vol. 3, pp. 1407–1411, September 1999.

[Knop95] R. Knopp and P. Humblet. Information capacity and power control in single-cell multiuser communication. In *IEEE International Conference on Communications*, vol. 1, pp. 331–335. Seattle, USA, June 1995.

[Kogi01] G. A. Kogiantis, N. Joshi, and O. Sunay. On transmit diversity and scheduling in wireless packet data. In *IEEE Proc. International Conference on Communications*, vol. 8, pp. 2433–2437, 2001.

[Kold01] T. E. Kolding, F. Frederiksen, and P. E. Mogensen. Performance evaluation of modulation and coding schemes proposed for HSDPA in 3.5G UMTS networks. In *The Fourth International Symposium on Wireless Personal Multimedia Communications*, no. P1B.3, pp. 307–312. Aalborg, Denmark, September 2001.

[Kold02] T. E. Kolding, F. Frederiksen, and P. E. Mogensen. Performance aspects of WCDMA systems with high speed downlink packet access (HSDPA). In *IEEE 56th Vehicular Technology Conference*, vol. 1, pp. 477–481. Vancouver, Canada, September 2002.

[Kold03a] T. E. Kolding. Link and system performance aspects of proportional fair scheduling in WCDMA/HSDPA. In *IEEE 58th Vehicular Technology Conference*, vol. 3, pp. 1717–1722. Orlando, USA, October 2003.

[Kold03b] T. E. Kolding, K. I. Pedersen, J. Wigard, F. Frederiksen, and P. E. Mogensen. High speed downlink packet access: WCDMA evolution. *IEEE Vehicular Technology Soceity (VTS) News*, 50(1):4–10, February 2003.

[Koro04] L. Korowajczuk, B. de Souza Abreu Xavier, A. M. Fartes Filho, L. Zurba Ribeiro, C. Korowajczuk, and L. Da Silva. *Designing cdma2000 Systems*. John Willey & Sons, LTD, 2004. ISBN 0-470-85399-9.

[Krau00] T. P. Krauss, M. D. Zoltowski, and G. Leus. Simple MMSE equalizers for CDMA downlink to restore chip sequence: comparison to zero-forcing and RAKE. In *IEEE International Conference on Acoustics, Speech, and Signal Processing*, vol. 5, pp. 2865–2868, June 2000.

[Krau02] T. P. Krauss, W. J. Hillery, and M. D. Zoltowski. Downlink specific linear equalization for frequency selective CDMA cellular systems. *VLSI Signal Processing Systems for Signal, Image, and Video Technology*, 30(1-3):143–161, Januar-March 2002.

[Kuch00] A. Kuchar, J. P. Rossi, and E. Bonek. Directional macro-cell channel characterization from urban measurements. *IEEE Transactions on Antennas and Propagation*, 48(2): 137–146, February 2000.

[Lao03] D. Lao, J. H. Horng, and J. Zhang. Throughput analysis for W-CDMA systems with MIMO and AMC. Technical Report TR-2003-48, New Jersey Institute of Technology and Mitsubishi Electric Research Laboratories, Cambridge, MA, May 2003.

[Lena01a] M. Lenardi, A. Medles, and D. T. Slock. Comparison of downlink transmit diversity schemes for RAKE and SINR maximizing receivers. In *IEEE International Conference on Communications*, vol. 6, pp. 1679–1683, June 2001.

[Lena01b] M. Lenardi and D. T. M. Slock. A SINR maximizing 2D RAKE receiver for multisensor WCDMA mobile terminals. 2001.

[Libe99] J. C. Liberti Jr and T. S. Rappaport. *Smart Antennas for Wireless Communication*. Prentice Hall, New Jersey, USA, 1999.

[Lin84] S. Lin, D. Costello, and M. Miller. Automatic-repeat-request error-control schemes. *IEEE Communications Magazine*, 22(12):5–17, December 1984.

[Lo99] T. K. Y. Lo. Maximum ratio transmission. *IEEE Transactions on Communications*, 47 (10):1458–1461, 1999.

[Love01] R. Love, A. Ghosh, R. Nikides, L. Jalloul, M. Cudak, and B. Classon. High speed downlink packet access performance. In *IEEE VTS 53rd Vehicular Technology Conference*, vol. 3, pp. 2234–2238, May 2001.

[Love03] R. Love, K. Stewart, R. Bachu, and A. Ghosh. MMSE equalization for UMTS HSDPA. In *IEEE 58th Vehicular Technology Conference*, vol. 4, pp. 2416–2420, October 2003.

[Luce01] Lucent, Nokia, Simens, and Ericsson. A standardized set of MIMO radio propagation channels. TSG1#23 R1-01-1179, 3GPP, Jeju, Korea, November 2001.

[Luce02] Lucent Technologies, H. Xu, and H. Huang. Performance metric for MIMO PARC system. Technical Report SCM-076, 3GPP/3GPP2 Joint Spatial Channel Modeling Adhoc, Teleconference, November 2002.

[Madh94] U. Madhow and M. Honig. MMSE interference suppression for direct-sequence spread-spectrum CDMA. *IEEE Transactions on Communications*, 42(12):3178–3188, December 1994.

[Mail01] L. Mailaender. Low-complexity implementation of CDMA downlink equalization. In *Second International Conference on 3G Mobile Communication Technologies*, no. 477, pp. 396–400, March 2001.

[Malk01] E. Malkamaki, D. Mathew, and S. Hämäläinen. Performance of hybrid ARQ techniques for WCDMA high data rates. In *IEEE VTS 53rd Vehicular Technology Conference*, vol. 4, pp. 2720–2724, May 2001.

[Mand74] D. M. Mandelbaum. An adaptive-feedback coding scheme using incremental redundancy. *IEEE Transactions on Information Theory*, 20(3):388–389, May 1974.

[Mart03] J. Mártires and P. Fernandes. MIMO scheduling and cooperative detection for systems beyond 3G. M.Sc. thesis, Aalborg University, Aalborg, Denmark, May 2003. supervised by Persefoni Kyritsi and Lars T. Berger.

[Mart04] C. Martin and B. Ottersten. Asymptotic eigenvalue distributions and capacity for MIMO channels under correlated fading. *IEEE Transactions on Wireless Communications*, 3 (4):1350 – 1359, July 2004.

[McBe03] S. McBeath, M. Ahmed, and K. Rohani. Impact of imperfect estimators on W-CDMA receiver performance with MIMO antenna systems. In *IEEE 58th Vehicular Technology Conference*, vol. 2, pp. 1152 – 1156, October 2003.

[METR01] METRA Consortium. Welcome to the IST-1999-11729 METRA project. web page, July 2001. http://www.ist_imetra.org/metra/index.html.

[Moon00] T. K. Moon and W. C. Stirling. *Mathematical Methods and Algorithms for Signal Processing*. Prentice Hall, Upper Saddler River, New Jersey, USA, 2000. ISBN 0-201-36186-8.

[Mosh96] S. Moshavi. Multi-user detection for DS-CDMA communications. *IEEE Communications Magazine*, 34(10):124–136, October 1996.

[Moto02] Motorola. Receiver implementation for system-level simulations. Technical Report SCM-068, 3GPP/3GPP2 Joint Spatial Channel Modeling Adhoc, Quebec City, Canada, October 2002.

[Nous02] S. Nousiainen, K. Kordybach, P. Kemppi, and V.-P. Kröger. Dynamic UMTS simulator for congestion studies and evaluation of resource management techniques. In *Working Conference on Personal Wireless Communications*, pp. 159–166. Singapore, October 2002.

[Oute04] J. Outes Carnero. *Uplink Capacity Enhancement in WCDMA*. Dissertation, Aalborg University, Aalborg, Denmark, March 2004.

[Oyma03] Ö. Oyman, R. U. Nabar, H. Bölcskei, and A. J. Paulraj. Characterizing the statistical properties of mutual information in MIMO channels. *IEEE Transactions on Signal Processing*, 51(11):2784–2795, November 2003.

[Papa90] S. J. Papantoniou. *Modelling the Mobile-Radio Channel*. Dissertation, Swiss Federal Institute of Technology, Zürich, Switzerland, 1990.

[Papu94] L. Papula. *Mathematische Formelsammlung für Ingemieure und Naturwissenschaftler*. Vieweg Verlagsgesellshaft, Braunschweig/Wiesbaden, Germany, 4th edition, 1994. ISBN 3-528-34442-3.

[Park01] S. Parkvall, E. Dahlman, P. Frenger, P. Beming, and M. Persson. The high speed packet data evolution of WCDMA. In *12th IEEE International Symposium on Personal, Indoor and Mobile Radio Communications*, vol. 2, pp. G–27 – G–31, September 2001.

[Park03] S. Parkvall, E. Englund, P. Malm, T. Hedberg, M. Persson, and J. Peisa. WCDMA evolved - high-speed packet-data services. *Ericsson Review*, (2):56–65, 2003.

[Paul97] A. J. Paulraj and C. B. Papadias. Space-time processing for wireless communications. *IEEE Signal Processing Magazine*, 14(6):49–83, November 1997.

[Paul03] A. Paulraj, R. Nabar, and D. Gore. *Introduction to Space-Time Wireless Communications*. Cambridge University Press, 2003. ISBN 0-521-82615-2.

[Paul04] A. J. Paulraj, D. A. Gore, R. U. Nabar, and H. Bölcskei. An overview of MIMO communications - a key to gigabit wireless. *Proceedings of the IEEE*, 92(2):198–218, February 2004.

[Pede97] K. Pedersen, P. Mogensen, and B. Fleury. Power azimuth spectrum in outdoor environments. *Electronics Letters*, 33(18):1583–1584, August 1997.

[Pede98] K. I. Pedersen, P. E. Mogensen, and B. H. Fleury. Spatial channel characteristics in outdoor environments and their impact on BS antenna system performance. In *IEEE 48th Vehicular Technilogy Conference Vehicular Technology Conference*, vol. 2, pp. 719–724. Ottawa, Canada, May 1998.

[Pede00] K. I. Pedersen, J. B. Andersen, J. P. Kermoal, and P. E. Mogensen. A stochastic multiple-input-multiple-output radio channel model for evaluation of space-time coding algorithms. In *IEEE 52nd Vehicular Technology Conference*, vol. 2, pp. 893–897. Boston, USA, September 2000.

[Pede03] K. I. Pedersen and P. E. Mogensen. Performance of WCDMA HSDPA in a beamforming environment under code constraints. In *IEEE 58th Vehicular Technology Conference*, vol. 2, pp. 995–999, October 2003.

[Pede04] K. I. Pedersen, T. F. Lootsma, M. Støttrup, F. Frederiksen, T. E. Kolding, and P. E. Mogensen. Network performance of mixed traffic on high speed downlink packet access and dedicated channels in WCDMA. In *IEEE VTS 60th Vehicular Technology Conference*. Los Angeles, USA, September 2004.

[Peis02] J. Peisa and E. Englund. TCP performance over HS-DSCH. In *IEEE 55th Vehicular Technology Conference*, vol. 2, pp. 987–991, May 2002.

[Pham99] T. Pham and K. Balmain. Multipath performance of adaptive antennas with multiple interferers and correlated fadings. *IEEE Transactions on Vehicular Technology*, 48(2): 342–352, March 1999.

[Poll04] A. Pollard and M. J. Heikkilä. A system level evaluation of multiple antenna schemes for high speed downlink packet access. In *IEEE 15th International Symposium on Personal, Indoor and Mobile Radio Communications*, vol. 3, pp. 1732–1735, September 2004.

[Pras98] R. Prasad and T. Ojanperä. An overview of CDMA evolution towards wideband CDMA. *IEEE Communications Surveys*, 1(1):2–28, 1998.

[Pric58] R. Price and P. E. Green. A communication technique for multipath channels. In *IRE*, pp. 555–570, March 1958.

[Proa87] J. G. Proakis. *Digital Communications*. McGraw-Hill International series in electrical engineering. Communications and signal processing. McGraw-Hill, Inc., 3rd printing edition, 1987. ISBN 0-07-Y66490-0.

[Proa01] J. G. Proakis. *Digital Communications*. McGraw-Hill International series in electrical engineering. Communications and signal processing. McGraw-Hill, Inc., 4th edition, 2001. ISBN 0-07-232111-3.

[Pukk03] M. Pukkila. *Iterative Receivers and Multichannel Equalisation for Time Division Multiple Access Systems*. Dissertation, Helsinki University of Technology Signal Processing Laboratory, Espoo, Finland, October 2003.

[Rale98] G. Raleigh and J. Cioffi. Spatio-temporal coding for wireless communications. In *IEEE Transactions on Communications*, vol. 46, pp. 357–366, 1998.

[Rami03a] J. Ramiro Moreno. *System Level Performance Analysis of Advanced Antenna Concepts in WCDMA*. Dissertation, Aalborg University, Aalborg, Denmark, July 2003.

[Rami03b] J. Ramiro Moreno, K. I. Pedersen, and P. E. Mogensen. Network performance of transmit and receive diversity in HSDPA under different packet scheduling strategies. In *IEEE 57th Vehicular Technology Conference*, vol. 2, pp. 1454–1458. Jeju, Korea, April 2003.

[Rami04a] J. Ramiro Moreno, L. T. Berger, L. Schumacher, and T. B. Sørensen. *Adaptive Antenna Arrays - Trends and Applications*, chapter Multiple Antenna Processing and Performance in WCDMA, pp. 568–584. Signals and Communication Technology. Springer, Heidelberg, Germany, June 2004. ISBN 3-540-20199-8.

[Rami04b] J. Ramiro Moreno, K. I. Pedersen, and P. E. Mogensen. Capacity gain of beamforming techniques in a WCDMA system under channelization code constraints. *IEEE Transactions on Wireless Communications*, 3(4):1199–1208, July 2004.

[Rant01] P. A. Ranta, M. Ventola, H. Berg, R. Wichman, and M. Heikkilä. On the evaluation of diversity reception in mobile terminals. In *The Fourth International Symposium on Wireless Personal Multimedia Communications*. Aalborg, Denmark, September 2001.

[Rao01] B. D. Rao, M. Wengler, and B. Judson. Performance analysis and comparison of MRC and optimal combining in antenna array systems. In *IEEE International Conference on Acoustics, Speech, and Signal Processing*, vol. 5, pp. 2949–2952, May 2001.

[Rapp99] T. S. Rappaport. *Wireless Communications, Principles and Practice*. Prentice Hall Communication Engineering and Emerging Technologies Series. Prentice Hall, Upper Saddler River, New Jersey, USA, 1999. ISBN 0-13-375536-3.

[Rata02] R. Ratasuk, A. Ghosh, and B. Classon. Quasi-static method for predicting link-level performance. In *IEEE 55th Vehicular Technology Conference*, vol. 3, pp. 1298–1302, May 2002.

[Rice88] J. A. Rice. *Mathematical Statistics and Data Analysis*. Wadsworth & Brooks, Belmont, USA, 1988. ISBN 0-534-08247-5.

[Rich00] K. W. Richardson. UMTS overview. *Electronics & Communication Engeneering Journal*, pp. 93–101, June 2000.

[Rosa04] C. Rosa. *Enhanced uplink packet access in WCDMA*. Dissertation, Aalborg University, Aalborg, Denmark, December 2004.

[Sama04] D. Samardzija, A. Lozano, and C. Papadias. Experimental validation of MIMO multiuser detection for UMTS high-speed downlink packet access. In *IEEE Global Telecommunications Conference*, vol. 6, pp. 3840–3844, November 2004.

[Scho94] R. A. Scholtz. The evolution of spread-spectrum multiple-access communications. In *IEEE Third International Symposium on Spread Spectrum Techniques and Applications*, vol. 1, pp. 4–13, July 1994.

[Schu00] L. Schumacher, K. I. Pedersen, J.-P. Kermoal, and P. Mogensen. A link-level MIMO radio channel simulator for evaluation of combined transmit/receive diversity concepts within the METRA project. In *Proceedings of IST Mobile Summit 2000*, pp. 515–520. IST, Galway, October 2000.

[Schu02a] L. Schumacher. *Description of the MATLAB implementation of a MIMO channel model suited for link-level simulations*. Aalborg University, Center for PersonKommunication, Cellular Systems Group, Aalborg, Denmark, 0.1 edition, March 2002.

[Schu02b] L. Schumacher, L. T. Berger, and J. Ramiro Moreno. Recent advances in propagation characterisation and multiple antenna processing in the 3GPP framework. In *XXVIth URSI General Assembly*. Maastricht, The Netherlands, August 2002. Session C2.

[Schu02c] L. Schumacher, K. I. Pedersen, and P. E. Mogensen. From antenna spacing to theoretical capacities - guidelines for simulating MIMO systems. In *PIMRC*, pp. 587–592, 2002.

[Schu04] L. Schumacher, L. T. Berger, J. Ramiro Moreno, and T. B. Sørensen. *Adaptive Antenna Arrays - Trends and Applications*, chapter Propagation Characterization and MIMO Channel Modeling for 3G, pp. 377–393. Signals and Communication Technology. Springer, Heidelberg, Germany, June 2004. ISBN 3-540-20199-8.

[SCM 03] SCM, Spatial Channel Model Ad-Hoc Group. Spatial channel model text description. Technical Report SCM-134 v6.0, 3GPP/3GPP2, April 2003.

[Shan48] C. E. Shannon. A mathematical theory of communications. *Bell Sys. Tech. Journal*, 27: 379–423, 623–656, 1948.

[Sore99] T. B. Sørensen. Slow fading cross-correlation versus azimuth separation of base stations. In *Electronic Letters*, vol. 35, pp. 127–129, January 1999.

[Stub97] G. L. Stüber. *Principles of Mobile Communication*. Kluwer Academic Publishers, Norwell, Massachusetts, USA, second printing edition, 1997. ISBN 0-7923-9732-0.

[Tann89] A. S. T. Tannenbaum. *Computer Networks*. Prentice Hall International, Englewood Cliffs, USA, 2nd edition, 1989. ISBN 0-13-166836-6.

[Tann04] R. Tanner and J. Woodard, editors. *WCDMA - Requirements and Practical Design*. John Wiley & Sons, Ltd, chichester, uk edition, 2004. ISBN 0-470-86177-0.

[Tela95] I. E. Telatar. Capacity of multi-antenna Gaussian channels. Technical Memorandum BL011217-950615-07TM, AT&T Bell Labs, June 1995. later published in European Transactions on Telecommunications, Vol. 10, No. 6, pp. 585-595, Nov/Dec 1999.

[Tokg04] Y. Tokgoz, B. D. Rao, M. Wengler, and B. Judson. Performance analysis of optimum combining in antenna array systems with multiple interferers in flat Rayleigh fading. *IEEE Transactions on Communications*, 52(7):1047–1050, July 2004.

[Toml02] M. Tomlinson, G. Wade, P. Van Eetvelt, and A. Ambroze. Bounds for finite block-length codes. *IEE Proceedings Communications*, 149(2):65–69, April 2002.

[Tran04] W. Tranter, T. S. Rappaport, K. S. Shanmugan, and K. L. Kosbar. *Principles of Communication Systems Simulation With Wireless Applications*. Prentice Hall, January 2004. ISBN 0134947908.

[Tse98] D. N. C. Tse and S. V. Hanly. Multiaccess fading channels. I. Polymatroid structure, optimal resource allocation and throughput capacities. *IEEE Transactions on Information Theory*, 44(7):2796–2815, November 1998.

[UMTS03] UMTS FORUM. Mobile evolution; shaping the future. web based publication, http://www.umts-forum.org/, London, UK, August 2003.

[Usud00] M. Usuda, Y. Ishikawa, and S. Onoe. Otimizing the number of dedicated pilot symbols for the forward link in WCDMA. In *IEEE 51st Vehicular Technology Conference*, vol. 3, pp. 2118–2122. Tokyo, Japan, May 2000.

[Vaug88] R. Vaughan. On optimum combining at the mobile. *IEEE Transactions on Vehicular Technology*, 37(4):181–188, November 1988.

[Vaug03] R. Vaughan and J. B. Andersen. *Channels, propagation and antennas for mobile communications*. IEE Electromagnetic Waves Series. The Institution of Electrical Engineers, London, UK, 2003. ISBN 0-85296-084-0.

[Vent03] M. Ventola, E. Tuomaala, and P. A. Ranta. Performance of dual antenna diversity reception in WCDMA terminals. In *The 57th IEEE Semiannual Vehicular Technology Conference*, vol. 2, pp. 1035–1040. Jeju, Korea, April 2003. Poster Session 4.

[Verd86] S. Verdú. Minimum probability of error for asynchronous Gaussian multiple-access channels. *IEEE Transactions on Information Theory*, 32(1):85–96, January 1986.

[Vill99] E. Villier. Performance analysis of optimum combining with multiple interferers in flat Rayleigh fading. *IEEE Transactions on Communications*, 47(10):1503–1510, October 1999.

[Visw02] P. Viswanath, D. N. C. Tse, and R. Laroia. Opportunistic beamforming using dumb antennas. *IEEE Transactions on Information Theory*, 48(6):1277–1294, June 2002.

[Walf88] J. Walfisch and H. L. Bertoni. A theoretical model of UHF propagation in urban environments. *IEEE Transactions on Antennas and Propagation*, 36(12):1788–1796, December 1988.

[Wang02a] H. Wang, V. Haikola, and J. Lilleberg. Advanced high speed packet access receiver for WCDMA multicode transmissions with high-order modulation. In *The 13th IEEE International Symposium on Personal, Indoor and Mobile Radio Communications*, vol. 3, pp. 1068 –1072, September 2002.

[Wang02b] H. Wang and J. Lilleberg. Interference suppression in multiple-input single-output antenna systems for WCDMA downlink transmissions. In *IEEE Seventh International Symposium on Spread Spectrum Techniques and Applications*, vol. 3, pp. 792–796, 2002.

[Weis99] A. J. Weiss and B. Friedlander. Channel estimation for DS-CDMA downlink with aperiodic spreading. *IEEE Transactions on Communications*, 47(10):1561–1569, October 1999.

[Wern99] S. Werner and J. Lilleberg. Downlink channel decorrelation in CDMA systems with long codes. In *IEEE 49th Vehicular Technology Conference*, vol. 2, pp. 1614–1617. Houston, USA, May 1999.

[Wint84] J. H. Winters. Optimum combining in digital mobile radio with cochannel interference. *IEEE Journal on Selected Areas in Communications*, 2(4):528–539, July 1984.

[Wint87] J. H. Winters. On the capacity of radio communication systems with diversity in a Rayleigh fading environment. *IEEE Journal on Selected Areas in Communications*, 5 (5):871–878, June 1987.

[Woln98] P. W. Wolniansky, G. J. Foschini, G. D. Golden, and R. A. Velenzuela. V-BLAST: An architecture for realizing very high data rates over the rich scattering wireless channel. In *URSI International Symposium on Signals, Systems, and Electronics*, pp. 295–300, September 1998.

[Zolt99] M. Zoltowski and T. P. Krauss. Two-channel zero forcing equalization on CDMA forward link: Trade-offs between multi-user access interference and diversity gains. In *33rd Asilomar Conference on Signals, Systems, and Computers*. Pacific Grove, Canada, October 1999.

[Zoub98] A. M. Zoubir and B. Boashash. The bootstrap and its application in signal processing. *IEEE Signal Processing Magazine*, 15(1):56–76, January 1998.